

Oxygen Transporter and Generator Devices to Treat Diabetic Retinopathy

Thesis by
Nicholas E. Scianmarello

In Partial Fulfillment of the Requirements for
the degree of
Doctor of Philosophy

The logo for the California Institute of Technology (Caltech), featuring the word "Caltech" in a bold, orange, sans-serif font.

CALIFORNIA INSTITUTE OF TECHNOLOGY
Pasadena, California

2019
(Defended May 8, 2019)

© 2019

Nicholas Scianmarello
ORCID: 0000-0002-1207-4029

All rights reserved

ACKNOWLEDGEMENTS

I would not have been able to complete this thesis without the unwavering support and encouragement of my mother, father, and brother. I will always be grateful for the time you spend helping me, and the advice you have given me. You have made me who I am today.

I greatly appreciate the help from my longtime friends, Dr. Gary Binder and Dr. Zagid Abatchev. Our many discussions over the years are been memorable. Gary, I appreciate your help with resolving PDEs and the intuition in physics with which you have helped me time and time again. Zagid, I will always be grateful that you converted me from a perpetual MATLAB user to a permanent Python user. I would also like to say thank you to my friends, Paul Suffoletta, Daniel Rosenberg, Casey Glick, Jan Petikiwietz, Amy Lam, Debbie Tsai and Joaquin Gabaldon, who have been there for me over the years. I would also like to mention my good friend, Prof. Constantine Sideris, who has been an invaluable source of advice on graduate school, and circuits.

The Caltech MEMS Lab would not be able to function without Trevor Roper's endless knowledge on machine and equipment. I am always amazed at how you have managed to keep everything running. I have learned so much from you about how lab equipment works. Christine Garske, you cut through bureaucracy for us, and made it possible for us to do research. I think nothing would ever get done without you. Thank you for all your help over the years. Professor Tai, thank you for giving me the opportunity to work in your world-renowned lab. I am grateful you took me on as a graduate student. It has been a unique opportunity be able to work on such cutting edge subject matters. Your guidance throughout my Ph.D. has molded my work.

When I began working in Caltech's MEMS Lab, Dr. Charles DeBoer mentored me. Thank you for patience and teaching me the Su-8 and the Parylene CVD coating processes. Your work laid the groundwork for much of what I have done in this thesis. Dr. Justin Kim and Dr. Jungwook Park, I appreciate your mentorship over the years. Dr. Kim trained me in many of the cleanroom processes I have used throughout my thesis; your care in explaining not just the how but the why for these processes has been invaluable. Dr. Park, your help with the dry film process, and your expertise in fabrication is the bedrock of this thesis. I cannot express enough gratitude for your help.

I am glad I had the chance to work with Dr. Dongyang Kang, Dr. Yang Liu, Dr. Yu Zhao, Dr. Han-Chieh Chang, Tzu Chieh Chou, and Kuang Min Shang. You have been splendid colleagues and I have learned a great deal from working alongside you all. I could not have asked for better lab mates. Aubrey Shapero, your sense of humor always brightened my day. I appreciate your advice and electrical engineering prowess, which I have come to rely on over the course of my Ph.D. I was fortunate to have the opportunity to work with Dr. Colin Cook. Your lateral thinking and ability to find efficiencies advanced my thesis work immensely. Your impact on the nanoporous device cannot be understated. You have made much of what I have done possible. I hope we have the opportunity to collaborate again in the future.

Professor Mark Humayun of USC has led this project. My thesis would have been very different without this Caltech-USC collaboration. Thank you for taking the time to meet and discuss, and for your patience with all the delays and setbacks in the design. Through this collaboration I had the opportunity to work with great people from USC, Dr. Karthik Murali and Dr. Juan Carlos Martinez-Camarillo. Karthik, I appreciate your friendship over the years. Your wisdom and advice helped this thesis move forward. I hope I have the opportunity to collaborate on some project with you in the future. I do not exaggerate when I say that a good portion of this work would not have happened without the aid of Dr. Juan Carlos Martinez-Camarillo. You implanted every single one of my devices, and helped shape them to best suit surgical requirements. I will always be at awe by your surgical skill and insight.

ABSTRACT

In recent years, Micro-Electrical Mechanical Systems (MEMS) have opened new areas of the human body to non-pharmacological treatment. Miniaturized implants have started to appear in volume or power constrained areas, such as the eye and the heart. In particular, the eye benefits from miniaturization, as it is very sensitive to pressure and volumetric changes, which can affect eyesight and blood flow.

Diabetic retinopathy is the worldwide leading cause of blindness among working age adults. As the numbers of diabetics increases, so does the number of retinopathies. By 2030, 191 million people are expected to be affected by the disease. As a patient's retinopathy progresses, the chronic hyperglycemia from diabetes causes permanent changes to the vasculature; vessels become leaky and occluded, tissue becomes hypoxic due to this ischemia and begins to release vascular endothelial growth factor (VEGF) to promote angiogenesis.

Currently, treatments exist only for severe non-proliferative or proliferative DR, and rely on blocking VEGF (vascular endothelial growth factor) or panretinal laser photocoagulation to reduce retinal metabolic demand. VEGF antagonists are expensive; costing up to \$164k per quality life adjusted year and must be administered by intravitreal injections monthly. Laser photocoagulation also requires retreatment and is known to reduce peripheral vision—up to 20% of the peripheral retina is ablated. Another treatment approach may be to supply oxygen. Oxygen is a strong vasoconstrictor and suppresses the hypoxic signaling that leads to release of VEGF. These two effects reduce the plasma volume leaked into tissue, which in turn reduces edema, and may help prevent ischemic related cell death. Literature supports this assertion. A study of nasally inspired oxygen in patients with macular edema showed a reduction of edema and improvement of visual acuity following 3 months of treatment. Another study on rabbits with an induced ischemia demonstrated that intravitreal oxygenation maintained the retina to a near healthy condition.

In this thesis, two devices, the oxytransporter and oxygenerator, that treat diabetic retinopathy are designed and tested. The former shuttles oxygen from areas of high concentration to the ischemic retina. The latter generates oxygen by electrolysis.

This thesis is grounded on a computational model of oxygen consumption in the retina. To estimate the oxygen consumption, the model accounts for the anatomical distribution of tissue and vasculature in the retina. Previous models in literature averaged over the effects in the inner retina. The model estimates that the devices must supply 0.25nmol/s of oxygen to the human macula with an oxygen tension dependent on the degree of ischemia.

A nanoporous filler material was developed and integrated into the oxytransporter to allow this device to operate in the high humidity environment of the eye. The material is capable of withstanding an environment with water vapor 1.4 times the bulk saturation pressure. Theory behind the material was tested and compared to simulation. Benchtop testing over a month demonstrated the stability of the device in conditions similar to the eye. This oxytransporter was implanted in rabbits and the diffusor, or output membrane, reached the favorable mark of 100mmHg in the vitreous humor from atmospheric oxygen alone. This is estimated to be sufficient to treat a mild to moderate ischemia in humans.

The oxygenerator is powered from a coil up to 3cm away, and can provide 0.25nmol/s continuously with an oxygen tension of up to 300mmHg for a human sized diffusor. A steady state test demonstrated the capability of maintaining the oxygen tension in the device by modulating the input power. The device is replenished through osmosis from the vitreous humor, and can absorb moisture at a rate comparable to the required oxygen consumption. One week implantation *in vivo* in rabbits demonstrated that the oxygen tension exceeded 200mmHg at the diffusor, which is estimated to be sufficient to treat severe ischemia.

Future work should involve a study of the long term effects of oxygen in an ischemic animal model.

TABLE OF CONTENTS

| | |
|--|-----------|
| CHAPTER 1 – INTRODUCTION | 1 |
| 1.1 ANATOMY OF THE HUMAN EYE, PATHOLOGY OF DIABETIC RETINOPATHY AND THE EFFECT OF OXYGEN | 2 |
| 1.1.1 THE STRUCTURE OF THE EYE..... | 2 |
| 1.1.2 THE STRUCTURE OF THE RETINA..... | 4 |
| 1.2 PATHOLOGY OF DIABETIC RETINOPATHY | 7 |
| 1.3 TREATING WITH OXYGEN..... | 11 |
| 1.4 REFERENCES | 12 |
| CHAPTER 2 – MODELING OXYGEN TRANSPORT IN THE RETINA | 17 |
| 2.1 SIMPLE, 4-LAYER, 1-DIMENSIONAL MODEL OF THE RETINA..... | 17 |
| 2.2 CAPILLARY OCCLUSION, 8-LAYER MODEL..... | 24 |
| 2.3 AXISYMMETRIC MODEL OF THE MACULA AND SURROUNDING PERIPHERY | 28 |
| 2.3.1 MODELING VEGF EXPRESSION IN THE RETINA | 33 |
| 2.3.2 MODELING AND OPTIMIZING THE DEVICE | 35 |
| 2.4 REFERENCES | 44 |
| CHAPTER 3 – HARVESTING OXYGEN: THE OXYTRANSPORTER | 48 |
| 3.1 THE OXYTRANSPORTER | 48 |
| 3.2 CONDENSATION | 53 |
| 3.3 A NANOSCALE FILLER MATERIAL | 60 |
| 3.3.1 HYDROPHOBIZATION OF NANOPOROUS GLASS | 62 |
| 3.3.2 VALIDATING THE NANOPOROUS ANTI-CONDENSATION FILLER | 63 |
| 3.3.3 DESIGNING THE IMPLANT | 68 |
| 3.3.4 IMPLANT TESTING: <i>IN VIVO</i> AND <i>IN VITRO</i> | 71 |
| 3.4 REFERENCES | 74 |
| CHAPTER 4 – GENERATING OXYGEN: THE OXYGENERATOR | 78 |
| 4.1 OXYGENERATOR DESIGN | 78 |
| 4.2 ELECTROLYSIS | 80 |
| 4.2.1 A TEST PLATFORM | 81 |
| 4.2.2 ELECTROLYSIS EFFICIENCY | 84 |
| 4.3 RECOMBINATION RATE | 88 |
| 4.4 REPLENISHMENT | 88 |
| 4.4.1 INJECTIONS INTO AN ELECTROLYTE RESERVOIR | 89 |
| 4.4.2 REPLENISHMENT BY OSMOSIS..... | 93 |

| | |
|--|------------|
| 4.5 REFERENCES | 100 |
| CHAPTER 5 – ELECTRICAL POWER | 102 |
| 5.1 OPTICAL POWER DELIVERY | 102 |
| 5.2 KINETIC ENERGY HARVESTING | 106 |
| 5.3 INDUCTIVE POWER COUPLING..... | 111 |
| 5.3.1 THEORY | 112 |
| 5.3.2 SECONDARY COIL FABRICATION..... | 121 |
| 5.3.3 QUANTIFYING THE COILS..... | 124 |
| 5.4 REFERENCES | 129 |
| CHAPTER 6 – FABRICATION..... | 132 |
| 6.1 BIOCOMPATIBLE MATERIALS | 132 |
| 6.1.1 SILICONE | 132 |
| 6.1.2 PARYLENE..... | 133 |
| 6.1.3 USE OF PARYLENE AND SILICONE IN A DEVICE | 135 |
| 6.2 MOLD FABRICATION | 135 |
| 6.2.1 NEGATIVE EPOXIDE PHOTORESIST: MICROCHEM SU-8..... | 135 |
| 6.2.2 DRY-FILM PHOTORESIST PATTERNING: DUPONT WBR2120..... | 137 |
| 6.3 SILICONE CASTING..... | 140 |
| 6.3.1 MAKING AN ENCLOSED SHAPE..... | 142 |
| 6.3.2 PARYLENE ON SILICONE RESERVOIR | 145 |
| 6.3.3 FUSED DEPOSITION PRINTING OF RESERVOIR MOLDS | 147 |
| 6.4 DEVICE ITERATIONS AND CONSIDERATIONS | 149 |
| 6.5 REFERENCES | 153 |
| CHAPTER 7 – OXYGEN DISTRIBUTION..... | 154 |
| 7.1 LONGEVITY OF THE OXYGENERATOR: ACCELERATED LIFETIME TEST | 154 |
| 7.2 OXYGEN PRODUCTION IN DEVICE WITH A RESERVOIR | 156 |
| 7.2.1 IMPLANTATION OF THE OXYGENERATOR IN RABBITS | 159 |
| 7.3 MODULATING OXYGEN PRODUCTION IN AN OSMOSIS REFILLABLE DEVICE | 167 |
| 7.3.1 OXYGEN PRODUCTION IN AN OSMOSIS REFILLABLE DEVICE | 167 |
| 7.3.2 PULSE-WIDTH MODULATION CONTROL OF OXYGEN TENSION..... | 170 |
| 7.4 METABOLIC CHANGES IN THE RABBIT | 173 |
| 7.5 CONCLUSION..... | 177 |
| 7.6 REFERENCES | 177 |

LIST OF FIGURES

| | |
|--|----|
| Figure 1.1: Cross section of the eye..... | 2 |
| Figure 1.2: Vascular network in the inner retina..... | 3 |
| Figure 1.3: Overlay and cross section of the macula..... | 4 |
| Figure 1.4: Diagram of the retina divided into its constituent layers.]..... | 5 |
| Figure 1.5: Oxygen profile of in a rat retina..... | 7 |
| Figure 1.6: Pathology of diabetic retinopathy..... | 9 |
| Figure 1.7: Oxygenating an ischemic rabbit retina..... | 12 |
| Figure 2.1: Layers of the retina for computational models..... | 18 |
| Figure 2.2: 4-layer computational model of the retina..... | 20 |
| Figure 2.3: 4-layer computational model of the retina with 100mmHg device..... | 21 |
| Figure 2.4: 4-layer computational model of the retina with 150mmHg device..... | 22 |
| Figure 2.5: Intraretinal oxygen profiles of mammals..... | 23 |
| Figure 2.6: VEGF mRNA expression in human eyes..... | 24 |
| Figure 2.7: OCT of human inner retinal vasculature..... | 25 |
| Figure 2.8: 8-layer computational model of the retina..... | 26 |
| Figure 2.9: Oxygen profile along the depth of the 8 layer retinal model..... | 27 |
| Figure 2.10: Diagram of the retinal layers in the model..... | 29 |
| Figure 2.11: 9-layer axisymmetric computational model of the retina..... | 31 |
| Figure 2.12: Perifoveal oxygen profile for the 9 layer computational model..... | 32 |
| Figure 2.13: Low oxygen tension in simulation versus human VEGF expression..... | 33 |
| Figure 2.14: Simulation of VEGF upregulation in the retina..... | 34 |
| Figure 2.15: 9-layer model with 200mmHg device..... | 36 |
| Figure 2.16: Simulation with 33 $\mu\text{L}/\text{min}$ and 200mmHg device (vitreous not plotted)..... | 36 |
| Figure 2.17: Ischemia model with varying device oxygen tension..... | 37 |
| Figure 2.18: Simulation VEGF upregulation for different device oxygen tension..... | 39 |
| Figure 2.19: Contour map of moles of oxygen in the inner macula..... | 41 |
| Figure 2.20: Contour map of oxygen consumption in the inner macula..... | 42 |
| Figure 2.21: Contour map of VEGF upregulation in the GCL an IPL..... | 43 |
| Figure 3.1: Oxytransporter concept..... | 48 |
| Figure 3.2: Fabricated oxytransporter devices with bent cannula..... | 51 |
| Figure 3.3: Simulation versus animal data for the oxytransporter..... | 52 |
| Figure 3.4: <i>in vivo</i> condensation in the device..... | 53 |
| Figure 3.5: Simulation of temperature profile of the oxytransporter..... | 55 |
| Figure 3.6: Simulation of water vapor partial pressure (mmHg) in the oxytransporter..... | 56 |
| Figure 3.7: Simulation of relative humidity inside the oxytransporter..... | 57 |
| Figure 3.8: Simulation of time progression for relative humidity in the oxytransporter..... | 58 |
| Figure 3.9: Simulation of condensation in the cannula..... | 58 |
| Figure 3.10: Simulation of Parylene coating on the lower half of the input..... | 59 |
| Figure 3.11: COMSOL simulation humidity in bent oxytransporter..... | 60 |
| Figure 3.12: Kelvin equation..... | 61 |
| Figure 3.13: SEM image of treated Vycor 2930 nanoporous glass..... | 62 |
| Figure 3.14: Hydrophobicity of silanized Vycor 2930..... | 63 |

| | |
|--|-----|
| Figure 3.15: Oxygen permeability of hydrophobic Vycor 2930. | 64 |
| Figure 3.16: Hydrophobic Vycor’s resistance to occlusion under high humidity..... | 68 |
| Figure 3.17: Exploded computer rendering of nanoporous-filled oxytransporter..... | 69 |
| Figure 3.18: Nanoporous-filled oxytransporter fabrication. | 70 |
| Figure 3.19: Soaking stability of device. | 72 |
| Figure 3.20: <i>In vivo</i> oxygen profile surrounding the device. | 73 |
| Figure 4.1: System diagram of the oxygen generating device..... | 79 |
| Figure 4.2: Electrolysis test chip..... | 82 |
| Figure 4.3: Electrolysis test chip fabrication. | 82 |
| Figure 4.4: Electrolysis test setup. | 83 |
| Figure 4.5: Microelectrodes boded to test chip. | 84 |
| Figure 4.6: I-V curve for Pt microwires with respect to MgSO ₄ concentration. | 86 |
| Figure 4.7: Oxygen generator device diagram.. | 89 |
| Figure 4.8: Needle fill of oxygen generator device..... | 90 |
| Figure 4.9: Silicone septum and leakage. | 91 |
| Figure 4.10: Leak in version 5 of the active device after electrolysis in rabbit..... | 92 |
| Figure 4.11: Microchannel formed by non-coring needle in silicone. | 93 |
| Figure 4.12: Osmosis through silicone. | 97 |
| Figure 4.13: Osmotically refilled device. | 98 |
| Figure 4.14: Time lapse images of diffusor filling up with water. | 99 |
| Figure 4.15: Snapshot of diffusor during electrolysis. | 100 |
| Figure 5.1: Optical transmittance of the conjunctiva. | 103 |
| Figure 5.2: Photovoltaic energy harvesting circuit. | 103 |
| Figure 5.3: Location for implantable photovoltaic cells. | 105 |
| Figure 5.4: Exposed conjunctiva on the rabbit eye. | 106 |
| Figure 5.5: Amplitude for a proof mass..... | 109 |
| Figure 5.6: Average power over a cycle for different damping factors..... | 110 |
| Figure 5.7: Concept of the inductive power transfer circuit. | 111 |
| Figure 5.8: Circuits for inductively coupled power transfer. | 112 |
| Figure 5.9: Plot of the total impedance of the primary without the secondary. | 115 |
| Figure 5.10: LT1206 amplifier.. | 116 |
| Figure 5.11: Primary side device. | 118 |
| Figure 5.12: Primary side impedance with a series capacitor..... | 119 |
| Figure 5.13: Measured impedance and phase for primary circuit. | 120 |
| Figure 5.14: DRIE etched silicon mold for coil. | 122 |
| Figure 5.15: An aluminum spindle. | 123 |
| Figure 5.16: Automatic coil winder..... | 124 |
| Figure 5.17: 20 Turn coil, with 5.4mm in diameter. | 124 |
| Figure 5.18: Coil test setup. | 125 |
| Figure 5.19: Polar plot of secondary side rectified voltage. | 126 |
| Figure 5.20: Rectified secondary coil voltage at angle of 0°. | 127 |
| Figure 5.21: Rectified coil voltage with 1k Ω load. | 127 |
| Figure 5.22: Received power on secondary coil with 1k Ω load..... | 128 |
| Figure 5.23: Power efficiency at 0°..... | 128 |
| Figure 5.24: Power efficiency with 1k Ω load. | 129 |
| Figure 6.1: Poly(p-xylylene) chemical structures. | 133 |

| | |
|--|-----|
| Figure 6.2: Parylene deposition process. | 134 |
| Figure 6.3: Oxygen tension on opposite sides of a device coated with parylene on one side. | 135 |
| Figure 6.4: Su-8 Spin curve. | 136 |
| Figure 6.5: Hotplate temperature curve for Su-8 soft baking and post-exposure baking. | 136 |
| Figure 6.6: DuPont WBR2120 dry film fabrication process. | 140 |
| Figure 6.7: Silicone molding process using dry film mold. | 141 |
| Figure 6.8: NuSil MED4-4210 silicone curing test. | 143 |
| Figure 6.9: Silicone bag resilience. | 145 |
| Figure 6.10: Parylene coated silicone bag resilience. | 146 |
| Figure 6.11: FDM 3-D printing molds. | 147 |
| Figure 6.12: 3D molded silicone device. | 148 |
| Figure 6.13: Different versions of the oxygen generating device. | 149 |
| Figure 6.14: Fabrication of version 1 of the oxygen generating device. | 151 |
| Figure 6.15: Computer rendering of parts of version 5 of the device. | 152 |
| Figure 7.1: Soak testing Parylene PCB. | 154 |
| Figure 7.2: Close up of Parylene PCB soak test. | 155 |
| Figure 7.3: Soak testing osmotically refilled device electronics. | 155 |
| Figure 7.4: Bench testing needle refilled oxygen generating device. | 156 |
| Figure 7.5: Oxygen profile during electrolysis for needle refilled device. | 157 |
| Figure 7.6: Simulation of partial oxygen distribution over time for needle refilled device. | 158 |
| Figure 7.7: Oxygen tension vs. distance from diffusor. | 159 |
| Figure 7.8: Rabbit implant procedure. | 160 |
| Figure 7.9: <i>In vivo</i> spatial oxygen distribution from the device. | 162 |
| Figure 7.10: <i>In vivo</i> oxygen tension during electrolysis. | 162 |
| Figure 7.11: <i>In vivo</i> vs. <i>in vitro</i> oxygen tension during electrolysis. | 163 |
| Figure 7.12: The decay time of 5 minute <i>in vivo</i> activation of the device. | 164 |
| Figure 7.13: Human diffusor versus rabbit diffusor. | 166 |
| Figure 7.14: Bench oxygen tension during electrolysis vs. activation time. | 167 |
| Figure 7.15: <i>In vivo</i> comparison of different device versions. | 169 |
| Figure 7.16: Effect of diffusor membrane thickness on oxygen response. | 169 |
| Figure 7.17: Power amplifier P.W.M. control circuitry. | 170 |
| Figure 7.18: Secondary side diode feedback circuit. | 171 |
| Figure 7.19: Implant bench test setup. | 171 |
| Figure 7.20: Pulse width modulated oxygen output from primary side control. | 172 |
| Figure 7.21: Laser-induced RVO on a rabbit. | 174 |
| Figure 7.22: Changes in protein expression in rabbit after laser-induced retinal vein occlusion. | 174 |
| Figure 7.23: Effect of oxytransporter on NF- κ B and IKK α expression in rabbit. | 175 |
| Figure 7.24: Effect of oxytransporter on PDH and JNK expression in rabbit. | 176 |

LIST OF TABLES

| | |
|--|-----|
| Table 1.1: Ischemia for different severities of DR. | 10 |
| Table 2.1: Capillary Density as per Campbell et al., 2011 | 25 |
| Table 2.2: Retinal layer thickness. | 25 |
| Table 2.3: AXSY model parameters. | 29 |
| Table 2.4: Oxygen consumption and severity of DR in the simulation..... | 30 |
| Table 2.5: VEGF upregulation by layer..... | 35 |
| Table 2.6: Simulated oxygen flux from diffusor. | 44 |
| Table 3.1: Partial pressures of a healthy adult inspiring atmospheric oxygen. | 49 |
| Table 3.2: Oxygen Permeability of different materials. | 50 |
| Table 3.3: Parameters for heat transport simulation..... | 55 |
| Table 3.4: Parameters for water vapor transport | 55 |
| Table 3.5: Parameters used in the COMSOL simulation of Vycor. | 65 |
| Table 4.1: Power efficiency of Au and Pt-Ir microelectrodes..... | 85 |
| Table 4.2: Faradic efficiency of Au and Pt-Ir microelectrodes..... | 85 |
| Table 4.3: Power efficiency of Pt microwires. | 85 |
| Table 4.4: Faradic efficiency of Pt microwires. | 85 |
| Table 4.5: The Tafel Equation fitted against the different solution concentrations. | 87 |
| Table 4.6: Recombination rate measurements for Pt microwires..... | 88 |
| Table 4.7: Fit parameters for osmosis through a silicone membrane. | 97 |
| Table 5.1: Lumens from standard household bulbs..... | 104 |
| Table 5.2: Parameters for estimation of energy extracted by a kinetic energy harvester..... | 109 |
| Table 5.3: Components in primary coil measured with the HP 4192A..... | 119 |
| Table 6.1: Exposure time for DuPont WBR2120..... | 140 |
| Table 6.2: Slopes for silicone curing test..... | 144 |
| Table 7.1: One week rabbit trials with devices with liquid reservoir. | 161 |

CHAPTER 1 – INTRODUCTION

The technology and techniques of Micro-Electrical Mechanical Systems (MEMS) allow implants to be miniaturized, so that some diseases can be treated non-pharmacologically. Recently, miniaturized implants are targeting the eye (SecondSight's Argus II retinal implant, Sensimed Triggerfish IOP sensor, Ahmed Glaucoma Drainage Valve [1.1]). The eye, being severely constrained, is an organ suitable for the application of MEMS technology.

The World Health Organization (WHO) identifies as the leading causes for blindness: cataracts, glaucoma, age-related macular degeneration, corneal opacities, diabetic retinopathy (DR), trachoma, and eye conditions such as vitamin deficiencies in children [1.2]. WHO's Global Data on Visual Impairments informs that 285 million have visual impairment, of which 39 million are blind [1.3].

Diabetic retinopathy (DR) lead the causes of blindness among working age adults [1.4], [1.5]. Even more troubling, all forms of diabetes related blindness are on the rise [1.2]. As of 2010, 95 million people have been diagnosed with some form of DR, of which 32 million suffer a form that may threaten vision. The number affected with DR is expected to increase to 191 million by 2030, of which the threatened with blindness is expected to increase to 56.3 million [1.6]. The Wisconsin Epidemiologic Study of Diabetic Retinopathy (WESDR) found that the 25-year cumulative rate of progression of DR was 83% for type 1 diabetes [1.7]. For patients diagnosed with diabetes before the age of 30, the WESDR found that 59% would develop retinopathy within 4 years of the study's start, of which 17% would develop proliferative DR (PDR) within 14 years [1.7]. The number of early detections is expected to increase even further with the new machine learning algorithms [1.8].

Notwithstanding these overwhelming statistics, current early treatments of DR are limited to managing glucose levels, lipids, and blood pressure. Pharmacological or laser interventions, costly and with side-effects, are only applied for the vision threatening stages of the DR.

MEMS technology has an important role to play in helping to treat DR.

1.1 ANATOMY OF THE HUMAN EYE, PATHOLOGY OF DIABETIC RETINOPATHY AND THE EFFECT OF OXYGEN

1.1.1 THE STRUCTURE OF THE EYE

As can be seen in **Figure 1.1**, the eye is comprised of two sections: the anterior chamber, where light enters the cornea and travels through the aqueous humor and the lens, focusing the light onto the retina, and the posterior chamber which contains the retina and a transparent gel, the vitreous humor.

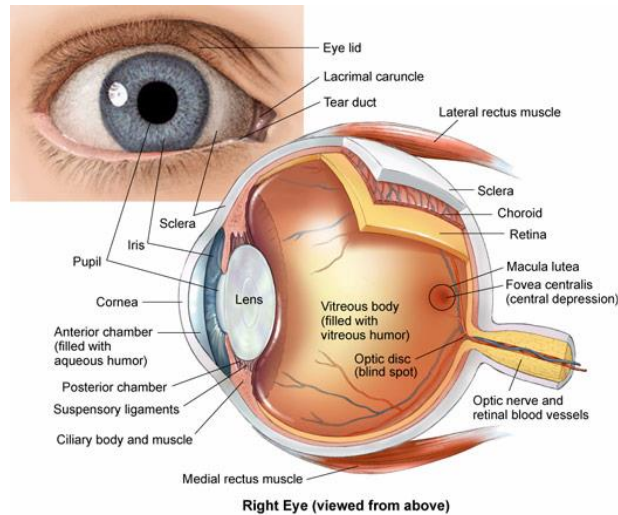


Figure 1.1: Cross section of the eye. Reprinted from [1.9]

Upon reaching the photoreceptor cells in the outer retina, the light is converted into an electrochemical signal, which signals the nerve and ganglion layers in the inner retina. This signal travels down the optic nerve to the brain. To maintain optical clarity few vessels lie within the optical path from the cornea until the surface of the retina. However, a sparse layer of blood vessels supply nutrients and oxygen the nerve cells of the inner retina, through the central retinal artery and returning through the central retinal vein. The outer retina, containing the photoreceptors, is primarily supplied by a dense network of vessels directly behind it, named the capillary lamina of choroid.

The exterior of the eye is covered by the (bulbar) conjunctiva, a thin membrane of epithelium, which surrounds the sclera, the white of the eye, and lines the inside of the eyelid (palpebral conjunctiva). The conjunctiva connects to the cornea in the anterior of the eye.

The sclera surrounds the cornea and extends to the optic nerve in the back of the eye. The sclera protects and maintains the shape of the eye. The choroid is a vascularized layer of tissue sandwiched between the retina and the sclera.

The central retinal artery connects to the capillaries of the choroid and to the inner retinal capillary beds. The circulation system connects between the central retinal capillary and the central retinal vein through arterioles. The artery branches out into capillaries that are diffused through the tissue before connecting to a venule. The choroid's dense blood vessel network feeds the rods and cones. The inner is supplied by its capillaries.

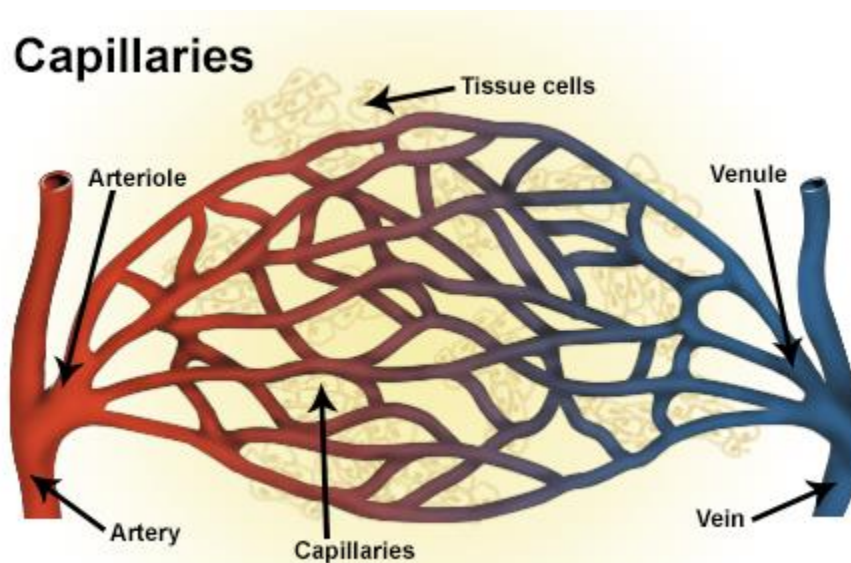


Figure 1.2: Vascular network in the inner retina. Reprinted from [1.10]

The human retina can be divided into the macula lutea and the peripheral retina. The center of the macula lutea contains the fovea centralis, a small pit with a high density of cone cells [1.11]. This fovea centralis allows for sharp vision. It is surrounded by the parafovea containing ganglion cells that receive signals from the cones of the fovea centralis as well as the densely packed cone cells in the parafovea. The parafovea has the thickest ganglion cell layer. Visual acuity falls off at the perifovea, the outermost ring of the macula [1.11]. The peripheral retina surrounds the macula and is comprised mostly of rod cells. Cone cells allow for color vision. There are three types of cone cells corresponding to different absorption spectrums. Rod cells respond solely to light intensity and are responsible for low light vision. The peripheral retina is therefore responsible for night vision. In a lighted environment, these cells are photo-bleached and desensitized (turned off).

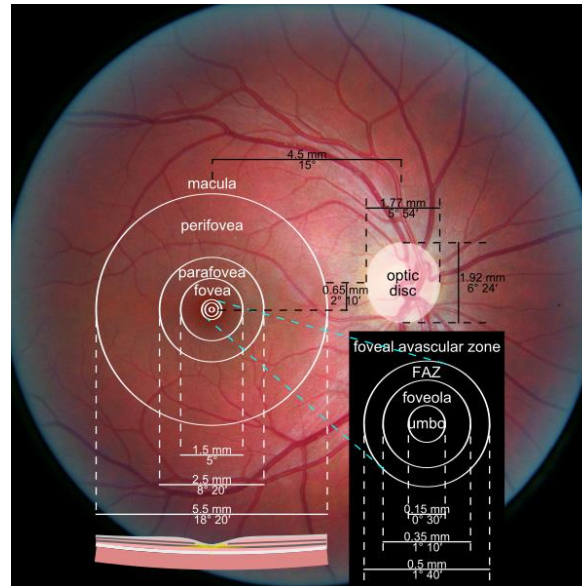


Figure 1.3: Overlay and cross section of the macula. Reprinted from [1.12]

Most large inner retinal capillaries (retinal branch arteries and veins) extend into the perifovea. Few other vessels extend into the parafovea or farther in. The vessels in the inner retina extend only up to the foveal avascular zone (1mm diameter). The foveal avascular zone thins out; consequently blood supply is exclusively from the choroid.

1.1.2 THE STRUCTURE OF THE RETINA

The retina may be broadly divided into the inner and outer retinas. The outer retina contains the photoreceptor cells (rods and cones) and the retinal pigment epithelium (RPE), which is in contact with the choroid. The photoreceptors are stacked vertically. The photoreceptor is divided into the outer segment of the photoreceptors (OSP), the inner segment of the photoreceptors (ISP) and the outer nuclear layer (ONL). The outer segment contains the photosensitive portions with photopsin's (cones) or rhodopsin (rods). The inner segment contains the photoreceptor cell's mitochondria and is responsible for the cell's oxygen consumption. The nucleus of the cell lies in the outer nuclear layer with its synaptic terminal extending into the outer plexiform layer that connects with bipolar and horizontal cells.

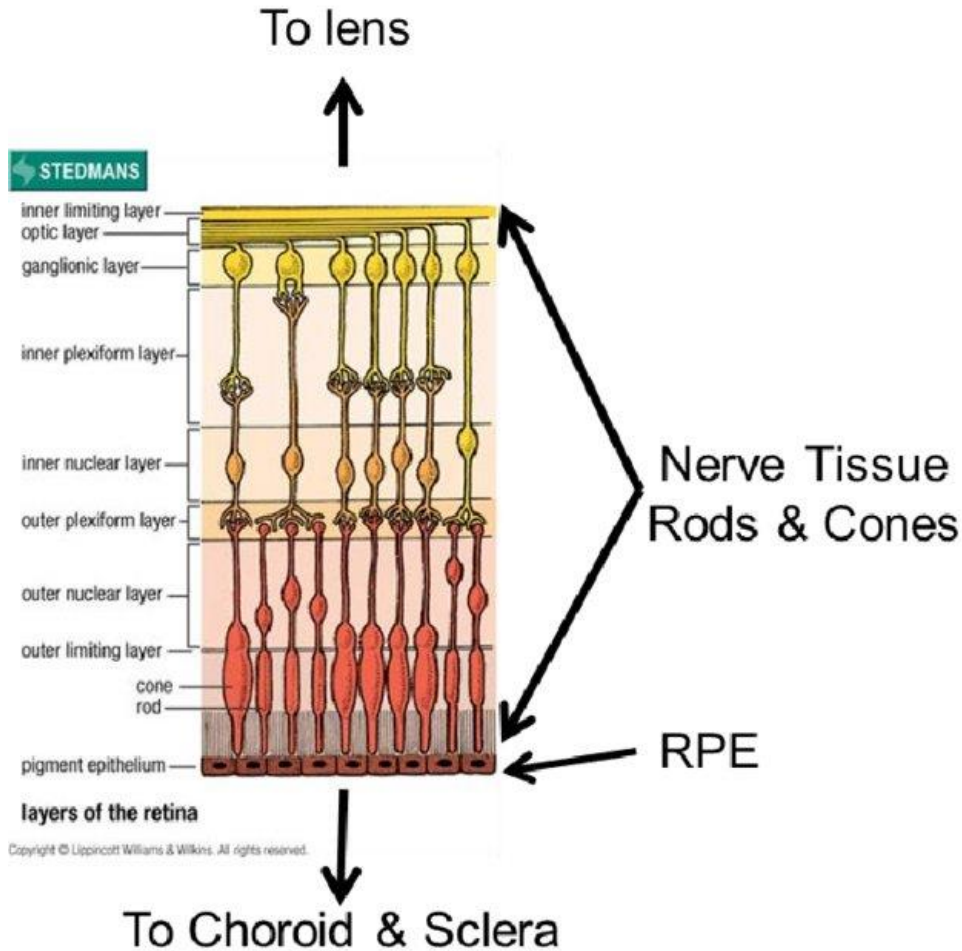


Figure 1.4: Diagram of the retina divided into its constituent layers. Reprinted from [1.13]

The inner retina contains the nerve cells and is responsible for transmitting the signal through the optic nerve to the brain. Bipolar cells act as intermediaries between ganglion cells and photoreceptors. Photoreceptors trigger ON bipolar cells to depolarize when light stimulates a photoreceptor, and cause OFF bipolar cells to hyperpolarize [1.14]. In the absence of light, photoreceptors will instead hyperpolarize ON bipolar cells, and depolarize OFF bipolar cells. This signal is transmitted to the ganglion cells either directly or indirectly. Horizontal cells form a negative feedback loop with neighboring photoreceptors; a photoreceptor will hyperpolarize a horizontal cell causing it to depolarize neighboring photoreceptor cells. Conversely, when no light is applied, a photoreceptor will depolarize horizontal cells, and hyperpolarize neighboring photoreceptor cells. This inhibition process results in increased contrast of images.

These bipolar and horizontal cells synapse with photoreceptors at the outer plexiform layer (OPL). The nuclei of these cells and cell bodies are located in the inner nuclear layer (INL). The INL is responsible for part of the inner retina's oxygen and nutrient consumption. The axons of bipolar cells interact with the dendrites of ganglion cells in the inner plexiform layer (IPL). Ganglion cells receive information from many rod and cone cells and transmit the signal through the optic nerve. The number of photoreceptors with which a given ganglion cell interacts vary along the eye. The density of ganglion cells is highest in the fovea centralis [1.15]. This higher density results in a thicker GCL in the macula [1.16]. The nuclei of ganglion cells lie in the ganglion cell layer (GCL) with their axons residing in the nerve fiber layer (NFL). Finally, the inner limiting membrane (ILM) acts as a boundary between the inner retina and the vitreous humor, and contains an extracellular matrix which acts as a substrate for retinal tissue.

The inner retina is served by a capillary network in the GCL, the superficial vascular plexus (SVP), and by a network in the INL, the deep capillary plexus (DCP) [1.16]. The highest density of these capillary networks corresponds to the layers containing inner retinal the nuclei and cell. Within the macula, the deep nuclear plexus divides into the intermediate capillary plexus (ICP) and the DCP [1.16]. The presence of these capillary networks and cells can be observed through the oxygen profiles of the mammalian retina. In a rat, the choroid, SVP, and DCP exhibited intraretinal oxygen peaks when Yu and Cringle [1.17] inserted an oxygen microprobe into the retina (**Figure 1.5**). The IPS consumption is reflected in the dip 250 μ m to 300 μ m.

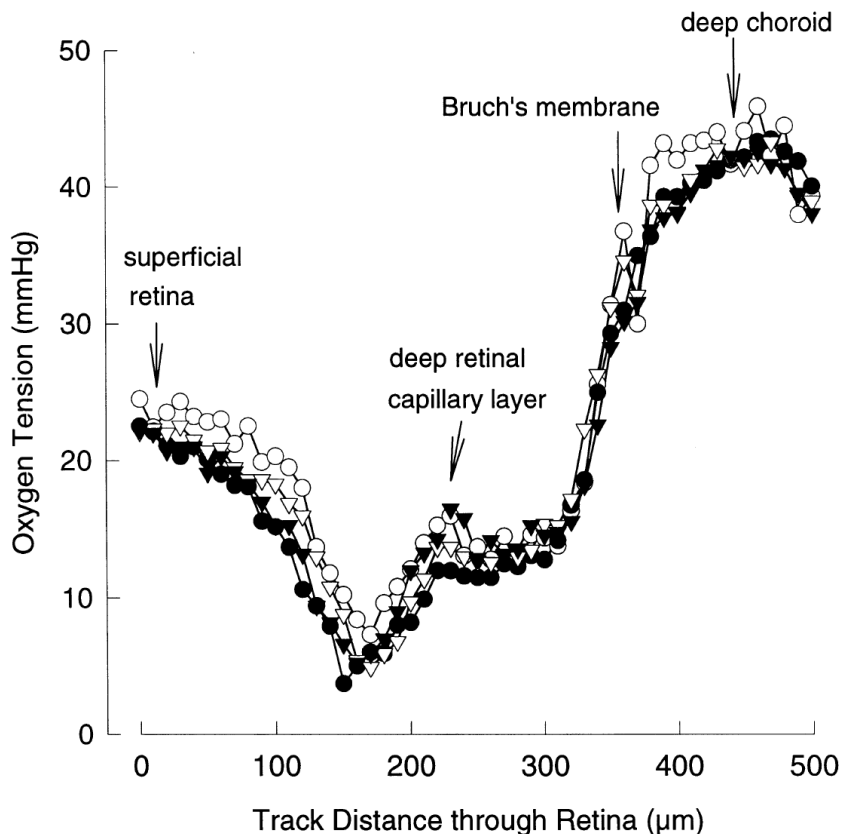


Figure 1.5: Oxygen profile of in a rat retina. Two sequential measurements by Yu et al. Reprinted from [1.17]

1.2 PATHOLOGY OF DIABETIC RETINOPATHY

Diabetic retinopathy is a microangiopathy resultant from chronic hyperglycemia, an excess glucose in blood plasma. This chronic hyperglycemia results in an increase of inflammatory cytokines, leukocyte activation [1.18], [1.19], and loss of capillary pericytes—multi-functional cells that wrap around capillaries and venules [1.18]. Pericyte cells are important for microvascular autoregulation. Their loss impairs the blood-retina barrier [1.18]. Pericytes are responsible for exerting pressure on the capillary walls to counteract blood pressure. Their loss results in venous dilation and vascular endothelial proliferation that eventually cause microaneurysms [1.18]. Hypertension is an additional risk factor for microaneurysms as the weakened vessel wall is exposed to increased pressure. Retinopathy is also known to thicken the capillary basement membrane through the vacuolization of the membrane's collagen [1.18]. This results in increased blood leakage from blood vessels. In addition, the tight junctions of the capillary are prone to failure (**Figure 1.6**) [1.19]. The weakened,

and now permeable, capillaries walls result in microaneurysms, which are the first clinically visible sign of DR [1.18]. These microaneurysms can be observed by either light microscopy or fluorescein angiography. Macular edema may result from the subfoveal fluid buildup from this breakdown of the blood-retina barrier. The edema may result in vision loss. This edema is usually treated with intravitreal corticosteroids (100mg doxycycline daily) to improve visual acuity and decrease foveal thickness [1.18]

The permeability of the vasculature is increased in the presence of vascular endothelial growth factor A (VEGF-A) [1.18]. The factor is known to promote neovascularization in the diabetic retina/ BEGF increases vascular permeability and risk of aneurysms. Cells downstream from an aneurysm become ischemic. The photoreceptor metabolism theory states this hypoxia coupled with the increased consumption of the dark adapted retina increases VEGF production [1.18]. This is because rods increase their ATP consumption by a factor of four when dark adapted versus light adapted. This is supported by the success of panretinal photocoagulation in treating diabetic retinopathy [1.18]. VEGF-A was found to be upregulated in the early stages of DR, with the loss of pigmented epithelium-derived factor (PEDF), an anti-angiogenic protein, and the accumulation of glutamate being driving factors [1.20], [1.21]. High VEGF-A levels can result in neurodegeneration of the retina [1.19]. As VEGF-A overexpression continues and PEDF is suppressed, the neovascularization that defines PDR occurs.

The early vascular changes of basement membrane thickening, tight junction failure and microaneurysms characterize mild and moderate non-proliferative DR (NPDR). DR is graded as severe NPDR when many intraretinal hemorrhages as well as microvascular abnormalities are observed in all 4 quadrants Signs of neovascularization mean the disease has advanced to the proliferative stage.

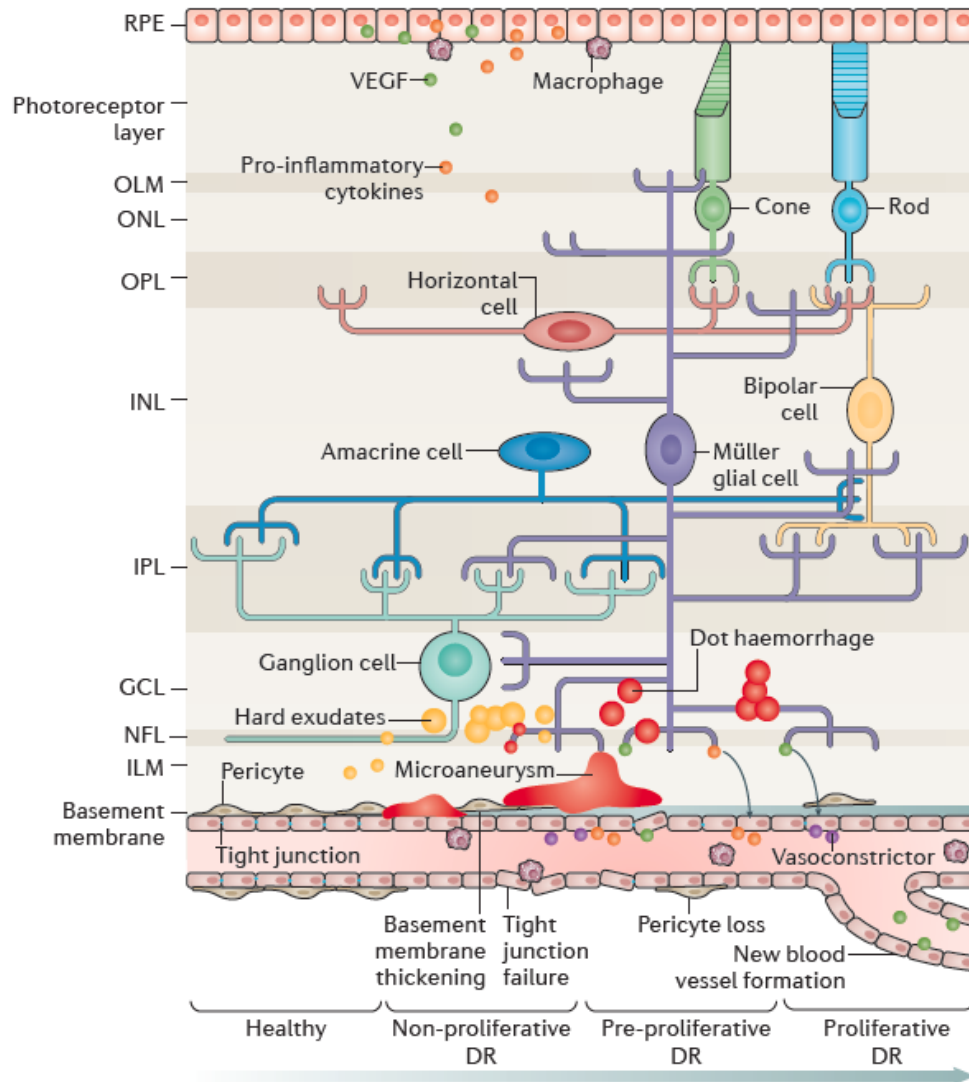


Figure 1.6: Pathology of diabetic retinopathy. Reprinted from [1.19].

The degeneration of retinal vasculature, which in turn leads to upregulation of VEGF-A, suggests an ischemic pathway for DR progression. Severe NPDR exhibits “cotton wool” spots which are lesions indicating retinal ischemia. Intraretinal veins exhibit abnormalities and aneurysms depriving downstream tissue from oxygen. Indeed, as NPDR progresses arterioles connected to now acellular capillaries can become occluded [1.18]. Tissue once supplied by these vessels can become hypoxic. Under hypoxia, hypoxia-inducible factors (HIF)-mediated signaling increases, which drives pro-angiogenic gene expression, and the production VEGF. VEGF binds to VEGF receptors (VEGFR) in the endothelial cells of blood vessels, which triggers angiogenesis [1.22]. The process is generally beneficial, but in DR, the new vessels are tortuous and irregular and prone to aneurysm. These vessels obstruct sight and lead to further bleeds which increases the quantity of floaters.

Table 1.1: Ischemia for different severities of DR. Measurements of retinal blood flow and oxygen saturation from Tayyari et al. [1.23] and Hammer et al. [1.24] are used to estimate retinal oxygen consumption with respect to DR severity. Note that Tayyari et al. presents a single value for mild to moderate NPDR. This value was used as an estimate for more severe retinopathy. Information on oxygen solubility in blood and plasma from other sources was applied to convert saturation in a molar flow [1.25], [1.26], [1.27].

| Severity | Retinal Blood | | | | | |
|---------------|---|------------------------------------|--------------------------------------|---|--|--------------------------------|
| | Flow Rate [1.23] ($\mu\text{L}/\text{min}$) | Venous Saturation [1.24] (%) | Arterial Saturation [1.23] (%) | Net O ₂ Consumption (nmol/s) | O ₂ Deficit in DR (mol/s) | Oxygen Deficit in DR (%) |
| Healthy | 42.7 | 63 | 92.9 | 1.90 | | |
| Mild NPDR | 33 | 69 | 94.7 | 1.26 | 0.62 | 33 |
| Moderate NPDR | 33 | 70 | 94.7 | 1.21 | 0.67 | 35 |
| Severe NPDR | 33 | 75 | 94.7 | 0.97 | 0.91 | 48.5 |
| PDR | 33 | 75 | 94.7 | 0.97 | 0.91 | 48.5 |

Observations of retinal blood flow and blood oxygen saturation in DR further suggest that there is an ischemic component to the disease. Recent studies of retinal blood flow and oxygen saturation (SO₂) allow the oxygen deficit from diabetic retinopathy to be estimated (**Table 1.1**) [1.23], [1.24]. Retinal blood flow is seen to be higher, 42.7 $\mu\text{L}/\text{min}$, in non-proliferative diabetic retinopathy (DR) compared to healthy retina, 33.0 $\mu\text{L}/\text{min}$ [1.23]. While arterial SO₂, remained close to identical for healthy and non-proliferative DR individuals, a larger change was observed for venous SO₂; control being 63%, non-proliferative DR being 70%, and proliferative DR being 75%. Assuming a constant CO₂ and pH, the oxygen-hemoglobin dissociation, results in an estimated oxygen deficit of 8.2% (5.8nmol/s) and 17.9% (12.7nmol/s) compared to a control patient for non-proliferative and proliferative DR, respectively. The trend shows a decrease in arterial oxygen supply, and a decrease in oxygen consumed in the retina. The elevated venous oxygen saturation suggests that oxygen in the retinal circulatory system is not consumed by the retina [1.23]. This is consistent with occlusions of the vasculature. Such occlusions would prevent tissue from receiving oxygen from capillaries. Since the oxygen is not consumed, venous saturation is not expected to drop. Tissue in ischemic areas will likely experience hypoxia, triggering HIF-mediated signaling. The estimate performed here assumes that nearly all oxygen consuming tissue is still alive albeit hypoxic.

Laser photocoagulation ablates photoreceptors to reduce the oxygen consumption of the retina to the level of reduced oxygen supply of the retinopathic eye.

When 20% of the photoreceptors have been ablated [1.28], the severe NPDR and PDR symptoms stop, suggesting that the upper bound for dead tissue is likely around 35% (using deficits from **Table 1.1**). The deficit in **Table 1.1** shows the maximum oxygen that must be provided for all severities of the disease. At this point, VEGF-A production has been reduced, which in turn reduced the permeability of vessels [1.18], [1.28]. Macular edema is also reduced because of the reduced water content entering the retinal tissue. This water content is reduced by the lower vessel permeability and the vasoconstriction from increased oxygen tension [1.28]. Reducing VEGF production has the added benefit of decreasing neovascularization, which helps reduce the impact of proliferative DR.

Current treatment to manage severe NPDR to PDR involves monthly or bimonthly intravitreal injections of VEGF antagonists, such as Bevacizumab and Ranibizumab [1.29], [1.30]. VEGF-A blocks the growth of abnormal blood vessels and reduces vessel permeability. A study of 854 eyes from 691 patients treated with Ranibizumab for 1 year, at intervals of 4 weeks, found that it performed as well as laser photocoagulation every 13 weeks, and that both resulted in significant improvement over the sham groups [1.18]. However, VEGF antagonist therapy is costly: lifetime intravitreal anti-VEGF therapy ranges from \$138k to \$164k per quality life adjusted year [1.31].

None of these approaches treat the underlying ischemia.

1.3 TREATING WITH OXYGEN

Using oxygen to treat DR allows earlier intervention in the ischemic pathway. Oxygen is used in many therapies [1.32]: hyperbaric chambers and normobaric hyperoxia have been well studied as a treatments for tissue hypoxia and for improvement of immune response [1.32]. In a study of macular edema, 43.5% patients treated with 3 months of 4L/min nasally inspired oxygen from oxygen canisters showed an improvement in visual acuity and a reduction in the thickness of the macula [1.33]. In addition, a study of vitreal oxygenation on 20 rabbits showed mitigation of the effects of retinal ischemia (**Figure 1.7**) [1.34].

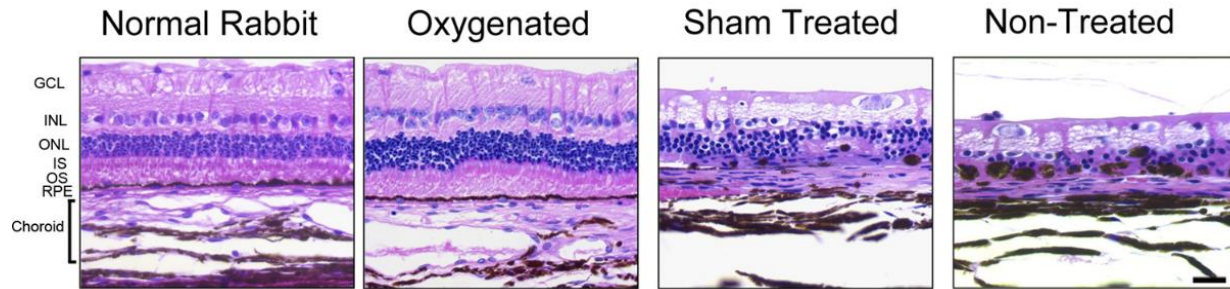


Figure 1.7: Oxygenating an ischemic rabbit retina. Reprinted from W. Abdallah et al. [1.34]. Ischemia was produced in 20 rabbits, with 10 being oxygenated by electrodes in the vitreous, 5 being treated with a sham device and 5 left untreated. Oxygenation preserved the rabbit retina.

There are two ways of balancing the supply and demand of oxygen in the eye: to reduce oxygen demand destroying retinal cells or to increase oxygen supply. Laser photocoagulation destroys photoreceptor cells. Oxygen canisters increase oxygen supply but are impractical and impoverish the patient's quality of life.

This thesis aims to the design of microelectromechanical devices to increase oxygen supply to the eye without the deleterious effects of laser photocoagulation or the burdensome oxygen canisters

1.4 REFERENCES

[1.1] Meng E., Yoon E., Gutierrez C., "MEMS enabled technologies for ocular monitoring and therapy," *2017 19th International Conference on Solid-State Sensors, Actuators and Microsystems (TRANSDUCERS)*, Kaohsiung, pp. 379-382 (2017). doi: 10.1109/TRANSDUCERS.2017.7994066

[1.2] World Health Organization. (2019). *World Health Organization*. [online] Available at: <http://www.who.int/topics/blindness/en/> [Accessed 12 Apr. 2019].

[1.3] Who.int. (2019). [online] Available at: <http://www.who.int/blindness/GLOBALDATAFINALforweb.pdf?ua=1> [Accessed 12 Apr. 2019].

[1.4] Nei.nih.gov. (2019). *Facts About Diabetic Eye Disease | National Eye Institute*. [online] Available at: <https://nei.nih.gov/health/diabetic/retinopathy> [Accessed 12 Apr. 2019].

[1.5] Lee R., Wong T.Y., Sabanayagam C. "Epidemiology of diabetic retinopathy, diabetic macular edema and related vision loss". *Eye and vision (London, England)*, 2(17). (2015) doi:10.1186/s40662-015-0026-2

- [1.6] Zheng Y., He M., Congdon N. “The worldwide epidemic of diabetic retinopathy.” *Indian journal of ophthalmology*, 60(5) pp.428–431. (2012). doi:10.4103/0301-4738.100542
- [1.7] Klein R1, Knudtson MD, Lee KE, Gangnon R, Klein BE. The Wisconsin Epidemiologic Study of Diabetic Retinopathy: XXII the twenty-five-year progression of retinopathy in persons with type 1 diabetes. *Ophthalmology*. 115(11) pp.1859-68. (2008). doi: 10.1016/j.ophtha.2008.08.023.
- [1.8] Gargeya, R., Leng, T. “Automated Identification of Diabetic Retinopathy Using Deep Learning, *Ophthalmology*.” 124(7) pp.962-969. (2017). doi: 10.1016/j.ophtha.2017.02.008
- [1.9] Biographixmedia.com. (2019). *eye anatomy drawing sketch image illustration*. [online] Available at: <http://www.biographixmedia.com/human/eye-anatomy.html> [Accessed 12 Apr. 2019].
- [1.10] National Cancer Institute, National Institutes of Health [Public domain]. En.wikipedia.org. (2019). *Arteriole*. [online] Available at: <https://en.wikipedia.org/wiki/Arteriole#/media/File:Capillaries.jpg> [Accessed 12 Apr. 2019].
- [1.11] Kolb H. “Simple Anatomy of the Retina.” 2005 May 1 [Updated 2012 Jan 31]. In: Kolb H, Fernandez E, Nelson R, editors. *Webvision: The Organization of the Retina and Visual System* [Internet]. Salt Lake City (UT): University of Utah Health Sciences Center; 1995. Available from: <https://www.ncbi.nlm.nih.gov/books/NBK11533/>
- [1.12] Hope, D. (2019). *Macula.svg*. [online] En.wikipedia.org. Available at: <https://en.wikipedia.org/wiki/File:Macula.svg> [Accessed 12 Apr. 2019].
- [1.13] Hirsch L.R., Holzer, J.R., Finn M.S., Cazares S.M., “Significance of Retinal Lesions Potentially Caused by Dazzling Lasers.” *Institute for Defense Analyses*. pp 9. (2015).
- [1.14] Kevin S. LaBar; Purves, Dale; Elizabeth M. Brannon; Cabeza, Roberto; Huettel, Scott A. “Principles of Cognitive Neuroscience”. *Sunderland, Mass: Sinauer Associates Inc*. p. 253. (2007). ISBN 0-87893-694-7.

- [1.15] Shinozaki A., Hosaka Y., Imagawa T., Uehara M. "Topography of ganglion cells and photoreceptors in the sheep retina". *J. Comp. Neurol.*, 518 pp.2305-2315. (2010) doi:10.1002/cne.22333
- [1.16] Campbell J.P., Zhang M., Hwang T.S, Bailey S.T., Wilson D.J., Huang J.&D., "Detailed Vascular Anatomy of the Human Retina by Projection-Resolved Optical Coherence Tomography Angiography," *Sci Rep.* 10;7:42201. (2017). doi: 10.1038/srep42201.
- [1.17] Yu D.Y., Cringle S.J., "Oxygen Distribution and Consumption within the Retina in Vascularised and Avascular Retinas and in Animal Models of Retinal Disease," *Prog. Retin. Eye Res.*, 2:2, pp.175-208. (2001) doi: 10.1016/S1350-9462(00)00027-6
- [1.18] Schachat A.P., Sadda S.V. *Ryan's Retina: Volume II*. 6ed. Edinburgh : Elsevier, pp. 1038-1121. 2018. ISBN: 9780323401975.
- [1.19] Wong T.Y., Cheung C.M.G., Larsen M., Sharma S., Simó R.. "Diabetic Retinopathy". *Nature Reviews Disease Primers.* 2:16012 (2016). doi: 10.1038/nrdp.2016.12
- [1.20] Kusari J., Zhou S.X., Padillo E., Clarke K.G., Gil D.W. "Inhibition of vitreoretinal VEGF elevation and blood-retinal barrier breakdown in streptozotocin-induced diabetic rats by brimonidine". *Invest. Ophthalmol. Vis. Sci.* **51**. 1044–1051. (2010). doi:10.1167/iovs.08-3293
- [1.21] Zhang S.X., Wang J.J., Gao G., Parke K., Ma J.X. "Pigment epithelium-derived factor downregulates vascular endothelial growth factor (VEGF) expression and inhibits VEGF-VEGF receptor 2 binding in diabetic retinopathy". *J. Mol. Endocrinol.* **37**, 1–12 (2006). doi: 10.1677/jme.1.02008
- [1.22] Sene A., Chin-Yee D., Apte R.S. "Seeing through VEGF: innate and adaptive immunity in pathological angiogenesis in the eye". *Trends Mol Med* **21**:1, 43-51 (2015).
- [1.23] Tayyari F., Khuu L.A., Flanagan J.G., Singer S., Brent M.H., Hudson C., "Retinal Blood Flow and Retinal Blood Oxygen Saturation in Mild to Moderate Diabetic Retinopathy," *IOVS*, Vol. 56, No. 11, 6796-6800. (2015) doi:10.1167/iovs.15-17481

- [1.24] Hammer M., Vilser W., Riemer T., Mandecka A., Schweitzer D., Kuhn U., Dawczynski J., Liemt F., Strobel J., "Diabetic patients with retinopathy show increased retinal venous oxygen saturation, " *Graefes Arch Clin Exp Ophthalmol* 247:1025–1030. (2009) doi: 10.1007/s00417-009-1078-6
- [1.25] Vanderkooi J.M., Erecinska M., Silver I.A., "Oxygen in mammalian tissue: methods of measurement and affinities of various reactions," *Am. J. Physiol. Physiol.*, 260: 6, pp. C1131–C1150, (1991).
- [1.26] Van Beekvelt M.C., Colier W.N., Wevers R.A., Van Engelen B.G. (2001). "Performance of near-infrared spectroscopy in measuring local O₂ consumption and blood flow in skeletal muscle". *J Appl Physiol.* 90 (2): 511–19. doi:10.1152/jappl.2001.90.2.511. PMID 11160049.
- [1.27] Silbernagl S., Despopoulos A., *Color atlas of physiology*. Thieme, 2009. ISBN 978-3135450070
- [1.28] Stefánsson E. "The Mechanism of Retinal Photocoagulation – How Does the Laser Work?," *Eur. Ophthalmic Rev.*, pp. 76–79, 2008. DOI: 10.17925/EOR.2009.02.01.76
- [1.29] Genentech, Inc. "Lucentis Prescribing Information," May 2018.
- [1.30] Gupta N., Mansoor S., Sharma A., Sapkal A., Sheth J., Falatoonzadeh P., Kuppermann B., Kenney M. "Diabetic retinopathy and VEGF." *Open Ophthalmol J.* 7:4-10. doi: 10.2174/1874364101307010004. Epub 2013 Feb 1. PubMed PMID: 23459241; PubMed Central PMCID: PMC3580758.
- [1.31] Lin, J., Chang, J.S., Smiddy, W.E. "Cost Evaluation of Panretinal Photocoagulation versus Intravitreal Ranibizumab for Proliferative Diabetic Retinopathy." *Ophthalmology*, **123**:9, 1912–1918 (2016). doi: 10.1016/j.ophtha.2016.05.037
- [1.32] Bitterman H. "Bench-to-bedside review: oxygen as a drug". *Crit Care*.**13**(1):205. (2009) doi: 10.1186/cc7151. Epub 2009 Feb 24. PubMed PMID: 19291278; PubMed Central PMCID: PMC2688103.

[1.33] Nguyen Q.D., Shah S.M., Anden W.V., Sung J.U., Vitale S., Campochiaro P.A. “Supplemental Oxygen Improves Diabetic Macular: Edema: A Pilot Study”. *IOVS* **45**:2, 617-624 (2004). doi:10.1167/iovs.03-0557

[1.34] Abdallah W., Ameri H., Barron E., Chader G.J., Greenbaum E., Hinton D.R., Humayun M.S. “Vitreous oxygenation in retinal ischemia reperfusion”. *Invest Ophthalmol Vis Sci.* **22**;52(2):1035-42. (2011) doi: 10.1167/iovs.09-4516. PubMed PMID: 21051734; PubMed Central PMCID: PMC3053094.

CHAPTER 2 – MODELING OXYGEN TRANSPORT IN THE RETINA

As explained in CHAPTER 1, oxygen is the key element in the treatment of DR of any degree of severity.

Current therapies of laser photocoagulation, or VEGF antagonists are, respectively, deleterious, or very expensive.

Alternatively, MEMS technology can design efficient devices to implant on the eye to provide the oxygen needed. To that end, it is necessary to thoroughly understand how oxygen is transported in the eye..

2.1 SIMPLE, 4-LAYER, 1-DIMENSIONAL MODEL OF THE RETINA

Magnus W. Roos's (2004) model is a starting point to estimate retinal oxygenation. It divides the retina into 4 layers: the inner retina, and 3 layers of the outer retina comprised of the outer segment of the photoreceptors (OPS), inner segment of the photoreceptors (IPS), and the outer nuclear layer (ONL) (**Figure 2.1**) [2.1]. Oxygen consumption occurs in the inner retina, which is highly vascularized, and in the inner segment of the photoreceptors, where the mitochondria (the powerhouses of the photoreceptors) lie. The outer retina is avascular, with most of the blood supply arriving from the choroid through the outer segments of the retina.

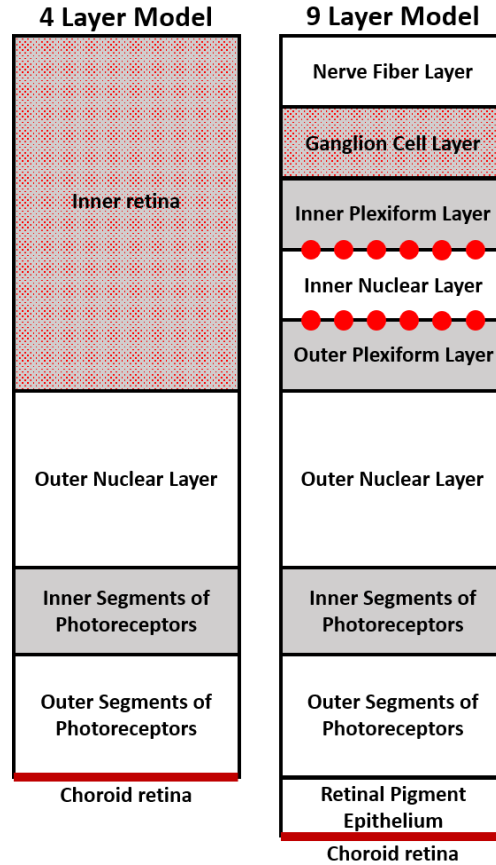


Figure 2.1: Layers of the retina for computational models. Grey shaded layers are oxygen consuming. Capillaries are shaded red. 4 Layer model contains blood vessels evenly distributed throughout the inner retina with consumption evenly distributed. The thicknesses used match those of Roos's paper (2004), [2.1]. The 9 layer model has 3 capillary networks: superficial vascular plexus which is evenly distributed over the nerve fiber layer (NFL), intermediate capillary plexus between the inner plexiform and inner nuclear layers, and the deep capillary plexus between the inner nuclear and outer plexiform layers (OPL).

Fick's diffusion equation with source, S , and reaction (consumption), R , terms describes a general model of oxygen transport:

$$\underbrace{\frac{dc}{dt}}_{0 \text{ for stationary solutions}} = \underbrace{D\nabla^2 c}_{\text{diffusive transport}} - \underbrace{R}_{\text{reaction (consumption) term}} + \underbrace{S}_{\text{source term}} \quad (2.1)$$

The constant of diffusion, D , is taken to be $1.97 \times 10^{-5} \text{ cm}^2/\text{s}$ as per Braun et al's paper [2.2]. Cellular oxygen consumption is described as a Michaelis-Menten reaction:



where oxygen is consumed, but the cell, E , is not. Of note, such kinetics assume the reaction is not ATP limited and is driven entirely by the availability of oxygen. Oxygen profiles of the cat retina by Braun et al., and upregulation of VEGF in diabetic retinopathy support this assumption [2.2], [2.3]. Michaelis-Menten reactions have the relationship:

$$R = q_{max} \left(\frac{p_{O_2}}{p_{O_2} + K_m} \right) \quad (2.3)$$

where q_{max} describes the maximum consumption rate achievable, p_{O_2} describes the oxygen tension and K_m describes the partial pressure or concentration at which the rate equals half the maximum rate.

The source term in equation (2.1) includes the difference between venous and arterial oxygen tensions in the capillaries of the inner retina. The source term accounts for oxygen dissolved in blood, and oxygen bound to hemoglobin. Oxygen bound to hemoglobin is described by the Hill equation, which estimates the amount of bound ligand, θ , (in this case oxygen) using the amount of unbound ligand, $[O_2]$, and the concentration, K , when half the ligand is bound. The equation is a sigmoid function:

$$\theta = \frac{[O_2]^n}{[O_2]^n + K^n} \quad (2.4)$$

where n describes the number of binding sites on hemoglobin. The oxygen tension, p_{O_2} , tracks the oxygen concentration ($p_{O_2} = H_{sol}[O_2]$). Therefore, the source term as per Roos's model averages over all capillaries:

$$S = BF \left[\underbrace{(p_{O_2,art} - p_{O_2,ven})}_{\text{dissolved gas}} + \underbrace{a * (\theta_{art} - \theta_{ven})}_{\text{hemoglobin transport}} \right] \quad (2.5)$$

$$a = \frac{[Hb] * \delta}{\text{maximum mol } O_2/L \text{ in hemoglobin}} * H_{sol,Hb} \quad (2.6)$$

where BF describes the blood turn-over rate (closely related to the retinal blood flow rate), and a defines appropriate oxygen partial pressure in hemoglobin concentration. Venous oxygen tension is

set to match local tissue oxygen tension ($p_{O_2,ven} = p_{O_2}$), and arterial oxygen, $p_{O_2,art}$, is a parameter in the model. For the inner segment of the photoreceptors (IPS), the maximal consumption rate, q_{max} , is different for light and dark adaptation.

Ischemia is modeled by decreasing the blood turn-over rate, which reduces the oxygen available (source term) to the inner retina. Decreases in blood flow mimic oxygen loss downstream from occluded capillaries. Certainly, ocular blood flow in patients with diabetic retinopathy decreases from $42.7\mu\text{L}/\text{min}$ to $33\mu\text{L}/\text{min}$ [2.4]. This is simulated in COMSOL version 5.0 with a varied set of retinal blood flow values. **Figure 2.2** plots the results for both the light and dark adapted retinas.

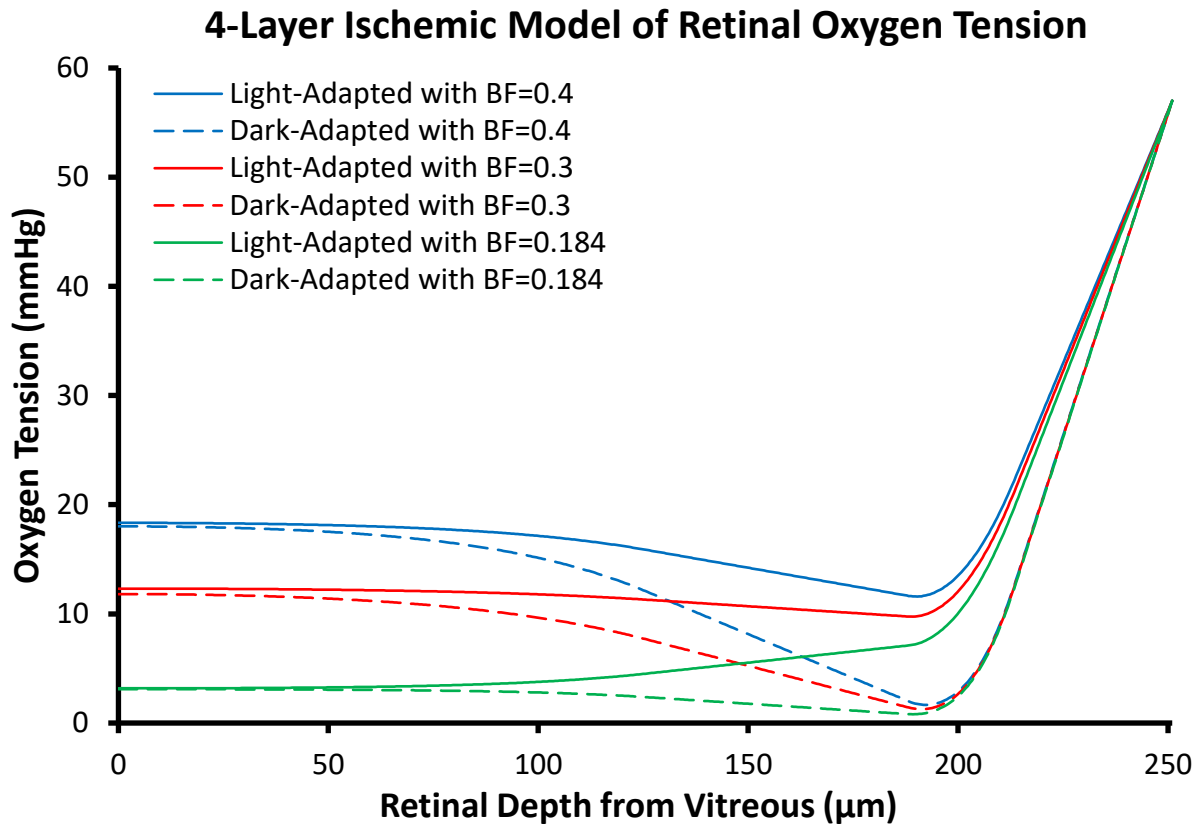


Figure 2.2: Four-layer computational model of the retina with a uniformly distributed capillary network throughout the inner retina, and uniform oxygen consumption throughout the retina. Inner retinal blood flow is modeled by BF, describes blood flow per unit mass into the inner retina. Decreasing this number acts as a decreasing availability of oxygen for the inner retina. A healthy retina is defined as having BF=0.4 in this model [2.1]. Note the light and dark time oxygen tension at the photoreceptor depth ($x > 180\mu\text{m}$) is different, with the inner segments dipping to below 5mmHg in dark adaptation. Inner retinal blood flow reduces light adapted oxygen tension in the photoreceptors, but oxygen tension at dark-adapted photoreceptors are unaffected.

Now that the profile of oxygen in the retina is known, the impact of oxygen supplying devices (oxygen transporter and oxygen generator) on the retina can be modeled. The oxygen source of a device is modeled as a concentration boundary condition on one end of a silicone layer. The results for devices with O₂ partial pressures of 100mmHg and of 250mmHg are plotted in **Figure 2.3** and **Figure 2.4**.

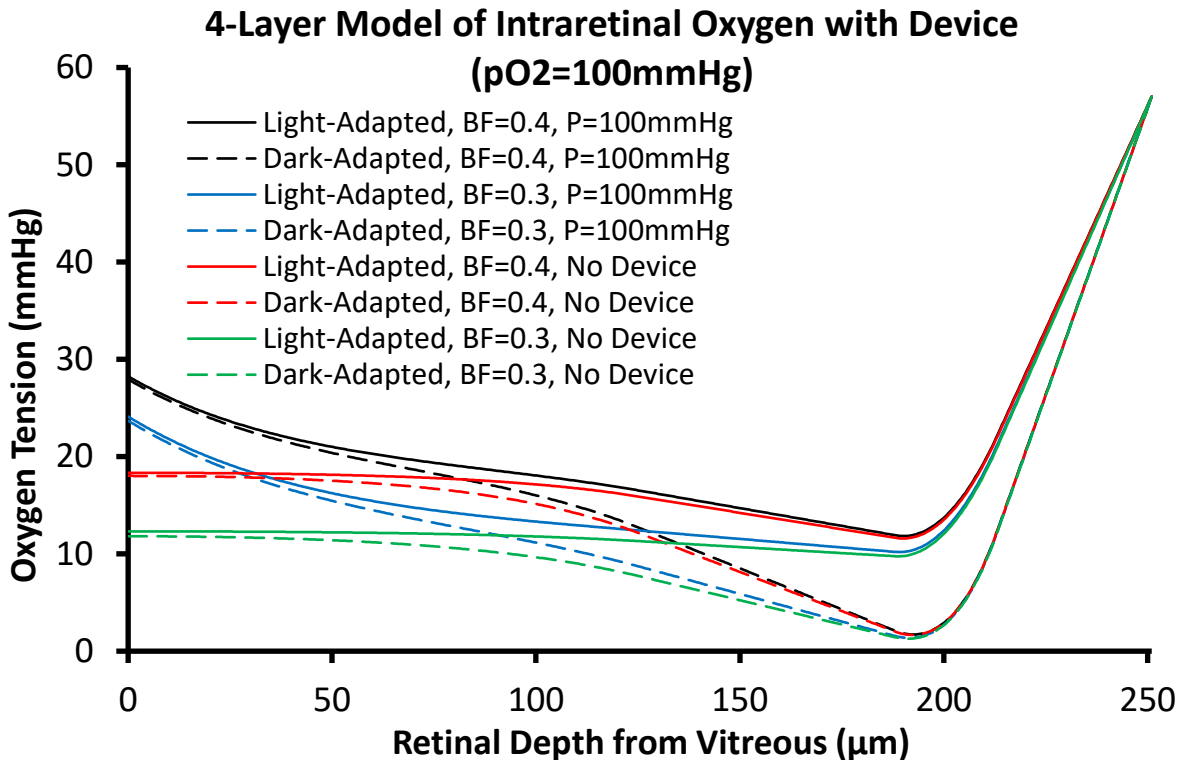


Figure 2.3: 4-layer computational model of the retina with 100mmHg device placed 1mm away from the retina. Healthy inner retinal blood flow is set to 0.4 [2.1], and the reduction to 0.3 estimates a mild retinopathy. Oxygen penetrates the entire inner retina, but the oxygen tension remains above the healthy case only for the inner 35μm. This however is not a useful metric, as the level of VEGF suppression, and therefore efficacy of this oxygenation, is unclear.

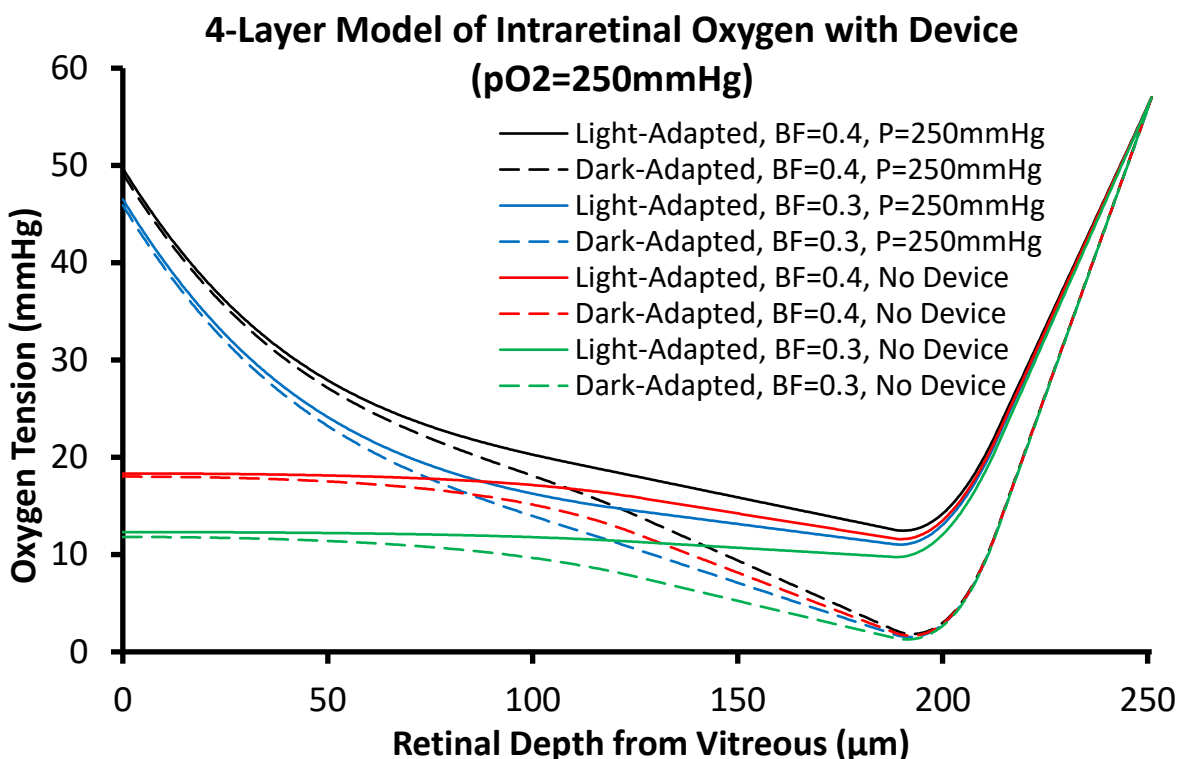


Figure 2.4: 4-layer computational model of the retina with 150mmHg device placed 1mm away from the retina. Healthy inner retinal blood flow is set to 0.4 [2.1], and BF= 0.3 estimates mild retinopathy. The device raises retinal pO_2 for dark-adapted retinas with a BF value of 0.3 above the dark-adapted healthy BF of 0.4 up for depths less than $75\mu\text{m}$.

When devices are placed near the retina, the oxygen levels near the vitreous approach those of the healthy retina, but quickly fall when approaching the outer retina. This means that the nerve fiber layer (NFL), the ganglion cell layer (GCL), and the inner plexiform layer (IPL) can be well oxygenated, but deeper tissue, such as the inner nuclear (INL) and the outer plexiform layers (OPL) cannot. It is difficult to draw conclusions from this, because the VEGF upregulation and the hypoxic levels for cells are not well understood.

Two aspects stand out about this particular model: (a) the inner retina is unaffected by the increased oxygen consumption of the dark adapted outer retina, and (b) the inner retina has a fairly uniform oxygen tension throughout that depends on the availability of oxygen. The former is supported by literature: measurements of a cat's inner retinal oxygen tension remained largely unaffected in light and dark adaptation, and mammalian photoreceptors are primarily supplied by the choroid [2.2], which in the model is defined as a fixed concentration boundary condition at 57mmHg of oxygen. However, literature disagrees with the latter: Cringle and Yu have found distinct peaks in a rat's

intraretinal oxygen curve corresponding to capillary layers (**Figure 2.5A**) [2.5], [2.6], [2.7]. Indeed, optical coherence tomography (OCT) of human retinas defines several layers of capillaries (oxygen source): the superficial vascular plexus (SVP) in the nerve fiber layer, and the intermediary capillary plexus (ICP) and the deep capillary plexus (DCP) surrounding the inner nuclear layer [2.8]. Oxygen consumption in the inner retina occurs mostly in the ganglion cell layer, in the inner plexiform layer and in the outer plexiform layer [2.5]. Together these layers point to a more complex picture of the inner retina than captured by this model. The oxygen tension value at the oxygen consuming layers is important in determining the severity of the oxygen deficit, which determines the upregulation of VEGF. **Figure 2.6** shows VEGF mRNA expression in those layers in a human retina. A multilayer model will better track oxygen tension in the human retina.

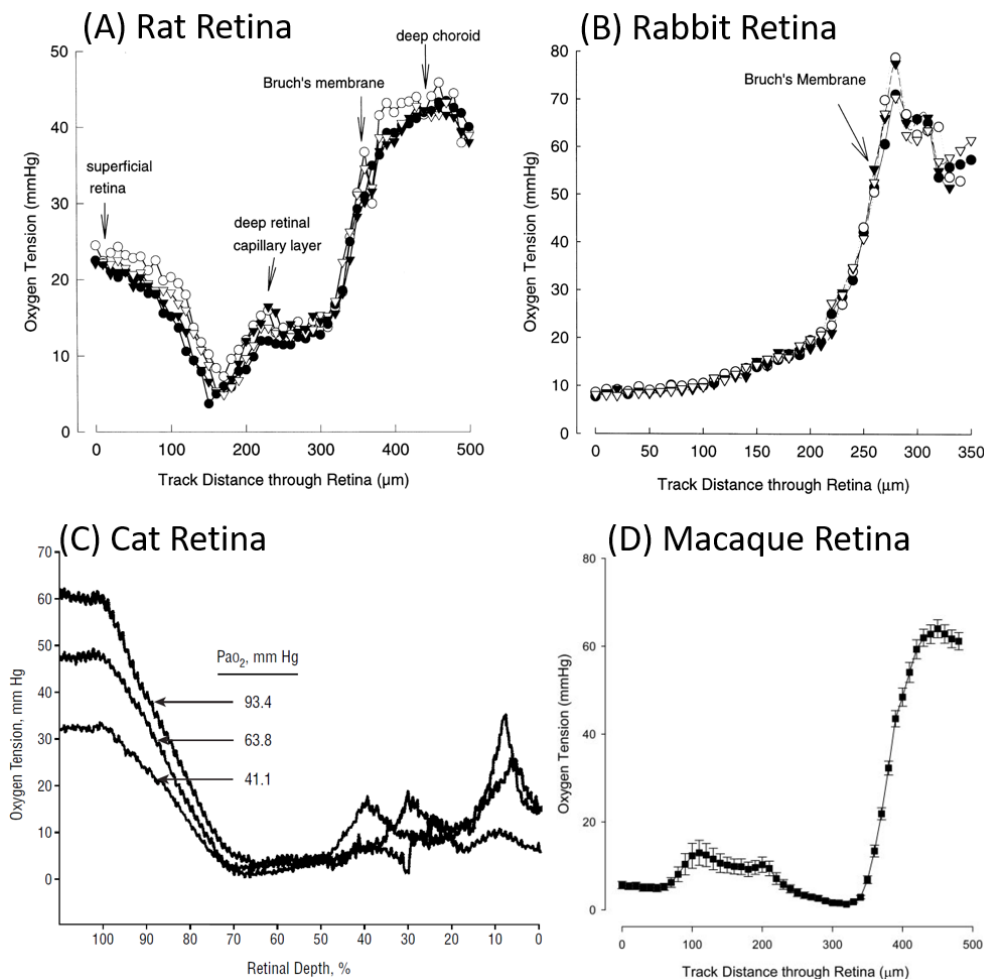


Figure 2.5: Intraretinal oxygen profiles of mammals. For vascularized inner retinas (A,B,D), inner retinal capillaries result in distinct peaks. (A) Rat retina. Reprinted from [2.11]. (B) Rabbit retina, which has an avascular inner retina. Reprinted from [2.12]. (C) Cat retina with direction reversed. Reprinted from [2.13]. (D) Macaque retina. Reprinted from [2.14].

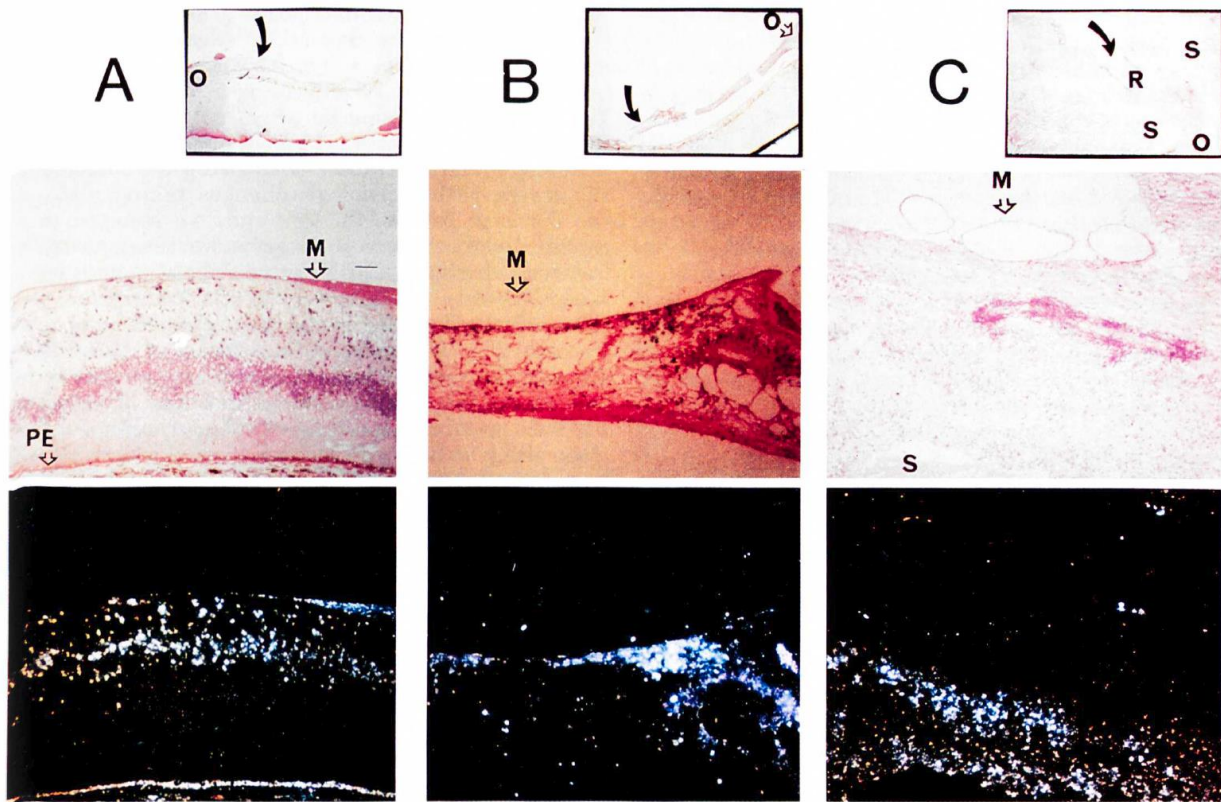


Figure 2.6: VEGF mRNA expression in human eyes. From Pe'er et al, VEGF mRNA staining in retina of patients with diabetic retinopathy. Reprinted from [2.15]. VEGF expression is concentrated two bands of the inner retina: the ganglion cell/inner plexiform layers, and in the inner nuclear/outer plexiform layers. No expression is seen in the outer nuclear layer.

2.2 CAPILLARY OCCLUSION, 8-LAYER MODEL

An 8-layer model of the retina (3 layers for the outer retina, and 5 layers for the inner retina) zoomed into a 2 dimensional slice (100 μ m wide) with individual capillaries within each capillary network allows the effect of inner retinal capillary occlusions to be modeled with the minimum number of assumptions (**Figure 2.1**). These capillaries are 4.6 μ m in diameter (as found in Wang et al, 2011 [2.16]), and match per layer the percentage area found in humans [2.8]. The capillary networks are the superficial vascular plexus, the intermediary vascular plexus, and the deep capillary plexus (**Figure 2.7**). Capillary density and retinal layer thicknesses are found in **Table 2.1** and **Table 2.2**.

Table 2.1: Capillary Density as per Campbell et al., 2011 [2.8]

| | PARAFOVEAL | PERIFOVEAL | PERIPHERAL |
|-----|------------|------------|------------|
| SVP | 0.28 | 0.31 | 0.17 |
| ICP | 0.22 | 0.21 | 0.22 |
| DCP | 0.13 | 0.15 | 0.22 |

Table 2.2: Retinal layer thickness. Periphery is taken to be similar to perifoveal. [2.8] [2.9], [2.10]

| LAYER | FOVEAL | PARAFOVEAL | PERIFOVEAL |
|----------------------------|------------------|------------------|------------------|
| NERVE FIBER LAYER | 4 μm | 34 μm | 44 μm |
| GANGLION CELL LAYER | 28 μm | 43 μm | 27 μm |
| INNER PLEXIFORM LAYER | 28 μm | 43 μm | 27 μm |
| INNER NUCLEAR LAYER | 23 μm | 38 μm | 30 μm |
| OUTER PLEXIFORM LAYER | 38 μm | 40 μm | 29 μm |
| OUTER NUCLEAR | 77 μm | 54 μm | 54 μm |
| INNER PHOTORECEPTOR LAYER | 25 μm | 25 μm | 25 μm |
| OUTER PHOTORECEPTOR LAYER | 42 μm | 37 μm | 37 μm |
| RETINAL PIGMENT EPITHELIUM | 22 μm | 22 μm | 22 μm |
| REGION RADIUS | 0.6 mm | 1.55 mm | 3 mm |

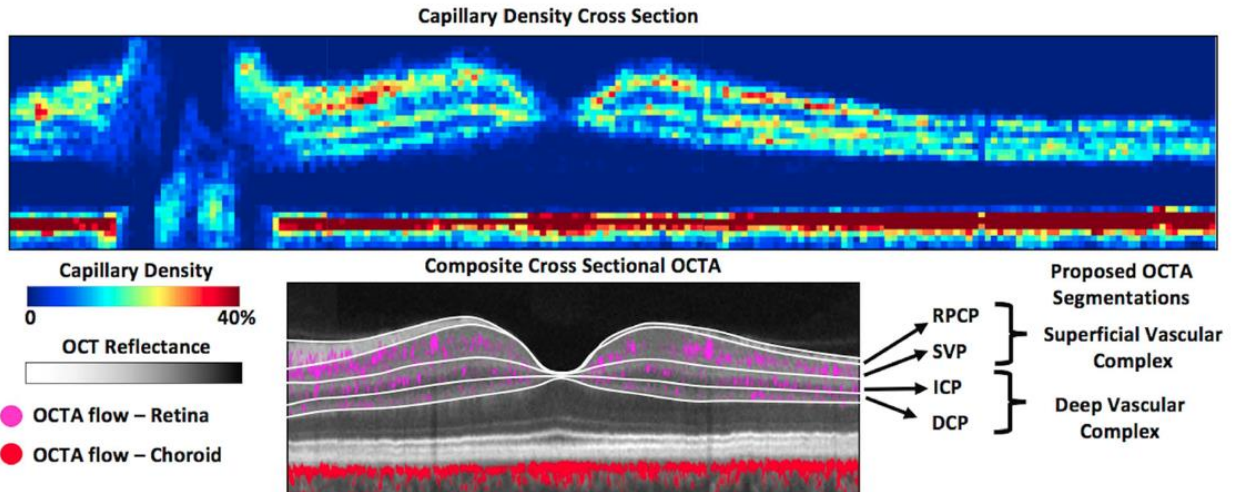


Figure 2.7: OCT of human inner retinal vasculature; reprinted from Campbell et al., 2017 [2.9]. Note the 3 distinct retinal layers, superficial vascular plexus, intermediate capillary plexus, and deep capillary plexus.

A symmetry boundary condition was placed at zero on the x-axis (retinal width). Capillaries were given a fixed oxygen concentration boundary condition and occlusions were modeled by removing said condition from the capillaries. Ischemia was increased by occluding capillaries moving away from zero at the x-axis (**Figure 2.8** and **Figure 2.9**). A color graph of the concentration is plotted in **Figure 2.8**.

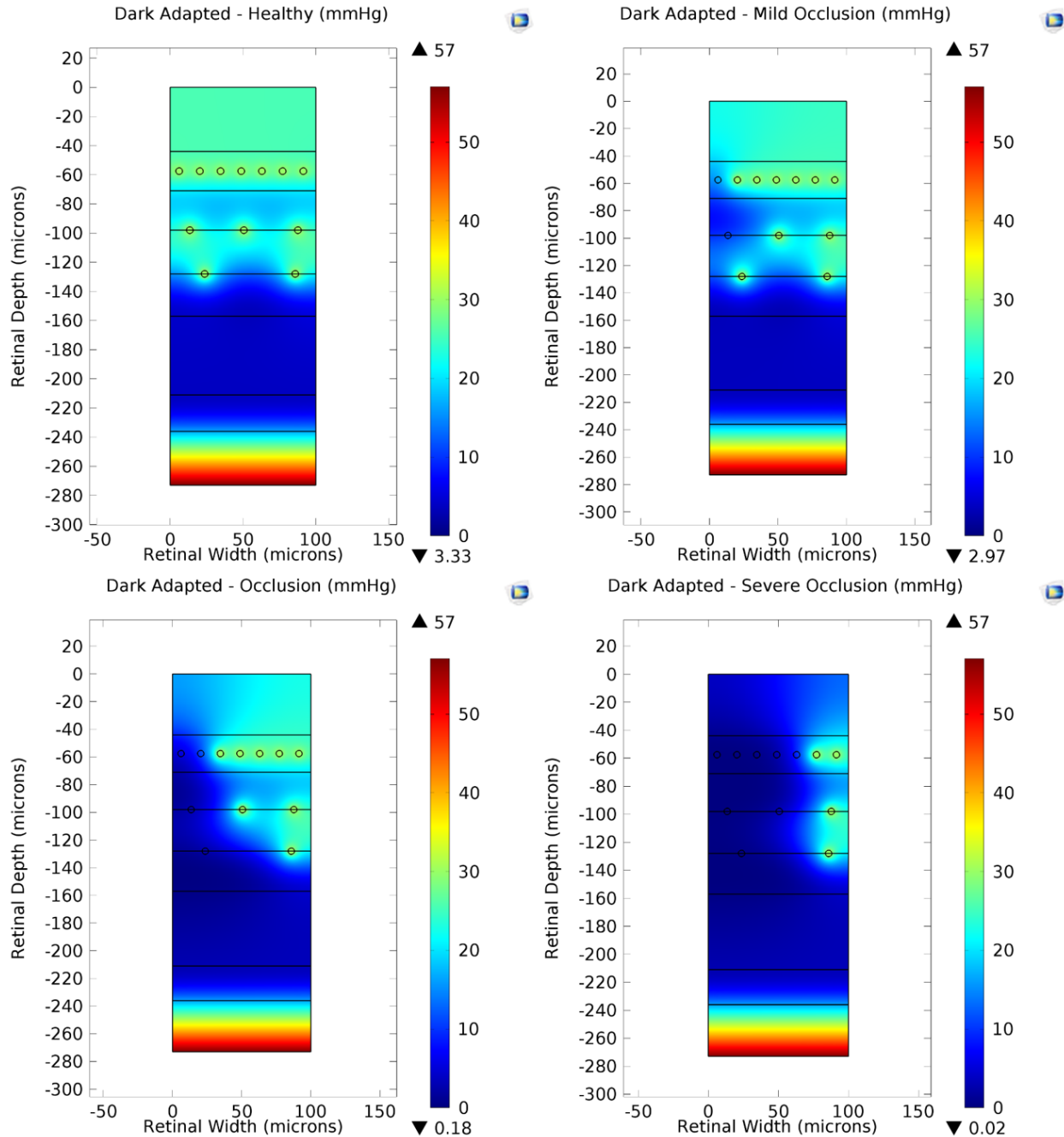


Figure 2.8: 8-layer computational model of the retina with individual capillaries for the dark adapted inner retina. The capillary spacing matches the capillary density in literature. The model has a symmetry boundary condition at $x=0$ (width). Capillaries are modeled as a concentration boundary condition set to $p_{capillary} = 30\text{mmHg}$. Mild occlusions to severe occlusions are modeled by turning off this condition to ever more capillaries moving away from the $x=0$ line.

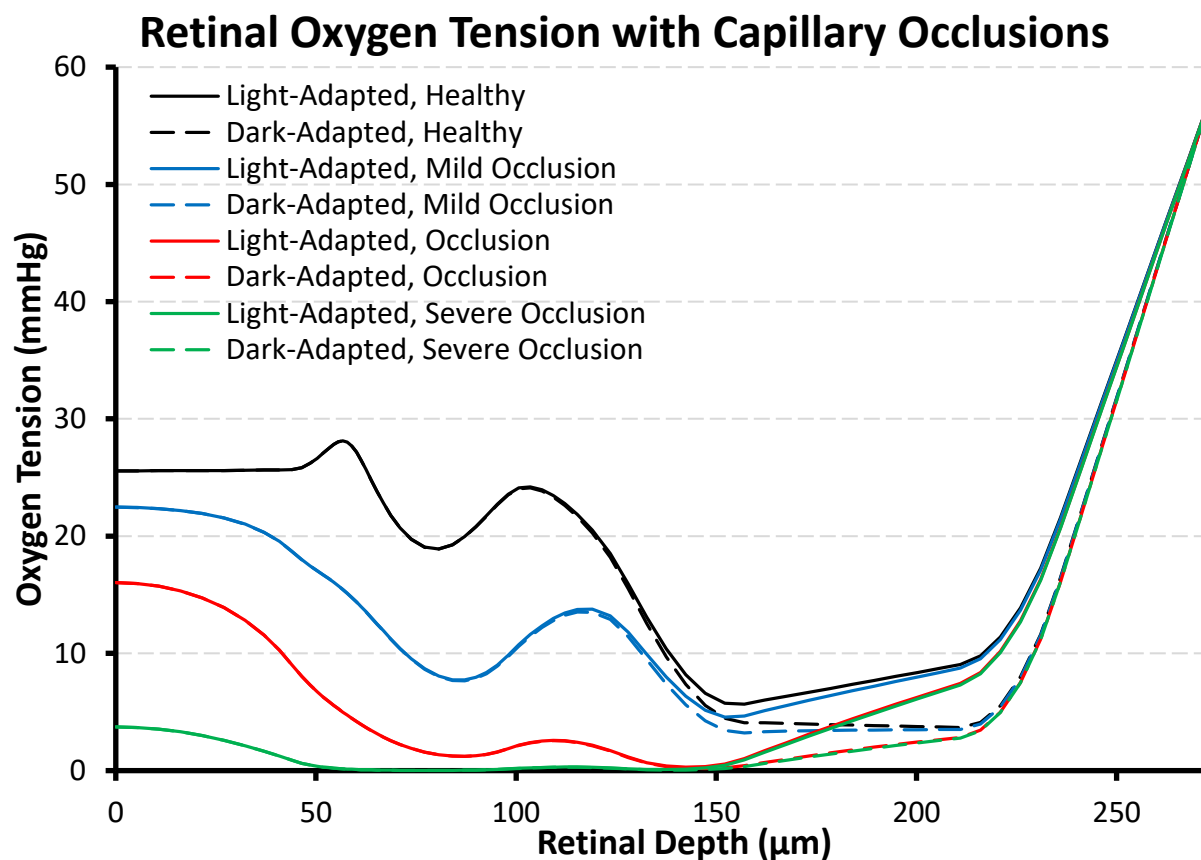


Figure 2.9: Oxygen profile along the depth of the 8 layer retinal model. Plotted oxygen tensions from $x=0$ line. Note the two distinct peaks from the SVP and ICP/DCP vessels. Looking at each progressive increase in occlusion, the peak height drops, and the peaks widen. As seen in the previous model, the inner photoreceptor segments are largely unaffected by the occlusions, but the ganglion cell and inner plexiform layers decrease. These layers are where VEGF has been found to express during diabetic retinopathy (**Figure 2.6**).

Intuition suggests that the retina has lower oxygen tension in oxygen consuming layers than those layers with capillaries networks, and this trend is confirmed in the mammalian vascularized inner retinas seen in **Figure 2.5A,B,D** [2.5], [2.6], [2.7]. **Figure 2.9** plots the dark-adapted retina with a dashed line, and the light-adapted retina with a solid line. Note that in the inner retina, in particular at the GCL and INL, the light and dark adapted oxygen curves are near identical. This would indicate that the effect of increased consumption in the photoreceptor layer does not impact the oxygen tension in the retina, even in severe occlusions. The effect occlusions have on the ganglion cell and inner plexiform layers indicates that this is where VEGF would be up-regulated. Indeed **Figure 2.6** shows VEGF mRNA expression in these layers in eyes affected by diabetic retinopathy [2.15]. Occlusions broaden and lessen peaks of oxygen tension, as oxygen diffuses from farther away. Intraretinal oxygen measurements will vary based on proximity to vessels. The distribution of

oxygen tension is seen to be non-uniform across a layer at this micro-level, and the model captures this fact in **Figure 2.8**. Intraretinal oxygen probes average measurements over a small but non-infinitesimal area (30 μ m in diameter [2.12]). Consequently, the oxygen tension measurements in literature are affected by the proximity of the probe to the vessels. This explains the varied oxygen curves seen for mammalian inner retinas (**Figure 2.5**).

Due to computational limitations this model cannot be extended to encompass the entirety of the retina, as there are many capillaries each with an individual boundary condition.

2.3 AXISYMMETRIC (AXSY) MODEL OF THE MACULA AND SURROUNDING PERIPHERY

The capillary oxygen supply rate will be averaged out into a source term similar to the first model. The model will be referred to as the AXSY model for clarity. This source term estimates the oxygen supply rate in the specific layers which contain the capillary networks (SVP, ICP, and DCP). As before, the source term is defined by the equation (2.5). As the choroid is expected to be mostly unaffected in retinopathy, the reduction in ocular blood flow was assumed to occur primarily in the inner retinal capillaries. Any deficit in blood flow was subtracted from the inner retina only:

$$BF_{InnerRetina} = BF - BF_{OuterRetina} \quad (2.7)$$

where the blood flow of the outer retina was defined to be 65% of the total blood flow of a healthy retina [2.17]. As seen in **Table 2.4**, this results in the same ratio between oxygen consumption in proliferative retinopathy and a healthy retina, as calculated in **Table 1.1**.

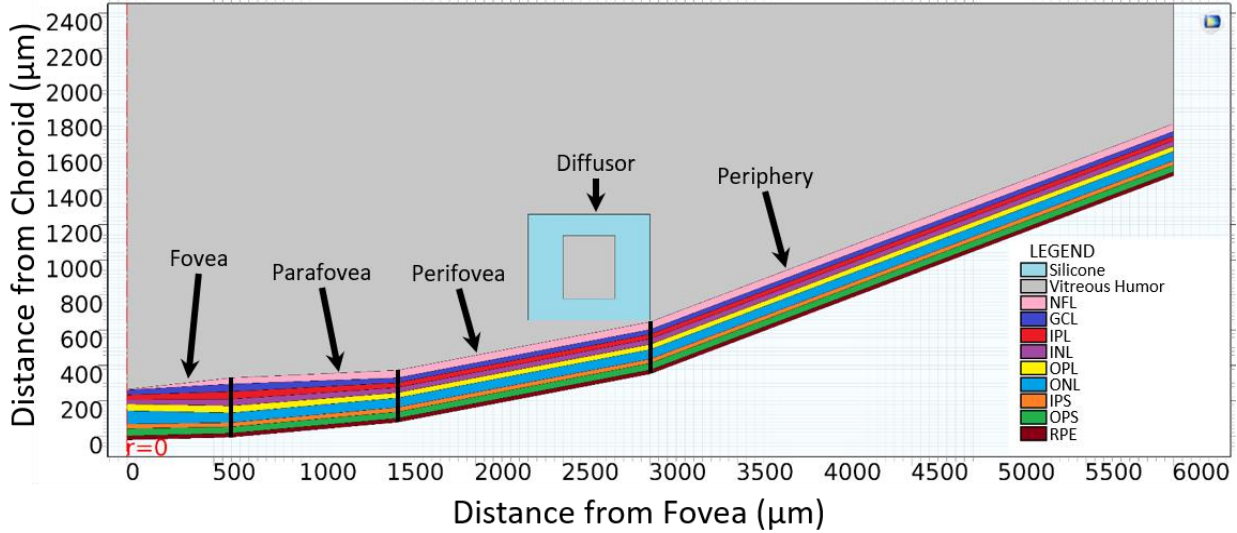


Figure 2.10: Diagram of the retinal layers in the model.

A 9-layer AXSY model of the retina (adding a retinal pigment epithelium layer) is implemented. The areas of each layer were made to differ across 4 distinct regions of the retina: the fovea, the parafovea, the perifovea, and the periphery. The oxygen consumption in the layers, GCL, IPL, OPL, and IPS, were taken from the values in literature. At the time of writing, the closest human analog whose intraretinal oxygen consumption has been measured was the macaque monkey, Birol et al. [2.18]. All model parameters are found in **Table 2.3**.

Table 2.3: AXSY model parameters.

| PARAMETER | DESCRIPTION | VARIABLE |
|--------------------|---|---|
| $D_{ox,vitreous}$ | Vitreous Diffusion coefficient [2.19] | $4 \times 10^{-5} \text{ cm}^2/\text{s}$ |
| $D_{ox,retina}$ | Retinal Diffusion coefficient [2.2] | $1.97 \times 10^{-5} \text{ cm}^2/\text{s}$ |
| $D_{ox,PDMS}$ | Silicone Diffusion coefficient [2.20] | $7.88 \times 10^{-5} \text{ cm}^2/\text{s}$ |
| $H_{sol,vitreous}$ | Vitreous Solubility of Oxygen [2.3] | $7.79 \times 10^4 \text{ Pa} \cdot \text{m}^3/\text{mol}$ |
| $H_{sol,retina}$ | Retinal Solubility of Oxygen [2.1] | $1.41 \times 10^5 \text{ Pa} \cdot \text{m}^3/\text{mol}$ |
| $H_{sol,PDMS}$ | Silicone Solubility of Oxygen [2.1] | $\frac{600 \text{ Ba}}{D_{ox,PDMS}} = 3.9 \times 10^4 \text{ Pa} \cdot \text{m}^3/\text{mol}$ |
| $H_{sol,Hb}$ | Solubility of Oxygen in Blood [2.1] | $8.89 \times 10^4 \text{ Pa} \cdot \text{m}^3/\text{mol}$ |
| K_{ox} | Michaelis Constant for Retinal Consumption [2.1] | 2 mmHg |
| K_{hem} | Hill half-concentration constant [2.1] | 26 mmHg |
| n | Hill cooperativity coefficient [2.1] | 2.7 |
| $[Hb]$ | Concentration of hemoglobin in blood [2.1] | 140 g/L |
| δ | Oxygen carrying capacity of hemoglobin [2.1] | 0.0616 mmol/g |
| $p_{O_2,blood}$ | pO ₂ of Arterial Blood [2.1] | 57 mmHg |
| BF | Healthy Retinal Blood flow [1.23] | 42.7 $\mu\text{L}/\text{min}$ |
| $q_{ox,OR,dark}$ | Macaque Dark-Adapted Outer Retinal Consumption [2.19] | 4.9 mL O ₂ · 100g ⁻¹ · min ⁻¹ |

| | | |
|-------------------|---|--|
| $q_{ox,OR,light}$ | Macaque Light-Adapted Outer Retinal Consumption [2.19] | $0.72 * q_{ox,OR,dark}$ |
| $q_{ox,IR}$ | Inner retinal consumption scaled from cat consumption [2.2] | $q_{ox,OR,dark} \cdot \frac{(3.91 \text{ mL O}_2 \cdot 100 \text{g}^{-1} \text{min}^{-1})}{(3.48 \text{ mL O}_2 \cdot 100 \text{g}^{-1} \text{min}^{-1})}$ |
| A_{ret} | Area of a human retinal | 1094 mm^2 |

The AXSY model implemented the effect of ascorbate in the vitreous as follows. It is well documented that ascorbate consumes oxygen in the vitreous as per the reaction:



which is beneficial in reducing the oxygen tension at the lens. Here reduced ascorbate acid is converted into dehydroascorbic acid (DHA) via a two-step process which consumes oxygen in the vitreous. Such a second order equation has a rate given by:

$$R = \frac{d[\text{O}_2]}{dt} = - \underbrace{k[\text{AscH}^-]}_{k'} [\text{O}_2] = -k' [\text{O}_2] \quad (2.9)$$

where k is the rate for this process. The concentration of ascorbate in the posterior vitreous is 0.376mM, and the rate is $1.61 \text{ M}^{-1}\text{s}^{-1}$ [2.21]. Ascorbate acid is renewed by eye, meaning one can assume the rate to be relatively constant. To simplify, it is replaced by a rate incorporating ascorbate concentration in the posterior vitreous, $k' = k[\text{AscH}^-] = 6.0536\text{s}^{-1}$.

Table 2.4: Oxygen consumption and severity of DR in the simulation. AXSY model consumption integrated and scaled by the surface area of the AXSY model's retina to the surface area of the retina.

| Source Parameter | | Light-Adapted | | Dark-Adapted | | DR Severity |
|--|-----------------------|---------------------------------------|-------------------------------------|---------------------------------------|-------------------------------------|--------------------|
| Blood Flow ($\mu\text{L}/\text{min}$) | Flow Reduction (%) | Total Retinal Consumption (nmol/s) | Total Retinal Oxygen Deficit (%) | Total Retinal Consumption (nmol/s) | Total Retinal Oxygen Deficit (%) | |
| 42.7 | 0% | 2.10 | 0% | 2.27 | 0% | |
| 38.43 | 10% | 2.05 | 2.3% | 2.21 | 2.6% | |
| 36.295 | 15% | 1.98 | 5.7% | 2.13 | 6.2% | Mild NPDR |
| 33 | 22.7% | 1.67 | 20.5% | 1.78 | 21.5% | Moderate NPDR |
| 29.89 | 30% | 1.23 | 41.4% | 1.33 | 41.4% | Severe NPDR to PDR |

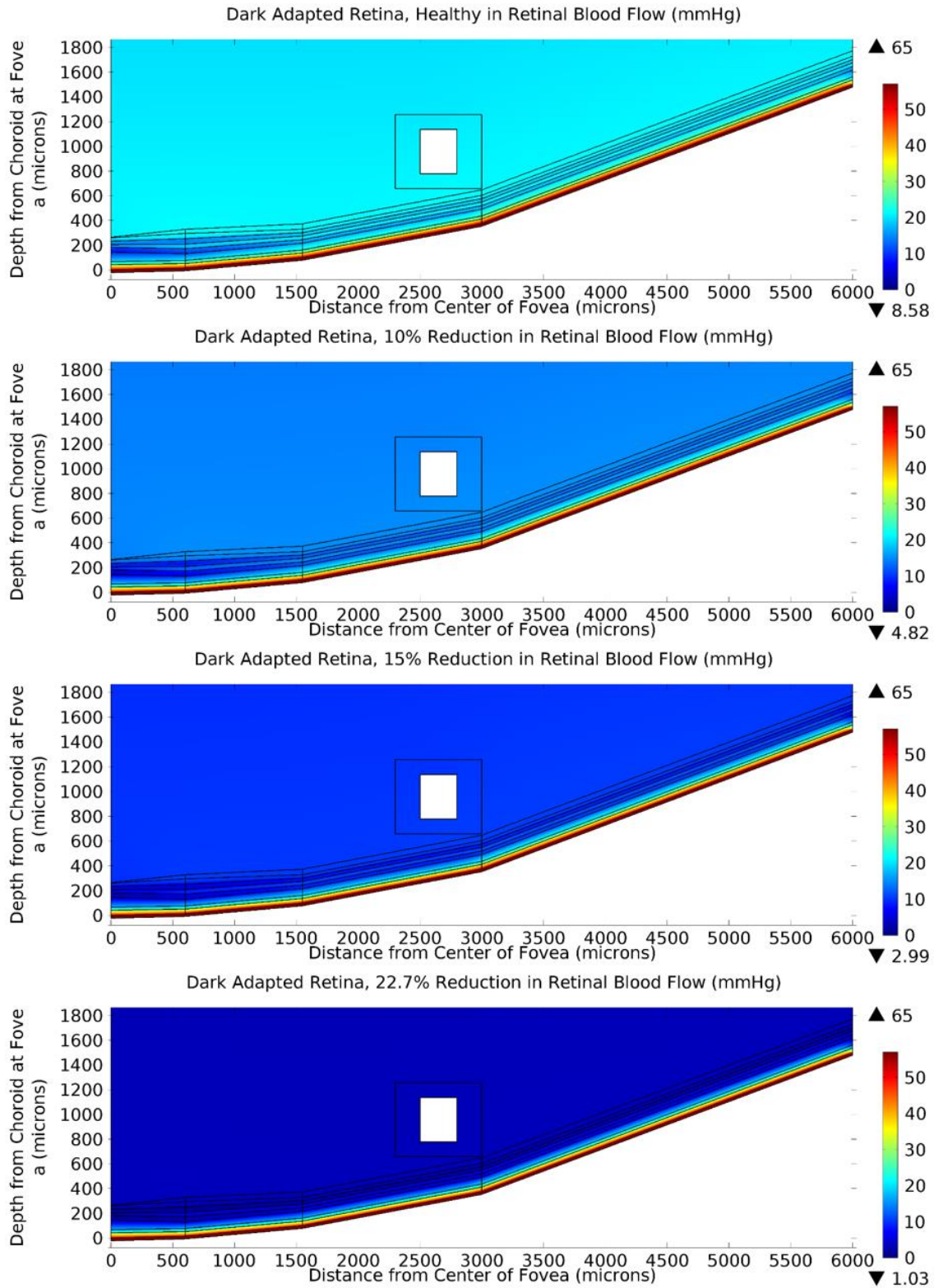


Figure 2.11: 9-layer axisymmetric computational model of the retina; oxygen profile for a dark adapted retina. The color bar represents the oxygen tensions in mmHg. The device is represented by a white box is not active with no boundary condition. Note the elevated oxygen tension at GCL, and INL with the band of lower oxygen tension at IPL.

The effects of reduced blood flow are shown in **Figure 2.11**. The reduction in blood flow is based on $42.7\mu\text{L}/\text{min}$ being defined as healthy human blood flow [2.22]. The resultant oxygen consumption for different blood flows is found in **Table 2.4**. An ischemia of 30%, results in a reduction in oxygen consumption of 41.4% (similar to proliferative DR). Blood flow reductions of 15% and 22.7% result, respectively, in 5.8% and 20.5% reduction in oxygen consumption (similar to mild and moderate non-proliferative DR). The AXSY model over estimates the total healthy oxygen consumption by 15% compared to healthy human retinas (see **Table 1.1**). Remember that the model uses the retinal tissue consumption from macaque and cat retinas.

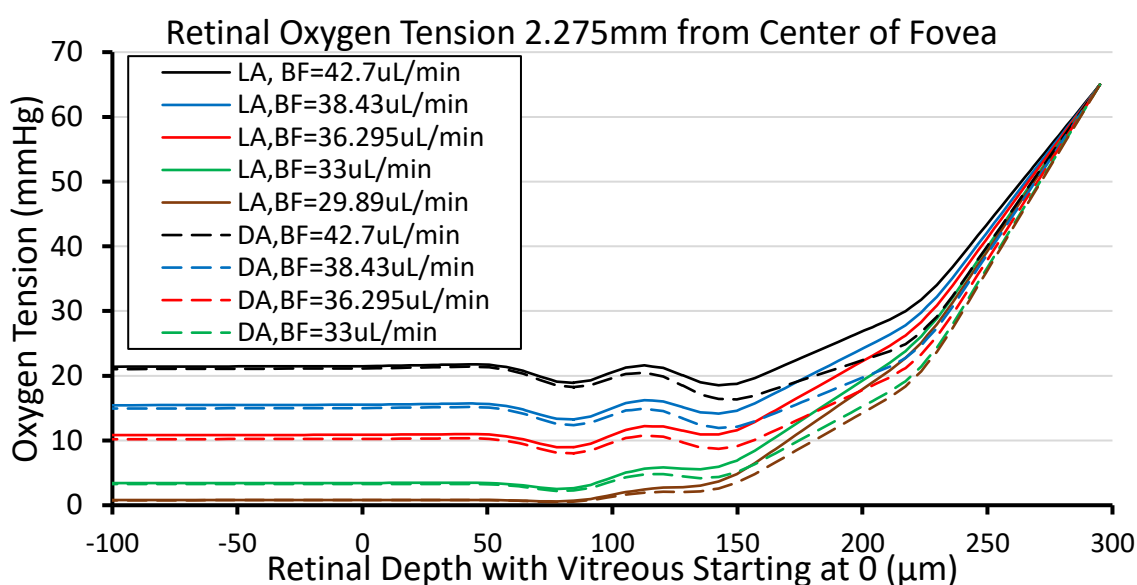


Figure 2.12: Perifoveal oxygen profile for the 9 layer computational model; midway in the band of the perifovea. Here, LA stands for light-adapted, and DA for dark-adapted. A blood flow, BF, of $42.7\mu\text{L}/\text{min}$ is the healthy human blood flow. $38.43\mu\text{L}/\text{min}$ is a 10% reduction in blood flow, $36.295\mu\text{L}/\text{min}$ is a 15% reduction in blood flow, $33\mu\text{L}/\text{min}$ is a 22.7% reduction in blood flow, and $29.89\mu\text{L}/\text{min}$ is a 30% reduction in blood flow.

Figure 2.11 shows a two dimensional color plot of the retinal oxygen tension. Note the minimum oxygen tension of the healthy retina is 8.58mmHg . **Figure 2.12** is generated intersecting surfaces of **Figure 2.11** at the same point in the x-axis (distance from center of fovea), and plotting the values on **Figure 2.12**; in this case the intersection was done at 2.275mm . In **Figure 2.12**, the black line represents healthy retinal blood flow, the blue line a 10% reduction in blood flow, the red line a 15% reduction in blood flow, the green line a 22.7% reduction in blood flow, and the brown a 30% reduction in blood flow. All lines have two dips in oxygen tension representing consumption: one at $75\mu\text{m}$ of retinal depth and one at $145\mu\text{m}$ of retinal depth. The dip at $75\mu\text{m}$ represents the

consumption of the GCL and the IPL, and the dip at 145 μ m represents the consumption of the OPL. These dips match the ones seen in vascularized inner retinas of the rat, the cat, and the macaque. The deficit in the GCL and IPL may manifest as "cotton wool" spots.

2.3.1 MODELING VEGF EXPRESSION IN THE RETINA

Using grey scale and reducing the range in the AXST model's output to 12mmHg, 15% blood flow deficit simulation shows agreement with VEGF staining in humans (**Figure 2.13**). Note that human VEGF expression is seen predominantly in the inner retina near the GCL and the IPL, these same regions exhibit decreased oxygen tension in the AXSY model.

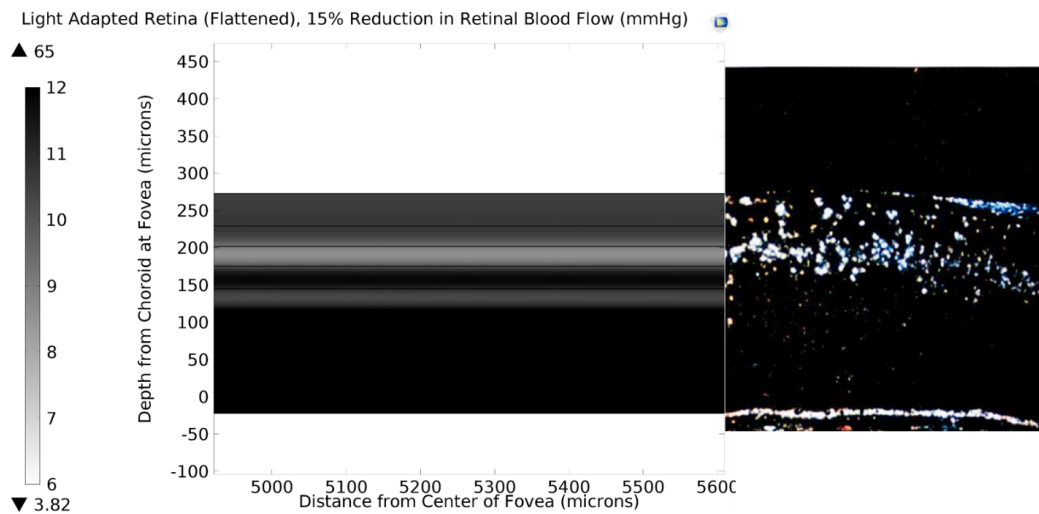


Figure 2.13: Low oxygen tension in simulation versus human VEGF expression. Simulation of light-adapted retina with a 15% reduction in retinal blood flow. Grey scale range was reduced to center on 9mmHg to 10mmHg leading to a sharp transition around those values. Human VEGF mRNA staining (Fig 2a of Pe'er et al [2.18]) is scaled to match choroid to choroid and NFL to NFL.

Based on the work of Chiarotto and Hill on cervical cancer cells [2.23], a sigmoid curve is used to model VEGF upregulation, equation (2.10):

$$\text{VEGF}(p_{O_2}) = 1 - \frac{p_{O_2}}{p_{O_2} + p_{O_2,1/2}} \quad (2.10)$$

The oxygen partial pressure for 50% upregulation, $p_{O_2,1/2}$, is set at the AXSY model's minimum oxygen tension for a healthy eye of 8.6mmHg (**Figure 2.11**). The estimated percentage VEGF upregulation by retinal layer is plotted in the color map of **Figure 2.14**.

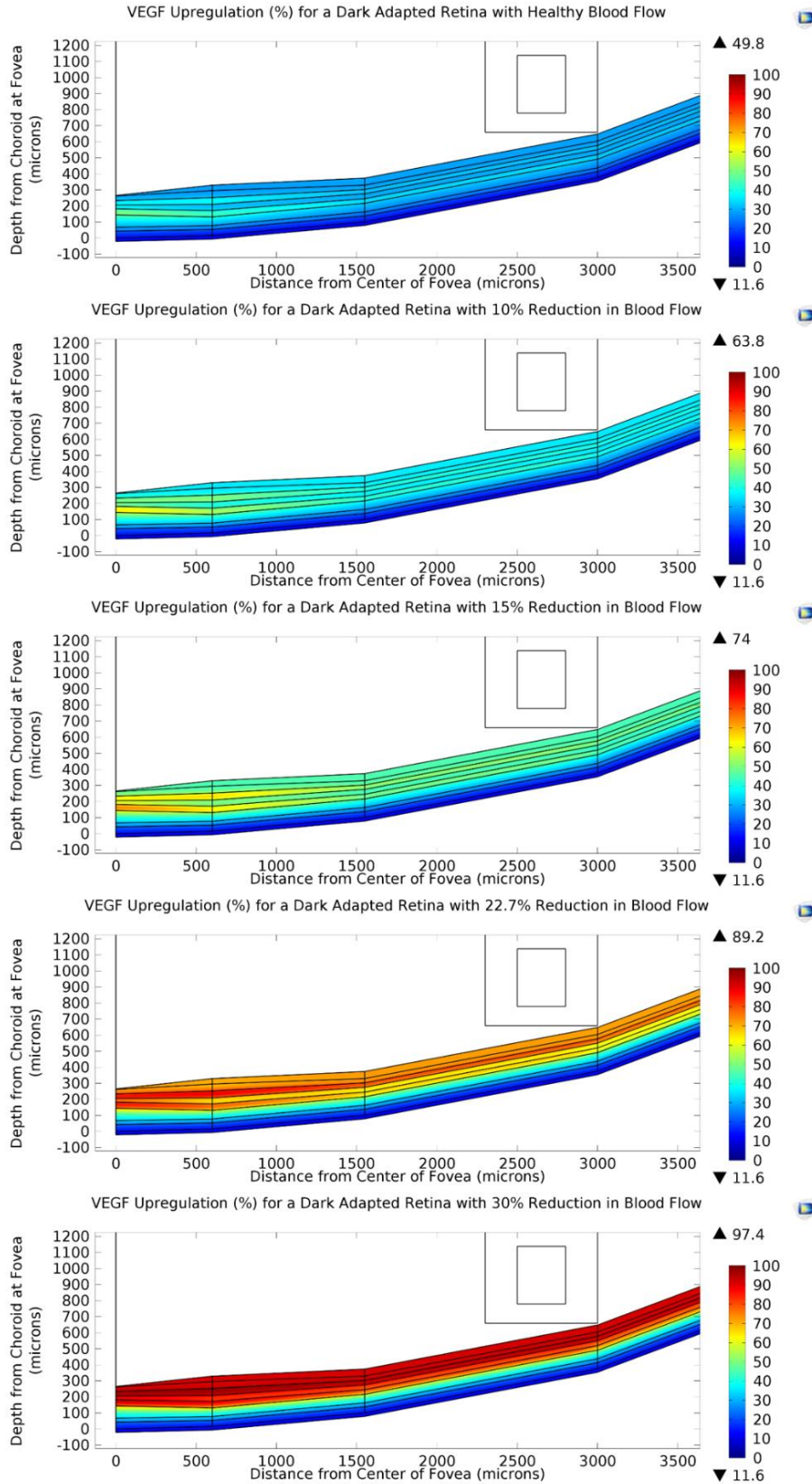


Figure 2.14: Simulation of VEGF upregulation in the retina. Percent VEGF Upregulation describes the rate of VEGF production with respect to the maximum percent.

Considering the maximal rate of VEGF expression of each layer is unknown, and not necessarily the same, one cannot average over different layers. Therefore, one must work with an independent average VEGF upregulation per layer. VEGF percentages of each retinal layer is normalized by dividing by the VEGF of the healthy retina, **Table 2.5**. In severe NPDR and PDR, the AXSY model's VEGF production in the GCL is 2.5× to 3× that of healthy tissue. The values in the AXSY model (**Table 2.5**) conform to VEGF mRNA expression in **Figure 2.6**, meaning where there are white spots in the photograph, there is a corresponding high value of VEGF upregulation in GCL, IPL, INL, and OPL. The AXSY model of the retina shows decreased oxygen tension in the same regions that exhibit VEGF mRNA in human eyes.

Table 2.5: VEGF upregulation by layer. Integrating VEGF Upregulation percentage over each layer and then dividing by the value of the healthy retina. The metric gives a comparison of the total change in VEGF expression by layer across different ischemic conditions.

| BLOOD FLOW ($\mu\text{L}/\text{min}$) | | NFL | GCL | IPL | INL | OPL | ONL | IPS | OPS | RPE |
|---|--------|------------|------------|------------|------------|------------|------------|------------|------------|------------|
| LIGHT | 42.7 | 1.00 | 1.00 | 1.00 | 1.00 | 1.00 | 1.00 | 1.00 | 1.00 | 1.00 |
| | 38.43 | 1.25 | 1.25 | 1.25 | 1.21 | 1.18 | 1.11 | 1.05 | 1.02 | 1.00 |
| | 36.295 | 1.54 | 1.55 | 1.55 | 1.44 | 1.37 | 1.20 | 1.09 | 1.04 | 1.01 |
| | 33 | 2.50 | 2.51 | 2.41 | 2.11 | 1.83 | 1.40 | 1.16 | 1.07 | 1.01 |
| | 29.89 | 3.23 | 3.20 | 2.98 | 2.70 | 2.18 | 1.51 | 1.20 | 1.08 | 1.02 |
| DARK | 42.7 | 1.01 | 1.01 | 1.03 | 1.04 | 1.08 | 1.12 | 1.13 | 1.06 | 1.01 |
| | 38.43 | 1.27 | 1.28 | 1.30 | 1.28 | 1.30 | 1.26 | 1.19 | 1.09 | 1.02 |
| | 36.295 | 1.59 | 1.61 | 1.63 | 1.55 | 1.53 | 1.38 | 1.25 | 1.11 | 1.02 |
| | 33 | 2.55 | 2.56 | 2.50 | 2.25 | 2.04 | 1.60 | 1.33 | 1.13 | 1.03 |
| | 29.89 | 3.24 | 3.22 | 3.02 | 2.83 | 2.39 | 1.72 | 1.37 | 1.15 | 1.03 |

2.3.2 MODELING AND OPTIMIZING THE DEVICE

An oxygen containing ring is placed around the macula at the edge of the perifovea. The ring is comprised of 120 μm thick silicone shell with hollow interior set at a fixed concentration. The ring prevents occlusions along the optical path of the macula, and reduces the risk of damage to the fovea if the ring were to contact the retina. The ring also provides an even oxygen distribution within the region of the macula compared to a point source (**Figure 2.15**). First, this section will confirm the device can improve oxygen tension, and reduce VEGF upregulation in the inner macula. The device will be swept across all parameters to determine the distance from the retina and the device oxygen tension required to treat DR.

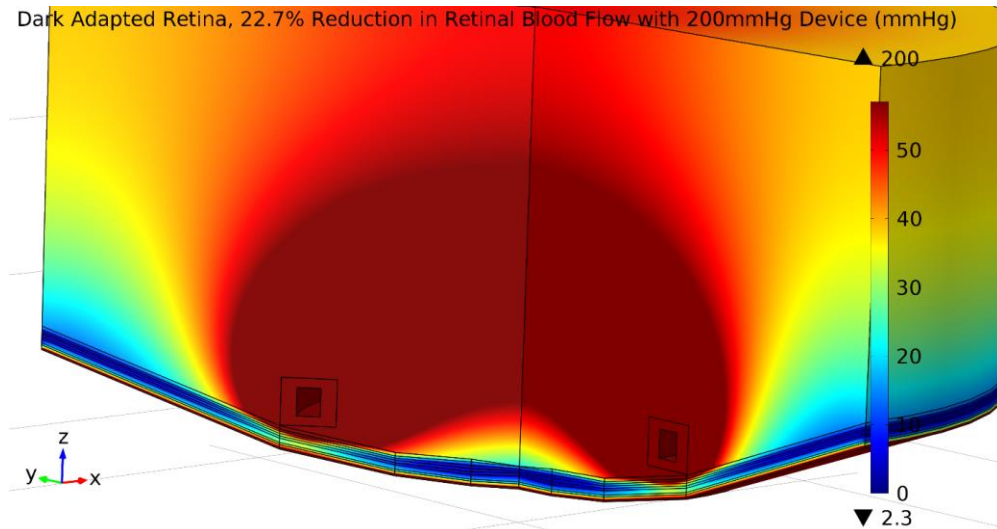


Figure 2.15: 9-layer model with 200mmHg device. Retina with 33 μ L/min blood flow.

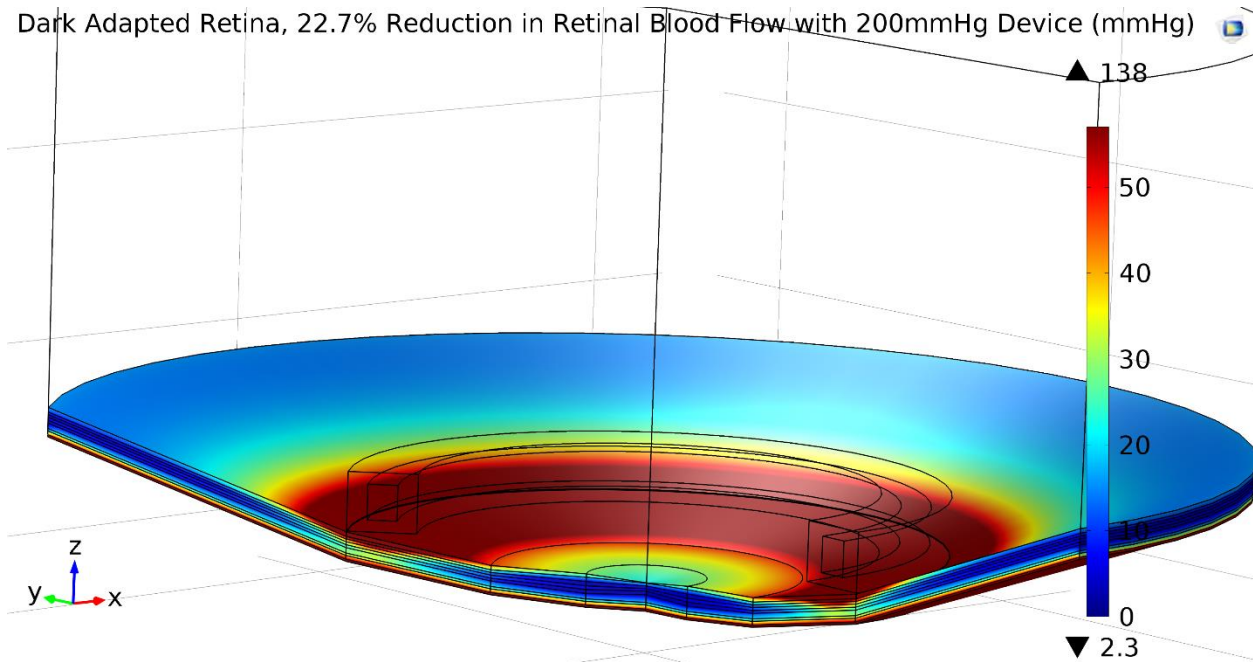


Figure 2.16: Simulation with 33 μ L/min and 200mmHg device (vitreous not plotted).

The AXSY model estimates three ratios with respect to a healthy retina: VEGF upregulation, moles of oxygen in the retina, and oxygen consumption in the retina. Animal models will be needed to validate the estimates, since these are just a starting point. The device's oxygen tension and position were independently swept for these ratios. The device's position was fixed at 10 μ m above the nerve fiber layer at the perifovea, and the oxygen tension swept values are shown in **Figure 2.17**. Note that oxygen's diffusion path length is much shorter in the retina than in the vitreous due to the lower diffusion and solubility constants. Furthermore, consumption in the GCL and IPL increases the

amount of oxygen deposited in those layers before it can diffuse deeper into the retina. This second effect efficiently deposits oxygen that enters the hypoxic tissue of the GCL and the IPL, where it is most needed (**Figure 2.11**).

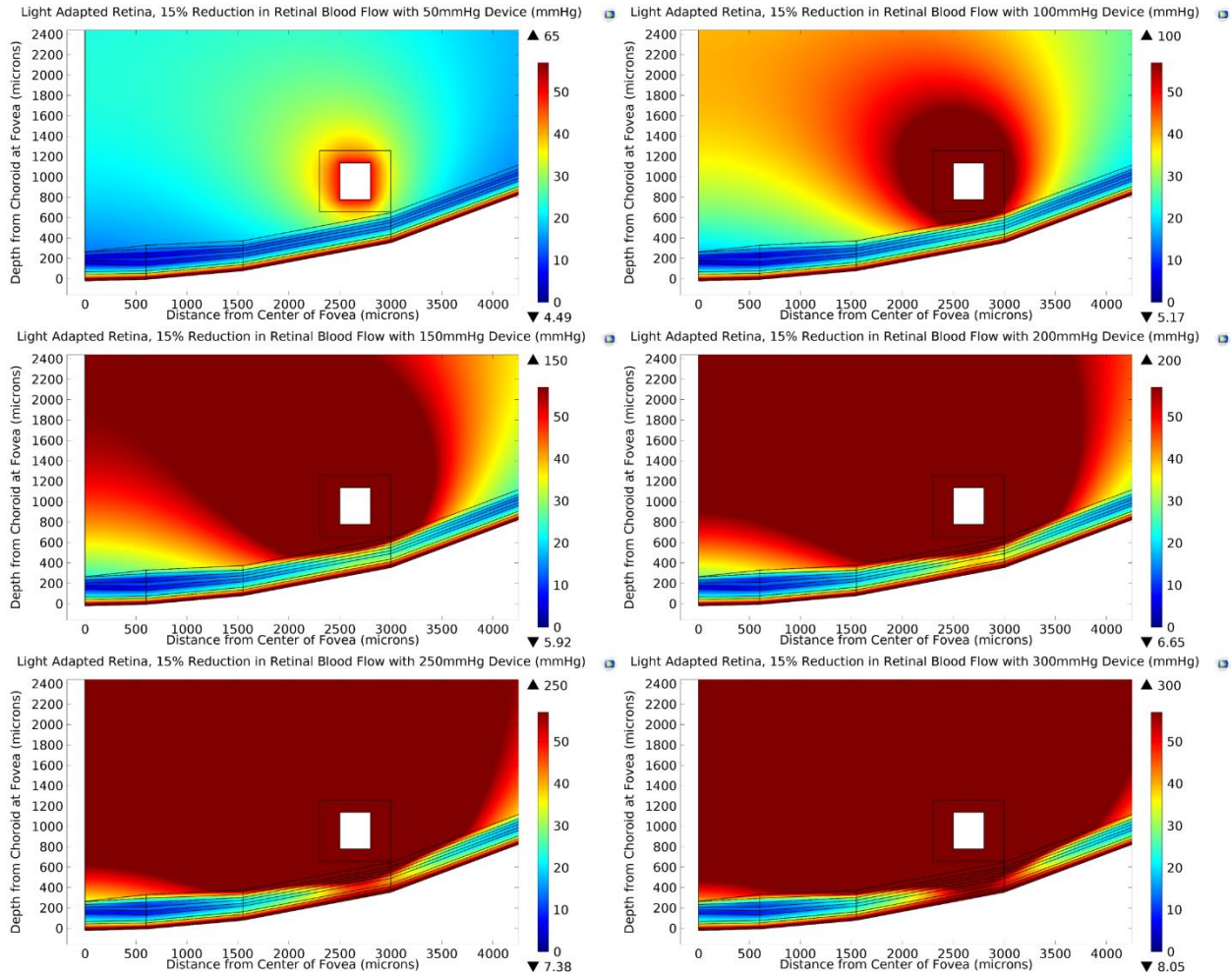
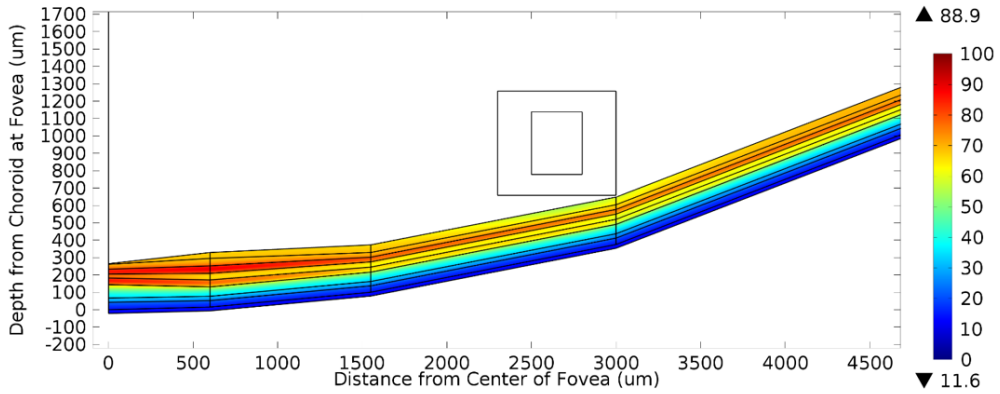


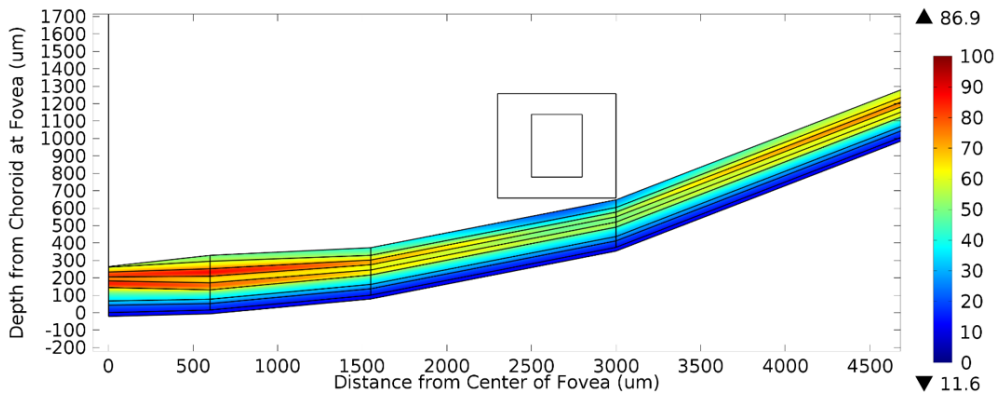
Figure 2.17: Ischemia model with varying device oxygen tension. Device placed $10\mu\text{m}$ from the perifovea and tested with a 15% reduction in retinal blood flow from the healthy $42.7\mu\text{L}/\text{min}$.

In the AXSY model, oxygen from the device is not transported through the vasculature. The vasculature normally transports oxygen along the layer. In the AXSY model, the vasculature does not shuttle oxygen, consequently the model overestimates the oxygen requirements from the device.

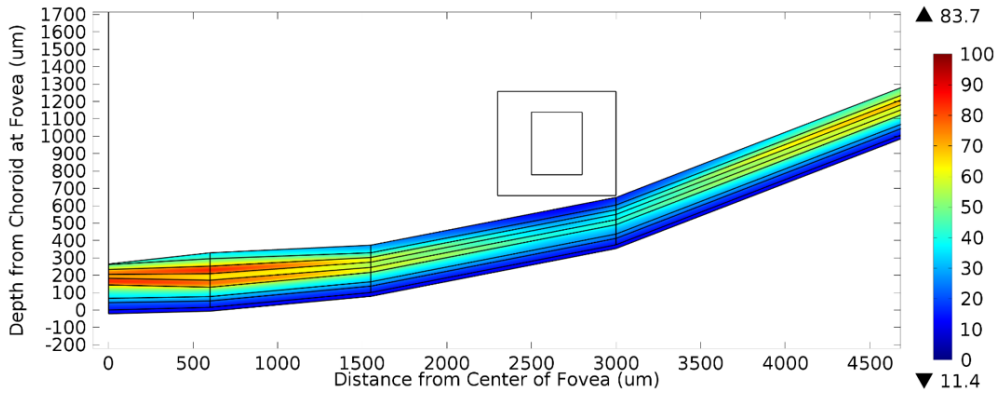
VEGF Upregulation (%) for a Dark Adapted Retina with 22.7% Reduction in Blood Flow with 10mmHg Device



VEGF Upregulation (%) for a Dark Adapted Retina with 22.7% Reduction in Blood Flow with 50mmHg Device



VEGF Upregulation (%) for a Dark Adapted Retina with 22.7% Reduction in Blood Flow with 100mmHg Device



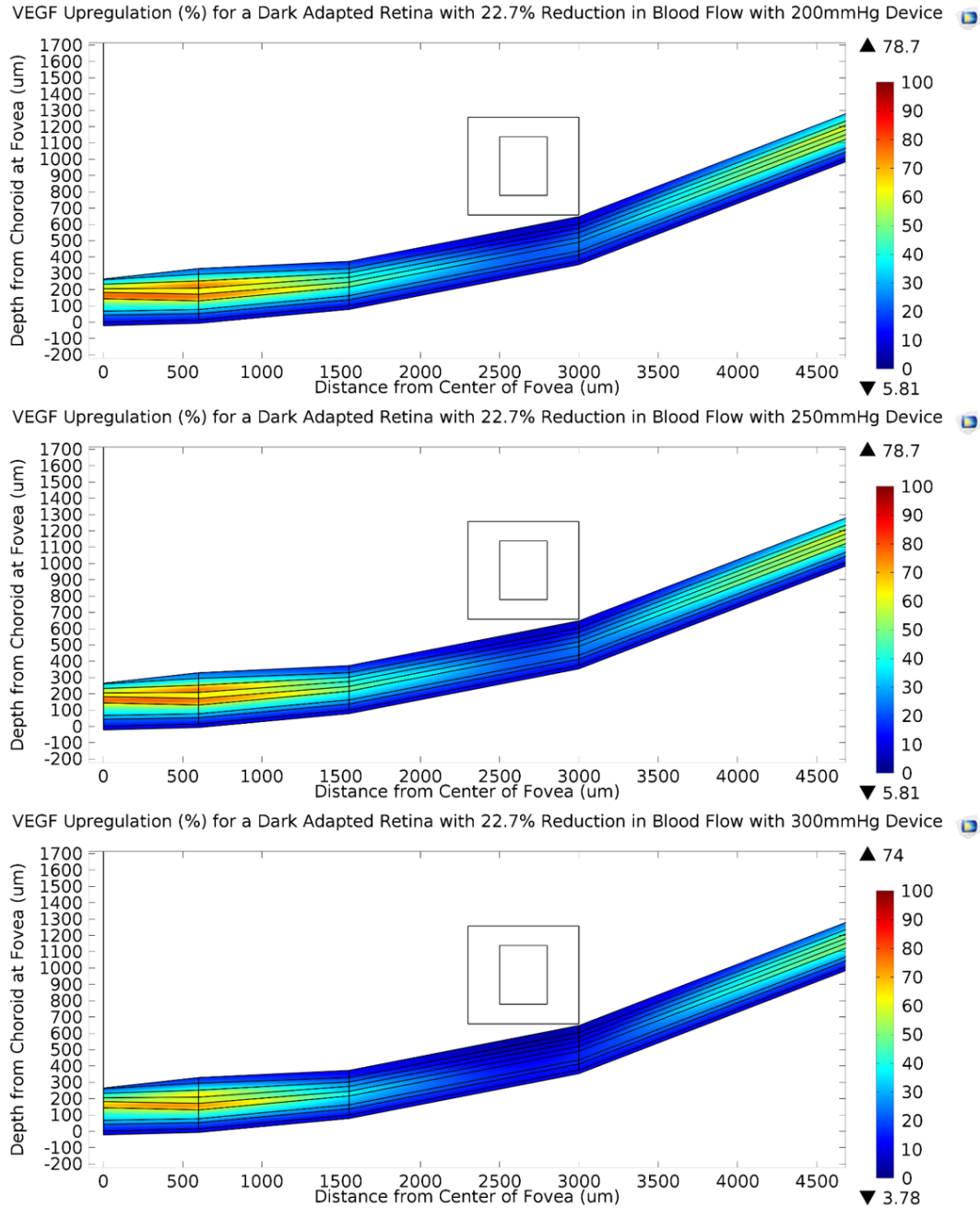


Figure 2.18: Simulation VEGF upregulation for different device oxygen tension. VEGF upregulation with $33\mu\text{L}/\text{min}$ retinal blood flow rate (22.7% reduction from the healthy $42.7\mu\text{L}/\text{min}$ flow rate) and a device with varied p_{O_2} .

The percentage of VEGF upregulation is plotted in **Figure 2.18**. VEGF upregulation starts to be suppressed at 100mmHg, and falls below 80% at 200mmHg. VEGF upregulation of $1.5\times$ the healthy retina's VEGF upregulation is considered unhealthy, considering that VEGF upregulation $1.4\times$ that of healthy retinal VEGF was not observed to overexpress in the IPS layer in severe ischemia (refer

to the outer retina of **Figure 2.6**). Now that the device produces a favorable effect on the hypoxia in the inner retina, the device will be optimized for different severities of DR.

Three contour plots are used to optimize the distance between the device and the macula, and to the device's oxygen tension: moles of oxygen in the inner macula (**Figure 2.19**), oxygen consumption in the inner macula (**Figure 2.20**), and VEGF upregulation ratios in the combined GCL and IPL (**Figure 2.21**).

For moles of oxygen and consumption in the inner macula, the positive slope of the contour line implies that reducing the oxygen tension from the device must also be followed with nearly linear reduction in distance between the device and the NFL. The values necessary for treatment depend on the level of ischemia. For a severe ischemia (30% reduction), which equates to PDR, either 175mmHg at 0 μ m from the NFL or 250mmHg at 500 μ m fall within the treatable range for moles of oxygen and for retinal consumption. Lower oxygen tension devices or devices farther away from the retina, such as 100mmHg with a 1000 μ m separation, are adequate to treat mild to moderate NPDR.

VEGF upregulation has an optimum distance around 200 μ m-400 μ m away from the NFL layer that is independent of oxygen tension. When the device is moved away from the retina, the thinner bottom membrane (the reason for thicker sidewalls can be found in section 6.3.1) has a more direct path length with tissue through vitreous, which is far more permeable than the retina. If the device is too close, oxygen is wasted oversupplying a smaller segment of the retina. As VEGF upregulation is more sensitive in the low oxygen tension, this effect is magnified in **Figure 2.21**. A 22.7% ischemia (moderate to severe non-proliferative DR) is best treated by a device of 150mmHg or greater oxygen tension at approximately 200 μ m. Since lower ischemia has a lower oxygen demand, such a device is adequate to treat those as well. PDR is best treated with a device of 250mmHg at 200 μ m from the nerve fiber layer.

Note that these simulations assume very little cell death in the inner retina's tissue; if sufficient oxygen could be supplied, retinal consumption would be the same as healthy. Therefore, the model overestimates the oxygen. The percentage of cell death is not modeled, as it would be a free parameter that is difficult to estimate correctly. Instead, the model sets an upper bound. As is seen in section 7.3.2, the provided oxygen tension may be modulated as desired.

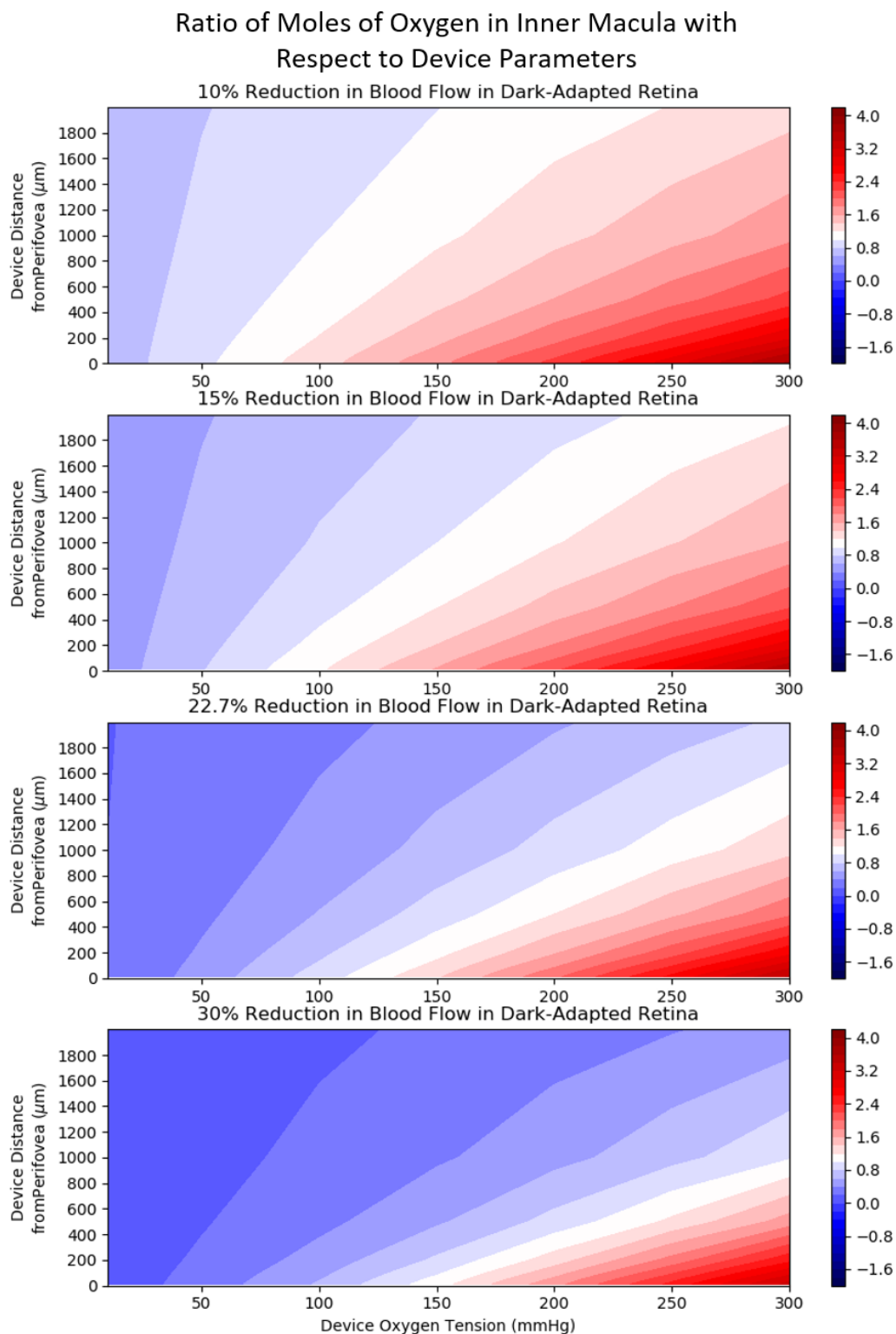


Figure 2.19: Contour map of the ratio between moles of oxygen in the inner macula (integration of concentration in the NFL, GCL, IPL, OPL) for treated ischemic tissue compared to the untreated healthy case. A value less than 1 (blue) means the oxygen concentration is less than the healthy case. A value greater than 1 (red) means the net oxygen tension is higher than the healthy case.

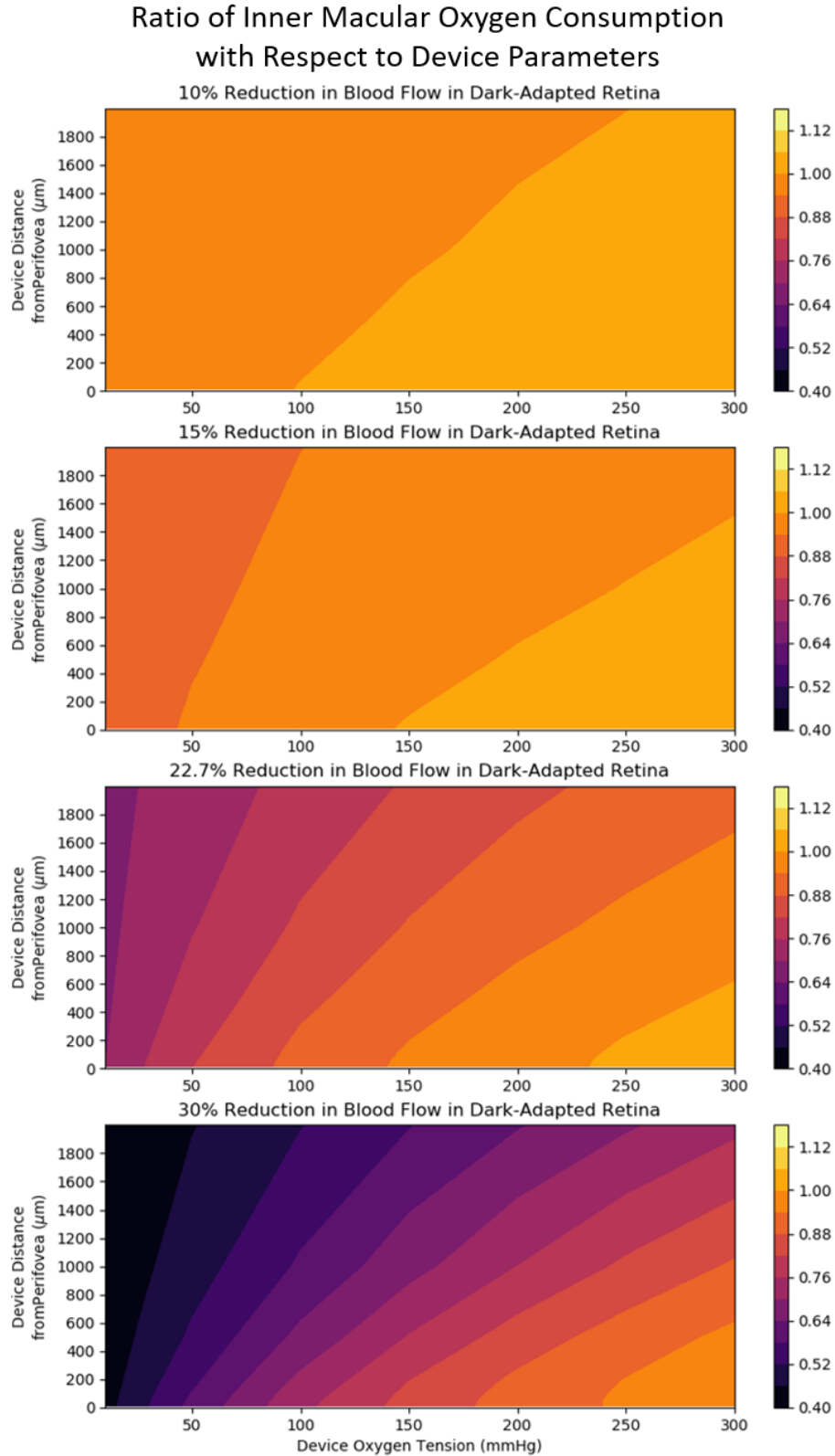


Figure 2.20: Contour map of oxygen consumption in the inner macula. Ratio oxygen consumption in the dark adapted inner macula between the treated ischemic and untreated healthy cases. A consumption of 1 or higher (orange to yellow) will be considered healthy.

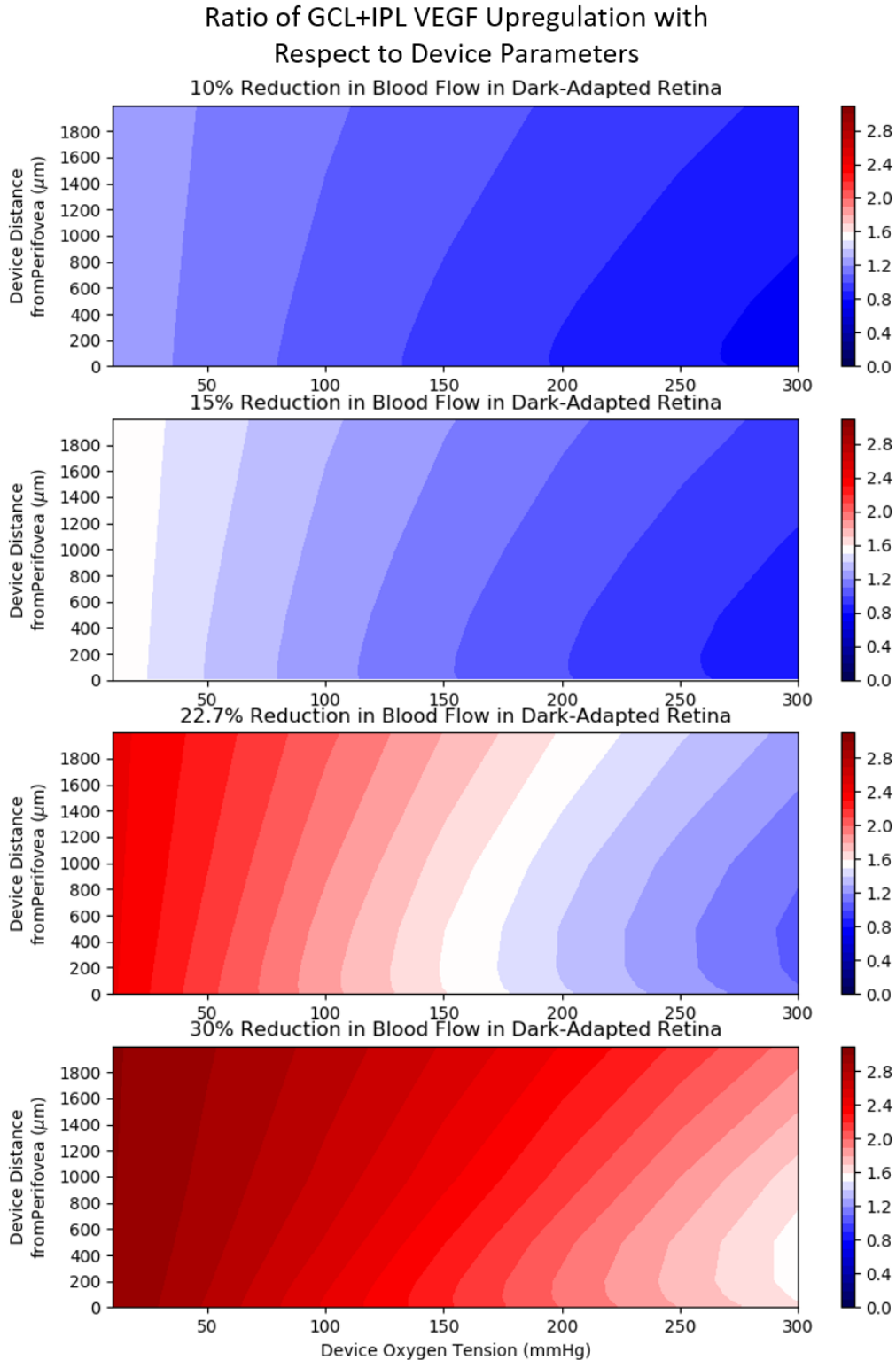


Figure 2.21: Contour map of VEGF upregulation in the GCL and IPL. Ratio between treated ischemic and untreated healthy case, for the integrated VEGF Upregulation in the GCL and IPL for a dark-adapted macula. The goal would be to minimize the amount of VEGF production in tissue to near the healthy value.

Finally, this device requires approximately 0.25nmol/s of oxygen to achieve treatment (**Table 2.6**). This requirement is only 3x the inner retinal deficit over the 6mm radius of the modeled retina (**Table 2.4**). This is an efficiency of at worst 36.4%. The flux has little variation between 200 μ m and 1mm separation from the retina, so the target maximum flux is accurate.

Table 2.6: Simulated oxygen flux from diffusor in nmol/s out of the device. The estimate was taken on the outer surface of the silicone wall. The top and bottom silicone walls are 120 μ m thick, and the device is 0.5mm from the NFL at perifovea.

| Diffusor Oxygen Flux at 0.5mm from Dark Adapted Perifovea (nmol/s) | | | | | | |
|---|------------|-------------|--------------|---------------|-----------|--------------|
| Blood Flow (μm) | | 42.7 | 38.43 | 36.295 | 33 | 29.89 |
| Device O₂ Tension (mmHg) | 25 | 0.004 | 0.008 | 0.012 | 0.017 | 0.020 |
| | 50 | 0.023 | 0.028 | 0.031 | 0.037 | 0.040 |
| | 100 | 0.063 | 0.067 | 0.069 | 0.075 | 0.080 |
| | 150 | 0.102 | 0.105 | 0.108 | 0.113 | 0.119 |
| | 200 | 0.140 | 0.143 | 0.146 | 0.150 | 0.156 |
| | 250 | 0.178 | 0.181 | 0.183 | 0.187 | 0.193 |
| | 300 | 0.215 | 0.218 | 0.220 | 0.223 | 0.228 |

2.4 REFERENCES

- [2.1] Roos, M.W., “Theoretical Estimation of Retinal Oxygenation during Retinal Artery Occlusion,” *Physiol Meas.* 25 (2004) 1523-1532. doi:10.1016/j.combiomed.2006.09.005
- [2.2] Braun, R.D., Linsenmeier, R.A., Goldstick, T.K. , “Oxygen Consumption in the Inner and Outer Retina of the Cat,” *Investigative Ophthalmology & Visual Science*, March 1995, Vol. 36, No. 3, pp.542-554.
- [2.3] Boulton, M., Foreman, D., Williams, G., McLeod, D. “VEGF localization in diabetic retinopathy,” *Br. J. Ophthalmol* 52:561-568 (1998). doi:10.1136/bjo.82.5.561
- [2.4] Tayyari, F., Khuu, L.A., Flanagan, J.G., Singer, S., Brent, M.H., Hudson, C. “Retinal Blood Flow and Retinal Blood Oxygen Saturation in Mild to Moderate Diabetic Retinopathy,” *IOVS*, October 2015, Vol. 56, No. 11, 6796-6800. doi:10.1167/iovs.15-17481

- [2.5] Yu, D.Y., Cringle, S.J., Yu, P.A., Su, E.N. "Intraretinal Oxygen Distribution and Consumption during Retinal Artery Occlusion and Graded Ventilation in the Rat," *Invest Ophthalmol Vis Sci*. 2007 May;48(5):2290-6. doi:10.1167/iovs.06-1197
- [2.6] Yu, D.Y., Cringle, S.J., Yu, P.A., Su, E.N. "Intraretinal Oxygen Consumption in the Rat In Vivo," *Invest Ophthalmol Vis Sci*. June 2002, Vol.43, 1922-1927.
- [2.7] Yu, D.Y., Cringle, S.J. "A multi-layer model of retinal oxygen supply and consumption helps explain the muted rise in inner retinal PO₂ during systemic hyperoxia," *Comp Biochem Physiol A Mol Integr Physiol*. 2002 May;132(1):61-6. doi: 10.1016/S1095-6433(01)00530-X
- [2.8] Campbell, J.P., Zhang, M., Hwang, T.S., Bailey, S.T., Wilson, D.J., Huang, J.&D. "Detailed Vascular Anatomy of the Human Retina by Projection-Resolved Optical Coherence Tomography Angiography," *Sci Rep*. 2017 Feb 10;7:42201. doi: 10.1038/srep42201.
- [2.9] LoDuca, A.L., Zhang, C., Zelkha, R., Shahidi, M. "Thickness Mapping of Retinal Layers by Spectral Domain Optical Coherence Tomography," *Am J Ophthalmol*. 2010 December; 146(6): 849–855. doi:10.1016/j.ajo.2010.06.034.
- [2.10] Karampelas, M., Sim, D.A., Kean, P.A., Papastefano, V.P., Sadda, S.R., Tufail, A., Dowler, J. "Evaluation of retinal pigment epithelium-Bruch's membrane complex thickness in dry age-related macular degeneration using optical coherence tomography," *Br J Ophthalmol*. 2013 Oct;97(10):1256-61. doi:10.1136/bjophthalmol-2013-303219. Epub 2013 Jul 10.
- [2.11] Yu, D.Y., Cringle, S.J. "Oxygen Distribution and Consumption within the Retina in Vascularised and Avascular Retinas and in Animal Models of Retinal Disease," *Prog. Retin. Eye Res* (2001), Vol. 2 Issue 2, pp.175-208. doi:10.1016/S1350-9462(00)00027-6
- [2.12] Wangsa-Wirawan, N.D., Linsenmeier, R.A. "Retinal Oxygen: Fundamental and Clinical Aspect," *Arch. Ophthalmol*. Vol. 121, Apr 2003. pp.547-557. doi:10.1001/archophth.121.4.547
- [2.13] Linsenmeier, R.A., Braun, R.D. "Oxygen distribution and consumption in the cat retina during normoxia and hypoxemia," *J Gen Physiol*. 1992 Feb 1; 99(2): 177–197. doi:10.1085/jgp.99.2.177

- [2.14] Yu, D.Y., Cringle, S.J., Su, E.N. “Intraretinal Oxygen Distribution in the Monkey Retina and the Response to Systemic Hyperoxia,” *Invest Ophthalmol Vis Sci*. December 2005, Vol.46, 4728-4733. doi:10.1167/iovs.05-0694
- [2.15] Pe’er, J., Shweiki, D., Itin, A., Hemo, I., Gnessin, H., Keshet, E. “Hypoxia-Induced Expression of Vascular Endothelial Growth Factor by Retinal Cells is a Common Factor in Neovascularizing Ocular Diseases,” *Lab Invest*. 1995 Jun; 72(6):638-45. doi:10.1007/BF00193171
- [2.16] Wang, Q., Kocaolgu, O.P., Cense, B., Bruestle, J., Jonnal, R.S., Gao, W., Miller, D.T. “Imaging Retinal Capillaries Using Ultrahigh-Resolution Optical Coherence Tomography and Adaptive Optics,” *Invest Ophthalmol Vis Sci*. 2011 Aug; 52(9): 6292–6299. doi:10.1167/iovs.10-6424
- [2.17] “Simple Anatomy of the Retina: Percent of Ocular Supply in Choroid” by Helga Kolb <https://webvision.med.utah.edu/book/part-i-foundations/simple-anatomy-of-the-retina/> (Retrieved Apr 5, 2019).
- [2.18] Birol, G., Wang, S., Budzynski, E., Wangsa-Wirawan, N.D., Linsenmeier, R.A. “Oxygen distribution and consumption in the macaque retina,” *Am J Physiol Heart Circ Physiol*. 2007 Sep;293(3):H1696-704. Epub 2007 Jun 8. doi:10.1152/ajpheart.00221.2007
- [2.19] Birol, G., Wang, S., Budzynski, E., Wangsa-Wirawan, N.D., Linsenmeier, R.A. “Oxygen distribution and consumption in the macaque retina,” *Am J Physiol Heart Circ Physiol*. 2007 Sep;293(3):H1696-704. Epub 2007 Jun 8. doi:10.1152/ajpheart.00221.2007
- [2.20] Kim, M.C., Lam, R.H.W., Thorsen, T., Asada, H.H. “Mathematical analysis of oxygen transfer through polydimethylsiloxane membrane between double layers of cell culture channel and gas chamber in microfluidic oxygenator,” *Microfluid Nanofluid* (2013) 15: 285. doi:10.1007/s10404-013-1142-8
- [2.21] Murali, K., Kang, D., Nazari, H., Scianmarello, N., Cadenas, E., Tai, Y.C., Kashani, A., Humayun, M. “Spatial Variations in Vitreous Oxygen Consumption,” *PLoS One*. 2016; 11(3): e0149961. doi:10.1371/journal.pone.0149961

[2.22] Tayyari F., Khuu L.A., Flanagan J.G., Singer S., Brent M.H., Hudson C., "Retinal Blood Flow and Retinal Blood Oxygen Saturation in Mild to Moderate Diabetic Retinopathy," *IOVS*, October 2011, Vol. 56, No. 11, 6796-6800. doi:10.1167/iovs.15-17481

[2.23] Chiarooto, J.A., Hill, R.P. "A quantitative analysis of the reduction in oxygen levels required to induce up-regulation of vascular endothelial growth factor (VEGF) mRNA in cervical cancer cell lines," *British Journal of Cancer* (1999) 80(10), 1518–1524. doi:10.1038/sj.bjc.6690555

CHAPTER 3 – HARVESTING OXYGEN: THE OXYTRANSPORTER

Efforts are being made towards improving the underwhelming pharmacokinetics of most new drugs [3.1]. To that end, current research focuses on drug delivery mechanisms that promise selective delivery and zero-order or near zero-order kinetics: mechanisms such as biodegradable nanoparticle carriers, drug elution devices and refillable pumps [3.2]. These mechanisms are ingested, injected, or implanted. In chronic disease management, these mechanisms must be replaced. This chapter is about a design of a permanent mechanism to treat diabetic retinopathy.

3.1 THE OXYTRANSPORTER

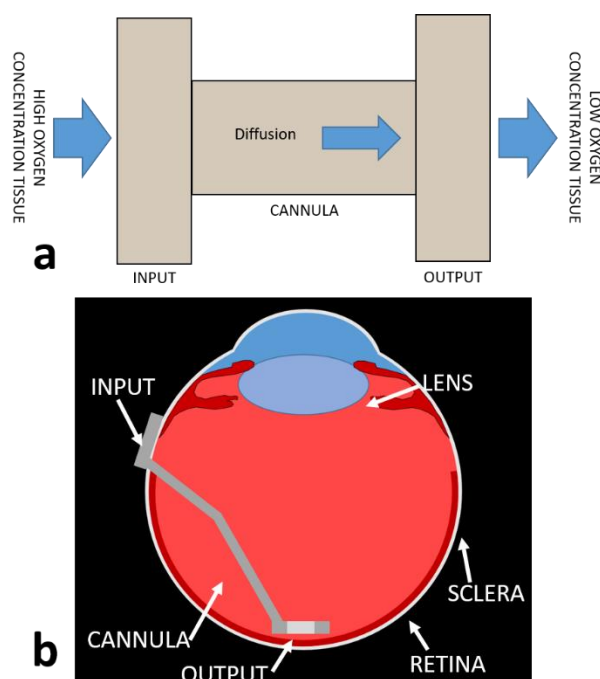


Figure 3.1: Oxytransporter concept. (a) Diagram of shunt. An input side accumulator is placed near a high oxygen tension source, and an output is placed near the target tissue. A high permeability thin cannula connects the two. The input and output have a larger area than the cannula to reduce the impedance through liquids and the silicone encapsulant used. (b) This shows the placement of the target device, where the input sits on the sclera, and the cannula penetrates at the pars plana to prevent tearing the retina. The output is a hook that surrounds the macula, to oxygenate it without occluding central vision.

The oxytransporter harvests oxygen from a region (the input) with high concentration and shuttles it to a region (the output) with low concentration, acting like a shunt. This shunt must have a non-occluding, non-fouling, and highly gas permeable pathway between the input and output (**Figure**

3.1a). There are several high oxygen concentration areas in the body, as seen in **Table 3.1**. Selection of the source depends on surgical considerations and on minimization of the conduit of the oxytransporter. Three factors must be determined: the location of the source, and the location output, and the path in between.

Since this oxytransporter will treat DR, one must look at the sources of oxygen tension in the eye: the choroid and the atmosphere. The choroid is relatively difficult to access, and surgeries increase the chances of retinal detachment. Therefore, the oxytransporter's input should be located in contact with the atmosphere. The input must be on the surface of the eye, and the oxytransporter must travel into the vitreous humor with an output in the vicinity of the macula of the retina. Animal studies by Abdallah et al. support the viability of oxygenating the vitreous to treat the inner retina [3.3]. Conferring with ophthalmologists at USC, the pars plana was chosen as it is a suitable and established region at which to transverse the sclera and can tolerate incisions of approximately 3mm.

Table 3.1: Partial pressures of a healthy adult inspiring atmospheric oxygen.

| OXYGEN SOURCE | OXYGEN PARTIAL PRESSURE [mmHg] |
|---|---------------------------------------|
| ALVEOLAR [3.4] | 107mmHg |
| ARTERIAL BLOOD GAS [3.5] | 75-100mmHg |
| CHOROIDAL CAPILLARIES [3.6], [3.7] | 57 mmHg |
| SUBCUTANEOUS [3.8], [3.9] | 86mmHg[3.8] or 65.7 mmHg [3.9] |
| ATMOSPHERE | 160mmHg |

Using the atmosphere as an input limits the treatment to mild to moderate NPDR that according to the AXSY model requires less than the 160mmHg provided by the atmosphere. The AXSY model (Section 2.3 estimates the inner macula requires 0.72nmol/min for 15% ischemia on a ring shaped output.

The permeability of the conduit material must be considered. The upper limit on the oxytransporter's cross-sectional area, A , for the portion (i.e. cannula) penetrating the sclera is 3mm^2 . The conduit must traverse half the length, L , of the human eye, which is 12mm (**Figure 3.1b**). The permeability of the conduit material is found by an approximation using Fick's first law

$$Q = -AP \frac{\partial p}{\partial x} \quad (3.1)$$

$$P = \frac{QL}{A(p_{O_2,atm} - p_{O_2,ret})} \quad (3.2)$$

where p is the partial pressure, P is the permeation constant, and Q is the net flux. The oxygen tension 5mmHg, near the retina, $p_{O_2,ret}$, [3.10], and 159mmHg in atmosphere, $p_{O_2,atm}$. Therefore, the required permeability is 6.9×10^3 Barrer. From **Table 3.2**, silicone, the state-of-the-art, falls short with a permeability of 600 Barrer [3.11]. Only an air-filled channel will satisfy this requirement, potentially with a thin layer of silicone sealing both ends.

Table 3.2: Oxygen Permeability of different materials. The permeability of a material is the product of the sorption equilibrium parameter and the diffusion constant. Permeation only occurs in solids, but one can represent the product of Henry's solubility and the diffusion constant in a similar fashion of liquids. For air, the relationship between concentration $c = n/V$, and pressure is given by the ideal gas law as $p = c/R_{gas}T$, where $1/R_{gas}T$ is similar to Henry's solubility and the sorption solubility constant. The "permeability" of air can be calculated by $D_{O_2,air}/R_{gas}T$.

| MATERIAL | PERMEABILITY [Barrer] |
|----------------------|-----------------------|
| PARYLENE-C [3.12] | 0.042 |
| POLYIMIDE [3.13] | 0.146 |
| WATER [3.14], [3.15] | 127.6 |
| SILICONE [3.11] | 600 |
| AIR [3.16] | 2×10^7 |
| DESIRED MATERIAL | 6.9×10^3 |

Following these basic principles, oxytransporters were built out of NuSil MED4-4210 silicone, Parylene-C, and stainless steel. Such devices had a square input, a bent cannula, and a hook shaped output (the diffusor). The hook shape of the diffusor allows a larger area to pass through the scleral incision than is permitted by a ring shape. Primary design of the input and cannula for this device was performed (D. Kang, 2015) [3.17]. This oxytransporter, referred as version 1, has a 3mm x 5mm input area with a 720 μ m tall cavity and an overall height of 1.44mm, top and bottom silicone is 360 μ m thick (**Figure 3.2**). Refer to CHAPTER 6 explains the method used to mold silicone. The device uses a 10mm long, stainless steel 304, 25-gauge tube for the cannula that has a hook with an inner radius of 3mm. On one inside, the input faces the sclera, and on the other is covered by the conjunctiva or directly faces the atmosphere. The diffusor is implanted at the mid- vitreous.

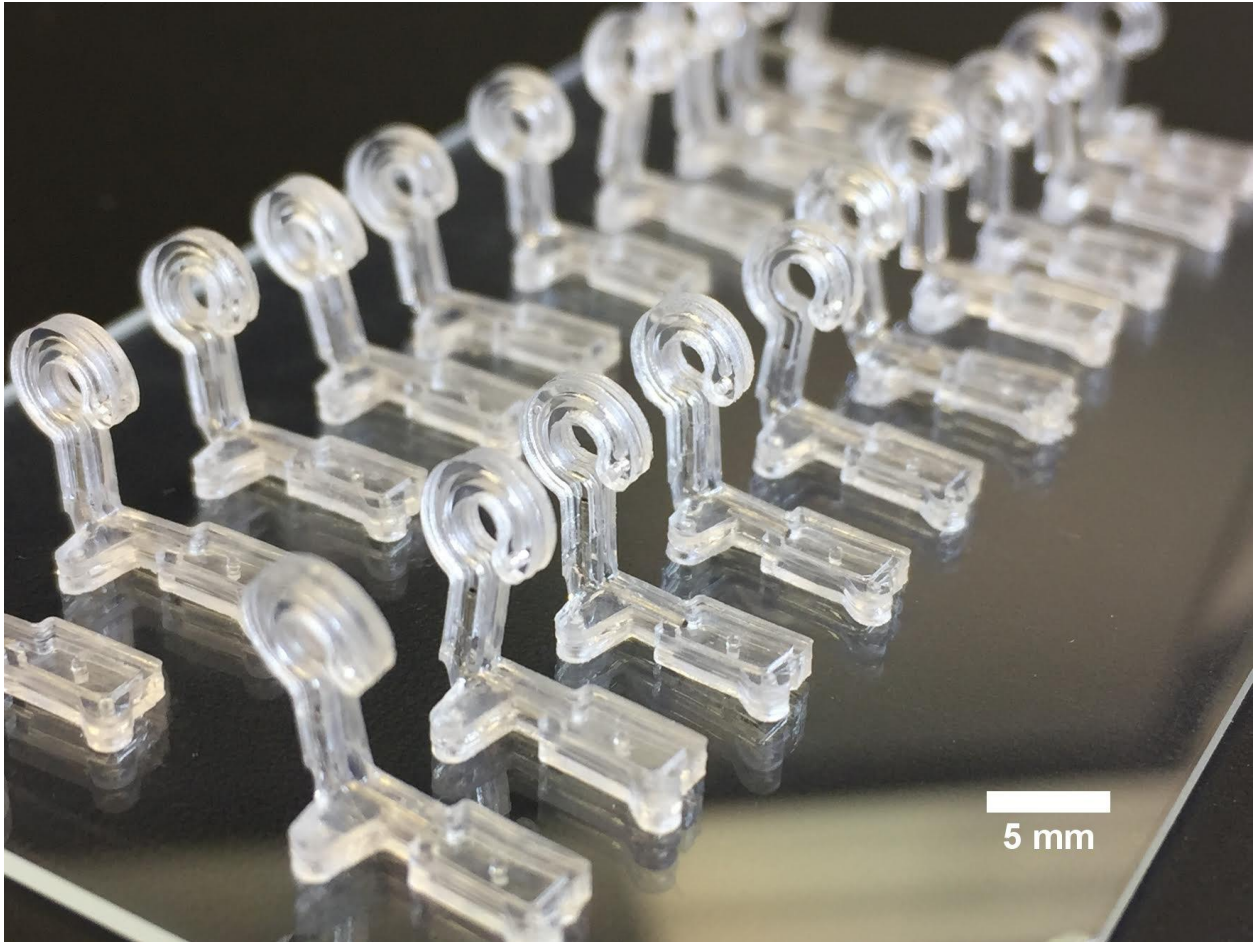


Figure 3.2: Fabricated oxytransporter devices with bent cannula. Diffusor (output) is aligns parallel to the lens in rabbits.

In early experiments, the oxytransporter was left uncovered by the conjunctiva. A simple finite element model (FEM) of oxygen transport can be constructed with stationary, Fickian diffusive transport:

$$0 = \frac{dc}{dt} = D_{ox}\nabla^2 c \quad (3.3)$$

The eye was modeled as a sphere with a 20mmHg concentration boundary condition everywhere except at the lens. The retina is supplied with more oxygen the closer the diffusor is to the retina. According to the AXSY model, vitreal oxygen consumption has a minor impact on the device's oxygen transport compared to the exact placement of the device; therefore vitreal oxygen consumption can be ignored. **Figure 3.3** shows agreement between this model and in vivo animal

measurements. In particular, the data from the rabbit and this simple FEM have a difference of less than 2% in the oxygen tension of the diffusor.

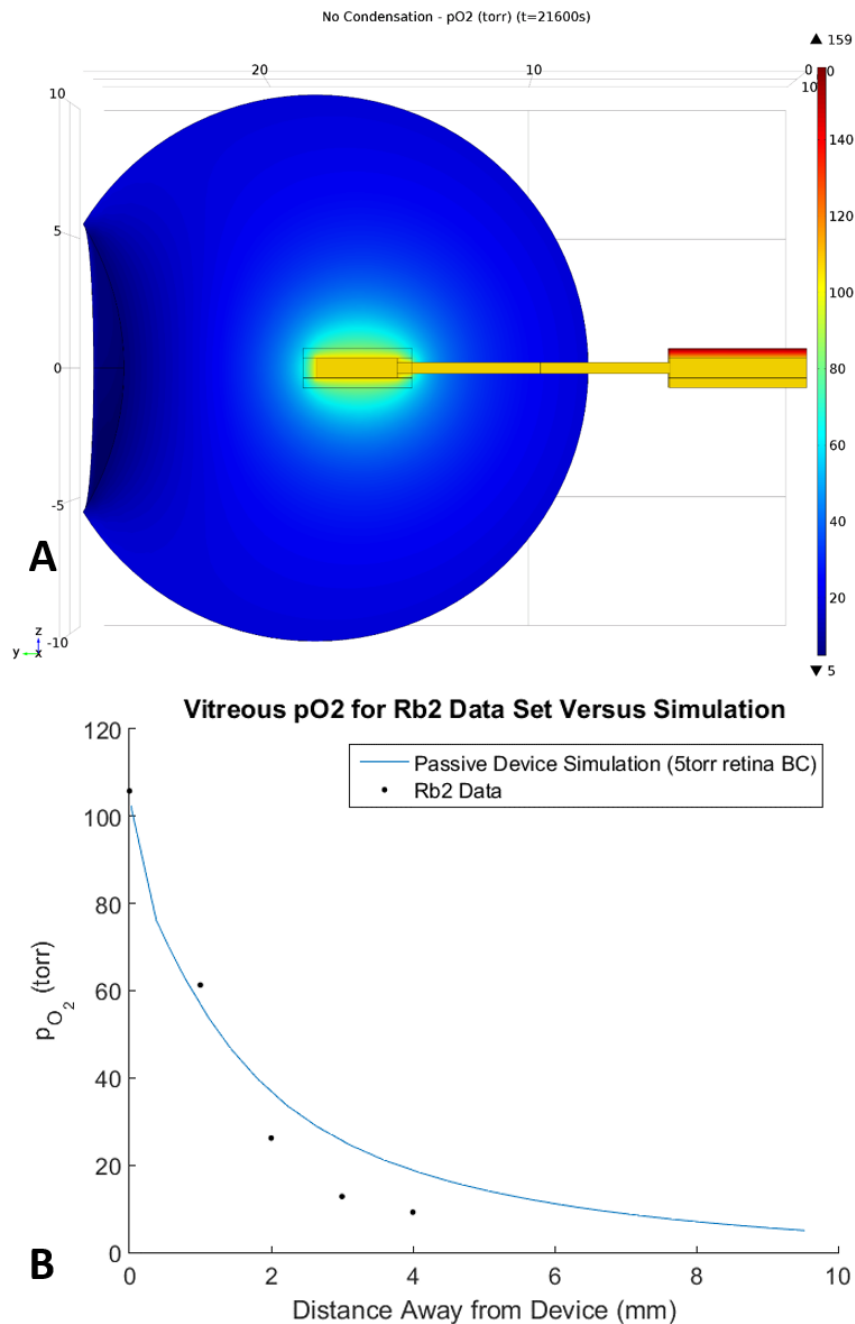


Figure 3.3: Simulation versus animal data for the oxytransporter. (A) A 3-dimensional COMSOL Multiphysics 5.0 model of oxygen transport through the device. No flux is assumed on the cannula (stainless steel), and bottom of the input side. The top of the input is assumed to be in contact with atmosphere. The diffusor is simplified to a 3mm disk with a 360 μ m top and bottom wall. (B) Oxygen tension in a line from the diffusor to the top of the eyeball as oriented in the model. This is compared to the oxygen profile in an acute rabbit experiment. In the rabbit, at 4mm the oxygen probe is near or touching the retina, but the dimensions of the human eyeball in the

model allow for a much longer profile. The two curves have a similar trend but a different slope. However, the value at the device's diffuser, 0mm in (B), has good agreement between both (within 2mmHg of each other). Therefore, the oxygen profile within the device is well modeled.

From the estimates in section 2.3.2 (**Figure 2.19**, **Figure 2.20**, and **Figure 2.21**), this device may treat a 15% reduction in blood flow at 1mm or smaller separation from the retina when exposed to atmospheric oxygen tension during the day. During sleep the eyelid is closed and the oxygen tension of the diffuser drops significantly. Oxygen tension under the eyelid has been reported to be around 58mmHg, which is approximate one-third that of atmospheric oxygen [3.37]. Nevertheless, this device may offer treatment for early mild diabetic retinopathies. The number of mild retinopathies identified will rise with new detection methods. Early treatment of mild retinopathies by photocoagulation reduces the rate of progress [3.38]; if early treatment can mitigate hypoxia as well, mild retinopathies may progress still slower if at all.

For more severe ischemia where higher oxygen tension and flux is required and for treatment at night, the device will need to generate its own oxygen.

3.2 CONDENSATION

Oxytransporters implanted on rabbits' mid vitreous resulted in elevated oxygen tension from the diffuser in acute experiments. However, one week follow-up experiments did not produce consistent results; some oxytransporters had no measureable response to oxygen, even with pure oxygen blown over the input. Water droplets observed in the device indicate that condensation may be affecting oxygen transport (**Figure 3.4**).

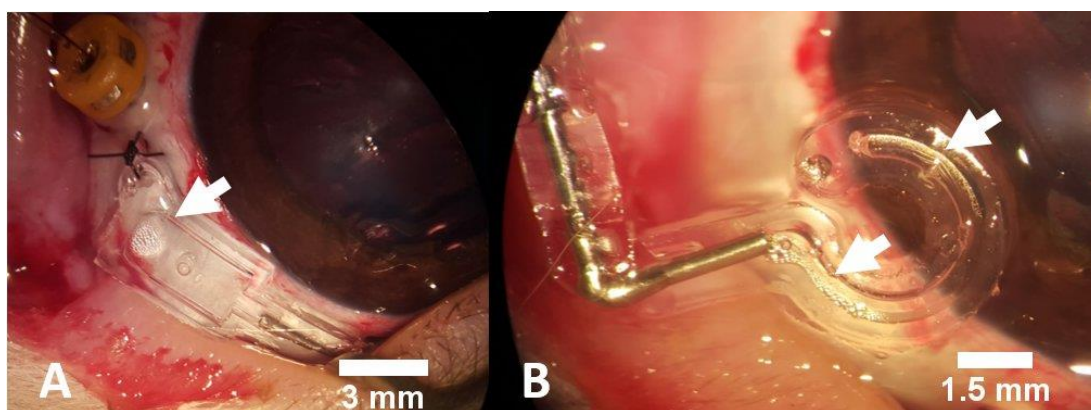


Figure 3.4: *in vivo* condensation in the device. The white arrows point to condensation occurring in the (A) input after being implanted, and (B) diffuser after being explanted. The condensation on

the input side was been observed to occur in the timescale of minutes (within 5 minutes for this particular case).

A thermal gradient between the surface of the eye and the vitreous humor is well documented [3.18], [3.19], [3.20]. The eye experiences, in the mm closest to its surface, the greatest deviation from body temperature [3.20]. In addition, the entire eye is a high humidity environment, with partial pressure of water near or at the saturation pressure for the given temperature ($p/p_{sat,bulk} \approx 1$). Bulk saturation pressure of water is highly temperature dependent, T [3.21]:

$$p_{sat,bulk} = 0.61078 \exp\left(\frac{17.27T}{T+237.3}\right), \quad (3.4)$$

As water vapor diffuses from the body temperature of the vitreous through the oxytransporter, which is near the atmosphere, the saturation limit is surpassed ($p/p_{sat,bulk} \geq 1$) and water condenses. Given that the diffusion coefficient of oxygen in water is 9000 times slower than in air [3.16], even minimal condensation would occlude the oxytransporter.

A model of condensation in the device was created to allow for rapid iteration of solutions. This model incorporates water vapor and heat transport, which are linked by equation (3.4). If $p/p_{sat,bulk} > 1$, then the relative humidity in the air exceeds 100% and water will begin to condense locally. Heat transport is dominated by conduction:

$$\frac{\rho C_p \partial T}{\partial t} = \nabla \cdot (k \nabla T), \quad (3.5)$$

where ρ is the density of the material, C_p is the specific heat, k is the conductivity of the material, and T is the temperature. Equation (3.5) is solved in the time-dependent domain. Boundary conditions between materials are defined as continuous in temperature and heat flux:

$$T_1(\mathbf{x}_0) = T_2(\mathbf{x}_0) \quad (3.6)$$

$$n \cdot (k \nabla T_1)|_{\mathbf{x}_0} = n \cdot (k \nabla T_2)|_{\mathbf{x}_0} \quad (3.7)$$

Table 3.3 and **Table 3.4** include the parameters used in this model. The sections of the oxytransporter inside the eye (the diffusor and 5mm of the cannula closest to the diffusor) and those

in contact with the sclera (the lower half of the device) were kept at body temperature, 37°C. The remaining parts of the device was set to ambient temperature. **Figure 3.5** shows the temperature distribution. Note the ambient and body temperature boundary conditions meet at the center of the cannula.

Table 3.3: Parameters for heat transport simulation [3.22], [3.23]

| MATERIAL | ρ (g/cm ³) | C_p (J/kg·K) | k (W/m·K) | γ |
|------------------|-----------------------------|----------------|-------------|----------|
| SILICONE | 0.965 | 1450 | 0.15 | |
| SS304 | 8.03 | 530 | 16 | |
| AIR | 1.1315 | 1005.6 | 0.02624 | 1.4 |
| PERFLUOROCARBONS | 1.908 | 446.8 | 0.067409 | 1 |

Table 3.4: Parameters for water vapor transport.

| MATERIAL | D (cm ² /s) | k_h (mol/kg·m ²) |
|----------------------|--------------------------|--------------------------------|
| Silicone [3.23] | 2E-5 | 8.9810E-6 |
| Air [3.30] | 0.22 | Ideal gas law |
| Water [3.14], [3.31] | 3E-5 | 1.2458E-5 |

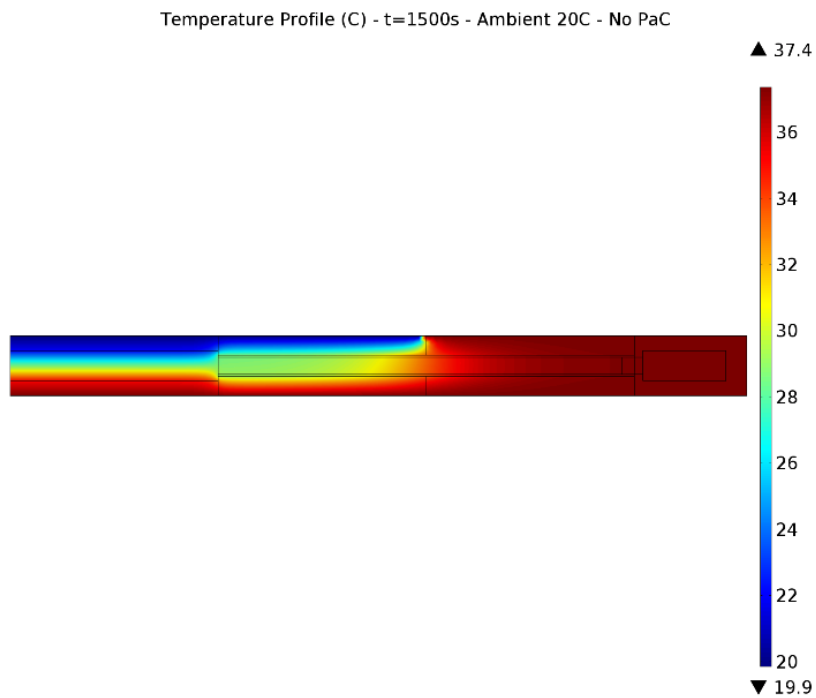


Figure 3.5: Simulation of temperature profile of the oxytransporter. The bent cannula is flattened out here to simplicity. While the model is fully 3-D with a cylindrical diffuser, the cross section where a symmetry line was placed to reduce mesh size is shown.

The same physics of oxygen transport applies to water vapor transport. To simplify the model, the process of “consuming” water vapor by condensation is not considered (to model the exact dynamics

of water condensing into a droplet would need to include a model of the volume taken up by the water droplets, adding unnecessary complexity).

The locations of the boundary conditions for water vapor transport match those of heat transport. Specifically, where the temperature was set to body temperature, the water vapor pressure is instead set to the saturation vapor pressure at body temperature, as defined by equation (3.4), and where the device had an ambient temperature boundary condition, the device now has a water vapor boundary condition that is a parameter in the simulation. The maximum value for the water vapor pressure in this region is defined by the saturation pressure of water vapor at the chosen ambient temperature. **Figure 3.6** plots this water vapor distribution inside the device.

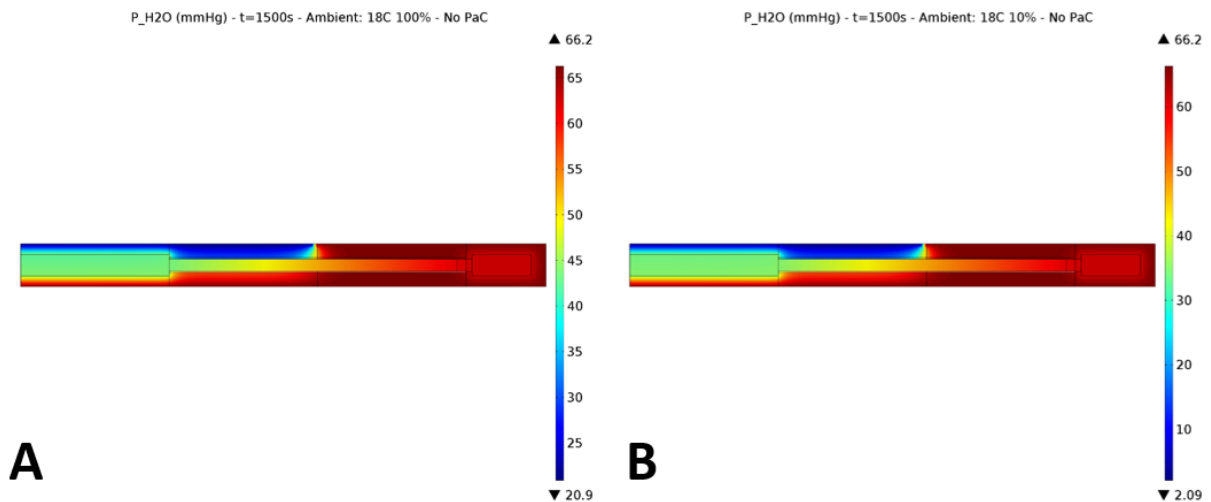


Figure 3.6: Simulation of water vapor partial pressure (mmHg) in the oxytransporter. 10% of saturation pressure at the ambient side. Notice the smoother change in water vapor tension through the cannula than in the case of the heat transport. Heat transport sees a sharper change in values since the tube walls conducts heat, while no oxygen transport occurs radially through the stainless steel tube walls.

Using the temperature and water vapor distributions, the relative humidity in the device is given by the ratio of water vapor pressure to saturation vapor pressure, $p_{H_2O}/p_{sat,bulk} = RH$ (**Figure 3.7**). In the case of 20°C at both 10% and 100% ambient relative humidity, condensation occurs in the top side of the input. This agrees with observations in implants in rabbits. **Figure 3.8** shows that it takes 90 seconds for the relative humidity in the top side of the input to surpass 1. The order of magnitude of the time for this effect agrees with observation. However, the condensation of the input membrane is insufficient to account for the complete blockage of oxygen. The simulation points to condensation

in the cannula as the culprit for decreased oxygen transport (**Figure 3.9**). **Figure 3.7** has a relative humidity >1 midway up the cannula.

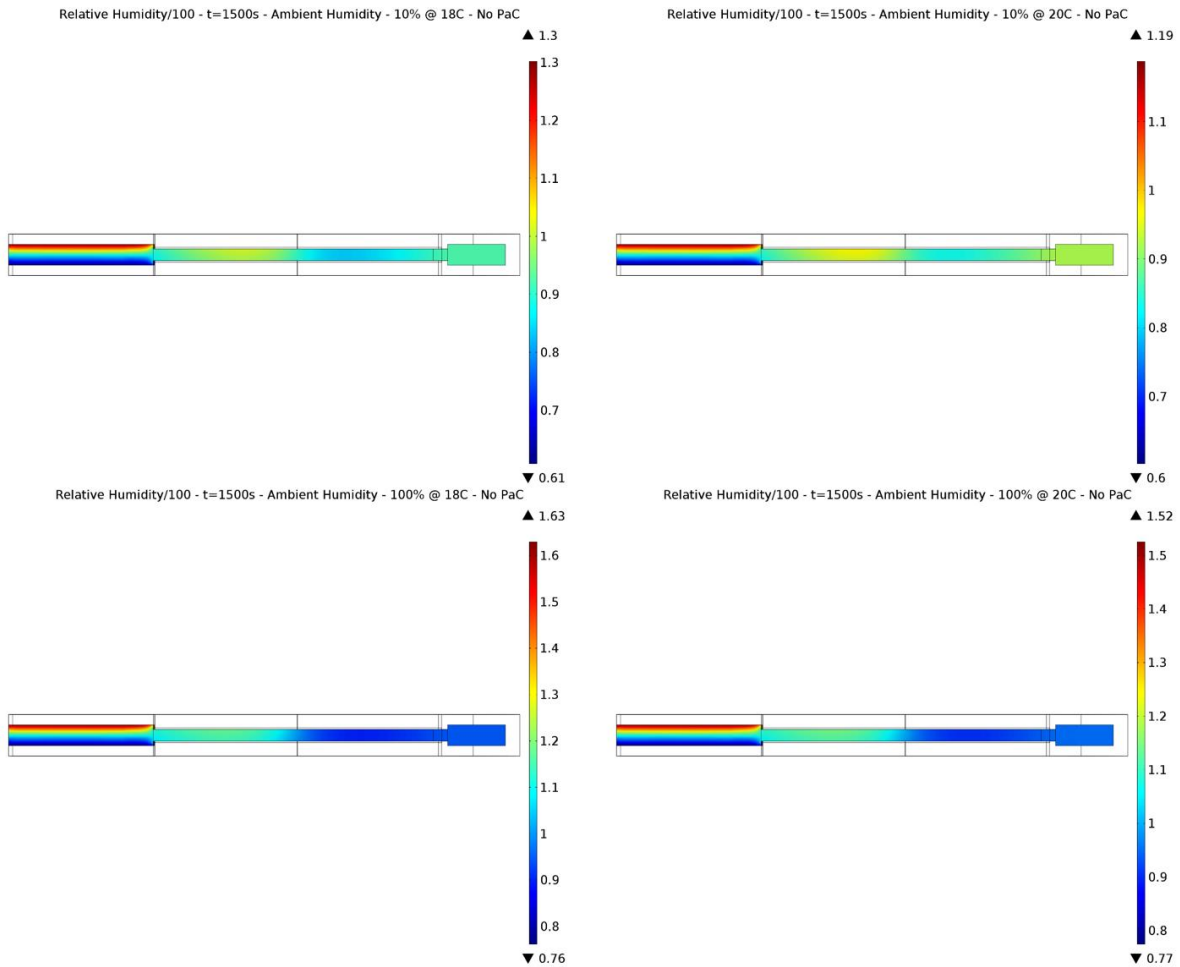


Figure 3.7: Simulation of relative humidity inside the oxytransporter. Note, in all 4 cases, the relative humidity on the top input side of the air chamber exceeds 1. This means that in nearly all conditions, the device will have condensation occur in that region (**Figure 3.4**). The definition for relative humidity only holds for air, and therefore these plots only include the region of the device filled with air.

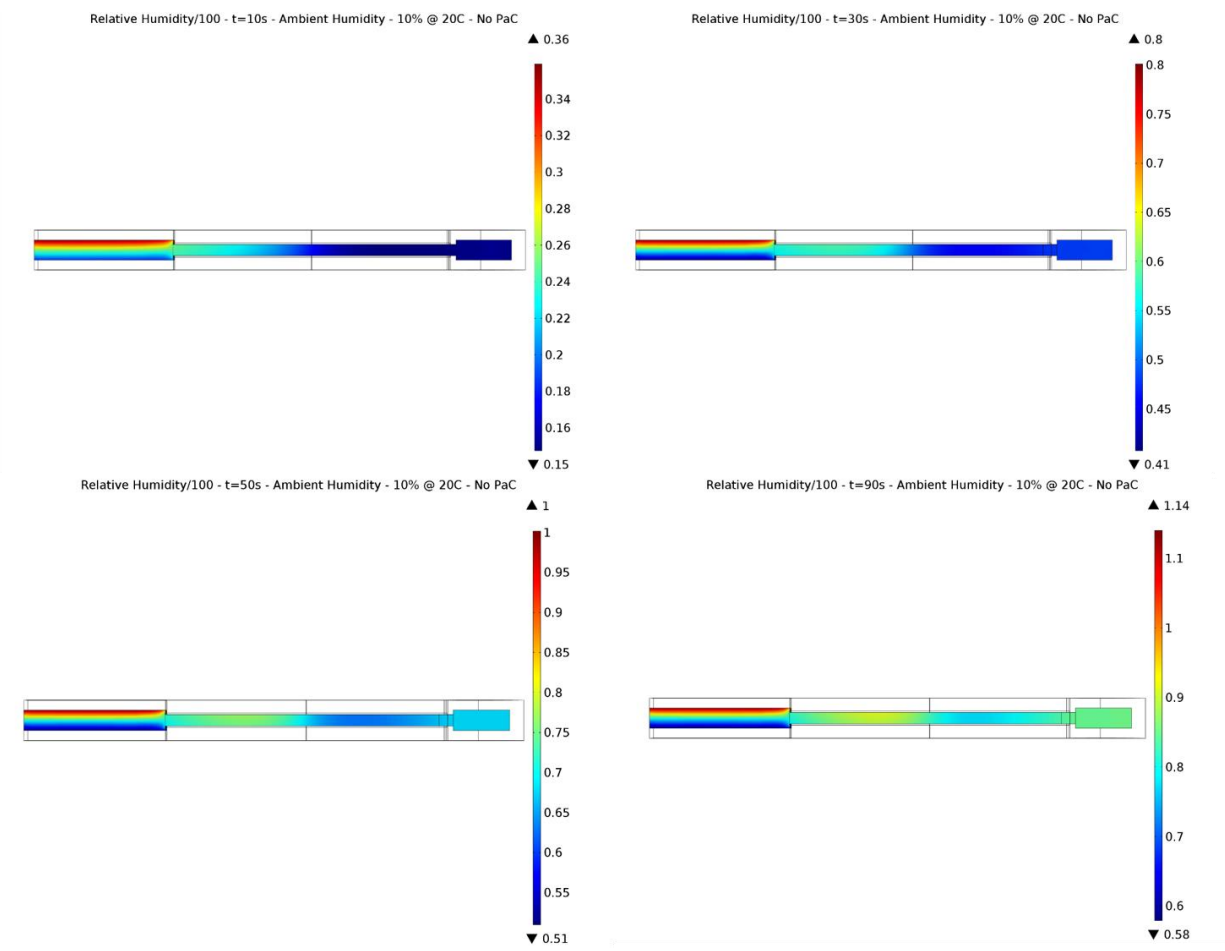


Figure 3.8: Simulation of time progression for relative humidity in the oxytransporter. Note the scale parts differ in each plot. Within 90 seconds, the critical value, $RH > 1$ is reached.

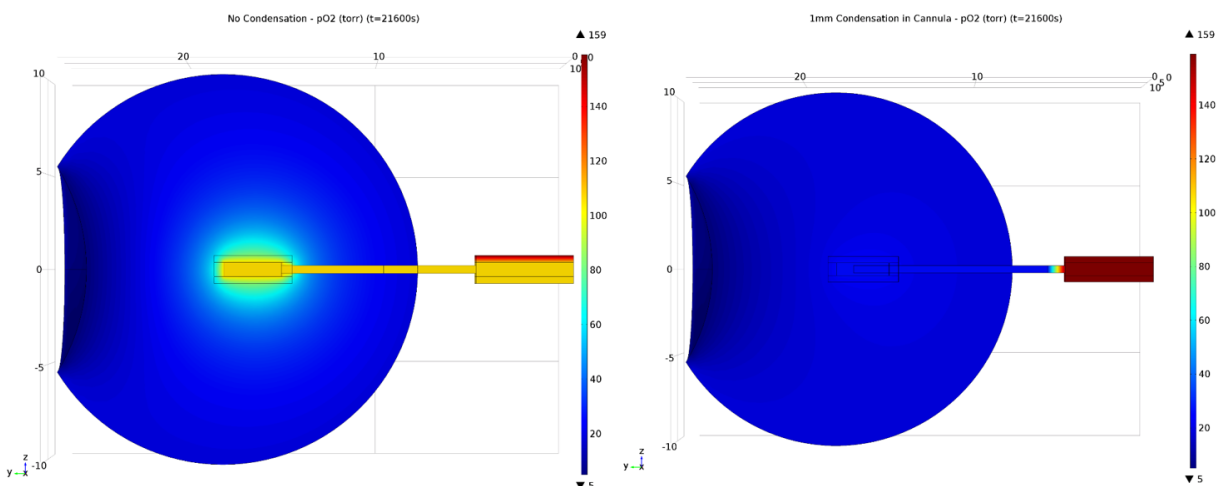


Figure 3.9: Simulation of condensation in the cannula. The left plot shows an un-occluded device. The right plot demonstrates the effect of a 1mm cylinder of water in the cannula. As predicted earlier, the significantly lower permeation coefficient of water greatly hinders oxygen transport.

Water vapor pressure at body temperature enters either from the bottom of the input side or from the diffusor, which is transported through the entirety of the cannula. As the path through the cannula is longer, and the diffusor's area is smaller than that of the input chamber, the lower side of the input chamber (the side in contact with the sclera) accounts for the majority of the water vapor entering the device. Replacing the silicone membrane of the lower section of the device, that was at a water vapor transmission rate of $1.73\text{-}3.11\text{g}\cdot\text{mm}\cdot\text{m}^{-2}\cdot\text{day}^{-1}$ with Parylene-C that has a water vapor transmission rate of $0.08\text{g}\cdot\text{mm}\cdot\text{m}^{-2}\cdot\text{day}^{-1}$, reduces the influx of water vapor into the device [3.24], [3.25]. Adding a no flux boundary condition on the bottom side of the input (meaning a sufficiently thick section of Parylene that little water vapor enters through that surface) results in a greatly reduced relative humidity in the device (**Figure 3.10**). This device will be called oxytransporter version 2.

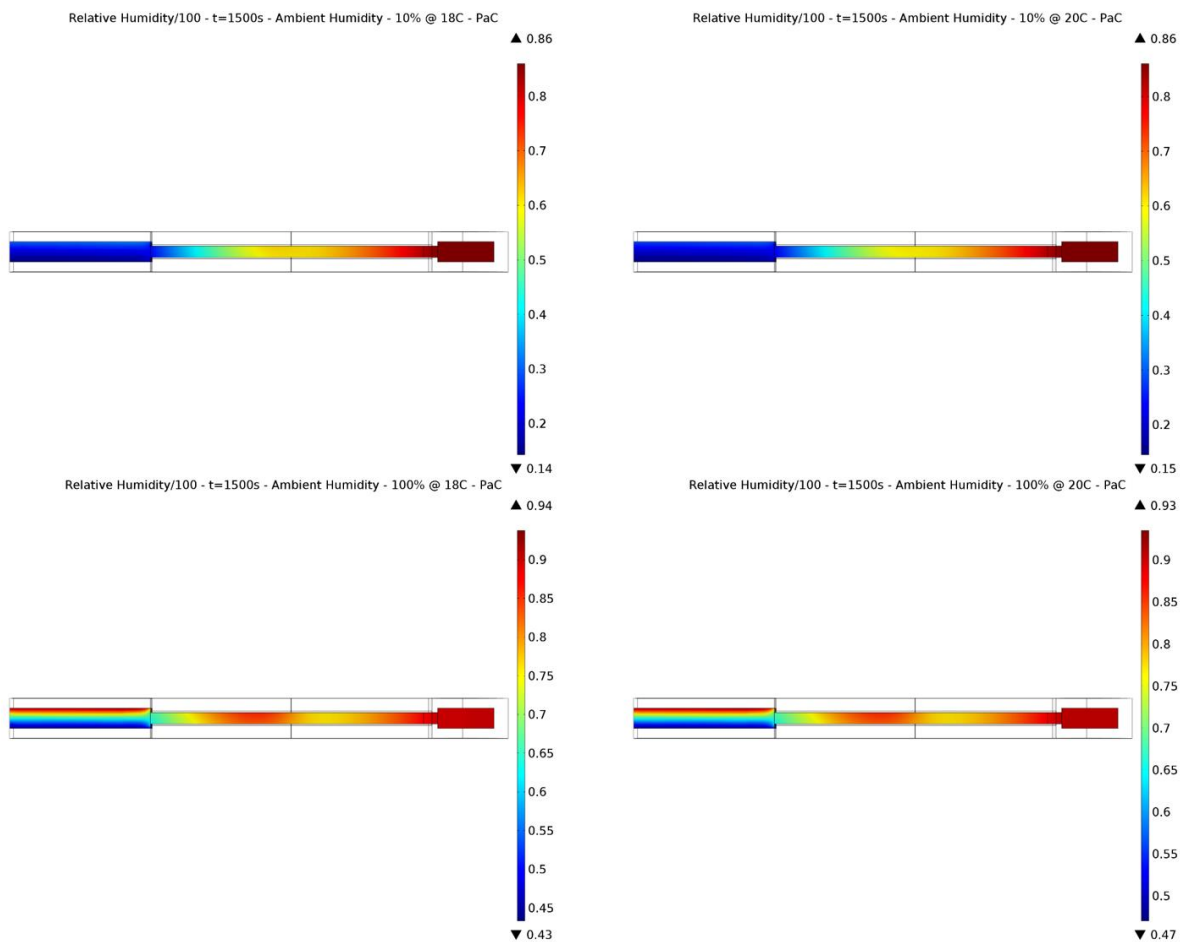


Figure 3.10: Simulation of Parylene coating on the lower half of the input. No flux boundary condition results lowered relative humidity throughout the device.

However, in the case of 100% relative humidity at the input (such as when the conjunctiva covers the device), the oxytransporter version 2 has an internal RH of 1; regardless condensation can still occlude, given a low enough temperature. A simulation of relative humidity with the proper geometry for a bent cannula, **Figure 3.11**, shows condensation in the cannula will reach $p/p_{sat} = 1.3$; explaining the occlusions of the devices *in vivo* (the devices worked after being dried, confirming the occlusion was only due to condensation).

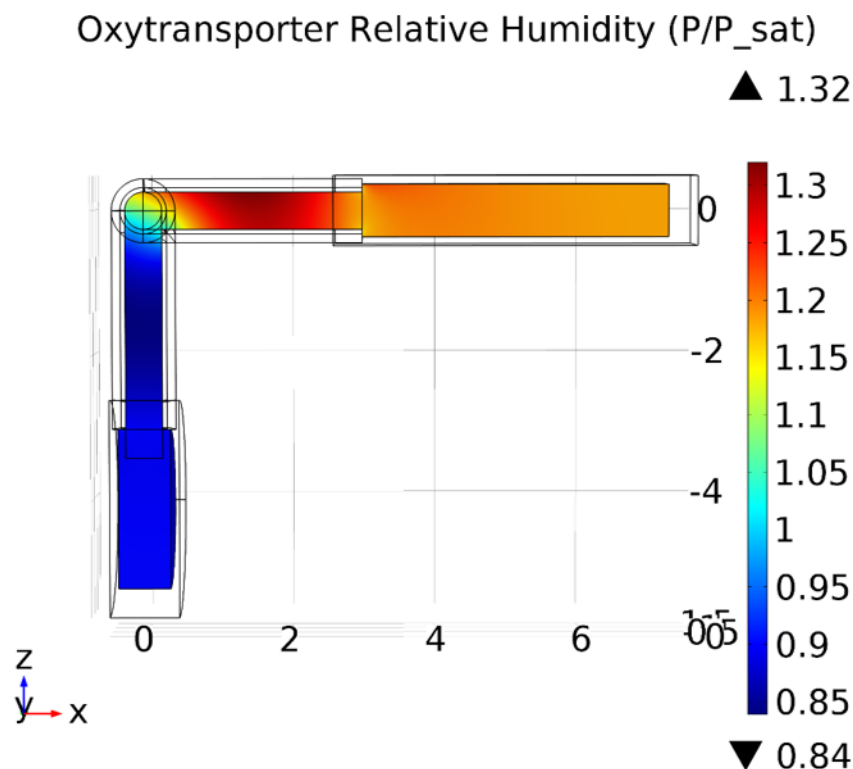


Figure 3.11: COMSOL simulation humidity in bent oxytransporter with 100% humidity on the top surface of the reservoir and on the diffuser. The vertical part is at body temperature, with the horizontal part having body temperature on the lower surface and ambient temperature, 20°C, on the upper surface. The lower surface of the diffuser is taken to be impermeable to gas transport. Note that on the horizontal portion of the cannula, the relative humidity exceeds 1.

3.3 A NANOSCALE FILLER MATERIAL

What is needed is a material to fill the area where condensation is likely to occur, thus preventing occlusion. Unfortunately, most materials have oxygen permeabilities that fall short of the required 6.9×10^3 Barrer (**Table 3.2**). Consequently, a novel filler material was developed.

If porous materials have sufficiently small pores, the equilibrium vapor pressure deviates from that of bulk material. This effect is governed by the Kelvin equation:

$$\frac{p}{p_{sat,bulk}} = \exp\left(\frac{2\gamma V_m}{rR_{gas}T}\right) \quad (3.8)$$

where $p_{sat,bulk}$ is the saturation pressure of bulk water, γ is the surface energy, V_m is the liquid molar volume, r is the droplet radius, R_{gas} is the universal gas constant, and T is the temperature. If a droplet is sufficiently small, the surface energy of the droplet exceeds the energy released by condensation and it becomes thermodynamically unfavorable to condensation. A pore with a convex curvature (hydrophobic) would constrain a droplet such that the equilibrium vapor pressure is above that of bulk, thereby increasing the vapor pressure at which condensation would occur. **Figure 3.12** plots equilibrium vapor pressure versus bulk equilibrium vapor pressure for different sizes of pores. This suggests that a hydrophobic material with pores $\leq 8.2\text{nm}$ is capable of withstanding condensation up to $p/p_{bulk} = 1.3$ (**Figure 3.11**).

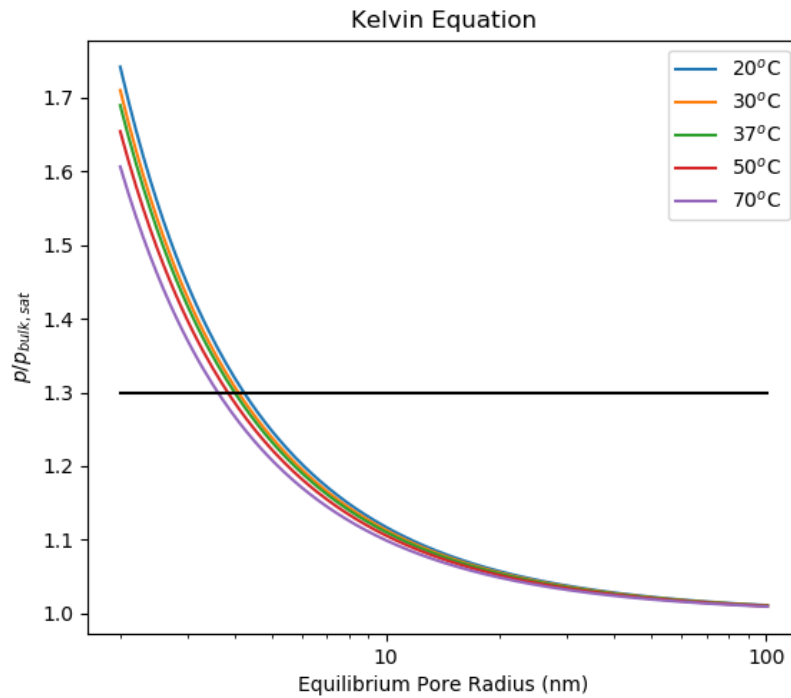


Figure 3.12: Kelvin equation plotted across multiple temperatures. From **Figure 3.11**, the material must tolerate $p/p_{bulk,sat} > 1.3$ without condensing (black horizontal line) at physiological temperatures. This intersects the Kelvin curves at 8.2nm at 37°C.

Porous glasses are commonly used in confined liquid physics [3.26]. These materials have open celled pores which are ideal for gas transport as they provide for continuous path for gaseous diffusion, despite the impermeability of the glass-phase. Furthermore, glass is generally inert in the human body and has a long history of use in implants [3.27], [3.28]. Both of these properties make porous glasses an ideal filler for the oxytransporter. Vycor 7930 in particular has pores averaging on the order of 44\AA in diameter, making it ideal for this application [3.26]. An SEM image of the surface of a Vycor 7930 sample is shown **Figure 3.13**. The image cannot resolve for pores down to 5nm, but 22% of the surface in the image is shown to be porous, with most of those pores being approximately 12nm or larger. This is in agreement with literature citing Vycor to be 28% porous [3.29]. However, glass is hydrophilic, and condense far too readily. To take advantage of the physics described by the Kelvin equation, the glass must first be hydrophobized.

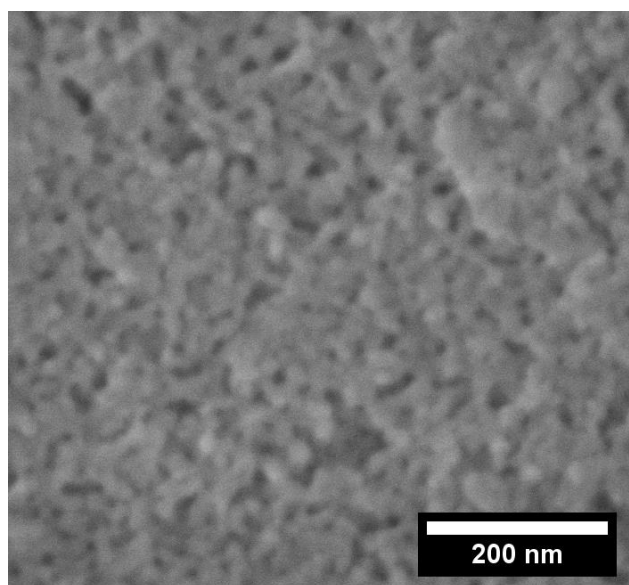


Figure 3.13: SEM image of treated Vycor 2930 nanoporous glass. Image acquired with the generous help of Dr. Matthew Hunt and the Kavli Nanoscience Institute. Pores comprise 22.6% of this image, with the smallest resolvable pores approaching 12nm in width. The porosity may be higher still, but pores down at 5nm are visible here.

3.3.1 HYDROPHOBIZATION OF NANOPOROUS GLASS

Hydrophobization of the glass is done by silanization with hexamethyldisilazane (HMDS). First, the nanoporous glass is piranha cleaned using 3:1 Nitric Acid to 30% Hydrogen Peroxide at 90°C for 2 hours or until the glass is no longer reacting with the mixture. Then, the glass is submerged into deionized water to rinse away any piranha. It is then heated to 80°C in a nitrogen environment to

drive off any moisture within the pores. Once dry, the glass is placed in a round bottom flask connected to a second flask where 3mL of HMDS (Shin-Etsu MicroSi, Inc. MicroPrime HP Primer) is placed. This is heated in a dry bead bath to 120°C for 6 hours. Then the flask with glass is separated and heated for 24 hours at 120°C. At this point, the glass has been made hydrophobic. The contact angle was measured and a float test was performed, both documented in **Figure 3.14**. Water fully wets untreated Vycor making it difficult to acquire a reading, while treated Vycor exhibits 105° indicating the material is hydrophobic on the surface. During the float test, the hydrophobized Vycor indents the surface of the water and does not take in liquid. These tests are a strong indicator of proper silanization in the material.

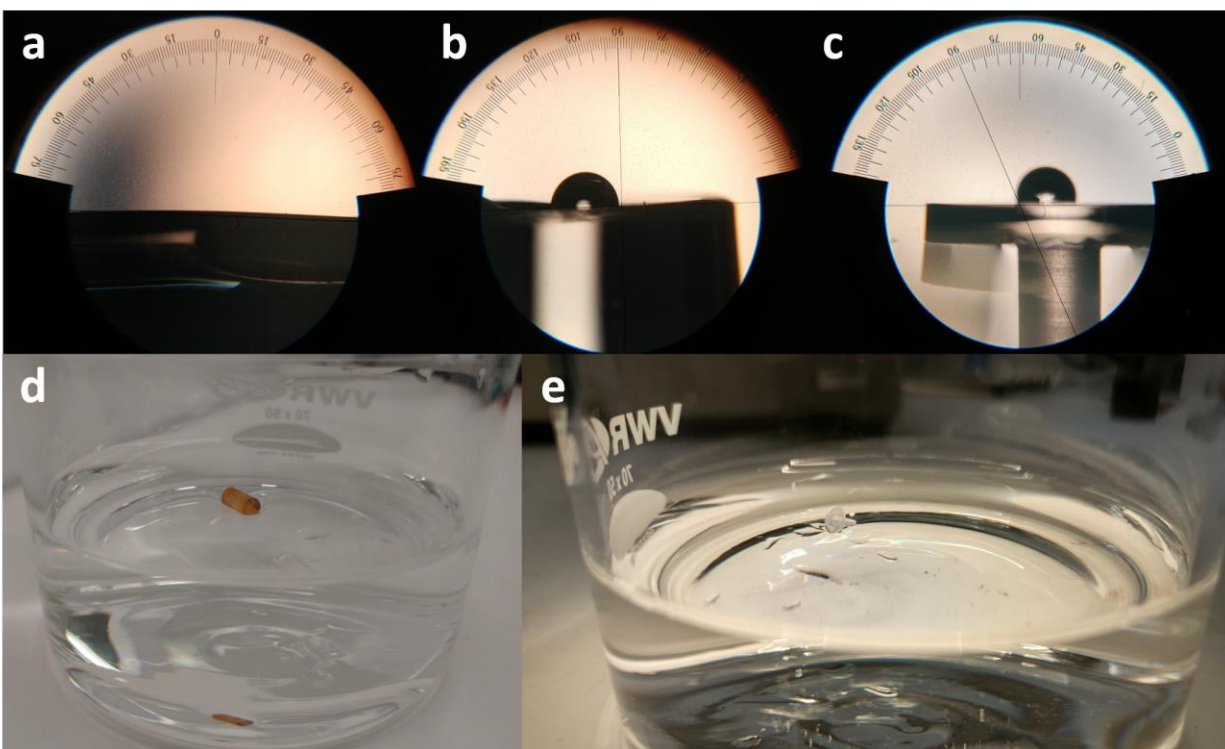


Figure 3.14: Hydrophobicity of silanized Vycor 2930. (a) Water droplet on untreated Vycor 2930 has no measurable contact angle. Untreated, Vycor 2930 is hydrophilic. (b) Silanized glass rod has a contact angle of 90°. (c) Silanized and machined Vycor 2930 tack has a contact angle of 105°. (d) Silanized Vycor 2930 floating on water, while unsilanized Vycor 2930 sinks (black circle). (e) Silanized Vycor 2930 tack floating on water.

3.3.2 VALIDATING THE NANOPOROUS ANTI-CONDENSATION FILLER

A treated Vycor sample were then tested for oxygen permeability (**Figure 3.15**). The sample was placed in a heated water bath. To reduce axial oxygen transport out of the sample, it was tightly jacketed by a polyolefin heat shrink tube. The top of the sample was left above the water bath and

exposed to a step function of gas which goes from atmosphere to 100% humidified oxygen. The oxygen was humidified by passing it through a 20°C bubbler between the oxygen source and the sample. An AL-300 AP-coat Fluorometrics Instruments oxygen probe and NeoFox reader were used to measure the response curve. This experiment was compared to an oxygen transport simulation in COMSOL.

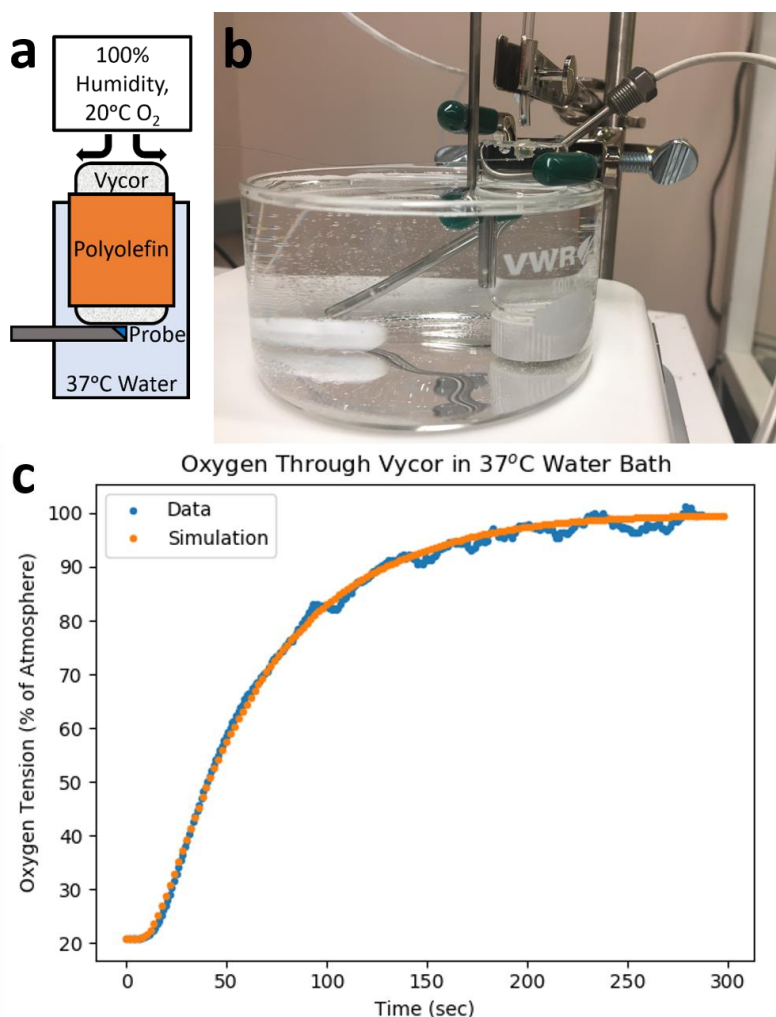


Figure 3.15: Oxygen permeability of hydrophobic Vycor 2930. (a) Diagram of test setup. Humidified oxygen is blown over silanized Vycor 2930. A polyolefin sheath surrounds the Vycor to prevent radial oxygen diffusion. The Vycor is placed inside a vial of water with ambient oxygen content. That vial is placed in a water bath on a hotplate which is agitated with a magnetic stirrer to maintain a constant temperature. Doing so assures an accurate temperature without introducing convective transport to the experiment. An AP coated oxygen probe (Fluorometrics Instruments) is placed against the Vycor's base to measure oxygen. This was run at several temperatures. (b) The resultant curve at 37°C was used to fit for the permeation constant of the material, which was found to be 3×10^4 Barrer, with a reduced- χ^2 of 1.14.

Simulation began with a time dependent transport equation without convection. Both the tank of water and sample begin at ambient concentration. The boundary condition for the top of the sample is a constant oxygen concentration at the top surface with 760mmHg of oxygen tension. The boundary with water is calculated such that the flux is continuous, $\nabla c_1|_{x_1=x} = \nabla c_2|_{x_2=x}$, and the partial pressures are continuous across the boundary. Concentration is converted to partial pressure by Henry's law, $c = Hp$, where H is the solubility constant. The permeability is the product of the diffusivity and solubility. Parameters for the model can be found in **Table 3.5**. The solubility of Vycor is assumed to be the product of air, $1/R_{gas}T$ and its porosity, 0.28 [3.29]. The diffusivity is approximated by scaling the diffusivity of air by a factor, a [3.30]:

$$D_{ox,vyc} = aD_{ox,air} = a \left(1.13 \times 10^{-9} \left[\frac{m^2}{s} \right] \left(\frac{T}{1[K]} \right)^{1.724} \right) \quad (3.9)$$

This accounts for the change in permeability over a wide range of temperatures. The exact division of solubility and diffusivity does not change the result of the simulation, only their product, the permeability, is relevant. The permeability of the material was swept until the curve matched the experiment at 37°C (**Figure 3.15c**), which was 3×10^4 Barrer at 37°C.

Table 3.5: Parameters used in the COMSOL simulation of Vycor. Most parameters are sourced from literature. The diffusion coefficient for Vycor was scaled from the diffusion coefficient from air. The scaling factor, a , was determined by the simulation to the experiment at 37°C. The solubility coefficient was taken from the equivalency for air to Henry's law, $p = c/R_{gas}T$, where it was scaled by the open pore percentage. Since Fick's law can be written in terms of permeation, $\frac{\partial p}{\partial t} = P \nabla^2 p$, the exact division between the solubility coefficient and diffusivity is unimportant; only their product affects the simulation.

| PARAMETER | VALUE |
|---|---|
| POROSITY OF VYCOR 2930 [3.29] | 0.28 |
| DIFFUSION COEFFICIENT OF O₂ IN AIR [3.30] | $1.13 \times 10^{-9} \left[\frac{m^2}{s} \right] \left(\frac{T}{1[K]} \right)^{1.724}$ |
| DIFFUSION COEFFICIENT OF O₂ IN VYCOR | $a \left(1.13 \times 10^{-9} \left[\frac{m^2}{s} \right] \left(\frac{T}{1[K]} \right)^{1.724} \right)$ |
| DIFFUSION COEFFICIENT OF O₂ IN WATER [3.31] | $3.33 \times 10^{-5} [cm^2/s]$ |
| SOLUBILITY OF O₂ IN WATER [3.14] | $1.3 \times 10^{-3} [mol \cdot L^{-1} \cdot atm^{-1}]$ |

| SOLUBILITY OF O ₂ IN VYCOR | $\frac{0.28}{R_{gas}T}$ |
|---|---|
| VYCOR 2930 MEAN PORE SIZE [3.26] | 44 [Å] |
| VYCOR 2930 STANDARD DEV. PORE SIZE [3.26] | 4 [Å] |
| CONDUCTIVITY OF VYCOR 2930 [3.32] | 1.4 [W·m ⁻¹ ·K ⁻¹] |
| CONDUCTIVITY OF POLYOLEFIN [3.33] | 0.2 [W·m ⁻¹ ·K ⁻¹] |
| POLYOLEFIN THICKNESS | 350 [μm] |
| VYCOR 2930 SHAFT RADIUS | 1 [mm] |
| VYCOR 2930 SHAFT LENGTH | 4 [mm] |

As the water bath is heated, the water vapor inside the Vycor sample will surpass the saturation pressure predicted by the Kelvin equation, at which point water would condense inside the pores (**Figure 3.16**). The time constant was determined by fitting the function:

$$p = Ae^{-t/\tau} + B \quad (3.10)$$

where τ represents the time constant. A smaller time constant is indicative of greater permeability as $\tau \propto 1/P$. As the water bath temperature increases the time constant is expected to drop, the pore saturation pressure is reached, at which point some pores will become occluded.

A multi-part COMSOL simulation calculated temperature, water vapor partial pressure, bulk saturation pressure, and $p/p_{sat,bulk}$. If $p/p_{sat,bulk}$ surpasses the ratio determined by the Kelvin equation, the diffusivity of the region is switched from that of hydrophobic Vycor to that of water. Heat transport is given by the equation:

$$\nabla \cdot (k\nabla T) = 0, \quad (3.11)$$

where k is the thermal conductivity of the material. The water bath is at uniform temperature. Contact between the Vycor and polyolefin coating is assumed to be continuous in temperature and thermal flux. Parameters for the model can be found in **Table 3.5**. Water vapor transport is calculated similar to oxygen transport with the boundaries in contact with water and fixed at concentrations given by

the saturation partial pressure of water vapor at their respective temperatures [3.21]. The results of these simulations are used to calculate $p/p_{\text{sat,bulk}}$.

Using the Kelvin equation, the critical pore radius above which condensation would occur can be found by:

$$r_{\text{pore}} = \frac{2\gamma V_m}{R_{\text{gas}} T \log(p/p_{\text{bulk}})} \quad (3.12)$$

Note that the pores of Vycor are not all uniform in size, and tend to be normally distributed with a mean diameter, μ_{pore} , of 44Å and a standard deviation, σ , of 4Å [3.26]. Since any section of the FEM mesh includes a large number of pores, the cumulative function for a normal distribution can be used to determine the percentage of pores above or below the critical pore diameter. The diffusion constant of un-occluded Vycor is scaled to the percent of pores that remain below the critical diameter. The percent of pores above this critical diameter is multiplied by the diffusivity of water. Therefore, for every mesh tetrahedral, there is a diffusion coefficient given by:

$$D_{\text{vyc}} = \begin{cases} D_{\text{ox,vyc}}(T), & p/p_{\text{sat,bulk}} < 1 \\ \frac{D_{\text{ox,vyc}}(T)}{2} \left[1 + \operatorname{erf}\left(\frac{2r_{\text{pore}} - \mu_{\text{pore}}}{\sigma\sqrt{2}}\right) \right] + \frac{D_{\text{H}_2\text{O}}}{2} \left[1 - \operatorname{erf}\left(\frac{2r_{\text{pore}} - \mu_{\text{pore}}}{\sigma\sqrt{2}}\right) \right], & p/p_{\text{sat,bulk}} \geq 1 \end{cases} \quad (3.13)$$

This diffusivity was then used on a simulation of the oxygen permeability of the Vycor sample. The time constant was found by fitting equation (3.10) to the simulated data (**Figure 3.16**). The experimental time constant increases sooner than the simulated one; suggesting the pore size may be 10Å to 20Å larger than expected from literature. Regardless, experiment and simulation agree that the nanoporous glass is resistant to condensation under typical physiological conditions.

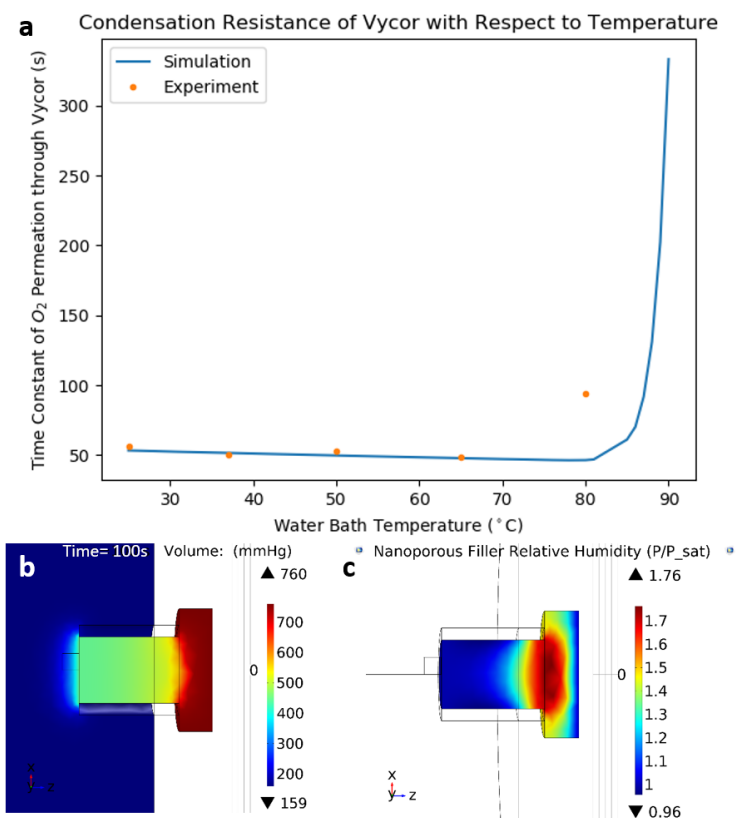


Figure 3.16: Hydrophobic Vycor's resistance to occlusion under high humidity. (a) The water bath was heated to various temperatures, and a step function of 100% oxygen was applied. The oxygen tension at the probe (**Figure 3.15a**) was measured over time. The time constant of the resultant curve, similar to **Figure 3.15c**, was fitted. The same procedure was done for the simulation. (b) The oxygen tension at 100s in 87°C water bath, and the ratio of pore equilibrium partial pressure to bulk partial pressure in 87°C water bath are shown. These time constants were then plotted. Below the equilibrium partial pressure of the pores, no condensation would be expected. Therefore, as temperature increases the time constant decreases or remains relatively flat. As the pores begin to condense, fewer high permeation paths through the material are left open and the net permeation decreases, thereby increasing the time constant. Both simulation and experiment demonstrate that hydrophobic Vycor is robust in physiological conditions.

3.3.3 DESIGNING THE IMPLANT

Glass can be brittle. However, concerns of breakage are minimized by encapsulating the material in a shell. Vycor is utilized in the outermost 5mm of the eye, where the majority of the temperature gradient occurs [3.20]. The nanoporous glass is encapsulated in medical grade silicone to give the device shape and suture points (**Figure 3.17**). Taking guidance from earlier work [3.34], [3.35], a mold was constructed to cast the silicone parts. The molds were made using DuPont WBR2120 dry film photoresist which was laminated onto a silicon wafer substrate at 95°C at a travel speed of 3.8mm/s on a General Binding Corporation Model No. Eagle 35 laminator. The wafer was soft baked

in a convection oven at 65°C for 20 minutes, before exposing the mask pattern as per specification in the datasheet [3.36]. The molds utilized two separate masks to cast half of a part, and so the dry film was laminated again over the mold, soft baked and exposed. Next, the mold was post-exposure baked at 95°C for 2 minutes, and developed for 20 minutes in 1:4 AZ Chemicals AZ340:DI water. The finished mold was coated with 5µm of Parylene-C to ease silicone release and reduce contamination from dry film debris.

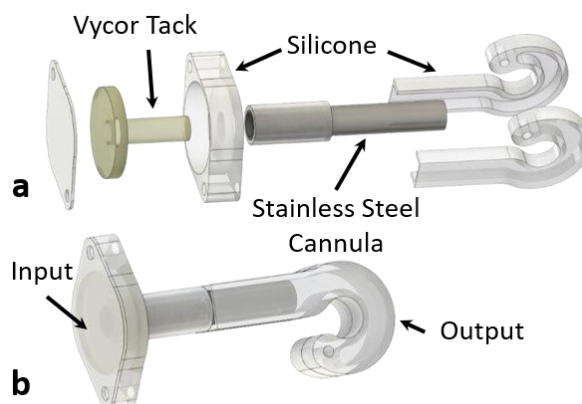


Figure 3.17: Exploded computer rendering of nanoporous-filled oxytransporter (a). The Vycor tack is encapsulated in an oblong silicone shell with 2 suture points on at the extremes and a stainless steel tube. The tube also acts to reduce radial permeation of oxygen from the device before reaching the output. (b) Computer rendering of the device.

NuSil MED4-4210 silicone is mixed at the specified 1:10 part A to part B ratio, and thoroughly mixed for 5 minutes before pouring onto the mold. The silicone is degassed in a vacuum chamber until bubble free, and then a flat object such as a glass slide is used to squeegee any excess. The mold is then partially cured for 5 minutes at 100°C in a convection oven to firm the silicone. Parts can then be peeled for device assembly.

For integration into the final device, the Vycor is machined by a CNC lathe (Specialty Glass Products Inc, PA, USA) into a tack with a 1mm diameter by 3mm long shaft, and a 3.4mm diameter by 0.5mm thick head. The tack shape allows the input accumulator to be much larger in area than that tolerated by the scleral incision, thereby reducing the input resistance. All cleaning and silanization was performed after machining. To support the tack, a 1.42mm outer diameter by 1.17mm inner diameter stainless steel tubing (McMaster Carr #8988K39) was machined into a support. As shown in **Figure 3.18c**, a slot was cut into the tube which formed wings supporting the head of the tack. To properly reach mid-vitreous from the pars plana, the tube was notched to allow it to be bent at 45°.

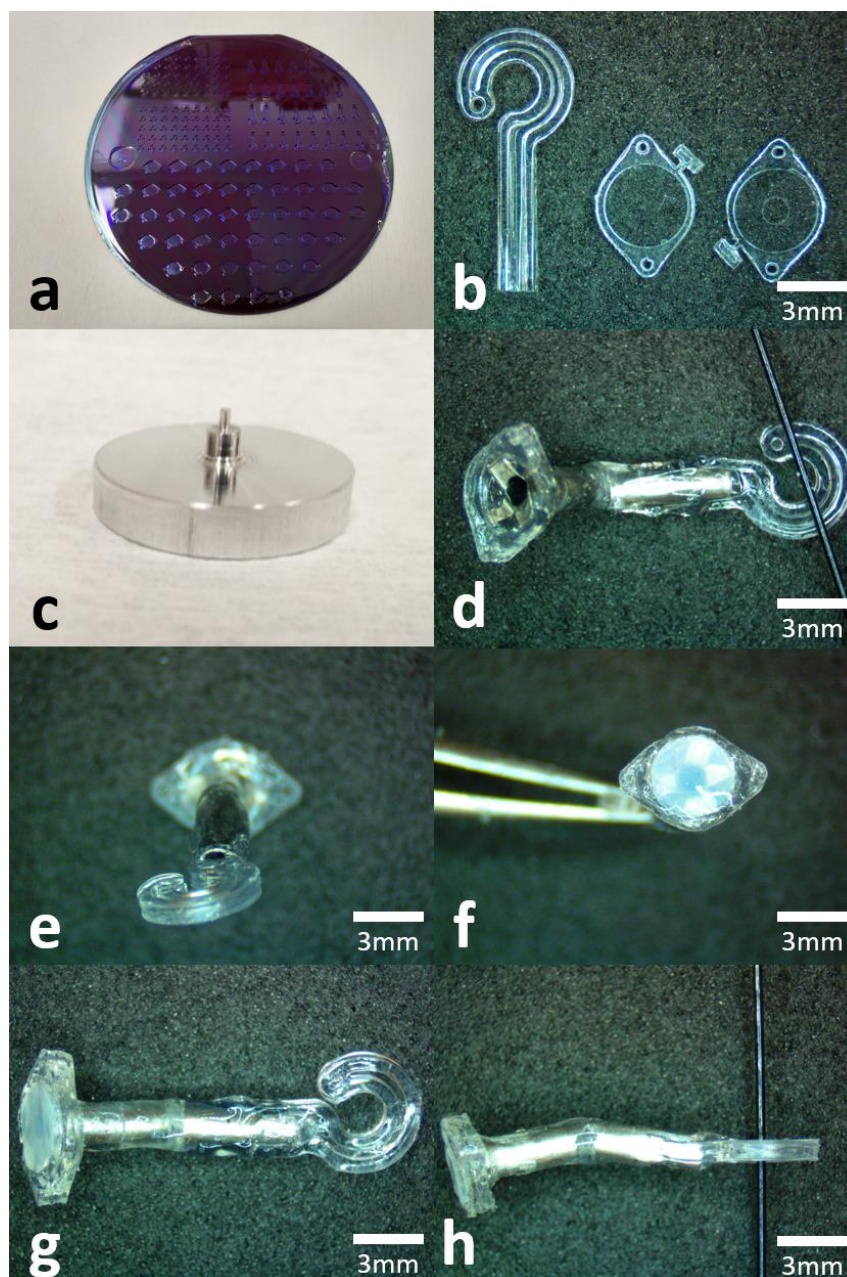


Figure 3.18: Nanoporous-filled oxytransporter fabrication. (a) Completed wafer mold. (b) NuSil MED4-4210 silicone parts after demolding. (c) The metal cannula and sections re assembled onto this custom spindle to allow them to be glued and cured together. The spindle has the same dimensions as the Vycor tack. (d) The resultant silicone device ready for assembly. The Vycor tack is inserted into the shape, and a top silicone film is applied. The entire device is then fully cured in an oven. (e) Device as seen from below. (f) Device as seen from above' note the 4 metal flaps supporting the Vycor tack. (g) Side profile; input is on the left side and output is the hook on the right. (h) The device's curve allows it to bend around the rabbit's lens.

Using a precision machined aluminum jig, the silicone parts (**Figure 3.18b**) were integrated onto the tube. The parts were adhered using uncured silicone, which was applied by spreading a thin layer of

degassed and uncured NuSil MED4-4210 onto a glass slide, where the parts were pressed against prior to integration.

The device output is shaped like a hook to increase the distribution area while allowing a surgeon to insert it through a thin incision in the pars plana. The shape was made by joining two mirrored parts under a microscope and the parts were then partially cured. This cannula is then slid over the stainless steel tube and adhered to other silicone parts. This lower half of the device was then partially cured for 5 minutes at 100°C in a convection oven before being removed from the jig. The tack was then inserted into the now completed bottom half, and a 120µm top section was adhered to the Vycor. The device was then cured for 2 hours at 150°C to fully crosslink the silicone. A brief soak in isopropyl alcohol cleaned the surface of the device. The device was sterilized using ethylene oxide (ETO).

3.3.4 IMPLANT TESTING: *IN VIVO* AND *IN VITRO*

The device was tested on benchtop for stability of the silanization, to assure that it would not exhibit any meaningful change over the implant period. To this end, a plate kept the head of the tack above the water level and the rest of the device below, insulating the rest of the device from the oxygen blown over the tack head (**Figure 3.19**). Oxygen was blown over the device daily and the oxygen response was measured using an AL-300 AP-coat Fluorometrics Instruments oxygen probe and a NeoFox reader. The water was maintained at body temperature by a hotplate. The measured time constant can be found in **Figure 3.19b**. When linear regression is applied to the time constants over 30 days of soaking, no meaningful slope is found ((0.0667 ± 0.1108) s/day) since the standard error greatly exceeds the slope. Therefore, with no statistically significant trend during the experiment, the device is considered to be stable.

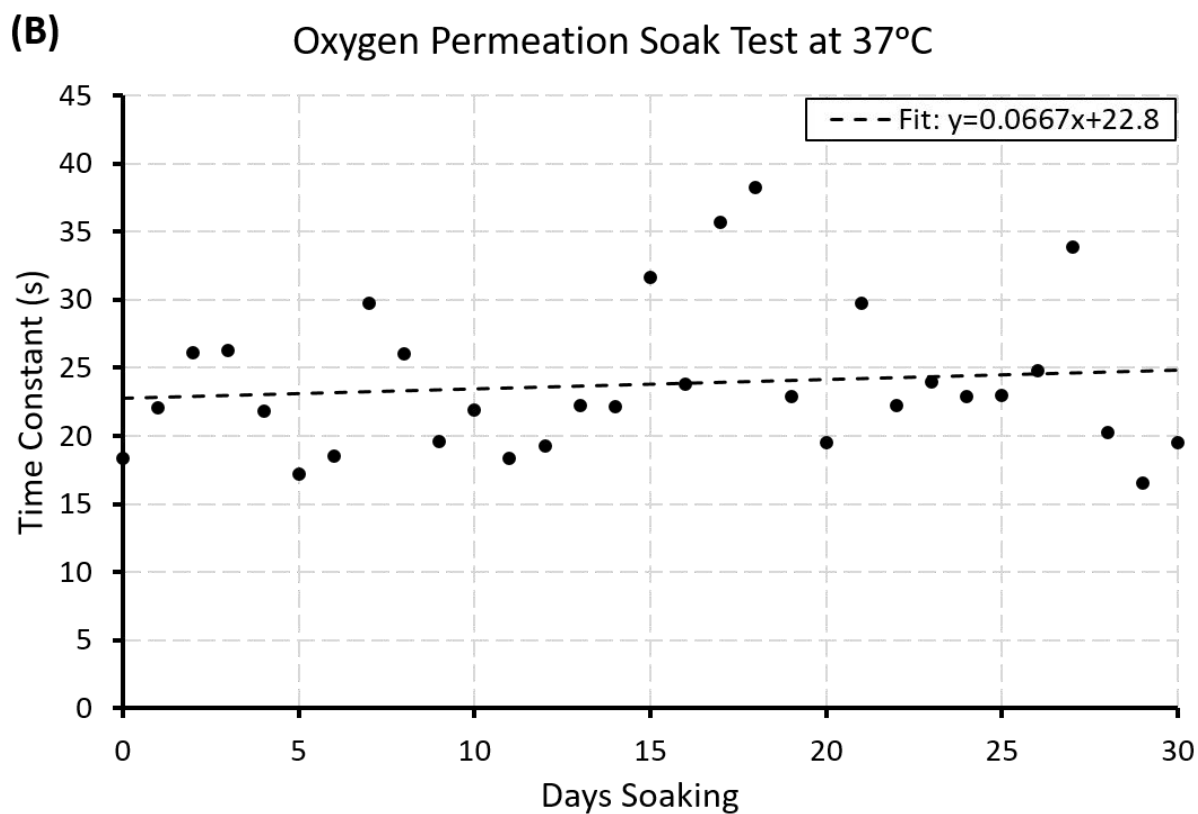
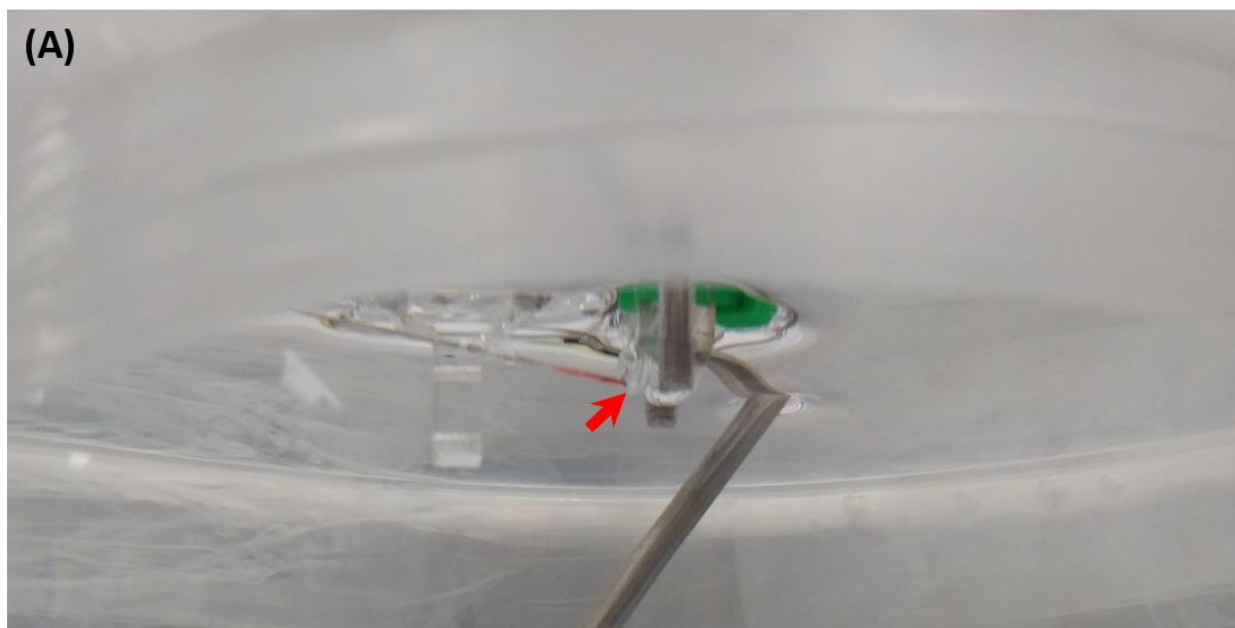


Figure 3.19: Soaking stability of device. (A) Soaking setup. The diffuser tip is indicated by the red hour. (B) Time constants of a 30 day soaking data, where each time constant was found by fitting equation (3.10) to the oxygen response curve measured at the diffuser of each device. Linear regression fits, $y = (0.0667 \pm 0.1108\text{s/day})x + (22.80 \pm 1.94\text{s})$, with $R^2=0.01234$; meaning there is no discernably trend over the 30 day soaking period.

Finally, the device was implanted three times in live rabbits for an acute experiment on permeability. For each rabbit, the oxygen profile surrounding the diffusor was recorded by moving a micrometer stage toward the retina and back, and then toward the incision (sclera) and back. The averaged data is presented in **Figure 3.20**. Comparing to the performance of oxytransporter version 1, this device is far more permeable.

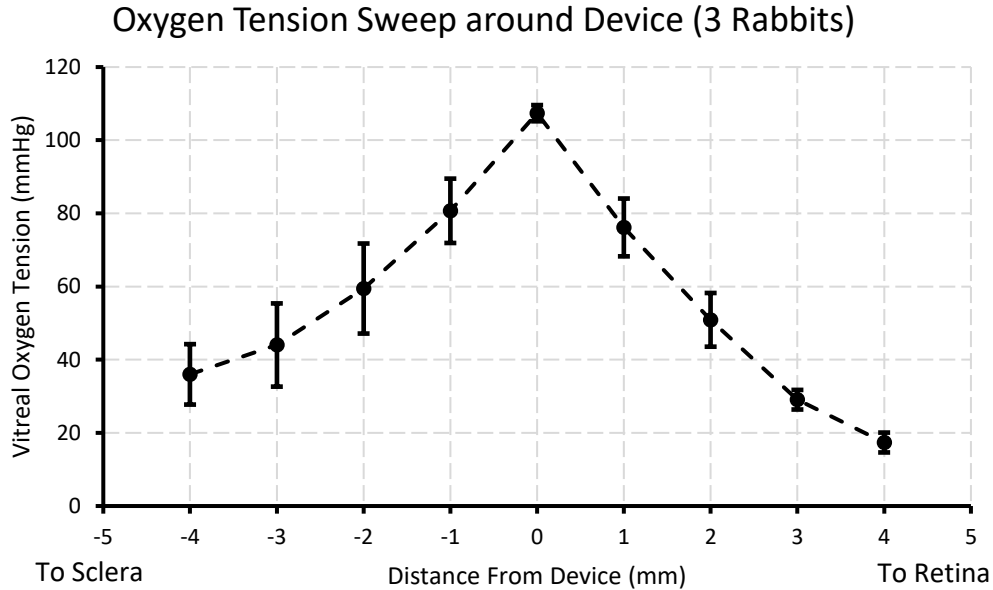


Figure 3.20: *In vivo* oxygen profile surrounding the device. An oxygen probe was placed against the diffusor and then moved away from that point using a micrometer stage toward the retina and back in live rabbits. This was repeated towards the incision point. An astute observer will note that the value and error towards the retina are both lower than the sweep towards the sclera. This is explained by the fact the diffusor is no more than 5mm from the optic nerve (the vascularized portion of the rabbit retina). Therefore, the oxygen tension tends to approach the retinal oxygen value, since it acts like a sink. On the other hand, the pars planar incision is farther away, and there is less consumption near that point. Therefore the oxygen tension exhibit a slower decline with greater variation in measurement, which is dependent on the proximity sweep path to the rabbit lens and the peripheral rabbit retina (which is mostly avascular).

By estimating the diffusion coefficient of the rabbit vitreous humor, and approximating the equal oxygen tension lines to be an oblate spheroid, the total flux from this device can be calculated:

$$J = AP_{O_2, H_2O} \frac{\Delta p_{O_2}}{\Delta r} = AP_{O_2, H_2O} \frac{p_{O_2, i+1} - p_{O_2, i}}{r_{i+1} - r_i} \quad (3.14)$$

$$A = 2\pi r^2 + \pi \frac{h^2}{e} \ln \left(\frac{1+e}{1-e} \right), \quad e = \sqrt{1 - h^2/r^2} \quad (3.15)$$

with the thickness of the device, h , being 0.7mm, and the radius of the oblate spheroid, r , being 2.5mm. Averaging through each data point in **Figure 3.20**, the flux, J , is $15 \pm 3 \text{ nmol/s}$.

3.4 REFERENCES

[3.1] Brayden, D.J. “Controlled release technologies for drug delivery”. *Drug Discov. Today* **8**, 976-978 (2003).

[3.2] Soppimath K.S., Aminabhavi T.M., Kulkarni A.R., Rudzinski W.E. “Biodegradable polymeric nanoparticles as drug delivery devices”. *Journal of Controlled Release* **70**, 1-20 (2001).

[3.3] Abdallah W., Ameri H., Barron E., Chader G.J., Greenbaum E., Hinton DR, Humayun MS. “Vitreous oxygenation in retinal ischemia reperfusion.” *Invest Ophthalmol Vis Sci.* 22;52(2):1035-42. (2011) doi: 10.1167/iops.09-4516. PubMed PMID: 21051734; PubMed Central PMCID: PMC3053094.

[3.4] Curran-Everett D. “A classic learning opportunity from Fenn, Rahn, and Otis (1946): the alveolar gas equation”. *Adv Physiol Educ.* **30**:2, 58–62 (2006). doi: 10.1152/advan.00076.2005

[3.5] Tipping R., Berry R., Nesbitt I. “Mechanisms of hypoxaemia and the interpretation of arterial blood gases”. *Surgery (Oxford)*. **33**:10, 461-466 (2015). doi: 10.1016/j.mpsur.2015.07.014

[3.6] Yu D.Y., Cringle S.J. “Retinal degeneration and local oxygen metabolism”. *Exp. Eye Res.* **80**, 745–751 (2005). doi: 10.1016/j.exer.2005.01.018

[3.7] Dopplery C.T., Bulpitt C.J., Kohner E.M. “Oxygen supply to the retina from the retinal and choroidal circulations at normal increased arterial oxygen tensions”. *Invest. Ophthalmol.* **8**, 588-594 (1969).

[3.8] Ikeda T., Tayefeh F., Sessler D.I., Kurz A., Plattner O., Petschnigg B., Hopf H.W., West J. “Local Radiant Heating Increases Subcutaneous Oxygen Tension”. *Am J Surg.* **175**:1 33-37 (1998). doi: 10.1016/S0002-9610(97)00237-7

- [3.9] Whitney J.D., Stotts N.A., Goodson W.H. "Effects of Dynamic Exercise on Subcutaneous Oxygen Tension and Temperature". *Res Nurs Health*, **18**, 97-104 (1995). doi: 10.1002/nur.4770180204
- [3.10] Murali K., Kang D., Nazari H., Scianmarello N., Cadenas,E., Tai Y.C., Kashani A., Humayun M. "Spatial Variations in Vitreous Oxygen Consumption," *PLoS One*. 11(3): e0149961. (2016) doi:10.1371/journal.pone.0149961
- [3.11] Robb W. L. "Thin silicone membranes - Their permeation properties and some applications". *Ann. N. Y. Acad. Sci.* **146**, 119–137 (1968). doi: 10.1111/j.1749-6632.1968.tb20277.x
- [3.12] Parylene Properties. *Paratech* (2018).
- [3.13] Dupont Kapton Summary of Properties. *DuPont* (2017).
- [3.14] Sander R. "Compilation of Henry's law constants (version 4.0) for water as solvent". *Atmos. Chem. Phys.* **15**, 4399-4981 (2015). doi: 10.5194/acp-15-4399-2015
- [3.15] Ferrell R.T., Himmelblau D.M. "Diffusion Coefficients of Nitrogen and Oxygen in Water". *J. Chem. Eng. Data.***12**:1, 111-115 (1967). doi: 10.1021/je60032a036
- [3.16] Cussler, E. L. *Diffusion: Mass Transfer in Fluid Systems*. (2nd ed.). New York: Cambridge University Press. (1997). ISBN 0-521-45078-0.
- [3.17] Kang D. *MEMS for Diabetic Retinopathy*. Ph.D. California Institute of Technology. (2015).
- [3.18] Freeman R.D., Fatt, I. "Environmental Influences on Ocular Temperature". *Inv. Opthal.* **12**:8 596-602 (1973).
- [3.19] Yeslin, A.R., Shurrager. P.S. "Temperature gradients in the rabbit eye". *Psychon. Sci.* **4**:40 (1966). doi: 10.3758/BF03342163
- [3.20] Schwartz, B., Feller, M.R. Temperature gradients in the rabbit eye. *Inv. Opthal.* **1**:4, 513-521 (1962).

- [3.21] Monteith, J.L., Unsworth, M.H. *Principles of Environmental Physics*. Third Ed. AP, Amsterdam, (2008). ISBN 9780123869104
- [3.22] Engineering ToolBox, (2003). *Air - Thermophysical Properties*. [online] Available at: https://www.engineeringtoolbox.com/air-properties-d_156.html [12 Apr 2019].
- [3.23] “Characteristic properties of Silicone Rubber Compounds.” ShinEtsu Silicone. (2016)
- [3.24] SCS Parylene Properties. Specialty Coating Systems (2007).
- [3.25] Nagy, N.J. “The Effectiveness of Water Vapor Sealing Agents When Used in Application with Thermoelectric Cooling Modules”, *TE Technology, Inc.*
- [3.26] Fernandes, N.E., Gavalas, G.R., “Gas transport in porous Vycor glass subjected to gradual pore narrowing”. *Chem. Eng. Sci.* **53**:5, 1049-1058 (1998). doi: S0009-2509(97)00399-0
- [3.27] Gruys, E., Schakenraad, J.M., Jruit, L.K., Bolscher J.M. “Biocompatibility of glass-encapsulated electronic chips (transponders) used for the identification of pigs”. *Vet Rec.* **133**:16, 385-388 (1993). doi: 10.1136/vr.133.16.385
- [3.28] El-Meliegy, E., van Noort, R. “Glasses and Glass Ceramics for Medical Applications”. Springer. New York (2012). ISBN 978-1-4614-1228-1
- [3.29] “What is Vycor glass?” *Applied Optics*, Vol. 18, No. 19. 1 October 1979.
- [3.30] Denny, M. “Air and Water: The Biology and Physics of Life’s Media”. pp. 89, Princeton University Press (1995). ISBN: 9780691025186
- [3.31] Ferrell R.T., Himmelblau D.M. “Diffusion Coefficients of Nitrogen and Oxygen in Water”. *J Chem Eng Data.* **12**:1, 111-115 (1967). doi: 10.1021/je60032a036
- [3.32] Goodfellow. “Vycor 7913 (SiO₂ 96) Material Information”. (2018). <<http://www.goodfellow.com/E/Vycor-7913.html>>

[3.33] Thermoplastic elastomers – Polymer Material Properties. eFunda, Inc. (2018) <http://www.efunda.com/materials/polymers/properties/polymer_datasheet.cfm?MajorID=TPE&MinorID=1 >

[3.34] Scianmarello N, Kang D., Murali K., Cook C., Han J., Humayun M.S., Tai Y.C. "Oxygen generation by electrolysis to treat retinal ischemia," *2016 IEEE 29th International Conference on Micro Electro Mechanical Systems (MEMS)*, Shanghai pp.399-402. (2016), doi: 10.1109/MEMSYS.2016.7421645

[3.35] Kang D., Murali, K., Scianmarello N., Park J., Chang J.H.C., Liu Y., Chang K.T., Tai Y.C., Humayun M.S., "MEMS oxygen transporter to treat retinal ischemia," *2015 28th IEEE International Conference on Micro Electro Mechanical Systems (MEMS)*, Estoril, pp.154-157. (2015) doi: 10.1109/MEMSYS.2015.7050909

[3.36] DuPont WBR 2000 Series. Rev 2.0. DuPont Electronic Technologies (2018).

[3.37] Efron, N., Carney, L.G. "Oxygen levels beneath the closed eyelid". *Investig. Ophthalmol. Vis. Sci.* **18**, 93-95 (1979).

[3.38] Royle P, Mistry H, Auguste P, et al. "Pan-retinal photocoagulation and other forms of laser treatment and drug therapies for non-proliferative diabetic retinopathy: systematic review and economic evaluation". Southampton (UK): NIHR Journals Library; 2015 Jul. (Health Technology Assessment, No. 19.51.) Chapter 2, The landmark trials: Diabetic Retinopathy Study and Early Treatment Diabetic Retinopathy Study. Available from: <https://www.ncbi.nlm.nih.gov/books/NBK305100/>

CHAPTER 4 – GENERATING OXYGEN: THE OXYGENERATOR

The goal of this thesis would be to provide therapeutic options at every stage of DR. The oxytransporter's input is taken from the atmosphere, consequently this device is limited to treatments of mild to moderate DR, that require an oxygen tension lower than the atmospheric of 160mmHg.

The treatment of severe DR requires a device that generates oxygen at higher tension: the oxygenator meets that requirement

4.1 OXYGENERATOR DESIGN

There are two methods to generate oxygen are by chemical decomposition, or through electrolysis of water.

Chemical decomposition requires the usage of reactive chemicals, such as peroxides, which tend to be toxic. Their use would require encapsulation and mechanical metering to control the rate. As any final device is expected to operate on the order of years, some method of refilling these chemicals would need to be devised. Assuring these substances do not make contact with the eye and assuring that no leaks occur after refill is a challenging issue, especially when the decomposition process generates excess pressure (see section 6.3.2).

Instead, this device uses electrolysis. Electrolysis requires an external power source (discussed in CHAPTER 5), but consumed water can be replenished safely with a needle, as it is non-toxic, or by osmosis. The amount of oxygen produced could be controlled by controlling the amount on time of the primary side (where power is being provided). Therefore, this chapter will characterize the electrodes used, justify their usage, and convert the desired oxygen flux, 0.25nmol/s, into an electrical specification

The oxygenator has two parts: an implant and an external power source with a controller, the primary side (**Figure 4.1**). The primary side can be built into a pair of glasses or into a sleeping mask. This primary side controls the duty cycle and frequency of the electrolysis. Methods of powering the implant are briefly discussed in CHAPTER 5. Only the design of the device is discussed here, see **Figure 4.1**.

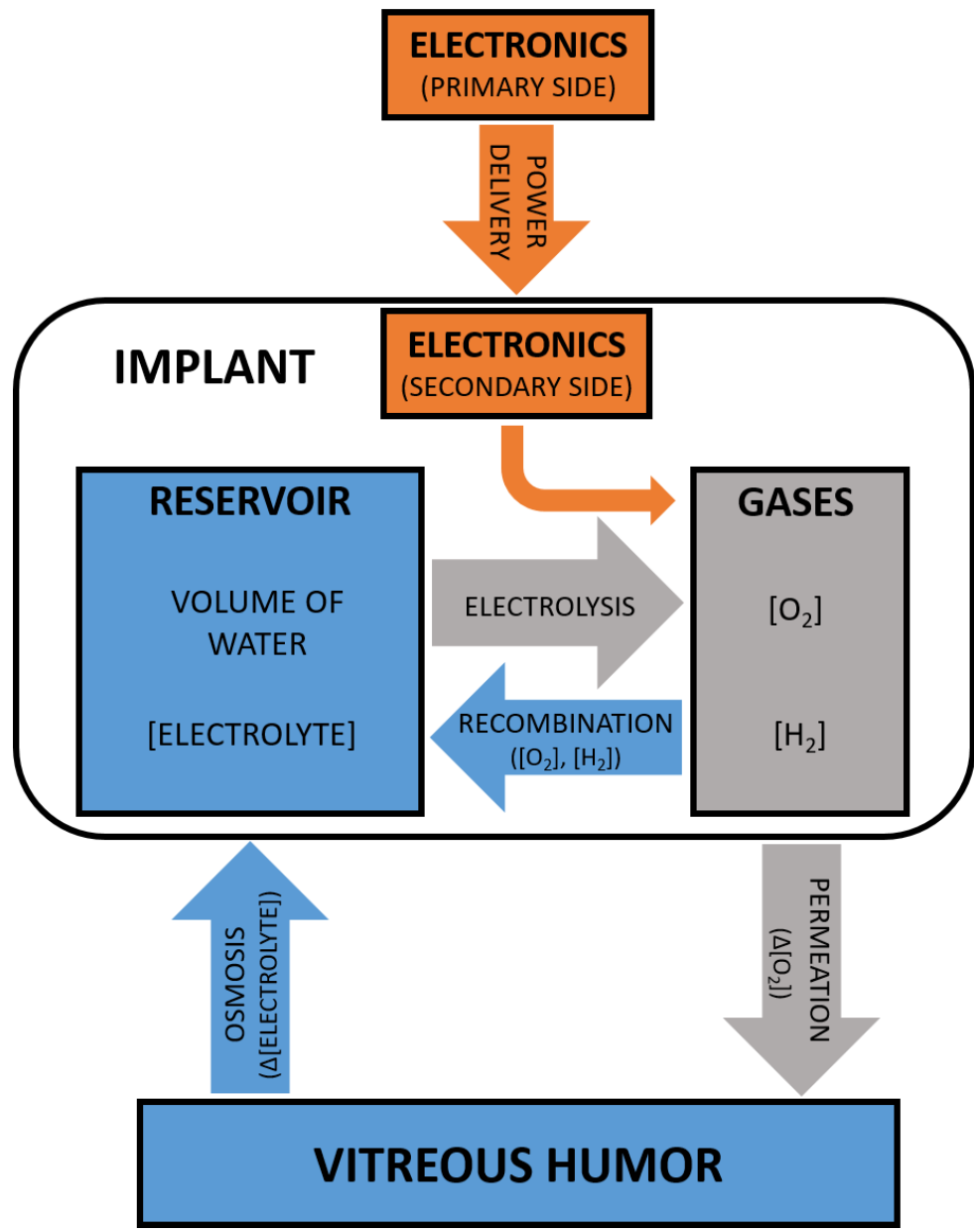
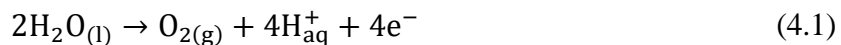


Figure 4.1: System diagram of the oxygen generating device. Power generation and transfer is discussed in CHAPTER 5. Power from the electronics in the implant drive electrolysis of water into gas. Any permeation out of the device (dependent on the difference in oxygen concentration and membrane permeations) contributes to supplying the retina with oxygen. This outflow of oxygen must be matched with an equal inflow of water through osmosis to prevent depleting the reservoir. Recombination of oxygen and hydrogen into water (dependent on oxygen and hydrogen concentrations) works to counteract gas generation in electrolysis.

4.2 ELECTROLYSIS

When the implant receives electrical power, the voltage is rectified and sent to the electrodes housed in a cell with a membrane that is permeable to gases, but impermeable to electrolyte salts. The electrochemical process releases oxygen and hydrogen as described by the half-reactions:



This process depends on protons, H_{aq}^+ , and electrons, e^- , to act as charge carriers. If pure water used, the cell's power efficiency would be very low and the overpotential quite high. Pure water has a low concentration of charge carriers, $10^{-7}\text{M H}_{\text{aq}}^+$ and $10^{-7}\text{M OH}_{\text{aq}}^-$ ions (implying low conductivity of $18\text{M}\Omega\cdot\text{cm}$), and would result in a high overpotential and a low current density. Therefore, electrolysis of pure water would have a high faradic efficiency (percent of electrons going towards electrolysis of water); current entering the electrolytic cell primarily used to split water and to produce hydrogen peroxide.

To reduce the over potential an electrolyte is added to the solution. The electrolyte must satisfy the following criteria:

- a. Safe and non-toxic.
- b. Reduction potentials of the cation must be lower than those of hydrogen, and oxidation potentials of the anion must be greater than those of hydroxide [4.1]; any redox reaction occurring in the electrolyte reduce the faradic efficiency of the system.
- c. No gaseous redox products must be produced (e.g. electrolytes with chlorine ions that produce chlorine gas), because membrane is only permeable to gas phase transport. Aqueous and solid phase products are safely encapsulated.

Magnesium sulfate, commonly sold as "Epsom salt", was chosen. The sulfate anion is difficult to oxidize, and its products, $\text{S}_2\text{O}_8^{2-}$, SO_2 and S , are not gases. Magnesium, Mg^{2+} , is a suitable cation as its potential is lower than that of a proton [4.1].

The overpotential of the system depends on the electrode material, the resistance, and the concentration of the electrolyte. The resistance is dependent on bubble formation at the electrodes and affects the current density at a given voltage. The Tafel equation, $I \propto e^{\eta/A}$, describes an exponential relationship between the current density and the overpotential, with A being the Tafel slope. The choice of electrode material and electrolyte concentration affects the overpotential and power efficiency of the system, see section 4.2.2. The rate of recombination and the rate of replenishment must be taken into consideration.

The rate of recombination needs to be significantly slower than the flux of oxygen, see section 4.3, because recombination of hydrogen and oxygen into water adds consumption on the oxygen flux out of the device.

The rate of replenishment of the device must match the rate of consumption of water.

4.2.1 A TEST PLATFORM

To test the electrode material and electrolyte concentration, a silicone microfluidic channel with markings every 0.2mm was designed (**Figure 4.2**). **Figure 4.3** describes the manufacturing process used to build the device. Different microelectrodes patterns were evaporated onto a glass substrate (the base of the microchannel). Electrolyte with green food coloring was injected into both chambers. The silicone was poured greater than 3mm thick to reduce the outward permeation. The microelectrodes were powered on for a predetermined amount of time, with continuous voltage and current recording using two HP 34401A. The power supply, Korad KA3005P, was controlled by python code. A microscope with an OMAX A3590U recorded video of the fluid. The setup is described in **Figure 4.4**. Analysis of the video determined the displacement, which is dependent on the gas volume. To measure recombination, the silicone and glass device was coated with Parylene-C to reduce outward permeation even further. Any shrinkage of the water column was then associated with recombination.

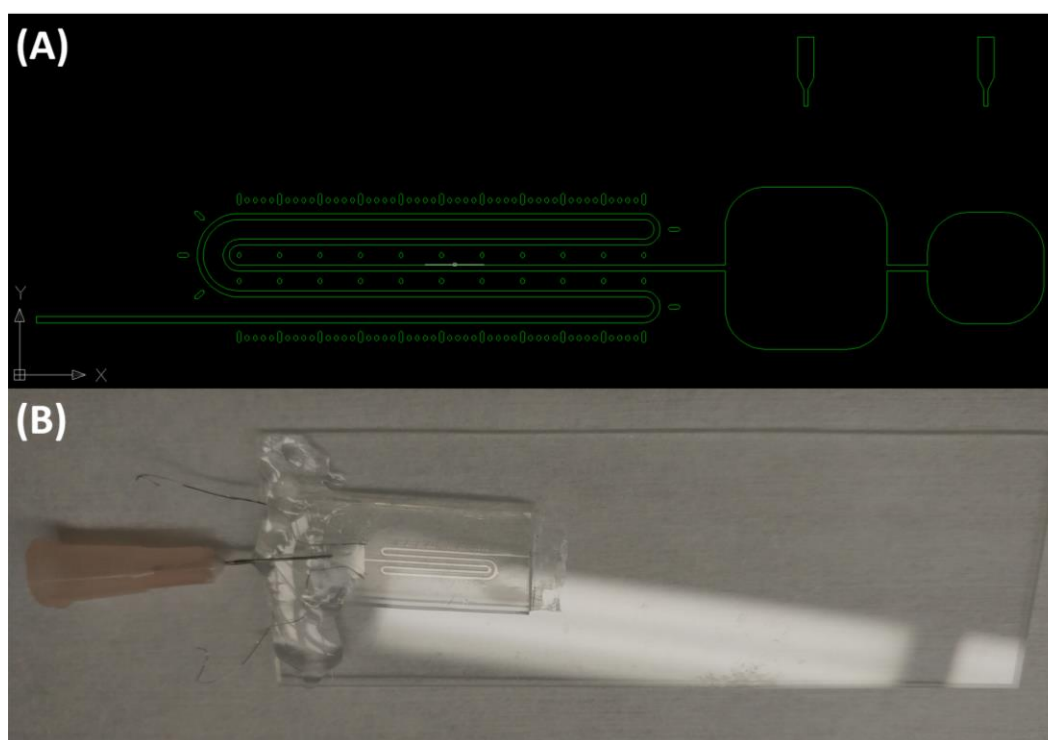


Figure 4.2: Electrolysis test chip. (A) Single Layer SU-8 100 mold design. The large dashes represent 1mm spacing. (B) Fabricated device with 30Ga needle glued in place using silicone.

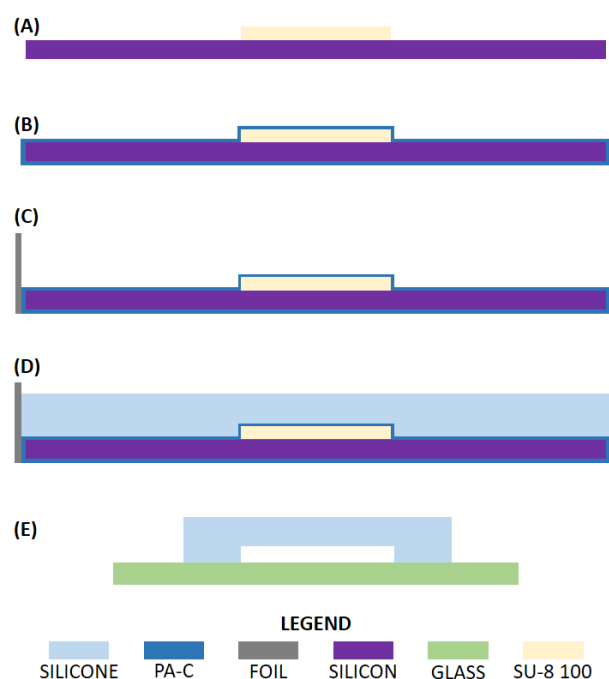


Figure 4.3: Electrolysis test chip fabrication. (A) Spin MicroChem Su-8 100 at 1krpm, expose mask, and develop (recipe in Section 6.2.1). (B) Parylene coat water to act as a mold release for the silicone. (C) Wrap aluminum foil around the sides to hold the silicone after pouring. (D) Pour NuSil MED4-4210 silicone into mold and degas in vacuum chamber until all bubbles are gone. Cure in oven at 100°C for 10 minutes. (E) Peel and cut silicone device. Place silicone upside down

(channel exposed) and a clean glass slide in the Technics PEII-A plasma etcher at 300mT of O₂ at 50W for 10s. Immediately vent and flip silicone piece over onto glass, bonding the two. The glass slide can be replaced by any desired microelectrode pattern (**Figure 4.5**).

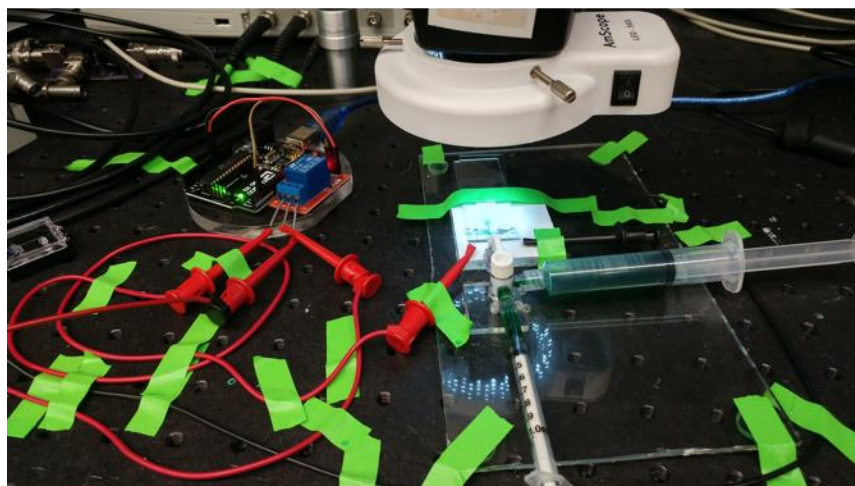
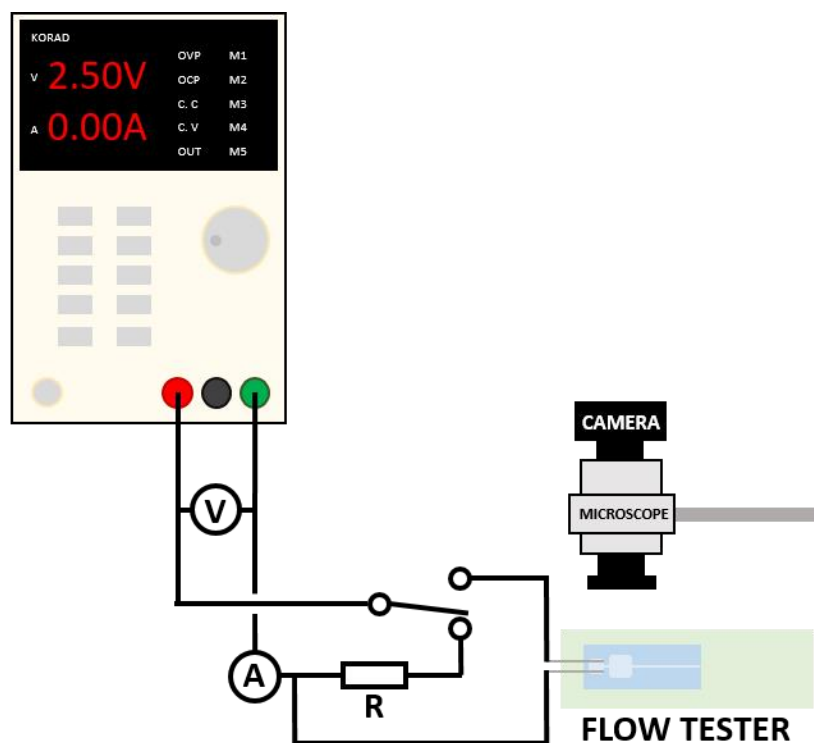


Figure 4.4: Electrolysis test setup. A 1000 Ω resistor on a relay allows the voltage to be set on the power supply accurately before applying a voltage to the microelectrodes. The relay is triggered by python code using an Arduino UNO R3 as an intermediary. Two HP 34401A multimeters perform the voltage and current measurements. Simultaneous video recording allowed movement of the water column in the microchannel to be measured.

4.2.2 ELECTROLYSIS EFFICIENCY

Three different electrodes were tested: platinum-iridium (Pt-Ir) micro-patterned electrodes, gold micro-patterned electrodes, and platinum wire electrodes. The microelectrodes were fabricated using the lift-off process (Microchemicals AZ1518 photoresist and MicroChem LOR3B) to pattern the interdigital design onto a soda lime wafer (**Figure 4.5**). Afterwards, 200Å titanium and 3000Å gold was evaporated using an e-beam evaporator. A bath in ST-22 positive resist stripper removed photoresist and metal from everywhere except on the electrodes. In the case of platinum-iridium, the electrodes were electroplated. Both were diced and bonded silicone flow cell with the oxygen plasma.

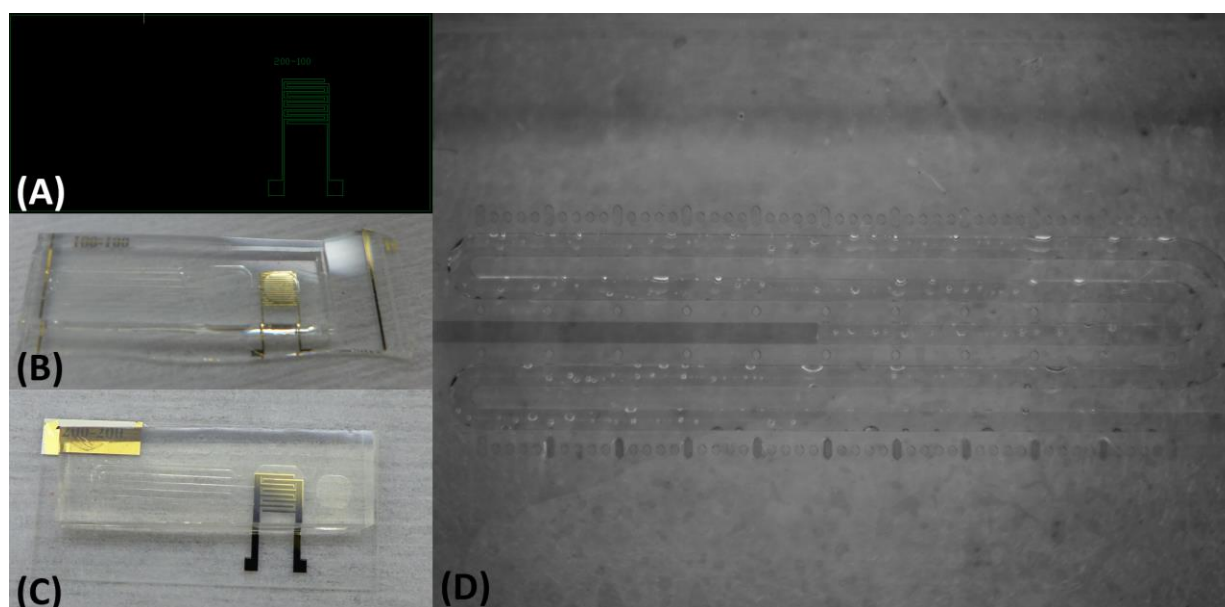


Figure 4.5: Microelectrodes boded to test chip. (A) Microelectrode pattern. (B) Electrodes patterned with Ti-Au and bonded to flow cell. (C) Electrodes electroplated with Pt-Ir and bonded to flow cell. (D) Microscope image of flow cell's microchannel with green dye to color the electrolyte.

Electrolysis tests were performed as described above. From **Table 4.1** and **Table 4.2**, gold performed better than the Pt-Ir, because gold does not exhibit significant recombination. However, significant degradation of the gold microelectrodes was observed, leading to concerns about longevity. The Pt-Ir coating survived well, but the underlying Au and Ti were etched through the pinholes.

Table 4.1: Power efficiency of Au and Pt-Ir microelectrodes.

| POWER | | 2.0V | 2.2V | 2.5V | 3.0V | 3.2V | 3.39V |
|----------------|------|------|------|------|------|------|-------|
| EFFICIENCY (%) | | | | | | | |
| Au | 0.5M | | | 5 | 13 | 18 | 27 |
| | 1.0M | | | 8 | 8 | 11 | 11 |
| | 1.2M | | | | 1 | 19 | 32 |
| Pt-Ir | 0.5M | 3 | 2 | 10 | 14 | 17 | 11 |
| | 1.0M | 9 | 2 | 12 | 14 | | |

Table 4.2: Faradic efficiency of Au and Pt-Ir microelectrodes.

| FARADIC | | 2.0V | 2.2V | 2.5V | 3.0V | 3.2V | 3.39V |
|----------------|------|------|------|------|------|------|-------|
| EFFICIENCY (%) | | | | | | | |
| Au | 0.5M | | | 11 | 31 | 48 | 75 |
| | 1.0M | | | 17 | 20 | 29 | 31 |
| | 1.2M | | | | 3 | 51 | 88 |
| Pt-Ir | 0.5M | 4 | 3 | 20 | 35 | 45 | 30 |
| | 1.0M | 16 | 3 | 25 | 34 | | |

Table 4.3: Power efficiency of Pt microwires. Electrolyte was injected into the chamber with care to prevent bubbles from being trapped in the chamber. The platinum electrodes were 4mm in length and separated by a gap of 2mm. Voltage and current were integrated and the theoretical amount of gas produced was compared to the actual volume displacement.

| POWER | | | | | | | | | | | | |
|----------------|------|------|------|------|-------|------|------|------|-------|------|------|--|
| EFFICIENCY (%) | 1.8V | 2.0V | 2.2V | 2.5V | 2.75V | 3.0V | 3.2V | 3.5V | 3.75V | 4.5V | 5.0V | |
| 0.2M | 0.0 | 5.3 | 0.0 | 13.3 | 12.4 | 14.2 | 23.7 | 23.6 | 15.9 | 19.1 | 15.2 | |
| 0.5M | 60.9 | 6.2 | 34.8 | 9.7 | 29.5 | 28.7 | 22.0 | 23.0 | 13.8 | 17.7 | 17.9 | |
| 0.8M | 0.0 | 3.4 | 11.1 | 45.3 | 21.6 | 31.2 | 25.3 | 25.8 | 26.4 | 18.2 | 20.3 | |
| 1.0M | 0.0 | 1.3 | 0.0 | 15.1 | 40.3 | 24.3 | 25.3 | 22.9 | 15.6 | 23.0 | 18.8 | |
| 1.2M | 0.0 | 0.0 | 0.0 | 3.3 | 19.0 | 25.4 | 15.2 | 12.9 | 13.7 | 25.4 | 13.6 | |
| 1.5M | 3.2 | 3.2 | 10.6 | 17.5 | 15.1 | 23.4 | 33.8 | 16.8 | 21.6 | 17.1 | 15.4 | |
| 1.8M | 20.7 | 0.0 | 7.8 | 8.5 | 14.5 | 33.7 | 30.0 | 24.6 | 27.6 | 19.3 | 23.3 | |
| 2.0M | 37.6 | 12.4 | 8.9 | 12.6 | 25.5 | 16.5 | 22.5 | 11.8 | 23.7 | 25.5 | 13.3 | |

Table 4.4: Faradic efficiency of Pt microwires. Electrolyte was injected into the chamber with care to prevent bubbles from being trapped in the chamber. The platinum electrodes were 4mm in length and separated by a gap of 2mm. Current was integrated and the theoretical amount of gas produced with that amount of current was compared to the actual volume displacement.

| FARADIC | | | | | | | | | | | | |
|----------------|------|------|------|------|-------|------|------|------|-------|------|------|--|
| EFFICIENCY (%) | 1.8V | 2.0V | 2.2V | 2.5V | 2.75V | 3.0V | 3.2V | 3.5V | 3.75V | 4.5V | 5.0V | |
| 0.2M | 0.0 | 8.6 | 0.0 | 27.1 | 27.7 | 34.6 | 61.8 | 67.2 | 48.4 | 70.0 | 61.8 | |
| 0.5M | 89.0 | 10.1 | 62.3 | 19.8 | 65.9 | 70.1 | 57.2 | 65.5 | 42.1 | 64.7 | 72.6 | |

| | | | | | | | | | | | |
|-------------|------|------|------|------|------|------|------|------|------|------|------|
| 0.8M | 0.0 | 5.6 | 19.9 | 92.1 | 48.4 | 76.3 | 65.8 | 73.4 | 80.6 | 66.6 | 82.5 |
| 1.0M | 0.0 | 2.2 | 0.0 | 30.7 | 90.2 | 59.4 | 65.9 | 65.0 | 47.6 | 84.3 | 76.7 |
| 1.2M | 0.0 | 0.0 | 0.0 | 6.7 | 42.5 | 62.0 | 39.6 | 36.6 | 41.7 | 93.2 | 55.5 |
| 1.5M | 4.6 | 5.2 | 19.0 | 35.7 | 33.7 | 57.2 | 87.8 | 47.9 | 65.7 | 62.7 | 62.4 |
| 1.8M | 30.3 | 0.0 | 13.9 | 17.5 | 32.3 | 82.2 | 77.9 | 70.1 | 84.2 | 70.6 | 94.7 |
| 2.0M | 54.9 | 20.2 | 16.0 | 25.9 | 56.9 | 40.2 | 58.5 | 33.7 | 72.3 | 93.4 | 54.2 |

Resorting to 0.004in (101.6 μ m) platinum wire (California Fine Wire Model No. M447640) resolved the electro-etching issue. Two wires were inserted into a flow cell bonded to a glass. The length of the electrodes was set by the length of the chamber in the flow cell, which was 4mm. Measurements are shown in **Table 4.3** and **Table 4.4**. The power efficiency for most concentrations is around 20%. The faradic efficiency (2.5V to 5.0V) is 59%, which is higher than the other microelectrodes; likely because of the lack of redox reactions etching the Pt electrodes. An overpotential of 1.2V (2.5V applied across electrodes) seems to be the turning point of the relationship between voltage and current in **Figure 4.6**.

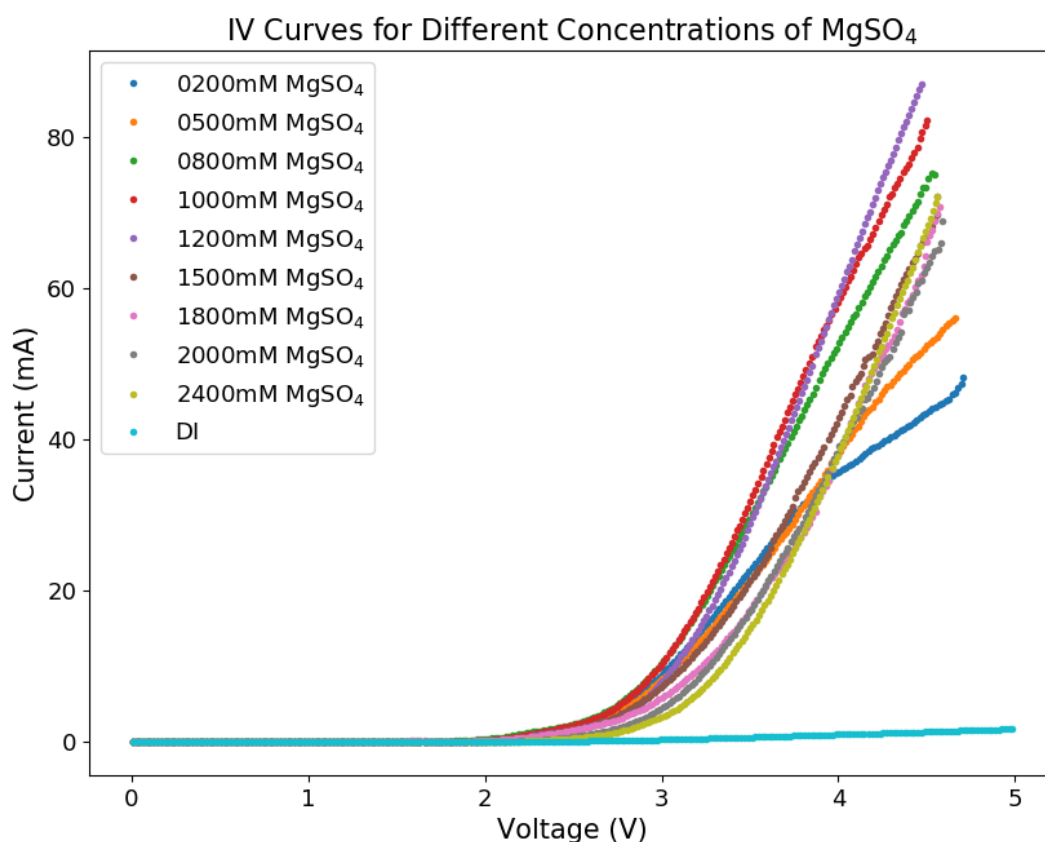


Figure 4.6: I-V curve for Pt microwires with respect to MgSO₄ concentration. Two platinum wires were submerged in a 15mL tube filled with 10mL of MgSO₄ solution. Voltage was swept

using a Korad KA3005P power supply and voltage and current were measured using HP 34401A digital multimeters.

Figure 4.6 shows a voltage sweep applied to two 2cm (submerged) platinum wires in a 15mL centrifuge tube. Current and voltage were measured using HP 34401A in a similar setup to the one previously described. The Tafel equation was curve fitted, **Table 4.5**, over the region 1.23V to 3.2V to remove the effects of heavy bubble formation on the electrodes that occur at higher overpotentials. When scaled by the wire length, the current requirements at 2.5V and 1M MgSO₄ solution is 0.576mA/mm (2.3mA for 4mm long Pt wires).

Table 4.5: The Tafel Equation fitted against the different solution concentrations with the voltages, 1.23V to 3.2V (overpotential of $\eta=0V$ to 1.97V).

| MgSO ₄ SOLUTION | CURRENT (mA) | TAFEL SLOPE (V) |
|----------------------------|--------------|-----------------|
| 0.2M | 4.29E-02 | 0.335 |
| 0.5M | 4.15E-02 | 0.338 |
| 0.8M | 6.90E-02 | 0.355 |
| 1.0M | 5.36E-02 | 0.338 |
| 1.2M | 2.21E-02 | 0.302 |
| 1.5M | 4.67E-02 | 0.352 |
| 1.8M | 5.30E-02 | 0.377 |
| 2.0M | 1.05E-02 | 0.293 |
| 2.4M | 6.70E-03 | 0.286 |
| DI | 1.14E-02 | 0.528 |
| AVERAGE SLOPE | | 0.331±0.01 |

All curves in **Figure 4.6** deviate from the Tafel equation at higher voltages, implying a decay in the current density that limits electrolysis. This happens for any electrode configuration, in part because bubble occlusions decrease the area of platinum wire in contact with the electrolyte. The decay in current density can be estimated by an exponential.

A theoretical understanding of the bubble mechanism needs modeling based upon the nucleation points in the electrode and upon the imbalances of supersaturated gas. This is a chaotic system hard to formulate.

One is now ready to calculate the oxygenerator's electrical power to supply a maximum 0.25nmol/s of oxygen to treat severe NPDR or PDR corresponding to 30% ischemia in the AXSY model. At the theoretical maximum power efficiency, the continuous power needed is 0.12mW, and 0.6mW at 20% power efficiency. According to the turning point of **Figure 4.6**, the circuit requires a minimum

of 2.5V, resulting in a continuous current of 0.24mA. If the circuit pulse-width modulated (powered on periodically), the current requirements scale as the ratio of the period to the on time. Pulsed power delivery also requires the device to be able to store sufficient oxygen to supply the off-state ($n_{O_2} = t_{off} \cdot 0.25\text{nmol/s}$ for 30% ischemia). This primary side pulse-width modulation can be tailored to different disease severities up to 30% ischemia with the same implant, see section 7.3.2.

4.3 RECOMBINATION RATE

The use of platinum raises concerns regarding recombination. Therefore, a flow cell was coated with 12um Parylene-C using the Specialty Coating Systems PDS. The Parylene coating reduces the permeation time constant of oxygen from $1.1 \times 10^3\text{s}$ to $1.4 \times 10^4\text{s}$ ($D_{H_2O,PaC} = 1.12 \times 10^{10}\text{cm}^2/\text{s}$) [4.2], [4.3]. This way, any shrinkage in water column can be attributed to recombination and not to permeation.

Electrolysis was performed in the column and video recorded. The reaction was measured from the point where the water column stopped moving forward. The distance traveled backwards by the water column was recorded as recombination.

Table 4.6: Recombination rate measurements for Pt microwires (0.004in thick and 4mm long)

| TIME (s) | RATE (mm ³ /s) | RATE (nmol/s) |
|----------------|---------------------------|---------------|
| 420 | 9.4821E-05 | 3.852E-3 |
| 420 | 6.0000E-06 | 2.4375E-4 |
| 120 | 3.4125E-05 | 1.3863E-3 |
| 121 | 4.0909E-05 | 1.6619E-3 |
| AVERAGE | | (1.8±0.8)E-3 |

Experiments with excess gas in the chamber after electrolysis were chosen for the recombination measurement (**Table 4.6**). The molar rate of recombination is 0.72% of the estimated oxygen consumption rate (0.25nmol/s) required for the eye. Therefore, recombination can be ignored.

4.4 REPLENISHMENT

Two methods of replenishment—injections and osmosis—are explored in this section, each leading to very different designs of the device.

4.4.1 INJECTIONS INTO AN ELECTROLYTE RESERVOIR

The implant involves injecting 1.5M MgSO₄ electrolyte into the electrolyte reservoir after Ethylene Oxide sterilization and immediately before implant. This design has 3 sections (**Figure 4.7**): the reservoir, the cannula, and the diffuser. The reservoir and the cannula are both impermeable to oxygen on all their outward surfaces, while the diffuser is semipermeable. All electronics for this design are located in the reservoir segment of the device sharing space with the liquid reservoir.

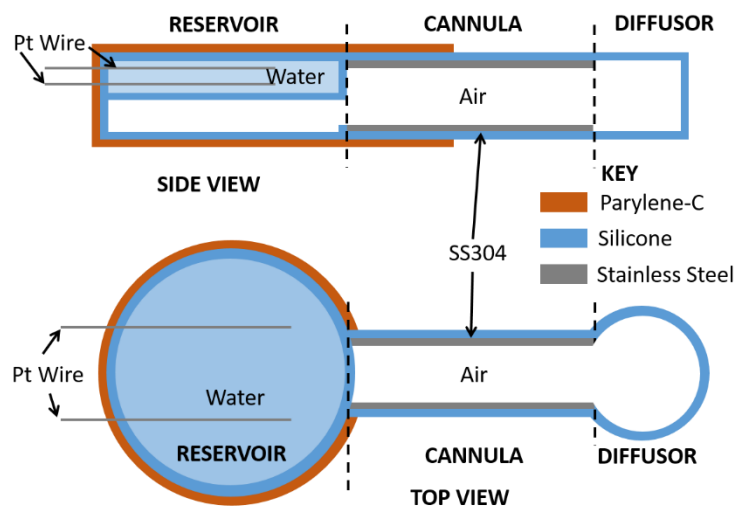


Figure 4.7: Oxygen generator device diagram. Device is split into 3 sections. The reservoir contains the electronics the power the device, the electrolyte reservoir and the input to the gas conduit, which passes unbroken through the cannula into the diffuser. A stainless steel cannula acts as a permeation barrier for oxygen and helps retain the position of the diffuser. The bottom of the liquid reservoir is made to be either a 50 μ m to 120 μ m thick silicone sheet (depending on iteration), with the lower conduit being only 120 μ m. The gas conduit is filled with air.

As this device is intended to be refilled infrequently by a physician, the liquid reservoir must provide sufficient electrolyte to operate continuously between refills. The minimum interval for such refills is one month with 3-months preferred (the maximum time between visits to the ophthalmologist for patients receiving anti-VEGF injections [4.4]). Such a large reservoir may only be situated in the temporal side of subconjunctival space between the two rectus muscles of the eye. Electrolysis occurs in this reservoir on the sclera to simplify design, because moving the electrolysis into the vitreous would require a pump to draw fluid over the electrodes.

The maximum footprint of the device on the sclera is 12mm \times 12mm \times 3mm (thick), as established by other implants (SecondSight's Argus II and Ahmed Glaucoma Valve). The maximum liquid volume of this footprint is 250 μ L (14millimoles of water); allowing for a 3-month interval between refills.

Converting $250\mu\text{L}$ of water to oxygen at a consumption rate of 0.25nmol/s (30% ischemia) allows for 324 days of continuous operation of the device. In 3 months, 28% of the liquid volume would be consumed.

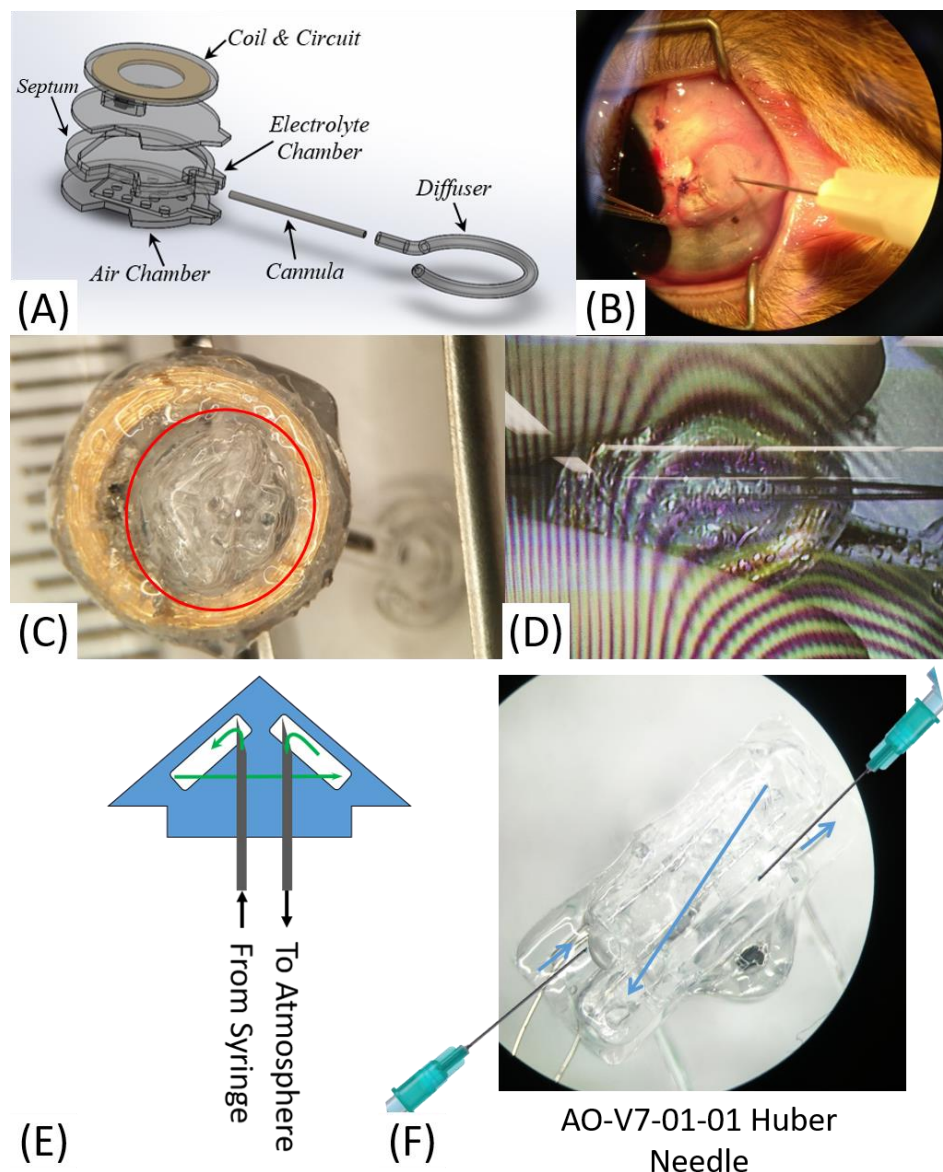


Figure 4.8: Needle fill of oxygen generator device. (A) Diagram of version 1 of the device. Note the thick silicone backside that acts as a septum. (B) Location of the reservoir on the eyeball. Injecting electrolyte into a silicone bag. (C) Version 5 of the active device with a septum layer (circled red). This separate layer reduced the chance of puncturing through the thin semipermeable membrane between the electrolyte and air chambers. (D) Two needles inserted to inject electrolyte before implant in live animal. (E) Diagram of septum layer. One needle acts as input for electrolyte, while the other acts as a vent. Electrolyte is added until it is seen exiting from the vent needle. (F) Having the two ports close together made it difficult to add both needles. Here each needle is inserted on an opposing end.

Needles of 32Ga (0.235mm outer diameter) or 31Ga (0.2604mm outer diameter) were chosen to minimize holes that do not seal in the material. The electrolyte is injected directly into the reservoir through a thick silicone septum (**Figure 4.8**). After filling, residual air is sucked out using the same needle. The chamber's side wall thickness is typically 300 μ m and the septum thickness is between 1mm to 5mm. Injections should enter at a shallow angle, so as to not penetrate the membrane. Any hole in that thin membrane will lead to device failure, because electrolysis will pump liquid into the gas conduit and occlude it.

Later versions of the device have a dedicated layer with a channel to the liquid reservoir to prevent the needle from damaging the membrane (**Figure 4.8E**). In these newer designs, two needles are used to allow all trapped gas to be pushed out by the incoming liquid. However, the location of the implant made it difficult to refill. For all current animal studies, the device was filled only at the start of the experiment. This difficulty calls for an alternative method of replenishment: osmosis

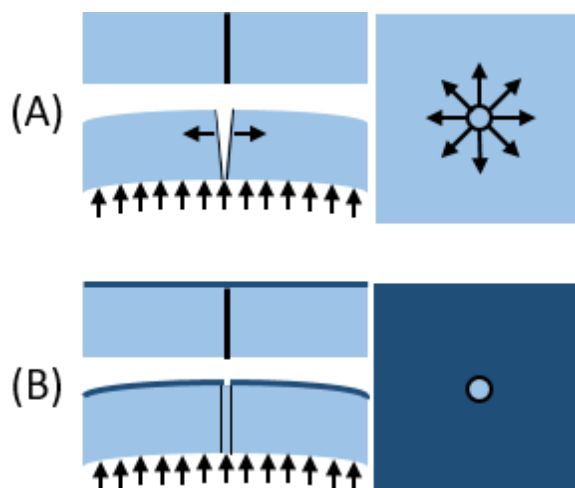


Figure 4.9: Silicone septum and leakage. (A) PDMS Only. Black line on top left cross section represents the needle's entry point. On the top view this damaged area is roughly circular. When pressure is applied from the inside the silicone (Young's modulus of 1.4MPa [4.5]), the material stretches and is prone to open along entry hole. Thickening the silicone here reduces the amount of stretching and makes the resultant microchannel longer as well. The hydraulic resistance of the microchannel is proportional to t/a^4 , therefore reducing the radius of the hole, a , increases the resistance greatly. The deflection of a plate is proportional to the inverse cube of the thickness [4.6]. As this deflection is reduced, the strain on the entry point is also reduced. Therefore, the radius remains small. The leak follows the relationship, $Q = \Delta P/R$. (B) Coating Parylene-C (Young's Modulus of 2.7GPa [4.7]) reduces the deformation of the outer surface immensely. The hole can be treated as having a fixed radius on the surface. Any applied pressure would therefore deform this microchannel inwards. This effect depends on the compressibility of silicone, and can be treated as small. Therefore the hydraulic resistance through a Parylene coated port will remain equivalent to the maximum dictated by the size of the tear regardless of the pressure. The leak rate

increases linearly with the applied pressure. For these reasons the injection ports for the devices featured long silicone coated regions with a parylene coat.

The perforation of the septum by the needle is prone to leak by the pressure of electrolysis gases. This risk is reduced by the Parylene coat over the chamber (**Figure 4.9**).

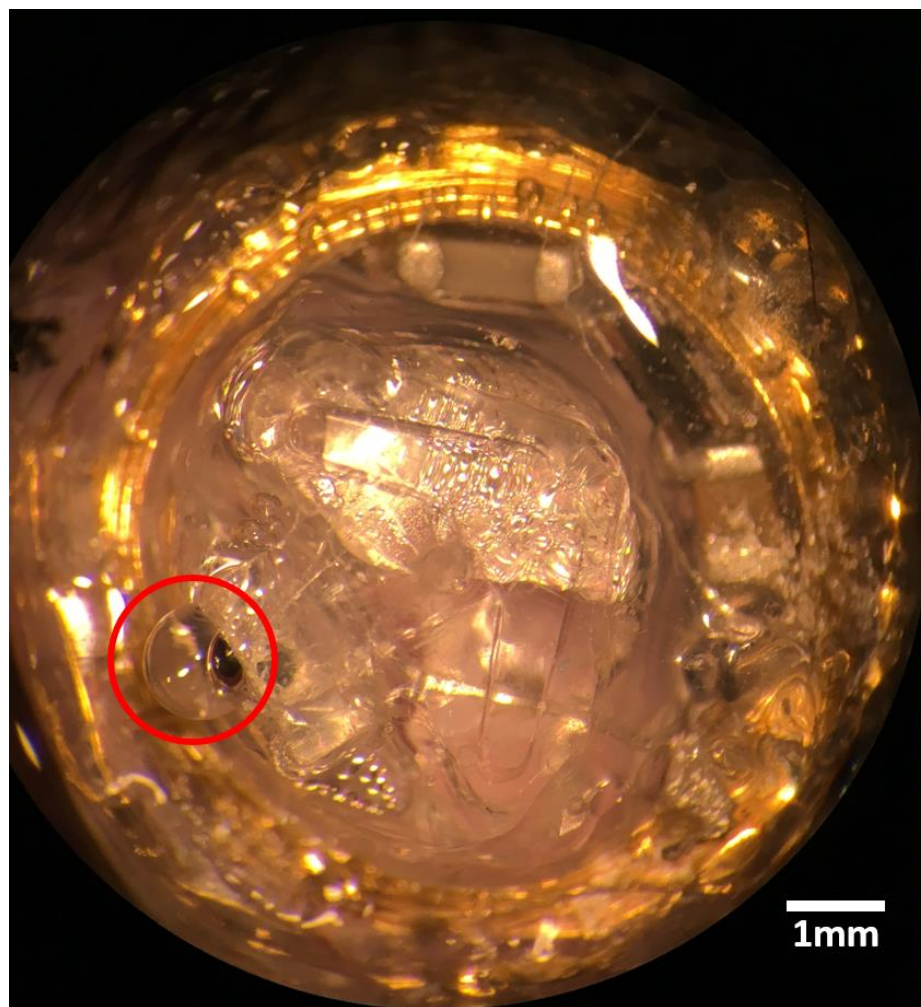


Figure 4.10: Leak in version 5 of the oxygenator after electrolysis in rabbit when under pressure (after electrolysis).

Even with a Parylene coating, damage from needles still resulted in microchannels in the septum (**Figure 4.10**). Regular needles were replaced with 30Ga non-coring (Huber) needles, which do not remove material upon puncturing silicone. However, a 63 μ m channel was observed from using a non-coring needle (**Figure 4.11**). A one way valve solution would be required to prevent openings in the septum.

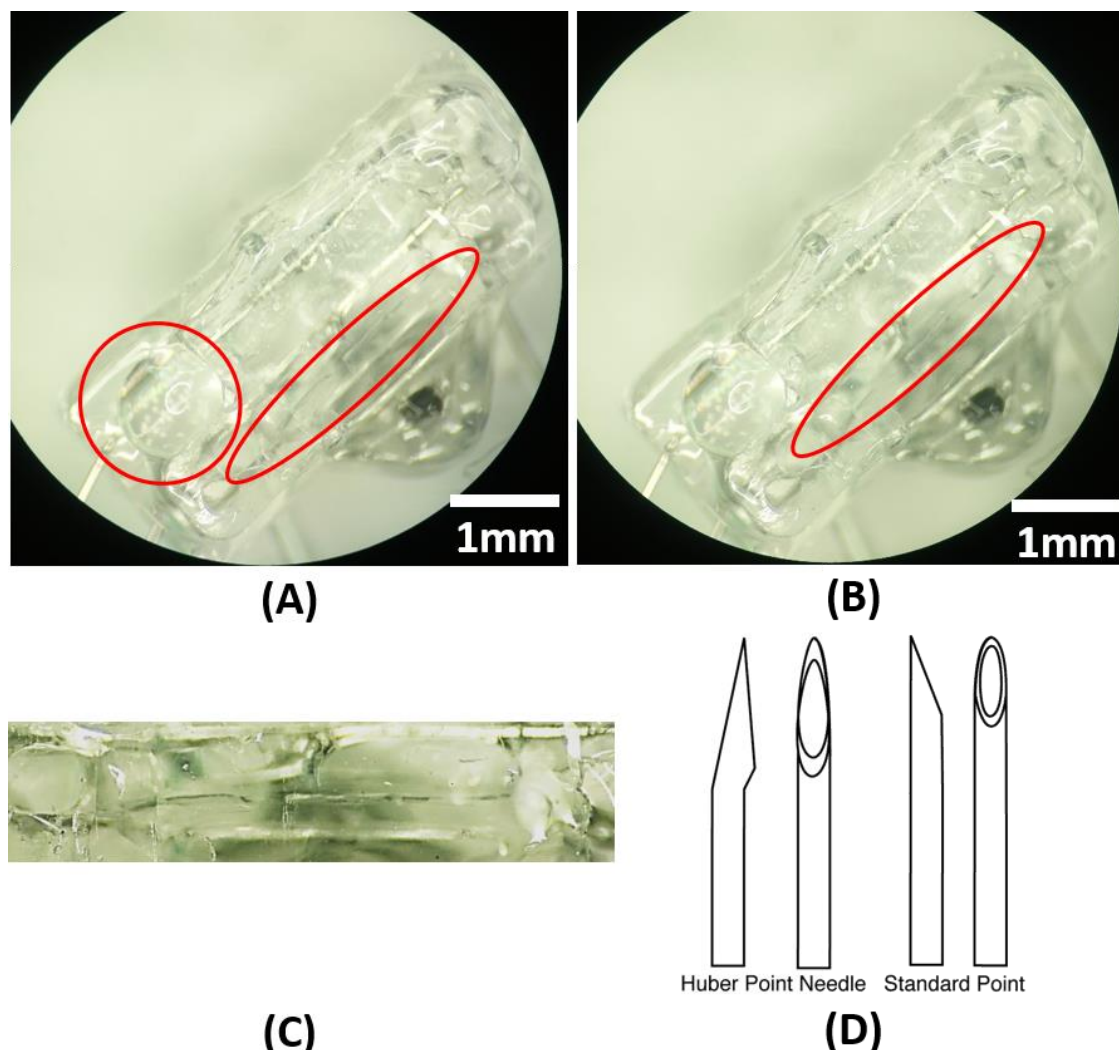


Figure 4.11: Microchannel formed by non-coring needle in silicone. (A) Leak (red circle) in version 7 of the device through the syringe plate. Note the channel formed by the non-coring needle (red ellipse), which has fluid moving through it (B) when under pressure. (C) Microchannel (63 μm in diameter) formed by non-coring (Huber) needle in the silicone-PaC syringe plate. (D) The geometry of a Huber point needle is supposed to prevent extensive damage, as it does not cut out a cylindrical core of material when injected.

4.4.2 REPLENISHMENT BY OSMOSIS

Replenishment by osmosis seems to be the solution to the above mentioned problems: the difficulty to inject in vivo, and the septum integrity. Water for electrolysis can be replenished from the vitreous. The oxygenator changes as follows: the diffusor contains the electrodes and the electrolyte, the reservoir contains the electronics, and the cannula provides an electrical connection through the sclera. This design reduces the footprint in the subconjunctival space.

If there is a gradient in concentration of a solution across a semipermeable membrane, water will flow from the low concentration to the high concentration. This is called osmosis, and the pressure is defined as:

$$\Pi = icRT \quad (4.3)$$

where i is the van t' Hoff factor, c is the concentration of the solute, R is the universal gas constant, and T is the temperature. The water flux across a membrane is approximated by:

$$J_{H_2O} = K\Delta\Pi \quad (4.4)$$

$$K = P_{H_2O}A/L \quad (4.5)$$

where K is the hydraulic permeability of the membrane, given by the area, A , thickness, L , and permeability of the membrane to water, P_{H_2O} .

Assuming NaCl in the vitreous humor and MgSO₄ in the diffusor, the water flux can be calculated using equation (4.4). For a device placed in the eye, the osmotic pressure difference must account for the two main salts in the system: NaCl in the vitreous humor, and MgSO₄ in the diffusor. The van t' Hoff factors are 1.9 for NaCl and 1.4 for MgSO₄ [4.8]. The salinity of the vitreous is that of saline at 0.154M NaCl. The permeability of silicone to water is about 36kBarrer [4.9]. For the body, RT is 2.577×10^6 Pa·L/mol. The area of the human device's diffusor is estimated to be 17.3mm². Given a thickness of 50μm for the membrane, the water flux is estimated as:

$$J_{H_2O} = \frac{P_{H_2O}A}{L} (1.4 \times c_{MgSO_4} - 1.9 \times 0.154M)RT \quad (4.6)$$

Assuming the desired salt concentration in the diffusor is 1M MgSO₄, the water flux is approximately 12μmol/s, which exceeds the oxygen consumption rate. The equilibrium salt concentration (where $J_{H_2O} = 0$) is 0.209M MgSO₄, meaning the salt will never dilute further than this concentration. The rate of oxygen consumption (0.25nmol/s) matches the rate of water intake when the salt concentration is 0.210M MgSO₄.

As the diffusor is initially dry before ETO sterilization (which includes a vacuum step), the salt must absorb moisture from a solution. As MgSO_4 is hygroscopic, water vapor in contact with the surface of the salt will be absorbed up to the equilibrium point. This creates a concentration gradient with the outside of the diffusor. If the diffusor is fully submerged in water, the relative humidity at the silicone membrane is 100%. Evidence presented later shows liquid water in the diffusor after soaking the silicone diffusor filled with MgSO_4 salt. The maximum solubility of MgSO_4 in water is 2.92M. Therefore, the inside of this diffusor has a concentration of at most 2.92M. Any higher value would involve water absorbed onto the surface of the salt, instead of dissolved, and would mean that no liquid would form.

A simple experiment confirms these estimation of the total flux of water. A silicone bag shaped like the diffusor, a 12mm disc with 0.24mm sidewalls, was constructed out of NuSiL MED4-4210, and filled with a 1.5mL of 2.4M MgSO_4 . The bag with the solution was dried in an oven. This bag was submerged in deionized water and weighed periodically to determine the rate of osmotic flux. The consequent osmosis can be explained by Darcy's law, where the molar flow rate of water is given by:

$$\frac{dn}{dt} = AP \frac{\Delta p}{L} \quad (4.7)$$

being A the area of the bag, P the permeation constant, L the wall thickness, and Δp the pressure differential across the walls of the bag. Since there is no pressure differential through the bag walls, only the osmotic pressure determines the water flux:

$$\Delta p = \Pi = icRT \quad (4.8)$$

$$\frac{dn}{dt} = AP \frac{icRT}{L} \quad (4.9)$$

The concentration of the solution is given by $c = \frac{n_{\text{MgSO}_4}}{V_{\text{H}_2\text{O}} n_{\text{H}_2\text{O}}}$. Since there is no water in the device to begin with, $n(0) = 0$, which results in:

$$n(t) = \sqrt{\frac{2P}{L} \left(\frac{n_{MgSO_4}}{V_{H_2O}} \right) iRTt} \quad (4.10)$$

Therefore, the concentration becomes:

$$c = \sqrt{\frac{n_{MgSO_4}}{V_{H_2O}} \left(\frac{L}{2iRTAP} \right) \sqrt{t}} \quad (4.11)$$

In a log-log plot, this becomes:

$$\log(c) = -\frac{1}{2} \log(t) + \log \left(\sqrt{\frac{n_{MgSO_4}}{V_{H_2O}} \left(\frac{L}{2iRTAP} \right)} \right) \quad (4.12)$$

Three bags were weighed using an analytical balance and the results are plotted in **Figure 4.12**. Each bag's concentration data was fitted by linear regression, $R^2 > 0.99$. **Table 4.7** contains the parameters of each regression. Note that the slopes are near $-1/2$, but statistically different, implying other variables had an effect on the results. This is particularly true when the salt is not in solution, as that process is technically not the result of osmosis. Knowing the membrane thickness and the total area of bag, one can solve the parameter, iP , which is inherent to the silicone membrane and the salt. With this result, the rate of osmosis for any other device can be calculated by simply knowing its dimensions. For the dimensions of the diffusor, the flow rate using equation (4.9) is estimated to be $5 \times 10^{-7} \text{L/s} \cdot c$. With an internal concentration of 1.2M, the diffusor would have a flow rate of $8.8 \times 10^{-7} \text{mol/s}$ of water inward. The flow rate is certainly sufficient.

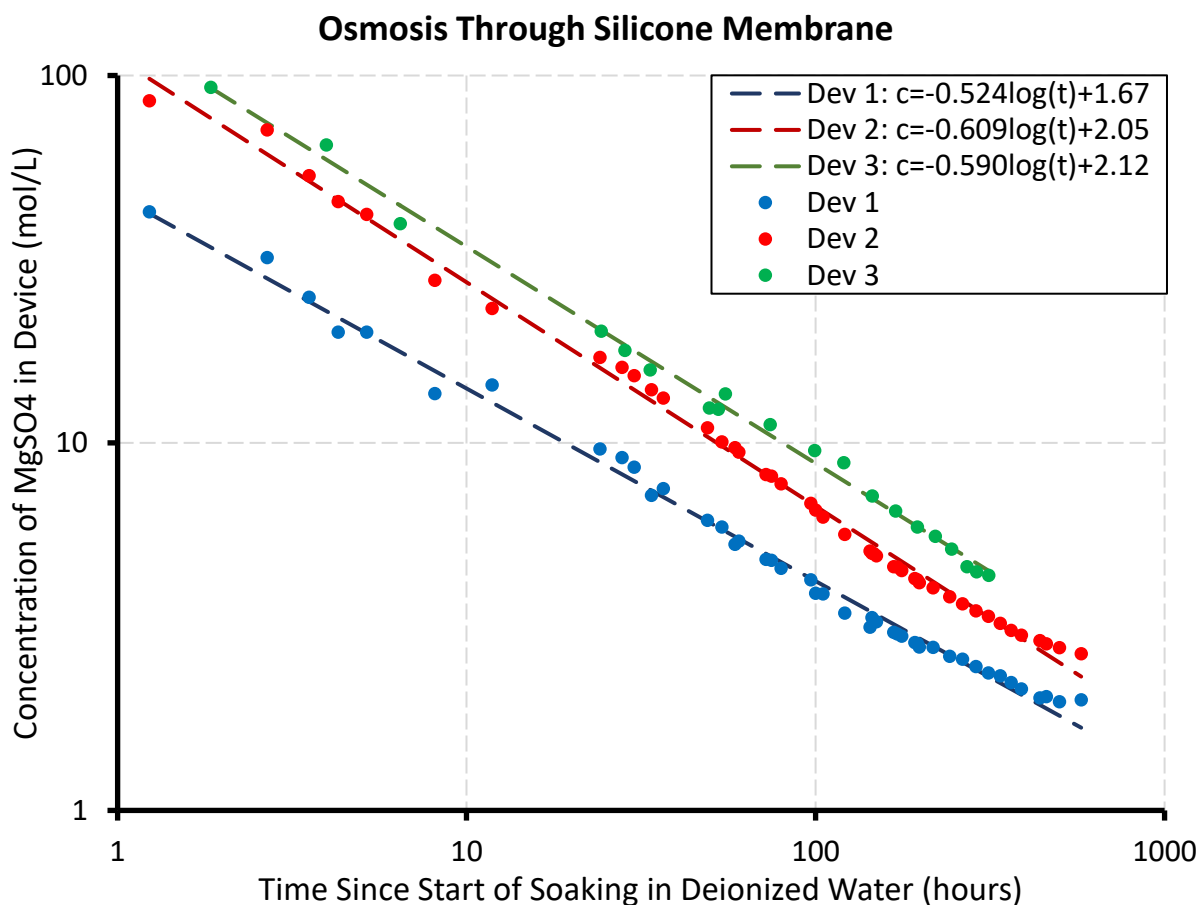


Figure 4.12: Osmosis through silicone. Linear regression of data for 3 test devices in log-log. The salt was not fully dissolved at first, so the model does not perfectly fit the data on the low end, meaning the slope is not $-1/2$. However, the R^2 values of 0.993, 0.995, 0.994 show that devices 1, 2, and 3 have good agreement with the linear fit.

Table 4.7: Fit parameters for osmosis through a silicone membrane.

| TEST DEVICE | SLOPE | Y-INTERCEPT | MGSO4 (mmol) | iP [$\text{mol} \cdot \text{s}^{-1} \cdot \text{Pa}^{-1} \cdot \text{m}^{-1}$] |
|----------------|---------------------|-------------------|-----------------|---|
| 1 | -0.524 ± 0.0066 | 1.672 ± 0.013 | 0.10 | 5.33×10^{-13} |
| 2 | -0.609 ± 0.0064 | 2.047 ± 0.013 | 0.21 | 1.99×10^{-13} |
| 3 | -0.590 ± 0.0097 | 2.123 ± 0.018 | 0.43 | 2.87×10^{-13} |
| AVG | | | | 3.4×10^{-13} |

To allow for osmotic replenishment a new diffuser is constructed (**Figure 4.13**). The platinum wire electrodes connect from the reservoir to the diffuser through the cannula. This cannula is thinner, because it does not require a gas conduit. By having the electrodes run along the entire length of the diffuser, this electrolyte filled diffuser generates oxygen uniformly throughout its shape. Providing a uniform oxygen gradient throughout. The diffuser is filled with 1.5M MgSO_4 , and dried in the oven. The top half of the silicone diffuser is glued over the dried salt, sealing it in. The platinum

wires run around the entire length of the diffuser, therefore electrolysis occurs evenly throughout the diffuser, and more oxygen can be generated before gas fully occludes the electrodes. The diffuser's top and bottom membranes were thinned to $50\mu\text{m}$ from $120\mu\text{m}$ to increase permeation and osmosis. This thinning reduces the fill time by $2.4\times$, since water flux scales as the inverse of the thickness.

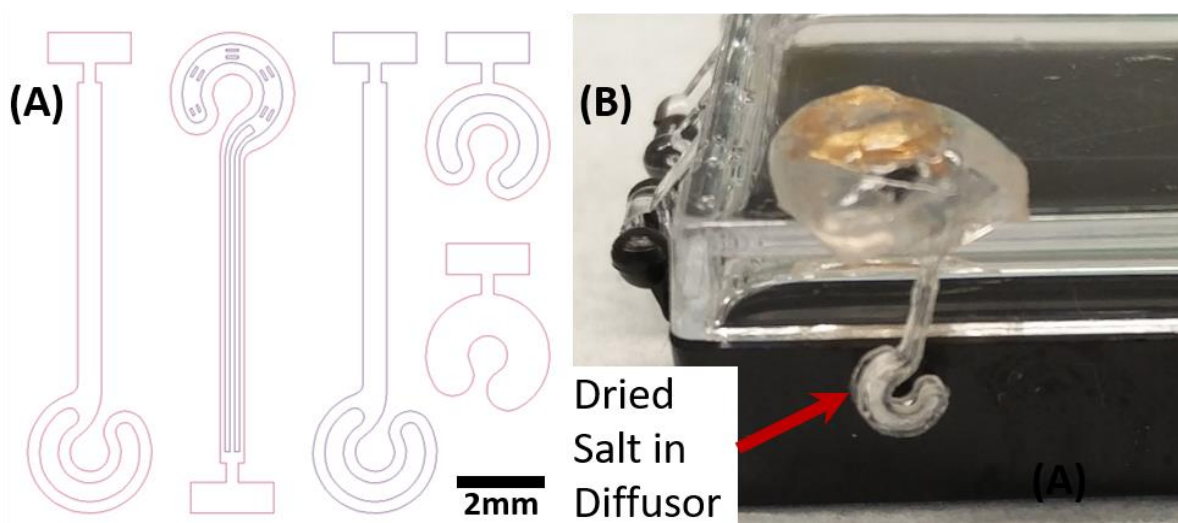


Figure 4.13: Osmotically refilled device. (A) Mask files for the diffuser. Purple represents the lower layer, and magenta represents the upper layer. This was fabricated using MicroChem Su8-100 spun at 1krpm for the lower layer, and Su8-50 spun at 1.5krpm for the upper layer; resulting in a $150\mu\text{m}$ lower layer and $50\mu\text{m}$ upper layer. This mold was coated in $5\mu\text{m}$ Parylene-C and then parts were cast using NuSil MED4-4210 silicone. The two platinum electrodes from the electronics (reservoir) were laid in their respective channels (second pattern from the left) and bent along the diffuser, being held in place by silicone tabs. (B) The assembled cannula and diffuser with the dried MgSO_4 salt can be seen attached to the complete device.

The diffuser was submerged in deionized water at room temperature (**Figure 4.14**). In 4 hours, the diffuser was significantly filled with water, and within 10 hours, it was mostly filled with water, confirming the functionality of the design.

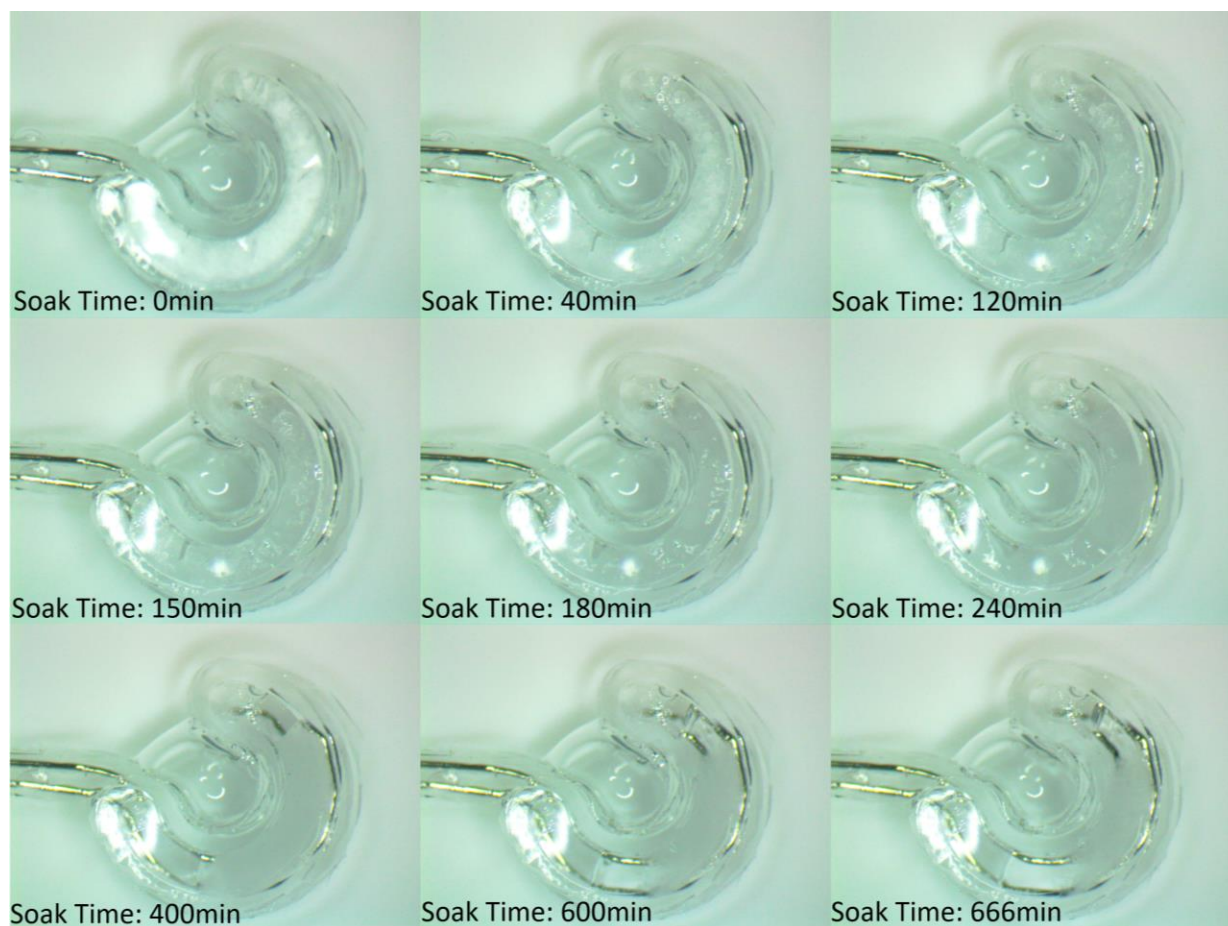


Figure 4.14: Time lapse images of diffuser filling up with water. Time lapse images of submerged diffuser in deionized water at 20°C. As the salt dissolves the underlying platinum wire electrodes become clear. Note that after 11 hours the diffuser is nearly completed filled with water. It is estimated to take 14.8hours for the salt to reach 0.5M MgSO_4 concentration using the above estimate for iP .

A video of the diffuser was taken while the electrodes were energized. Snapshots are presented in **Figure 4.15**. Note that gas formation occurs throughout the extent of the diffuser. As time passes gas builds up uniformly along the top of the diffuser with significant volumetric expansion occurring in under 1 second.

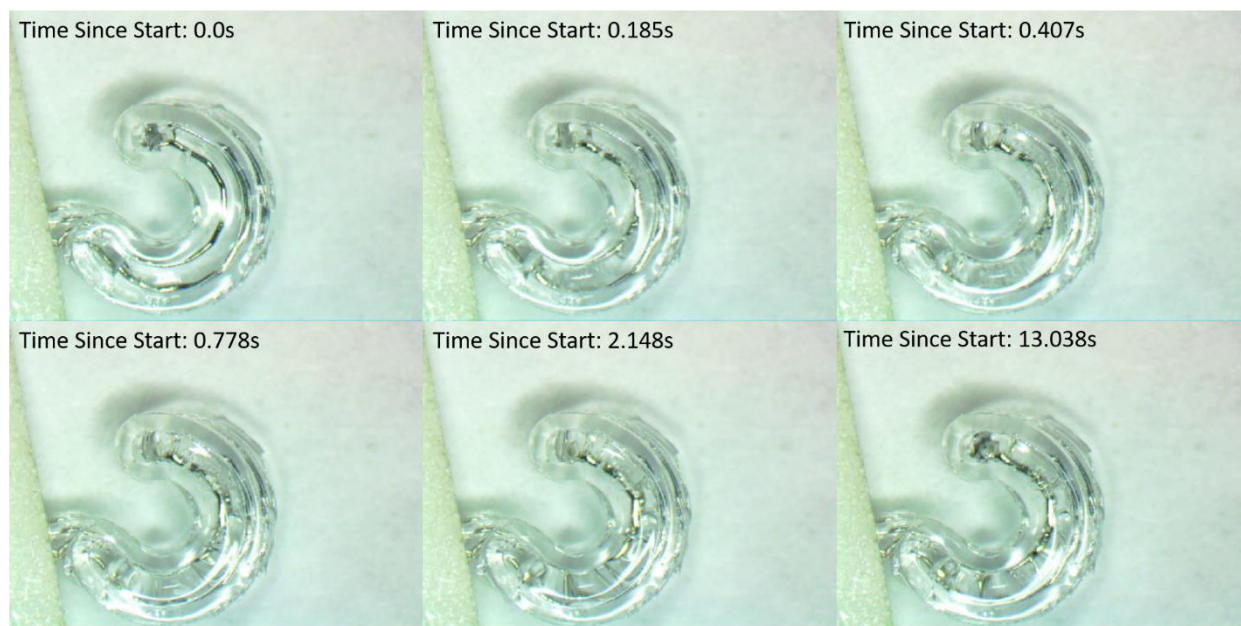


Figure 4.15: Snapshot of diffuser during electrolysis when energized with 3.5V. Note that gas bubbles are uniformly spread through the diffuser and within 0.778s a significant volume of the diffuser is filled with gas.

4.5 REFERENCES

- [4.1] Vanysek, P. (n.d.). *Electrochemical Series*. [online] Available at: https://sites.chem.colostate.edu/diverdi/all_courses/CRC%20reference%20data/electrochemical%20series.pdf [Accessed 10 Apr. 2019].
- [4.2] Kim, M.C., Lam, R.H.W., Thorsen, T., Asada, H.H. “Mathematical analysis of oxygen transfer through polydimethylsiloxane membrane between double layers of cell culture channel and gas chamber in microfluidic oxygenator,” *Microfluid Nanofluid* (2013) 15: 285. doi:10.1007/s10404-013-1142-8
- [4.3] Davis, E. (2013). *Water Sorption and Diffusion in Glassy Polymers*. Ph.D. Drexel University.
- [4.4] Ferreira, A. Sagkriotis, A., Olson, M., Lu, J., Makin, C., Milnes, F. “Treatment Frequency and Dosing Interval of Ranibizumab and Aflibercept for Neovascular Age-Related Macular Degeneration in Routine Clinical Practice in the USA” [published correction appears in PLoS One. 2015;10(8):e0136515]. *PLoS One*. 10(7):e0133968. (2015) doi:10.1371/journal.pone.0133968

[4.5] DeBoer, C. (2012). *Biomimetic Accommodating Intraocular Lens*. Ph.D. California Institute of Technology.

[4.6] Wygant, I.O., Kupnik, M., Khuri-Yakub, B. T. "Analytically calculating membrane displacement and the equivalent circuit model of a circular CMUT cell," 2008 IEEE Ultrasonics Symposium, Beijing, pp. 2111-2114. (2008). doi: 10.1109/ULTSYM.2008.0522

[4.7] Specialty Coating Systems™. "SCS Parylene Properties," SCS, A Kisco Company, (2016).

[4.8] Chem.libretexts.org. (2019). *13.9: Solutions of Electrolytes - Chemistry LibreTexts*. [online] Available at: [https://chem.libretexts.org/Bookshelves/General_Chemistry/Map%3A_General_Chemistry\(Petrucci_et_al.\)/13%3A_Solutions_and_their_Physical_Properties/13.09%3A_Solutions_of_Electrolytes](https://chem.libretexts.org/Bookshelves/General_Chemistry/Map%3A_General_Chemistry(Petrucci_et_al.)/13%3A_Solutions_and_their_Physical_Properties/13.09%3A_Solutions_of_Electrolytes) [Accessed 10 Apr. 2019].

[4.9] Robb, W.L. "Thin Silicone Membranes-Their Permeation Properties and Some Applications". *Annals of the New York Academy of Sciences*. **146**: 119–137. Bibcode:1968NYASA.146..119R. doi:10.1111/j.1749-6632.1968.tb20277.

CHAPTER 5 – ELECTRICAL POWER

Power autonomy is essential for any device permanently implanted. The implant cannot recharge through electric contacts. In the previous chapter it was determined that 0.6mW (0.24mA at 2.5v) are required to drive the electrodes of the oxygenator. Assuming a checkup period of 1 month, 180mAh would be required from a 3.7V nominal lithium ion battery. Given a volumetric energy density of 693Wh/L [5.1], the minimum volume of the battery would be 1.9cm³. The battery needs to be sealed to prevent water ingress. Quallion Medical grade batteries are sealed as required but do not hold sufficient charge in the constrained volume of 0.25 cm³ allowed by the eye.

Approaches to electrical power other than lithium ion are needed. There are four to consider: optical (solar cells), kinetic harvesters, inductive coupling for power transfer, and thermoelectric energy harvesters. Thermoelectric systems, according to literature, have very low power densities of 1.0 μ W/cm⁻², for small temperature differentials, $\Delta T = 5^{\circ}\text{C}$, making their power output far too low for this application [5.2].

5.1 OPTICAL POWER DELIVERY

Optical power delivery is an attractive approach. Photovoltaics have made great advances in recent decades achieving up to 44.7% efficiency [5.3]. The eye regularly washes away particulates; leaving a clear path for light, thereby reducing the effect of dust on the maximum power point of solar cells [5.4]. Most optical power transfer for implants occurs in near-infrared (IR), since visible light has low transmittance through tissue [5.5]. Transmittance through 2mm of human skin in near-IR is 10-20% [5.6]. It is common for such devices to rely on irradiation around 810nm. However, this wavelength can elevate tissue temperature, which should be maintained to less than 1.4 $^{\circ}\text{C}$ [5.7]. Fortunately, the conjunctiva is transparent in the visible region with a transmittance of 19% at 400nm to 65% at 800nm [5.8]. Implants underneath the conjunctiva would be sufficiently exposed to solar radiation to make optical energy harvesting viable.

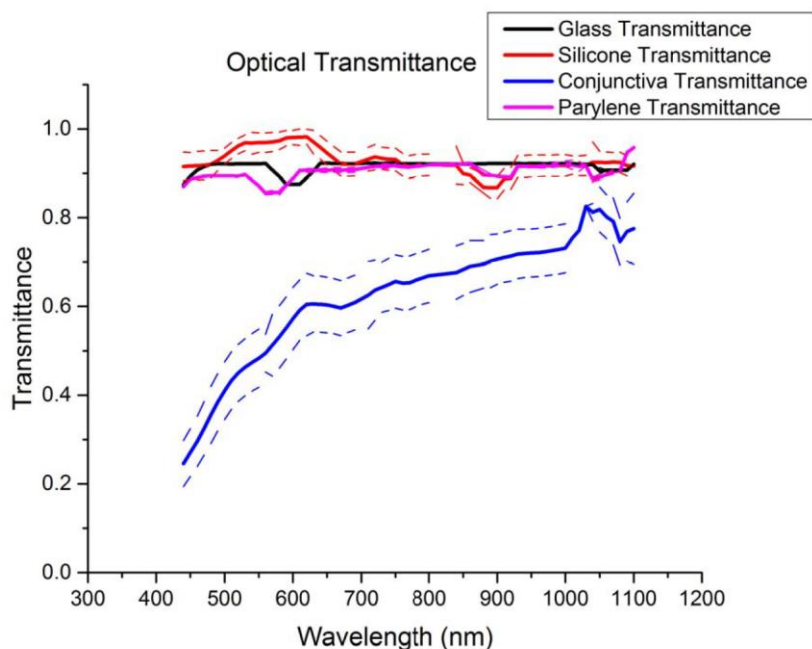


Figure 5.1: Optical transmittance of the conjunctiva as well as several biocompatible materials. Reprinted from K. Murali et al.'s paper [5.8]. Note that borosilicate glass, silicone, and parylene are highly transmissive over the region of interest, and therefore are ideal encapsulants for such an array.

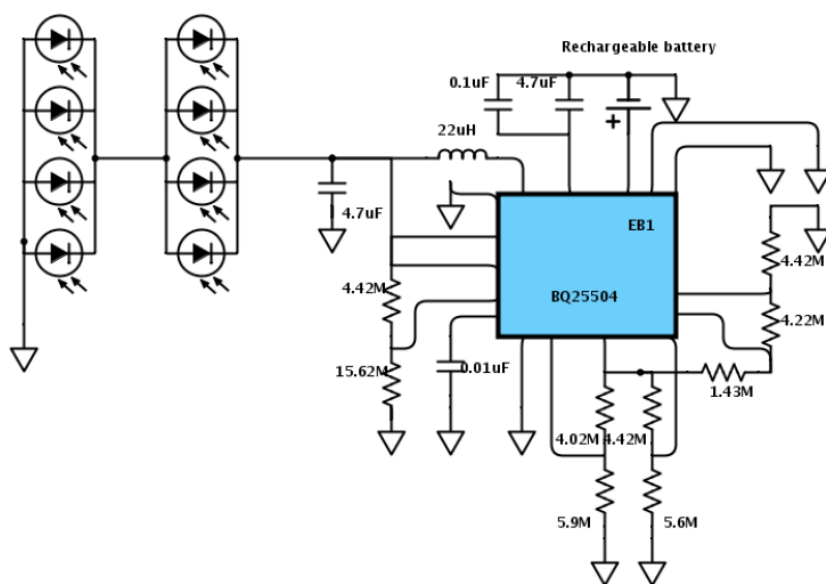


Figure 5.2: Photovoltaic energy harvesting circuit. Reprinted from K. Murali et al.'s paper [5.8].

With the help of Dr. Karthik Murali at USC, the viability of photovoltaic (PV) energy harvesting was explored [5.8]. On benchtop, the subconjunctival photovoltaic implant, produced 3.13mW, 2.13mW, and 1.26mW with $1000\text{W}/\text{m}^2$, $667\text{W}/\text{m}^2$, and $333\text{W}/\text{m}^2$, respectively [5.8]. In the circuit, eight OSIOptoelectronics photovoltaic cells were wired in 2 sets of 4 parallel cells in series (**Figure**

5.2) [5.8]. With the Texas Instruments BQ25504 energy harvesting IC acting as a boost converter, the circuit managed a suitable 3.2V with 0.38mA, 0.28mA, and 0.14mA for 1000W/m², 667W/m², and 333W/m², respectively [5.8]. Such a circuit utilized only 7.8mm² of the ocular surface; equivalent to 49μA/mm², 36μA/mm², and 18μA/mm² per unit area of solar cell, respectively.

Given that humans tend to not stare directly at the sun, the actual incident illumination is much lower than the solar maximum. Scattered light provides a more accurate irradiance of the PV circuit. A perusal of common building materials shows a wide range of albedos from 0.05 up to 0.8 [5.9]. For a common material, concrete, ranges from 0.2 to 0.4. Given that solar irradiance onto the ground is between 1kW/m² to 1.3kW/m², and light reflected off of the ground is on the order of 200W/m² to 520W/m²; the lower value of 18μA/mm² is likely the most accurate. Given the oxygenerator's requirement of 0.25mA, a collection area of 14mm² is needed.

Table 5.1: Lumens from standard household bulbs [5.10]

| OLD INCANDESCENT BULB (WATTS) | ENERGY STAR BULB BRIGHTNESS (MINIMUM LUMENS) |
|--|---|
| 40 | 450 |
| 60 | 800 |
| 75 | 1100 |
| 100 | 1600 |
| 150 | 2600 |

This collection area needed is larger when indoor illumination is considered. Elderly patients likely spend most of their time indoors. From **Table 5.1**, the luminous energy for 100W (1600Lumens) equivalent bulbs is:

$$1600 \left(\frac{1}{683} \text{W} \times \text{Steradian} \right) = 2.34\text{W} \times \text{Steradian} \quad (5.1)$$

assuming all energy is transmitted at 555nm [5.10]. If a human were to stand 2m away from and staring at the bulb, the human eye will receive:

$$(2.34\text{W} \times \text{Steradian}) / \left(\frac{\text{Steradian}}{4\pi(1\text{m})^2} \right) = 0.186\text{W/m}^2 \quad (5.2)$$

This result matches previously reported values of indoor light being 10^{-4} less than solar intensity [5.11]. The circuit's efficiency is found to be:

$$\frac{3.2\text{V} \times 0.14\text{mA}}{0.33\text{mW}/\text{mm}^2 \times 4.1\text{mm} \times 1.9\text{mm}} = 17.3\% \quad (5.3)$$

Therefore, the photovoltaic cells would provide $3.2 \times 10^{-2} \mu\text{W}/\text{mm}^2$, and would need to cover 500cm^2 of area to supply the retina. Given that the eyeball can be approximated by a 24mm diameter sphere, this solar cell array would cover 13.5 times the surface of the eye, which is clearly unachievable.

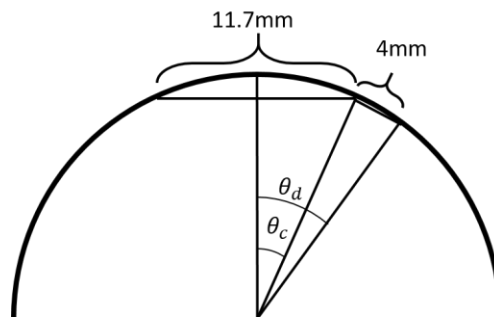


Figure 5.3: Location for implantable photovoltaic cells.

Patients wearing such a solar harvesting devices would, therefore, need to spend a significant portion of time outside. Indeed a large implant covering a 4mm ring around the cornea would have a surface area given by [5.12]:

$$A = 2\pi(12\text{mm})^2 \int_{\theta_c=29^\circ}^{\theta_d=39^\circ} \sin \theta d\theta = 88.2\text{mm}^2 \quad (5.4)$$

where θ_c is the angle for the corneal radius, 11.7mm, **Figure 2.1**, and θ_d is the angle for the device end (**Figure 5.3**). This device would harvest 1.59mA on a sunny day. Given that daily power requirements were found to be 0.25mA, the user would need to spend 3.8 hours outside on a sunny day to generate sufficient oxygen. This is likely a large lifestyle change for most patients, and may result in low compliance.

A further flaw of this approach is that no oxygen generation would occur at night when oxygen demand is highest due to rod stimulation. Solar cell oxygen harvesting would therefore be reliant on a rechargeable battery or would need to increase vitreal oxygen tension sufficiently to act as a source

for nocturnal oxygen demands of the retina. The Quallion QL0003I, 3mAh with an 11.8mm height and 2.9mm diameter, is appropriate [5.13]. The battery would be fully charged in 1.88 hours of sunlight. A single battery would power electrolysis for 12 hours.



Figure 5.4: Exposed conjunctiva on the rabbit eye. Reprinted from [5.14].

In addition, this approach is problematic in animal models, especially in a rabbit (**Figure 5.4**), where the sclera is fully covered by the eyelid. In such a scenario, the cells would only receive near-IR. Since surgical experiments would be done indoors, this would necessitate a near-IR source to power the device.

5.2 KINETIC ENERGY HARVESTING

Kinetic energy harvesters made their way into commercial devices since 1989 with the Seiko's Kinetic Quartz wristwatch [5.15]. Seiko tested a pacemaker in a dog which harvests 13 μ J per heartbeat [5.16]. Such devices relied on a rotating or an oscillating weight, whose motion induces a voltage on a coil which in turn charges an energy storage device such as a battery or capacitor.

Miao et. al. demonstrated a MEMS inertial power generator, which utilizes a proof mass attached to one plate of a variable capacitor [5.17]. As the device underwent acceleration, the proof mass would lag, causing the two plates to separate, which lowered the capacitance and therefore increased the voltage. Such a device produced 120nJ for an 11mm x 11mm device [5.17]. In the literature are found for values of 60 μ W in a 1cm² footprint for piezoelectric harvesters based on aluminum nitride

[5.18]. The principle of kinetic harvesting is generally similar in all these cases: a proof mass forms an oscillator with the device, and the energy generation mechanism acts as a damper. Work done by dampening the oscillation is converted into electricity.

In the case of the eye, a small energy harvester would have a footprint with a maximum length of 10mm, and sit on the side of the eye. Taking inspiration from literature, the harvester could be modeled as a proof mass, m , traveling in a tube on the surface of the eye, with a restoring force, $k\Delta x$, and a viscous damping force, $c\Delta\dot{x}$. The saccades of the eye occur incredibly rapidly, and reach 10° - 30° of movement at up to $300^\circ/\text{s}$ to $500^\circ/\text{s}$, or 30Hz to 16Hz , respectively [5.19]. These major saccades are infrequent, and therefore are an inconsistent source of power. Microsaccades of up to 1.2° in amplitude are common and have frequencies between 40Hz - 150Hz , with frequency decreasing with increasing amplitude [5.20]. Their recurrence makes them a more reliable source of power generation. These microsaccades can be modeled as an oscillatory angular motion, $\theta_{eye}(t) = A \sin(\omega t)$. The difference between the mass position and the eyeball's rotation determines the elongation of the spring, $k(x - r\theta_{eye})$, where r is the radius of the eye. Likewise, the relative motion of the mass and the eye is described as $c(\dot{x} - r\dot{\theta}_{eye})$. Putting this together:

$$m\ddot{x} + c(\dot{x} - r\dot{\theta}_{eye}(t)) + k(x - r\theta_{eye}(t)) = 0 \quad (5.5)$$

The driving force can be found by separating the ocular motion:

$$F_{driving} = kr\theta_{eye}(t) + cr\dot{\theta}_{eye}(t) \quad (5.6)$$

$$m\ddot{x} + c\dot{x} + kx = kr\theta_{eye}(t) + cr\dot{\theta}_{eye}(t) \quad (5.7)$$

Let $c/m = \gamma$, and $k/m = \omega_0^2$, the undamped resonant frequency is:

$$\ddot{x} + \gamma\dot{x} + \omega_0^2 x = \omega_0^2 r\theta_{eye}(t) + \gamma r\dot{\theta}_{eye}(t) \quad (5.8)$$

since ocular motion was defined as $\theta_{eye}(t) = A \sin(\omega t)$. The terms for the driving force are defined as $F_0 = \omega_0^2 rA$ and $f_1 = \gamma rA$, resulting in:

$$\ddot{x} + \gamma\dot{x} + \omega_0^2 x = F_0 \sin(\omega t) + \omega f_1 \cos(\omega t) \quad (5.9)$$

Testing the solution of $x = B_0 \sin(\omega t) + B_1 \cos(\omega t)$:

$$\begin{aligned} -B_0 \omega^2 \sin(\omega t) - B_1 \omega^2 \cos(\omega t) + \gamma(B_0 \omega \cos(\omega t) - B_1 \omega \sin(\omega t)) \\ + \omega_0^2 (B_0 \sin(\omega t) + B_1 \cos(\omega t)) = F_0 \sin(\omega t) + \omega f_1 \cos(\omega t) \end{aligned} \quad (5.10)$$

Separating all sine and cosine terms, as that is the only solution for which the equation is true for all values:

$$-B_0 \omega^2 \sin(\omega t) - B_1 \gamma \omega \sin(\omega t) + B_0 \omega_0^2 \sin(\omega t) = F_0 \sin(\omega t) \quad (5.11)$$

$$-B_1 \omega^2 \cos(\omega t) + B_0 \gamma \omega \cos(\omega t) + B_1 \omega_0^2 \cos(\omega t) = \omega f_1 \cos(\omega t) \quad (5.12)$$

The solution is found to be:

$$x(t) = \frac{\gamma \omega^2 f_1 + (\omega_0^2 - \omega^2) F_0}{(\omega_0^2 - \omega^2)^2 + \gamma^2 \omega^2} \sin(\omega t) + \frac{(\omega_0^2 - \omega^2) f_1 - \gamma F_0}{(\omega_0^2 - \omega^2)^2 + \gamma^2 \omega^2} \omega \cos(\omega t) \quad (5.13)$$

The force exerted by the eye is given by:

$$F_{driving} = F_0 \sin(\omega t) + f_1 \omega \cos(\omega t) \quad (5.14)$$

The device will reach steady state over time, and instantaneous power absorbed by the device from the eye is given by the force the eye is driving into the device:

$$P_{inst} = F\dot{x} = m * (F_0 \sin(\omega t) + f_1 \omega \cos(\omega t))\dot{x} \quad (5.15)$$

Averaging over a cycle, $(0, 2\pi/\omega)$ gives a more useful power equation:

$$P_{avg} = \frac{m\omega}{2\pi} \int_0^{2\pi/\omega} F\dot{x} dt = \frac{m\omega}{2\pi} \int_0^{2\pi/\omega} (F_0 \sin(\omega t) + f_1 \omega \cos(\omega t))\dot{x} dt \quad (5.16)$$

which solves to:

$$P_{avg} = \frac{\gamma\omega^2}{2} \left(\frac{\omega^2 f_1^2 + F_0^2}{(\omega_0^2 - \omega^2)^2 + \gamma^2 \omega^2} \right) \quad (5.17)$$

Plugging in $F_0 = \omega_0^2 r A$ and $f_1 = \gamma r A$:

$$P_{avg} = \frac{\gamma m \omega^2 r^2 A^2}{2} \left(\frac{\omega^2 \gamma^2 + \omega_0^4}{(\omega_0^2 - \omega^2)^2 + \gamma^2 \omega^2} \right) \quad (5.18)$$

Power is maximized when the harvester's resonant frequency matches the driving frequency, $\omega_0 = \omega$, resulting in the simplified expression:

$$P_{avg} = \frac{\gamma m \omega_0^2 r^2 A^2}{2} \left(\frac{\gamma^2 + \omega_0^2}{\gamma^2} \right) \quad (5.19)$$

Table 5.2: Parameters for estimation of energy extracted by a kinetic energy harvester.

| PARAMETER | VALUE [UNIT] |
|---|---------------------------|
| SACCADE AMPLITUDE (A) [5.20] | $1.2^\circ/2 = 0.6^\circ$ |
| SACCADE DRIVING FREQUENCY (ω_0) [5.20] | 40[Hz] |
| STAINLESS STEEL PROOF MASS (10MM \times 5MM \times 2MM) | 0.77[g] |
| RADIUS OF THE EYE | 12[mm] |
| DAMPING FACTOR | 6.31854[s ⁻¹] |

Amplitude for the Proof Mass – Driven at 40 Hz, 0.6 ° Amplitude

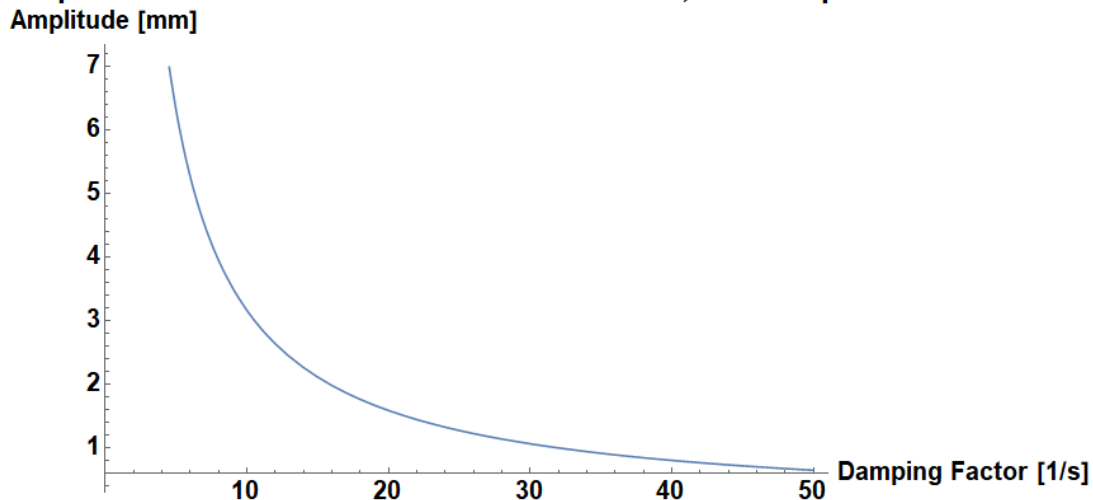


Figure 5.5: Amplitude for a proof mass. Plot of $x(t)$, equation (5.13), when driven at resonance. This sweeps the amplitude of the motion of the proof mass over all values of γ . The amplitude is less than 5mm when $\gamma \geq 6.31854\text{s}^{-1}$.

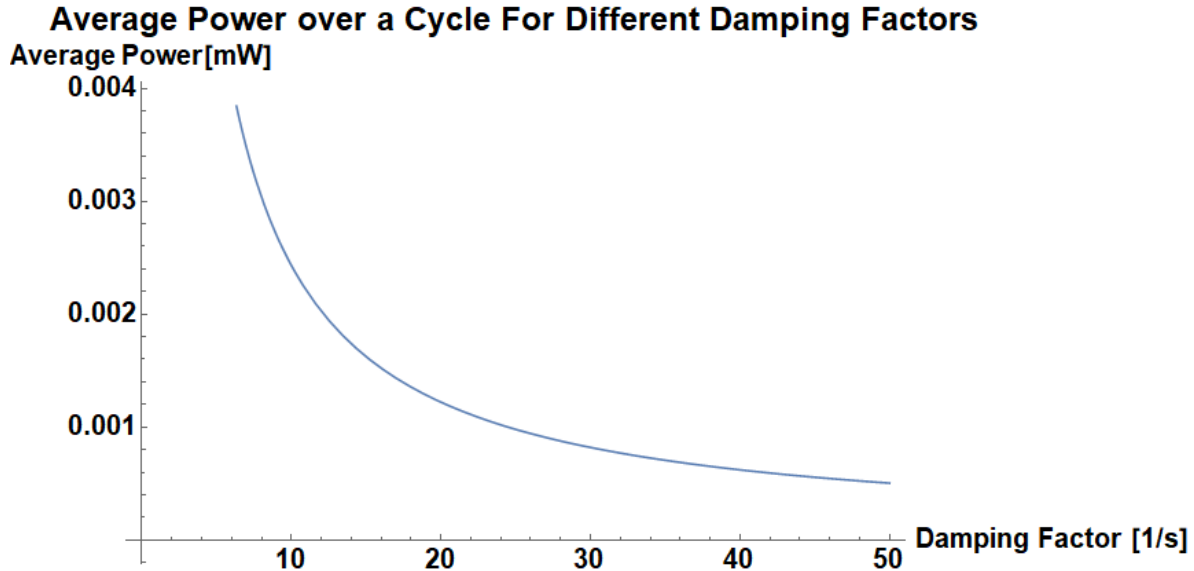


Figure 5.6: Average power over a cycle for different damping factors. This plots the average power, equation (5.19), versus the damping factor under resonance, $\omega = \omega_0$, with the eye having a 40Hz, 0.6° microsaccade. For low damping factors, the power added by the eye in steady state increases as the damping factor decreases, therefore the maximum that satisfies the amplitude requirement of $|x(t)| \leq 5\text{mm}$ is $\gamma = 6.31854\text{s}^{-1}$. The time average power of 3.84mW is associated with that damping factor.

The parameters are listed in **Table 5.2**. The mass, 0.77g, is assumed to be a stainless steel weight $10\text{mm} \times 5\text{mm} \times 2\text{mm}$, to keep the entire device footprint within $10\text{mm} \times 10\text{mm} \times 3\text{mm}$. The damping factor, $\gamma = c/m$, is determined from the value which maximizes P_{avg} , while keeping the amplitude below 5mm (1/2 the total travel distance), since anything above that would be wasted by slamming into the limits of the device (**Figure 5.5**). Damping values of $\gamma \geq 6.31854\text{s}^{-1}$, keep the amplitude below 5mm. **Figure 5.6** plots the average power at resonance, equation (5.19), over all values of γ . For low damping factors, power increases as the damping factor is reduced. Therefore, the maximum that satisfies the amplitude requirement is $\gamma = 6.31854\text{s}^{-1}$, which yields an average power of 3.84mW over a cycle. This value assumes complete conversion of energy from mechanical to electrical. Power supply conversion losses boosting the voltage to a suitable 2.5V normally would range in the range of 5%-10%. Electrical energy harvesting techniques, such as piezoelectricity or a linear alternator, have power losses as well. Furthermore, such a design expects the entirety of the damping force to be energy harvesting. In actuality, mechanical losses would account for a substantial fraction of the “damping” force calculated here; meaning $\gamma = \gamma_{loss} + \gamma_e$. Other energy harvesting devices for biomedical applications from literature have $0.778\text{mW}/\text{cm}^3$ (35Hz) to $8.24\text{mW}/\text{cm}^3$ (149.3Hz) for electromagnetic energy harvesting devices, and $0.76\mu\text{W}/\text{cm}^3$ to

6mW/cm³ for piezoelectric devices; resulting in a maximum of 2.472mW/cm³ for a 150Hz operating frequency, or 1.8mW at 50Hz [5.2]. There is little margin for such a device, and it would only achieve this power during the REM portion of the sleep cycle, and during saccades. The time averaged power harvested is likely to be much lower. For these reasons, though enticing for its power autonomy, kinetic energy harvesting was not pursued as power source for the oxygenerator.

5.3 INDUCTIVE POWER COUPLING

Inductive power coupling is the most promising approach. While it does not offer the same power autonomy as kinetic energy harvesting or solar cells, it works well in a rabbit eye, can penetrate an eye lid, and provides a high power density for the implant size. Furthermore, other devices, such as SecondSight's Argus II, have demonstrated the technology is viable in humans.

The basic concept of inductively coupled power transfer is to provide a radio frequency signal from an oscillator to a primary coil. That primary coil induces an electromotive force on a secondary coil, and the received power is rectified to DC.

A sleep mask could contain the primary coil and driver circuitry, and power the oxygenerator throughout the night when oxygen demand is highest and the disease is believed to progress (CHAPTER 1 and CHAPTER 2). During the day, the sleep mask can easily be recharged. The engineering of such a sleep mask is rather simple, is not tackled here, nor such mask was tried in humans.

Resonant inductive power coupling relies on the primary and secondary side to be in resonance with each other (**Figure 5.7**). The signal is then rectified, and utilized to power electronics, which can be thought of as an equivalent load, R .

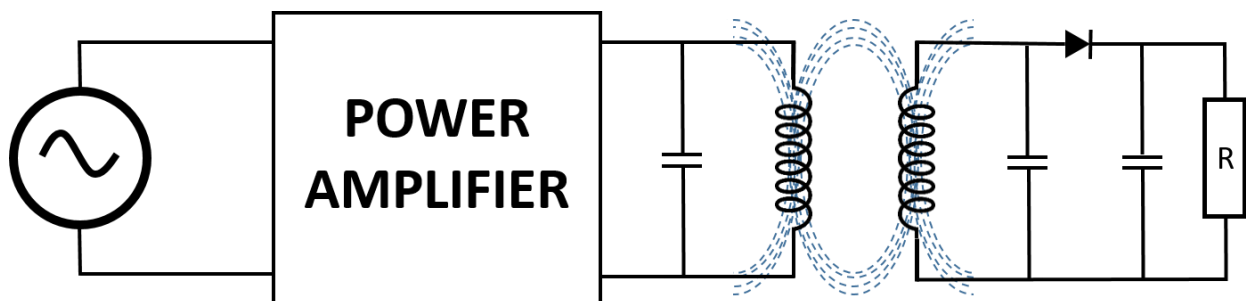


Figure 5.7: Concept of the inductive power transfer circuit.

5.3.1 THEORY

The primary side consists of an RF generator, whose signal is passed through a power amplifier before going to the resonant primary coil, usually configured as an LC tank (**Figure 5.8**). Mutual inductance, M , between the primary and secondary coils induces the electromotive force onto the secondary coil. The mutual inductance can be written as:

$$M = k\sqrt{L_1L_2} \quad (5.20)$$

where k , is the coupling coefficient, and L_1 and L_2 are the primary and secondary coil inductances, respectively. The primary coil experiences an impedance, Z_m , from the presence of the secondary, which in the frequency domain can be written as:

$$V_1 = Z_1I_1 + Z_mI_2 \quad (5.21)$$

where Z_1 represents the primary side without the secondary coil.

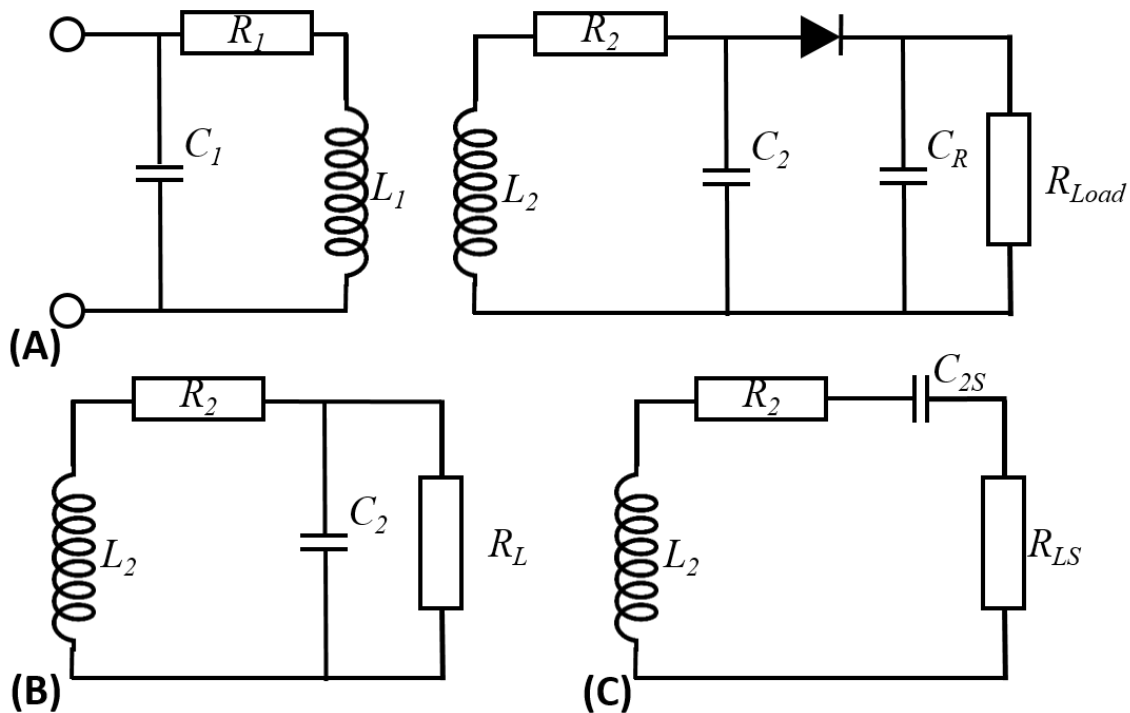


Figure 5.8: Circuits for inductively coupled power transfer. (A) Complete circuit. The resistances, R_1 and R_2 , represent the resistances of the inductors, L_1 and L_2 , while C_1 and C_2 are the coupling capacitors. (B) The rectifying circuit and load, R_{Load} can be combined into an

approximate A.C. load R_L . (C) The parallel capacitance and parallel resistance form an equivalent circuit to (B).

The secondary side contains an LC tank circuit with a connected load, $R = R_L$. There is no external driving voltage, $V_2 = 0$, since all power is generated from mutual inductance with the primary side:

$$Z_2 I_2 - Z_m I_1 = 0 \quad (5.22)$$

where the secondary side impedance, Z_2 . Mutual inductance generates an electromotive force from the current of the partner coil, $v = M di/dt$. When transformed into the frequency domain, $V = i\omega MI$, the impedance from the mutual inductance is found to be $Z_m = V/I = i\omega M$. Using this in equation (5.22), one finds a relationship between I_1 and I_2 :

$$I_2 = Z_m I_1 / Z_2 = i\omega M I_1 / Z_2 \quad (5.23)$$

Combining with equation (5.21),

$$\frac{V_1}{I_1} = Z_1 + \omega^2 M^2 / Z_2 \quad (5.24)$$

the impedance reflected on the primary side is found to be $Z_{refl} = \omega^2 M^2 / Z_2$. Before proceeding, however, the secondary side must be dealt with. Assuming that the voltage drop from the diode is minor, the rectifying circuit and load can be replaced with an A.C. load, R_L (**Figure 5.8b**). A purely series circuit is easier to deal with, and so the parallel capacitance, C_2 , and resistance, R_L , of the secondary side can be converted to a series resistance, R_{LS} and capacitance, C_{2S} :

$$R_{LS} + \frac{1}{i\omega C_{2S}} = R_L \parallel \frac{1}{i\omega C_2} \quad (5.25)$$

$$R_{LS} + \frac{1}{i\omega C_{2S}} = \frac{R_L}{1 + \omega^2 R_L^2 C_2^2} - \frac{i\omega R_L^2 C_2}{1 + \omega^2 R_L^2 C_2^2} \quad (5.26)$$

So the series resistance becomes:

$$R_{LS} = \frac{R_L}{1 + \omega^2 R_L^2 C_2^2} \quad (5.27)$$

The series capacitance can be further solved to be:

$$\frac{1}{C_{2S}} = \frac{\omega^2 R_L^2 C_2}{1 + \omega^2 R_L^2 C_2^2} \quad (5.28)$$

$$C_{2S} = \frac{1 + \omega^2 R_L^2 C_2^2}{\omega^2 R_L^2 C_2} \quad (5.29)$$

The series capacitance is dependent on the load. If the load is well defined and in a range such that $1 \ll \omega^2 R_L^2 C_2^2$, the series capacitance approaches the value of the parallel capacitance, $C_2 \approx C_{2S}$. The secondary circuit will have values in the range of $\omega \approx 6\pi$ [MHz], $C_2 \approx 1$ [nF], and $R_L \approx 1$ [k Ω], such that

$$\omega^2 R_L^2 C_2^2 \approx 355 \gg 1 \quad (5.30)$$

Therefore, the resonant frequency for the series capacitance, $\omega_0 = 1/\sqrt{L_2 C_{2S}}$, is approximately equal to that of the original, $\omega_0 = 1/\sqrt{L_2 C_2} \approx 1/\sqrt{L_2 C_{2S}}$. The same estimation results in an approximation of the series load to be, $R_{LS} \approx 1/\omega^2 R_L C_2^2 = L_2/R_L C_2$. The series resistance, R_{LS} , and capacitance, C_S , determine the impedance of the secondary circuit:

$$Z_2 = R_2 + R_{LS} + i\omega L_2 + \frac{1}{i\omega C_{2S}} \quad (5.31)$$

$$Z_2 = R_2 + R_{LS} + \frac{1 - \omega^2 L_2 C_{2S}}{i\omega C_{2S}} \quad (5.32)$$

At resonance, $\omega = \omega_0$ the impedance of the secondary becomes:

$$Z_2 = R_2 + R_{LS} \quad (5.33)$$

Meaning that at resonance, assuming the diode voltage drop, V_D , is small compared to the induced voltage, the efficiency of power conversion is given by:

$$\eta_{2-load} = \frac{R_L}{R_2 + R_{LS}} \quad (5.34)$$

$$\eta_{2-load} = \frac{R_L}{R_2 + L_2/R_L C_2} \quad (5.35)$$

The input power into the secondary side can be found by finding the power input into the reflected impedance of the secondary side from the primary side. The configuration in figure **Figure 5.8a** is similar to a parallel RLC circuit, meaning the impedance increases at resonance (**Figure 5.9**). Driving such a circuit with a voltage amplifier would result in a reduction in the current passing through the inductor, and therefore a reduction in the resultant magnetic field. A current amplifier, on the other hand, would result in a constant amplitude through the inductor, and therefore such a circuit (**Figure 5.10**) was chosen.

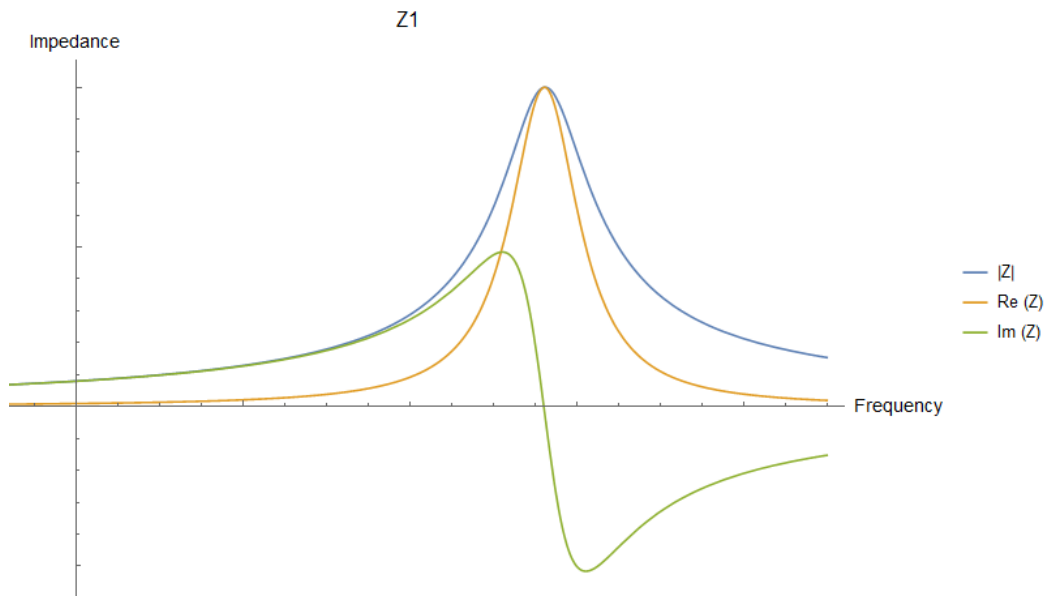


Figure 5.9: Plot of the total impedance of the primary without the secondary. Plot of the total impedance of the primary when there is no coupling with the secondary, $M(k = 0) = 0$. Note that at resonance, the impedance rises sharply. Such a circuit benefits from a current A.C. source to maximize power delivery.

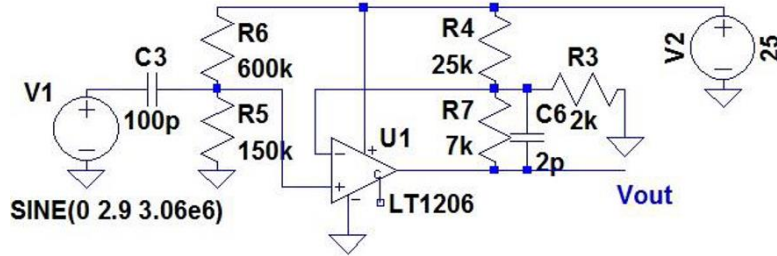


Figure 5.10: LT1206 amplifier. (Top) LT1206 schematic. (Bottom) LT1206 diagram (PCB).

To determine the steady state current through the inductor and the reflected mutual inductance, the voltage, $V_1 = Z_1 I$, and impedance of the inductor's branch, $Z_L = i\omega L_1 + R_1 + \omega^2 M^2 / Z_2$, are combined:

$$I_1 = \frac{V_1}{Z_L} = I \frac{Z_1}{Z_L} \quad (5.36)$$

The impedance, Z_1 , is calculated to be:

$$Z_1 = \frac{1}{i\omega C_1} || Z_L = \frac{Z_L \left(\frac{1}{i\omega C_1} \right)}{\left(\frac{1}{i\omega C_1} \right) + Z_L} = \frac{Z_L}{1 + i\omega C_1 Z_L} \quad (5.37)$$

The ratio, Z_1/Z_L , is paramount to finding the current through the inductor, I_1 , therefore equation (5.37) is used to find:

$$\frac{Z_1}{Z_L} = \frac{1}{(1 - \omega^2 L_1 C_1) + i\omega C_1 (R_1 + \omega^2 M^2 / Z_2)} \quad (5.38)$$

Which at the parallel resonance, $\omega_{0P} = 1/\sqrt{L_1 C_1}$, increases to:

$$\frac{Z_1}{Z_L} = \frac{Z_2}{i\omega_0 (R_1 Z_2 C_1 + M^2 / L_1)} \quad (5.39)$$

The magnitude of the current is, therefore, using equation (5.33), calculated:

$$|I_1| = |I| \left| \frac{Z_1}{Z_L} \right| = \frac{|I|}{\omega_0} \left(\frac{R_2 + R_{LS}}{R_1 (R_2 + R_{LS}) C_1 + M^2 / L_1} \right) \quad (5.40)$$

The power onto the secondary side from equation (5.22) at resonance is:

$$P_2 = \omega_0 M |I_1|^2 = M \left(\frac{R_2 + R_{LS}}{R_1 (R_2 + R_{LS}) C_1 + M^2 / L_1} \right)^2 |I|^2 \quad (5.41)$$

whichm given that $M = k\sqrt{L_1 L_2}$, is:

$$P_2 = \omega_0 M |I_1|^2 = |k| \sqrt{L_1 L_2} \left(\frac{R_2 + R_{LS}}{R_1 (R_2 + R_{LS}) C_1 + k^2 L_2} \right)^2 |I|^2 \quad (5.42)$$

Therefore the power available to the load is given by the product of the power incident on the secondary from the primary side, equation (5.41), and the efficiency of the power conversion to the load, equation (5.34):

$$P_{Load} = P_2 \eta_{2-load} = |k| \sqrt{L_1 L_2} \left(\frac{R_2 + R_{LS}}{R_1 (R_2 + R_{LS}) C_1 + k^2 L_2} \right)^2 \left(\frac{R_L}{R_2 + R_{LS}} \right) |I|^2 \quad (5.43)$$

$$P_{Load} = |k| \sqrt{L_1 L_2} \frac{R_L (R_2 + R_{LS})}{(R_1 (R_2 + R_{LS}) C_1 + k^2 L_2)^2} |I|^2 \quad (5.44)$$

This implies that the power into the secondary side is proportional to the square of the current. Given previous estimates, one can write $R_2 R_L C_2 \ll L_2$ for the approximate values chosen. This means an approximation of the power available to the load can be approximated as:

$$P_{Load} \approx \frac{|k||I|^2\sqrt{L_1L_2}}{L_2C_2(R_1C_1 + k^2R_LC_2)^2} = \frac{|k||I|^2}{(R_1C_1 + k^2R_LC_2)^2\sqrt{C_1C_2}} \quad (5.45)$$

Note that decreasing R_LC_2 compared to R_1C_1 will increase the power on the secondary side. Since R_1 and R_L are difficult to modify, decreasing C_2 compared to C_1 will increase the transmitted power. However, as the frequency is set, the inductor must increase in size proportional to the decrease in capacitance. Therefore, as the secondary inductor increases in size compared to the primary inductor, the power transfer efficiency improves.

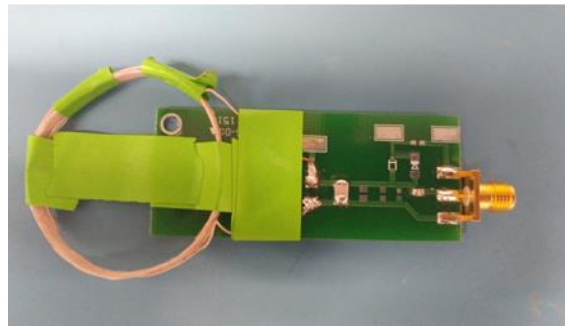
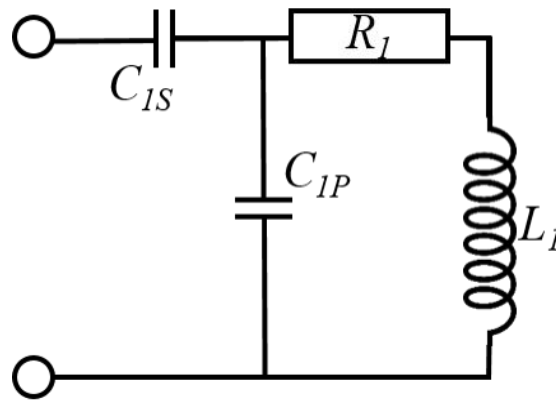


Figure 5.11: Primary side device. To shift the impedance at resonance to $|Z_1| = 50[\Omega]$, a series capacitor was added to the circuit. Circuit was built on a PCB with solder points for different capacitors, to find the optimum. Tape helps protect the fragile Litz wires.

Actually, the current amplifier (**Figure 5.10**) provides maximum power when impedance was matched to 50Ω . A second series capacitor is added to the circuit to shift the impedance at resonance (**Figure 5.11**). The addition of the series capacitor gives a circuit with a series resonance and parallel resonance, where the impedance reaches a minimum at approximately, $\omega_{0,S} \approx 1/\sqrt{L_1C_{1S}}$, and a maximum at approximately, $\omega_{0,P} \approx 1/\sqrt{L_1C_{1P}}$ (**Figure 5.12**). Such a circuit can be modeled as:

$$Z_1 = \frac{1}{i\omega C_{1S}} + \left(\frac{1}{i\omega C_{1P}} \parallel \left(i\omega L_1 + R_1 + \frac{\omega^2 M^2}{Z_2} \right) \right) \quad (5.46)$$

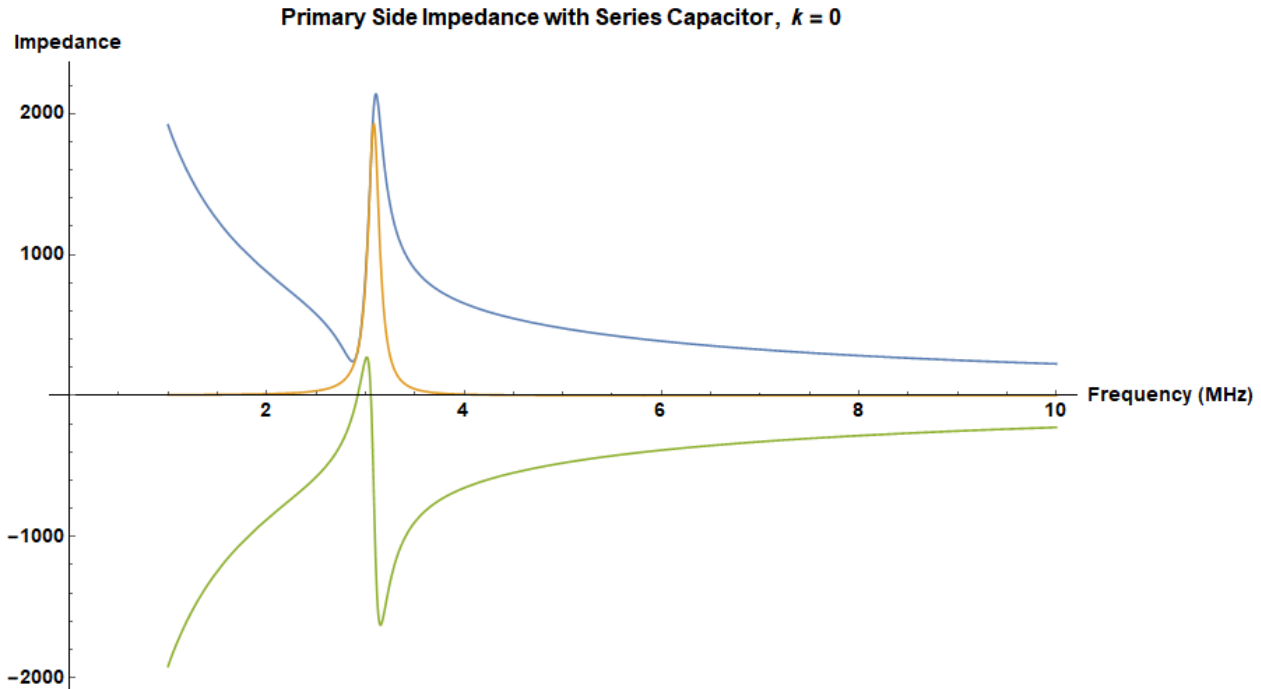


Figure 5.12: Primary side impedance with a series capacitor. Using the coil parameters in **Table 5.3**

A 5 turn, 38mm diameter solenoid coil was wound from 40/44 Litz wire (40 insulated strands of 44AWG copper wire) to reduce impedance due to the skin effect at 3MHz. Using the HP 4192A, the inductance was measured to be $4.527\mu\text{H}$ at the circuit's operating frequency of 2.94MHz (**Table 5.3**). The capacitors C_{1P} (0.5875nF) and C_{1S} (81.6pF) were chosen to achieve 50Ω at approximately 3MHz. Their values were also measured using the HP 4192A (**Table 5.3**). The impedance of the assembled circuit was measured over a range of frequencies and plotted into **Figure 5.13**. Note the model matches the data closely.

Table 5.3: Components in primary coil measured with the HP 4192A

| PART | VALUE | SERIES RESISTANCE |
|--------------------|--------------------|-------------------|
| COIL | $4.524\mu\text{H}$ | 0.86Ω |
| SERIES CAPACITOR | 81.6pF | 1Ω |
| PARALLEL CAPACITOR | 0.5875nF | 1Ω |

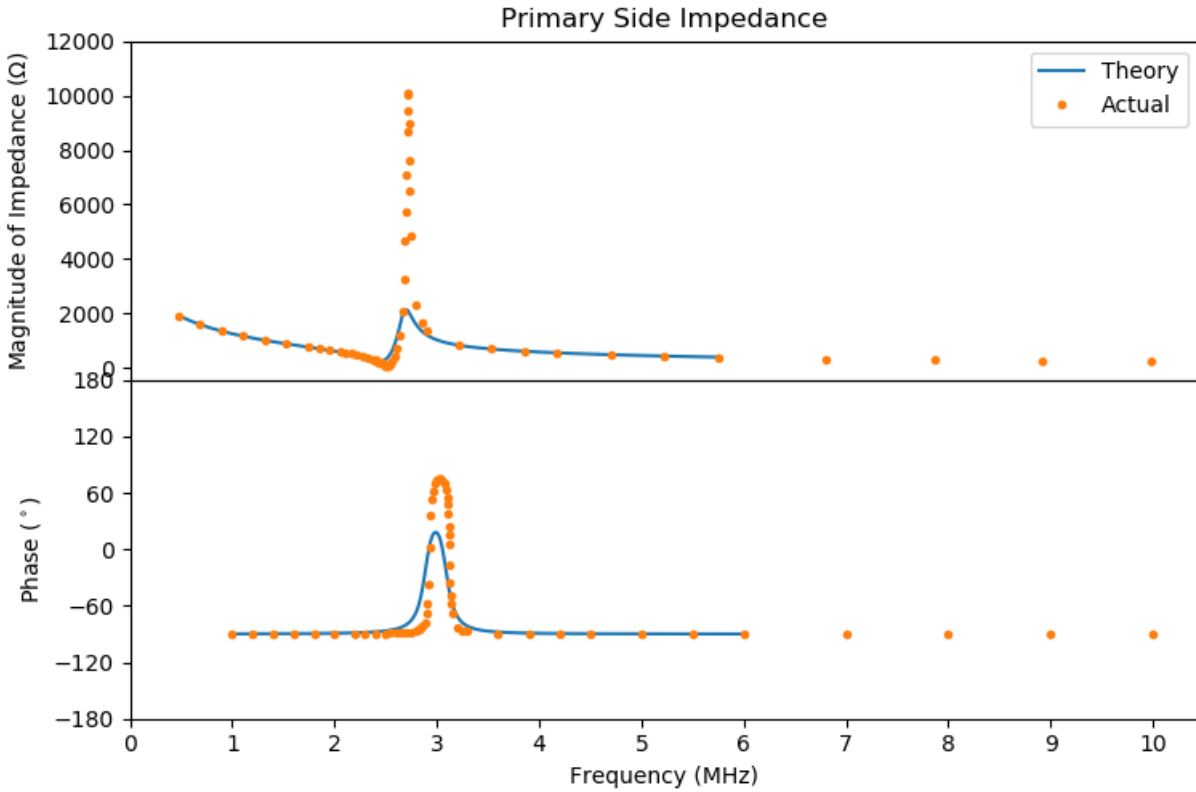


Figure 5.13: Measured impedance and phase for primary circuit versus the calculated curve from measuring the component values.

Given that the load $|Z_1| \approx 50[\Omega]$, the transmitted power onto the secondary side can be calculated.

The magnitude of the current is therefore:

$$|I_1| = \left| \frac{Z_1}{Z_L} \right| |I| = \frac{|Z_1||Z_2||I|}{\sqrt{\omega^2 L_1^2 Z_2^2 + (R_1 Z_2 + \omega^2 M^2)^2}} \quad (5.47)$$

This current into the primary coil (inductor) can be used to find the power into the secondary side, as per equation (5.40):

$$P_2 = \frac{\omega |k| |Z_1|^2 |Z_2|^2 |I|^2 \sqrt{L_1 L_2}}{\omega^2 L_1^2 Z_2^2 + (R_1 Z_2 + \omega^2 k^2 L_1 L_2)^2} \quad (5.48)$$

If the secondary side is driven at its resonance, the power available to the load is then given by:

$$P_{Load} = P_2 \eta_{2-Load} = \frac{\omega_0 |k| |Z_1|^2 R_L (R_2 + R_{LS}) |I|^2 \sqrt{L_1 L_2}}{\omega_0^2 L_1^2 (R_2 + R_{LS})^2 + (R_1 (R_2 + R_{LS}) + \omega_0^2 k^2 L_1 L_2)^2} \quad (5.49)$$

The power in the primary is based on the current into the circuit, and the impedance, $P_1 = |Z_1| |I|^2$, which gives a total efficiency of:

$$\eta = \frac{P_{Load}}{P_1} = \frac{\omega_0 |k| |Z_1| R_L (R_2 + R_{LS}) \sqrt{L_1 L_2}}{\omega_0^2 L_1^2 (R_2 + R_{LS})^2 + (R_1 (R_2 + R_{LS}) + \omega_0^2 k^2 L_1 L_2)^2} \quad (5.50)$$

This is a useful result, as the coupling constant, k , can be determined by measuring the voltage and current on the load and input into the primary circuit. Since all other parameters have been measured, the equation can be numerically solved for the coupling constant. As the coupling constant and, therefore, efficiency depend on the separation and angle between the coils, this can be plotted with respect to the separation between the two centers.

5.3.2 SECONDARY COIL FABRICATION

This section will discuss coil manufacturing methods. The secondary coil will be implanted under the conjunctiva. Therefore, it must be biocompatible and resist degradation so as to function over the lifetime of the oxygenator. For animal trials, that period maybe measured in months, but a human implant would require years of service. The coil was therefore built out of solid core gold wire. To reduce the size of the coil, the cross section would ideally be small, but power losses in the resistance of the coil should be minimized. The skin depth at 3MHz is calculated to be $\delta = \sqrt{2\rho/(\omega\mu_r\mu_0)} = 44.6\mu\text{m}$ [5.21]. Since the A.C. current density at any given depth is an exponential equation, $J = J_s e^{-(1+i)d/\delta}$, the first δ in depth would contain 63% of the charge. Therefore, a wire with a radius equal to the skin depth would have only 1.58× the resistance of bulk material at 3MHz; A-M Systems Catalog #75100 PFA (perfluoroalkoxy alkane) coated wire with a gold wire diameter of 76.2μm is suitable.

Coil size and design depends on the entire device. To batch out devices, coil properties would need to be repeatable. The manufacturing processes are discuss below.

5.3.2.1 ETCHED SILICON MOLDS

Early oxygenator utilized a flat coil laid on top of a liquid reservoir (**Figure 5.14**). In this configuration, the injections occurred in the plane of the reservoir. The coil was 2 layers deep. To create the coil, a silicon mold was etched using the Deep Reactive Ion Etcher (DRIE). The design spiraled inward 8 times starting with a diameter of 8mm and ending in a diameter of 5.6mm with 0.15mm trenches and 0.15mm grooves. The silicone molds were broken off of the silicon wafer and coated in Parylene-C.

The coil was formed by pressing the PFA-coated gold wire into the mold grooves. NuSil MED4-4210 silicone was then poured over the mold, degassed and partially cured in the oven. The spiral was then peeled from the mold, and the second half of the coil was created by repeating the process. With the second spiral peeled from the mold, both spirals were loosely held together by the gold wire. This wire was tucked into the middle as the two spirals were bonded together with more silicone. The mold was then ready to be soldered to the coupling capacitor, C_2 , the rectifying diode, and the smoothing capacitor, C_r . The circuit, **Figure 5.14**, is 9mm in diameter, and 1.5mm tall. The coil was bonded with silicone onto the top of the reservoir, and the platinum electrodes were soldered onto the smoothing capacitor. The whole reservoir is then coated in Parylene-C to protect the electronics from water ingress, and reduce oxygen loss at the reservoir.

This approach is slow, and had a low yield. Wires frequently broke during the peeling process. Out of a batch of five coils, only two would be useable when they needed to be soldered.

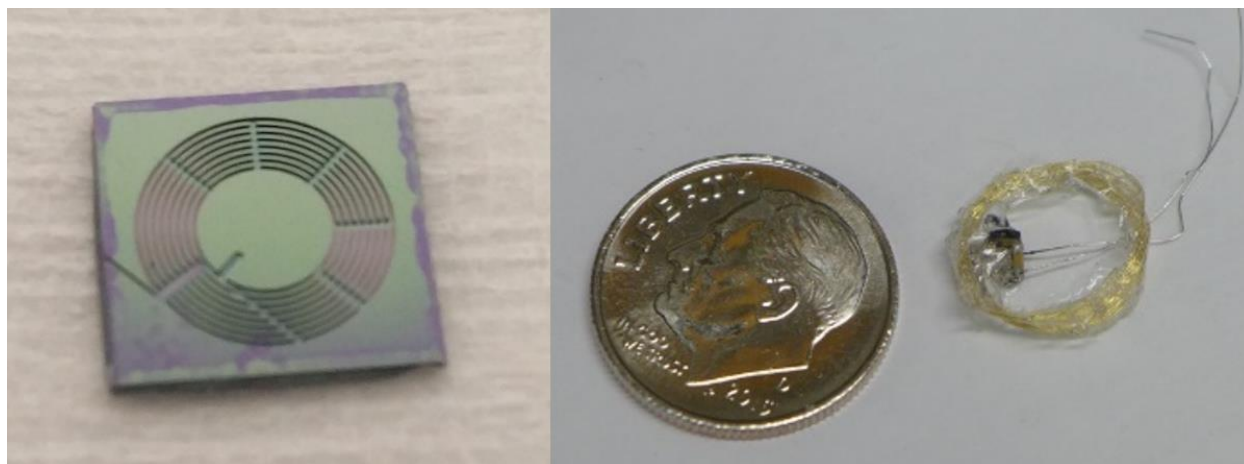


Figure 5.14: DRIE etched silicon mold for coil. The silicon mold is a 10mmx10mm square with the pattern for a flat coil (left). The right image shows the final electronics next to a penny (right).

5.3.2.2 TWO PART SPINDLE

A more traditional approach replaced the etched mold, with greater success. An aluminum spindle was machined in two parts with the desired inner diameter (8mm) and thickness (0.3mm) (**Figure 5.15**). The surface was polished to a mirror finish to reduce the adhesion of cured silicone to the mold. To create a coil, firstly, NuSiL MED4-4210 silicone was painted onto the surface of the mold where the coil was to be wound. Then, wire was taped onto the side of the spindle, and wound 10 times. The spindle was then allowed to partially cure in the oven for 5 minutes at 100°C such that the silicone would no longer be tacky. The spindle was then submerged in isopropyl alcohol to swell the silicone, and the screw holding both halves of the spindle was removed. The spindle was carefully separated, leaving the coil and its silicone flashing on one side of the aluminum cylinder (**Figure 5.15**). The excess silicone was removed with a razor blade. Finally, the coil was removed from the aluminum. The 3 components were then soldered and adhered with further silicone to the inner side of the coil. The remaining opening was filled with silicone. The result is a thin disk containing the electronics. The package was glued using silicone to the reservoir. Such a design was relatively successful and was used for the oxygenator versions 3-4 (see section 6.4).

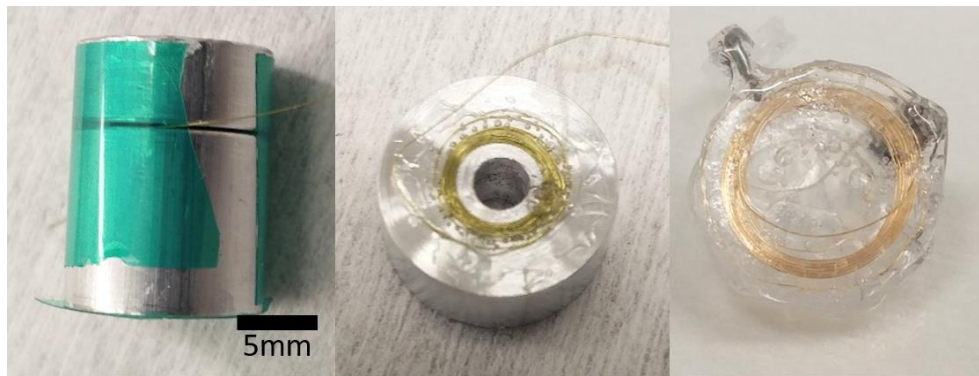


Figure 5.15: An aluminum spindle (left image) was turned on a lathe to allow the gold coil (middle image) to be 2 wires deep. The large open space in the center and flat design means the device (right image) can be filled up from the sides and the chamber can be seen clearly from above, which is used to confirm function after implant. Note that some turns are separate from the rest due to the difficulty of maintain consistent tension on the gold wire.

5.3.2.3 AUTOMATED COIL WINDER

The reliability of manufacturing the coil was further improved by automating the winding process (**Figure 5.16**). Using a 200-step stepper motor, the spindle could be turned an arbitrary number of rotations with 1.8° accuracy leading to highly repeatable coils. The process of creating the coils followed the earlier approach. The stepper was connected to an EasyStepper driver board, with the

A3967 microstepping driver, which was controlled by an Arduino. Once the stepper wound the coil the appropriate number of turns, the spindle was detached and placed in the oven to partially cure. The coil would then be removed and integrated as before with the remaining electronics. This approach was used for coils in oxygenator versions 5-8 (see section 6.4).



Figure 5.16: Automatic coil winder. (Left) Coil winder device. (Right) Active device electronics, V5. Coil surrounds the outside of the device. The coil is far more consistent in shape.

5.3.3 QUANTIFYING THE COILS

Here, the coil used in the oxygenator version 8 was placed on a linear track from Thor Labs, which is bolted onto an optical bench. Both the primary and secondary coils were held by plastic fixtures away from the table and track. The coils were zeroed so that the primary and secondary coils' nearest face were on the same plane. The secondary coil was centered onto the primary coil.

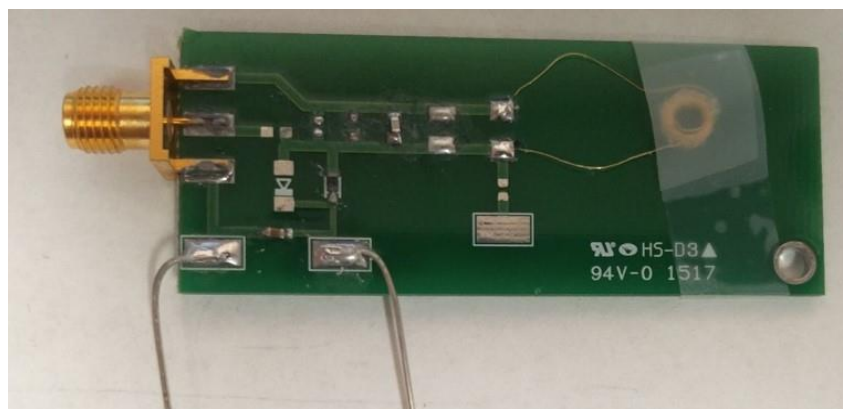


Figure 5.17: 20 Turn coil with 5.4mm in diameter. The circuit is as shown in the diagram on Figure 5.8a

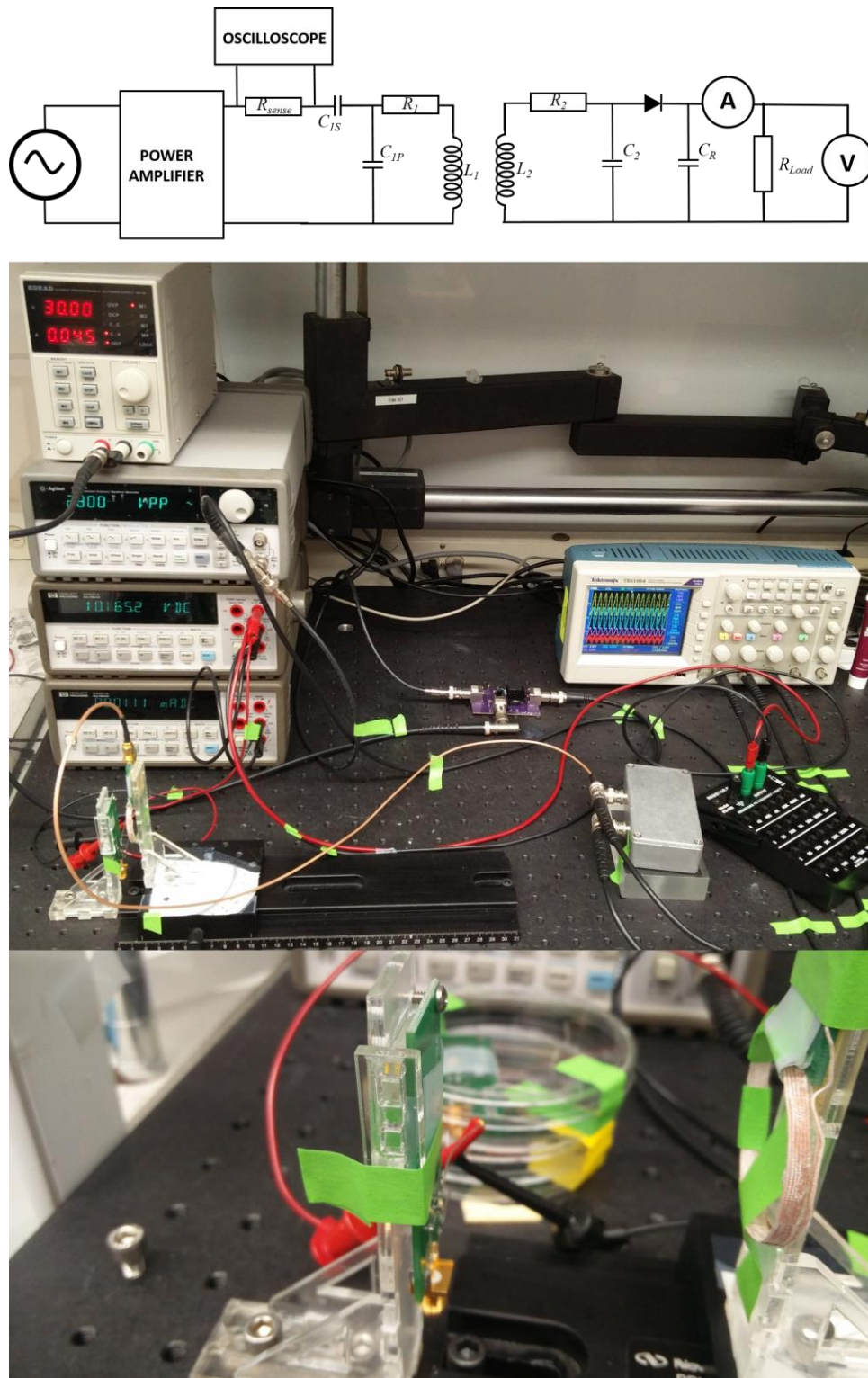


Figure 5.18: Coil test setup. Complete test diagram on top. Actual setup below. Angles and distance are both swept. V_{RMS} on either side of the sense resistor, as well as the current and voltage through the load resistor, R_{Load} , are also measured.

The final version of the secondary coil was a 20 turn device using A-M Systems Catalog #75100 PFA-coated gold coil with 5.4mm outer and 2.5mm inner diameter, and 0.94mm thickness (**Figure 5.17**). A 1600pF coupling capacitor (GRM188SC1H162JA01D) was chosen to maximize power delivered at 2.94MHz. A shottky diode and a 1 μ F smoothing capacitor formed the rectifying circuit. Two wire leads outputted the rectified D.C. signal to be measured by HP 34401A multimeters (**Figure 5.18**). A variable resistor box set the load across the secondary side's output.

The primary side was driven by an Agilent 33120A waveform generator at 2.94MHz and 2.8Vpp, which was fed into a current amplifier circuit based on the LT1206 IC (**Figure 5.10**). The current amplifier provides a maximum power of 250mA at 50 Ω . The amplifier was supplied by a 30V D.C. power supply. The output was sent through a 1.061 Ω (actual) non-inductive sense resistor (MP91S-1.00-1%) before going to the 5-turn primary (**Figure 5.11**). The waveforms on both sides of the sense resistor were connected to a Tektronix TBS 1072B oscilloscope, which measured the root mean squared signal of both sides of the resistor (**Figure 5.18**). The system swept all combinations of 0mm to 70mm, and 0 $^\circ$ to 45 $^\circ$. The results are presented below in **Figure 5.19**, **Figure 5.20**, **Figure 5.21**, **Figure 5.22**, **Figure 5.23**, and **Figure 5.24**.

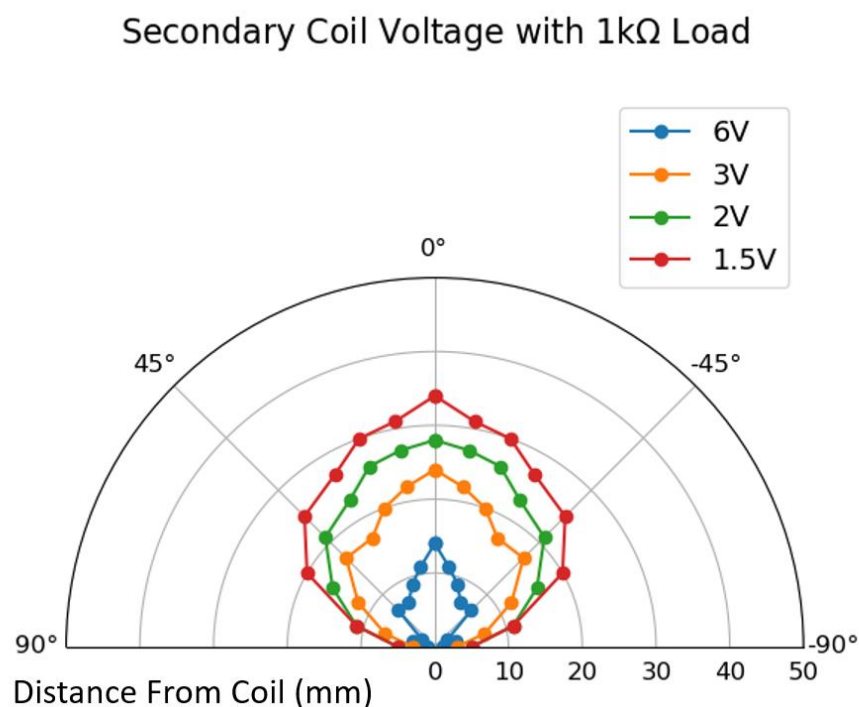


Figure 5.19: Polar plot of secondary side rectified voltage. Mirrored along the 0 $^\circ$ line.

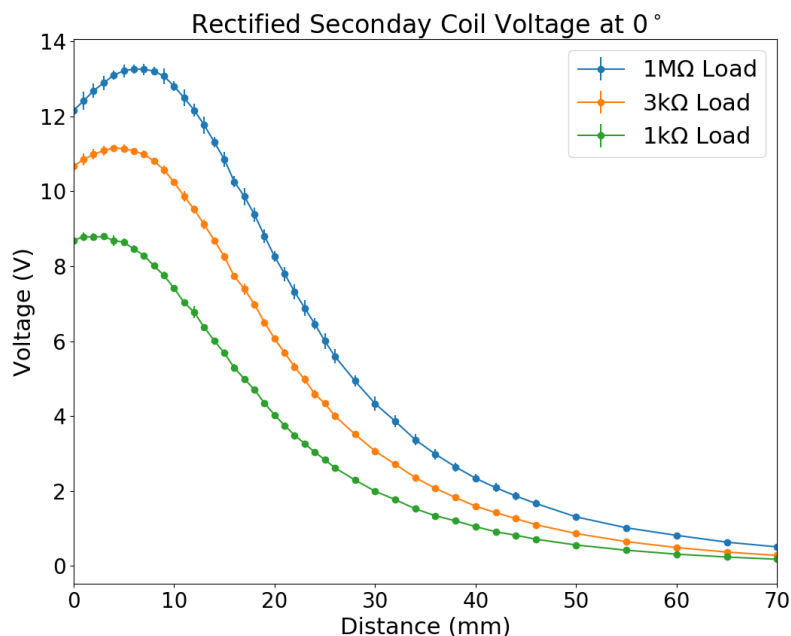


Figure 5.20: Rectified secondary coil voltage at angle of 0° . Secondary coil was moved away from primary 1mm at a time. Both voltage and current were measured together. The loads in the index refer to the load resistor from the resistor box used.

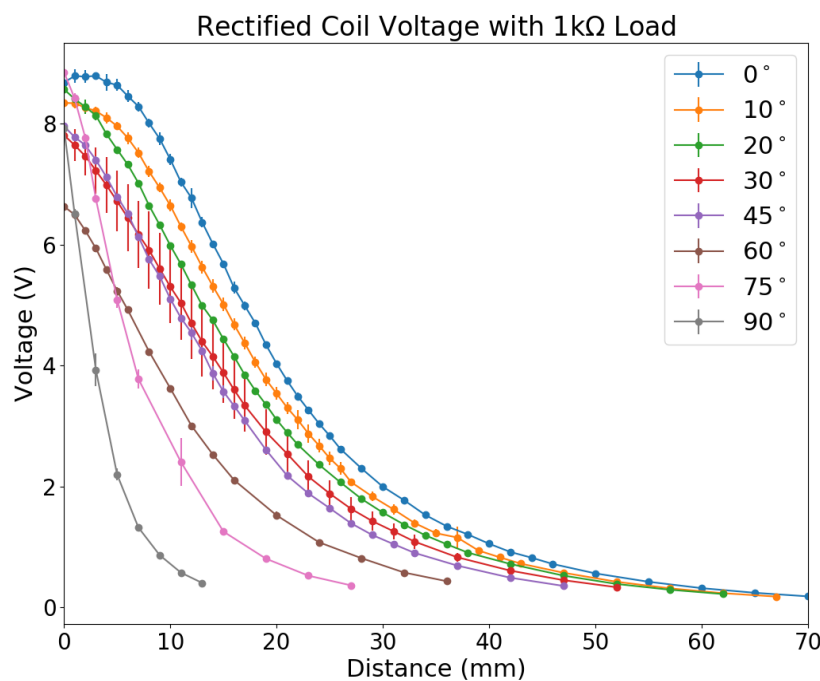


Figure 5.21: Rectified coil voltage with $1k\Omega$ load. The 0mm distance for any given angle was chosen as the point where the secondary coil touched the plane of primary coil. This was accomplished by placing a paper against the primary and finding the point where the secondary coil touched the paper. This offset was then subtracted from the value on the linear rail.

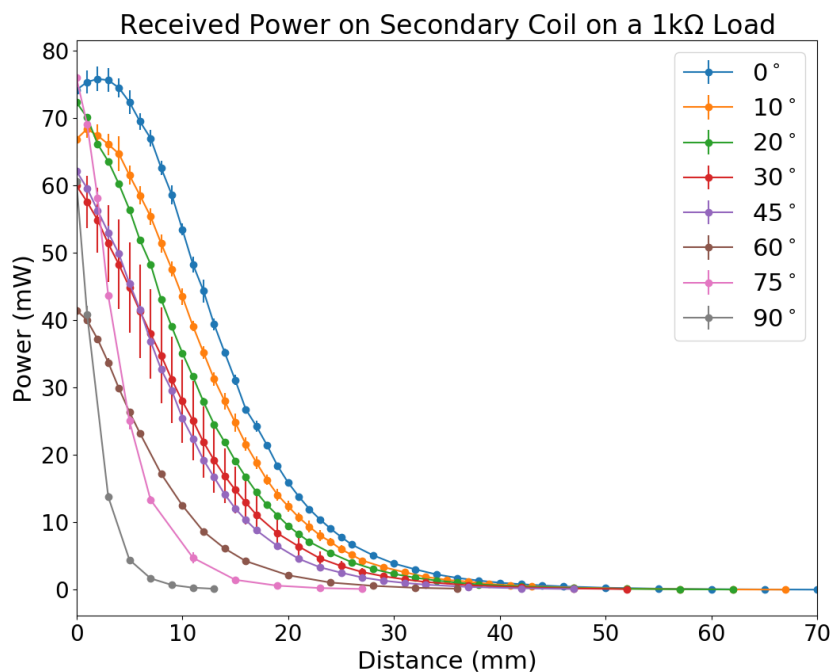


Figure 5.22: Received power on secondary coil with 1kΩ load.

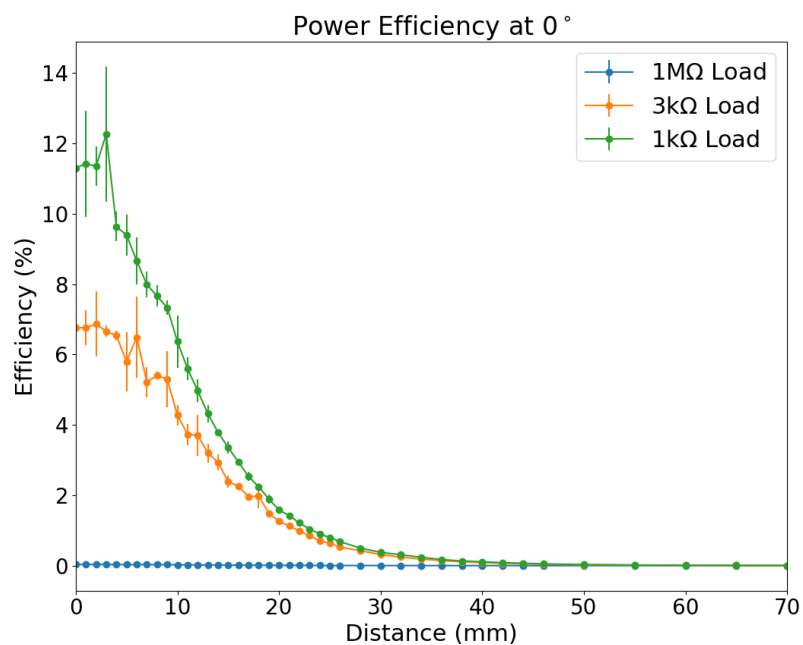


Figure 5.23: Power efficiency at 0°. The primary side root mean square voltage on either side of the sense resistor was measured using an oscilloscope. The power in the secondary was then divided by the power in the primary to get the efficiency. Propagation of errors was performed. Measurements of the primary side voltages were far noisier than the secondary and dominates the errors in the efficiency sweep.

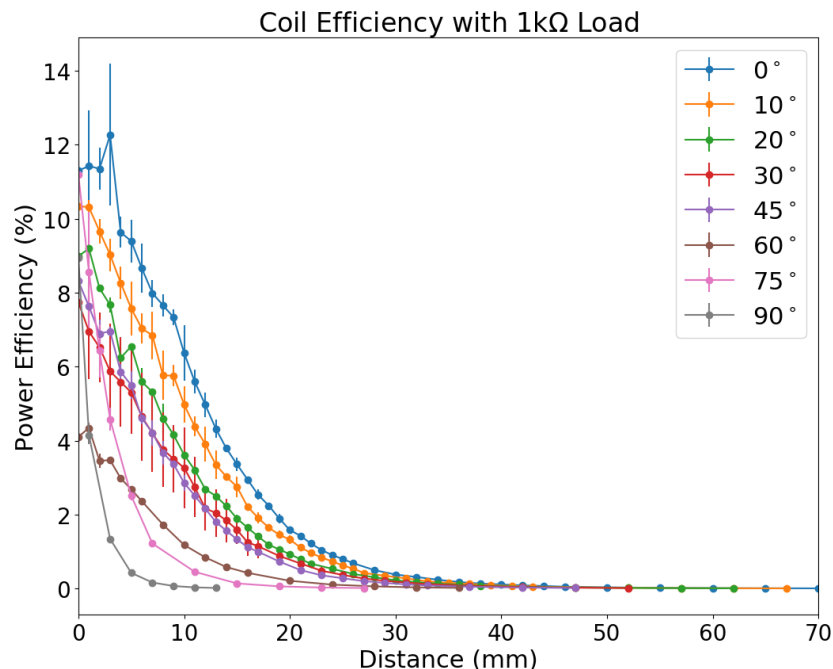


Figure 5.24: Power efficiency with 1k Ω load. Similar to **Figure 5.23**, but here the sweep depends on voltage.

With a 1k Ω load on the secondary, the power transfer efficiency peaks at over 12%. Even at 25mm the efficiency remains around 1%. The primary and secondary coil coupling was sufficient to drive electrolysis at up to 25mm away.

5.4 REFERENCES

- [5.1] "NCR18650GA" (PDF). Panasonic. Retrieved 2 July 2017. (<https://cdn.shopify.com/s/files/1/0674/3651/files/panasonic-ncr18650-ga-spec-sheet.pdf>)
- [5.2] Cook-Chennault K.A., Thambi N., Sastry A.M. "Powering MEMS portable devices— a review of non-regenerative and regenerative power supply systems with special emphasis on piezoelectric energy harvesting systems" *Smart Mater. Struct.* 17 (2008) 043001 (33pp) 10.1088/0964-1726/17/4/043001
- [5.3] Dimroth F., Grave M., Beutel P., Fiedeler U., Karcher C., Tibbits T.N., Oliva E., Siefer G., Schachtner M., Wekkeli A., Bett A.W., Krause R., Piccin M., Blanc N., Drazek C., Guiot E., Ghyselen B., Salvetat T., Tauzin A., Signamarcheix T., Dobrich A., Hannappel T., Schwarzburg K.

“Wafer bonded four-junction GaInP/GaAs//GaInAsP/GaInAs concentrator solar cells with 44.7% efficiency”. *Prog. Photovolt: Res. Appl.*, 22: 277-282. (2014). doi:10.1002/pip.2475

[5.4] A. Molki (2010). "Dust affects solar-cell efficiency". *Physics Education*. **45**: 456–458. Bibcode:2010 PhyEd..45..456M. doi:10.1088/0031-9120/45/5/F03

[5.5] Goto K., Nakagawa T., Nakamura O., Kawata S. "An implantable power supply with an optically rechargeable lithium battery," *IEEE Transactions on Biomedical Engineering*, 48:7, pp. 830-833, (2001). doi: 10.1109/10.930908

[5.6] Kanai H. “Properties of biomaterials (7): Optical properties” (in Japanese), *Jpn. J. Med. Electron. Biol. Eng.*, 15, pp. 48–56, (1977).

[5.7] Goto K., Nakagawa T., Nakamura O., Kawata S. "An implantable power supply with an optically rechargeable lithium battery," in *IEEE Transactions on Biomedical Engineering*, 48:7, pp. 830-833, (2001). doi: 10.1109/10.930908

[5.8] Murali K., Scianmarello N., Humayun M.S. "Harvesting solar energy to power ocular implants," *2015 IEEE Biomedical Circuits and Systems Conference (BioCAS)*, Atlanta, GA, pp.1-4. (2015) doi: 10.1109/BioCAS.2015.7348291

[5.9] VanGeem M. (2019). *ALBEDO OF CONCRETE AND SELECT OTHER MATERIALS*. [online] www.concretepromotion.com. Available at: <http://www.concretepromotion.com/pdf/PCA%20Albedo%20of%20concrete.pdf> [Accessed 11 Apr. 2019].

[5.10] Energystar.gov. (2019). *Learn About Brightness*. [online] Available at: https://www.energystar.gov/products/lighting_fans/light_bulbs/learn_about_brightness [Accessed 11 Apr. 2019].

[5.11] Mathews I., King P.J., Stafford F., Frizzell R. "Performance of III–V Solar Cells as Indoor Light Energy Harvesters" *IEEE Journal of Photovoltaics*, 6:1, pp. 230-235, (2016). doi: 10.1109/JPHOTOV.2015.2487825

- [5.12] Rüfer F, Schröder A, Erb C. "White-to-white corneal diameter: normal values in healthy humans obtained with the Orbscan II topography system." *Cornea*. 24:3.pp.259-61. (2005)
- [5.13] Quallion Medical Batteries. July2016.pdf (in references folder)
- [5.14] petMD, L. (2019). *Eye Inflammation in Rabbits / petMD*. [online] Petmd.com. Available at: https://www.petmd.com/rabbit/conditions/eyes/c_rb_anterior_uveitis?page=show [Accessed 11 Apr. 2019].
- [5.15] Hayakawa M. "Electronic wristwatch with generator," U.S. Patent 5001 685, (1989).
- [5.16] Goto H., Sugiura T., Harada Y., Kazui T. "Feasibility of using the automatic generating system for quartz watches as a leadless pacemaker power source," *Med. Biol. Eng. Comput.*, 37:1, pp.377–380, (1999) doi: 10.1007/BF02513315
- [5.17] Miao P., Mitcheson P., Holmes A., Yeatman E., Green T., Stark B. "MEMS inertial power generators for biomedical applications," *Microsyst.Technol.*, 12:10-11, pp.1079–1083, (2006) doi: 10.1007/s00542-006-0152-9
- [5.18] Olivo J., Carrara S., De Micheli G. "Energy Harvesting and Remote Powering for Implantable Biosensors," in *IEEE Sensors Journal*, 11:7, pp. 1573-1586, (2011) doi: 10.1109/JSEN.2010.2085042
- [5.19] Bahill, A. Terry; Clark, Michael R.; Stark, Lawrence (1975). "The Main Sequence, A Tool for Studying Human Eye Movements". *Mathematical Biosciences*. **24** (3–4): 191. doi: 10.1016/0025-5564(75)90075-9
- [5.20] Fulton, James T., Processes in Biological Vision {online} {Corona Del Mar, CA. USA} Vision Concepts, {published 2000-08-01}, {revised 2000-08-01},{cited 2000-08-01}. Available on the Internet: URL:<http://neuronresearch.net/vision/>
- [5.21] Mit.edu. (2019). *Gold*. [online] Available at: <http://www.mit.edu/~6.777/matprops/gold.htm> [Accessed 11 Apr. 2019].

CHAPTER 6 – FABRICATION

Fabrication techniques and materials used to make the devices are discussed, along with the different versions of the oxygenator.

6.1 BIOCOMPATIBLE MATERIALS

6.1.1 SILICONE

Silicones are a series of siloxane backed polymers with a functional group attached. They are elastomers with good heat resistance, and low chemical reactivity. Silicones begin as a highly viscous liquid, which cures into a solid. There are three methods to polymerize silicone: platinum-based, condensation, and peroxide cures. The acetoxy cure system is common in silicone caulking. Most medical grade silicones are based on a platinum cure, since the process produces no byproducts.

Platinum cure silicones are two component silicones: a part A that contains silicones with vinyl groups and a platinum catalyst, and a part B with similar vinyl grouped silicones and a hydrogen cross-linker [6.1]. The process is an addition chemistry, where the cross-linker and vinyl groups result in an ethylene bridge (double carbon bond). The resultant silicone is biocompatible because the process does not produce byproducts and pure silicone is relatively chemically inert. Silicone has a high elasticity and a low Young's modulus, which makes silicone a good material for medical applications. The compliance of silicone approaches that of the human body better than harder materials such as steel or glass. For these reason, silicone has made its way into all sorts of medical implants, where mechanical compliance is important. Cochlear implant uses silicone to sheath its platinum electrodes, cables and transmitter coil [6.2]. Silicones also have high gas and water vapor permeability, making them ideal for the semipermeable membrane used in this thesis.

Processing silicone is a well understood process with soft lithography of poly(dimethylsiloxane) (also called PDMS) being a common process in microfluidics. The techniques involve pouring and curing PDMS over a mold (pattern) and peeling it afterwards. The PDMS part can then be bonded to another PDMS part or to a substrate. Bonding to itself is generally done by using different mixtures of part A and part B, where each piece would have an excess of a different part. PDMS can also be bonded to substrates like glass using oxygen plasma to make both the glass and the PDMS hydrophilic. Manufacturing techniques for silicone parts will be discussed further below.

Silicone NuSil MED4-4210 was predominantly used in the devices, as it is considered a medical grade material and was used successfully in animal implants. These facts reduced biocompatibility concerns in the experiments with rabbits.

Manufacturing techniques for silicone parts will be discussed further below.

6.1.2 PARYLENE

Parylene is a name for polymer called poly(p-xylylene). There are several different Parylene polymers (**Figure 6.1**), all of which contain a phenyl (6 carbon) ring connected to a carbon atom as the monomer. Each Parylene type contains different elements attached to the basic carbon structure.

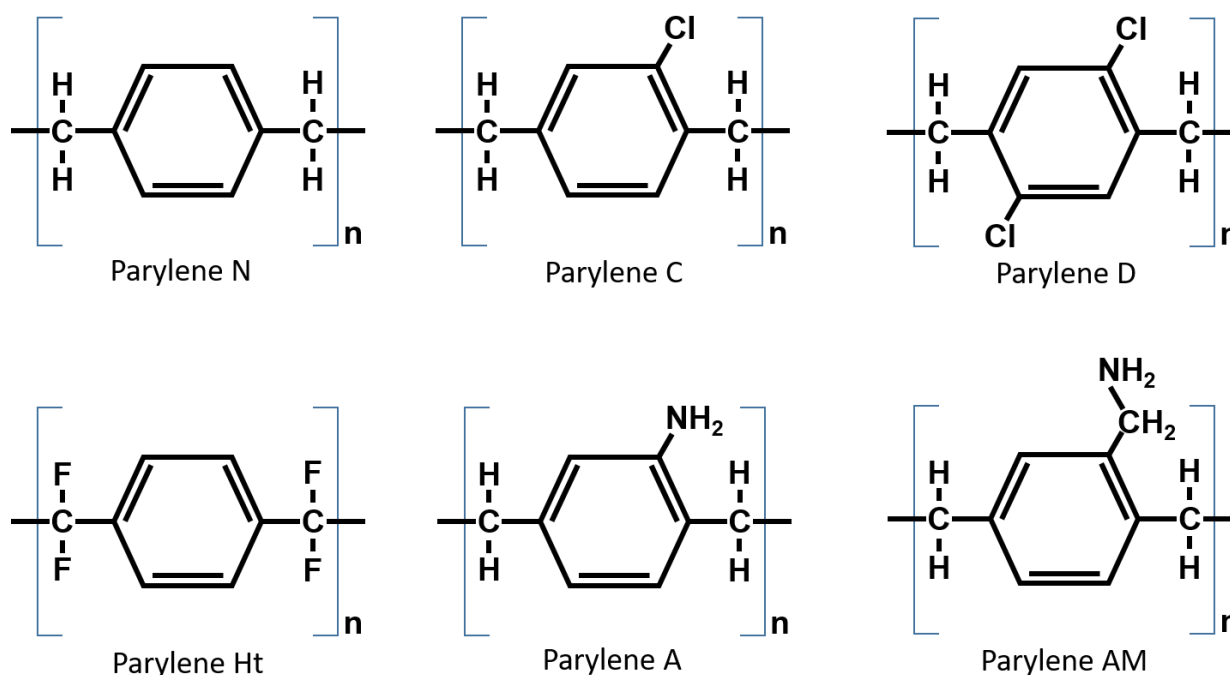


Figure 6.1: Poly(p-xylylene) chemical structures. Parylene-C is the most commonly deposited polymer with low gas and moisture impermeability. Parylene D has better barrier properties but general has worse film uniformity. Parylene Ht is a fluorinated parylene with good high temperature properties. Parylene A and AM contain an amine group making them slightly hydrophilic and more reactive than other parylenes.

Parylene is applied to substances by chemical vapor deposition, in which the Parylene dimer is decomposed into a monomer in a Pyrolysis tube at high temperature (690°C for Parylene-C) and then deposited onto a substrate downstream. The polymer is coated at vacuum in specialized CVD machines, such as the ubiquitous Specialty Coating Systems™ PDS2010, and the Specialty Coating Systems™ PDS2035. These machines have 4 parts: a vaporizer chamber, where the dimer

sublimates at temperatures between 120°C and 180°C, a pyrolysis tube, where the dimer is cleaved into a polymer, a deposition chamber, where the monomer polymerizes at ambient temperature onto the target device, and a cold trap that collects any remaining monomer to protect the downstream mechanical vacuum pump (**Figure 6.2**).

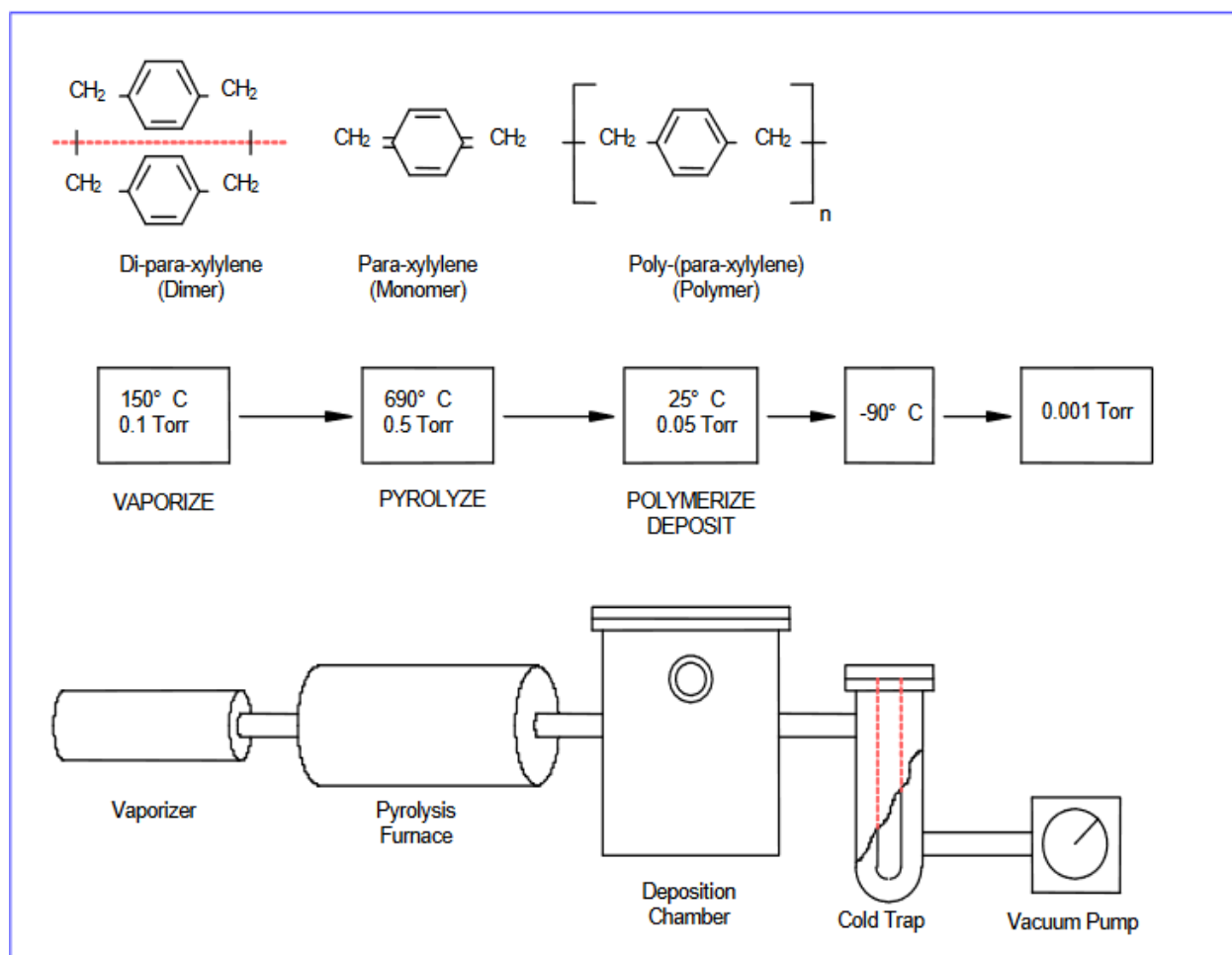


Figure 6.2: Parylene deposition process; reprinted from PDS 2010 Owner's Manual.[6.3].

This vacuum process conformally coats the polymer onto surfaces with very few, if any, defects. The resultant defect-free polymer coat is used as a barrier material for electronics due to its low gas permeability (0.042Ba for O₂ for Parylene-C) and low moisture (WTVR 0.08g·mm·m⁻²·day⁻¹) permeability [6.4], [6.5], [6.6]. The polymer is very chemically inert and biocompatible (USP rating class VI [6.7]). These properties make the material ideal for medical use and for the oxygenator.

6.1.3 USE OF PARYLENE AND SILICONE IN A DEVICE

In the devices, Parylene was used to protect electronics from water ingress and to restrict oxygen permeation. Silicone was used for the semipermeable membrane to allow for transport of oxygen while leaving the salts in solution. **Figure 6.3** shows that a 5 μ m Parylene-C coat on one side of a diffusor greatly reduces the oxygen readings on that side.

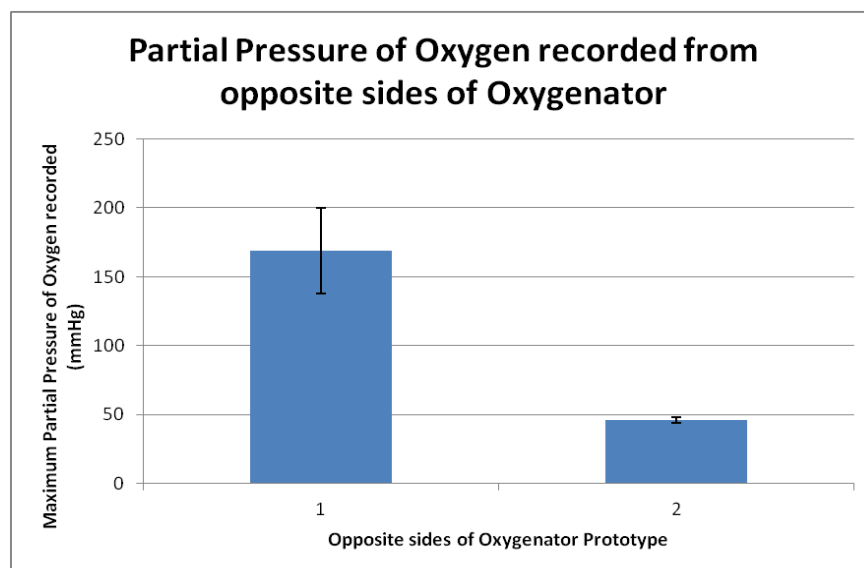


Figure 6.3: Oxygen tension on opposite sides of a device coated with parylene on one side. 5 μ m Parylene-C coated on side 2 of the device. Side 1 is only comprised of silicone. An oxygen probe was placed against the device in anoxic deionized water.

However, Parylene is difficult to bond to given its chemical inertness. The fact that silicone does not bond to Parylene allows to use it as a mold release on micropatterned molds for silicone. However, when Parylene is deposited on silicone, it forms a strong bond (see below). It is reported that Parylene-C penetrates several microns into PDMS, with a peel force of 1.4N for an 8mm wide Parylene-C film [6.8]. This mechanical bond in which Parylene “caulks” silicone lowers silicone’s gas permeability.

6.2 MOLD FABRICATION

6.2.1 NEGATIVE EPOXIDE PHOTORESIST: MICROCHEM SU-8

Su-8 is an epoxy-based negative photoresist. The material is made of a base chain with an average of 8 epoxy groups. When exposed to ultraviolet light (I-line 365nm), the triarylsulfonium salt in the Su-8 resin produces an acid, which under the heat, catalyzes the cross linking reaction between Su-

8 molecules. To make a mold with it, the photoresist must be spun, soft baked, exposed, post exposure baked (PEB), and finally developed.

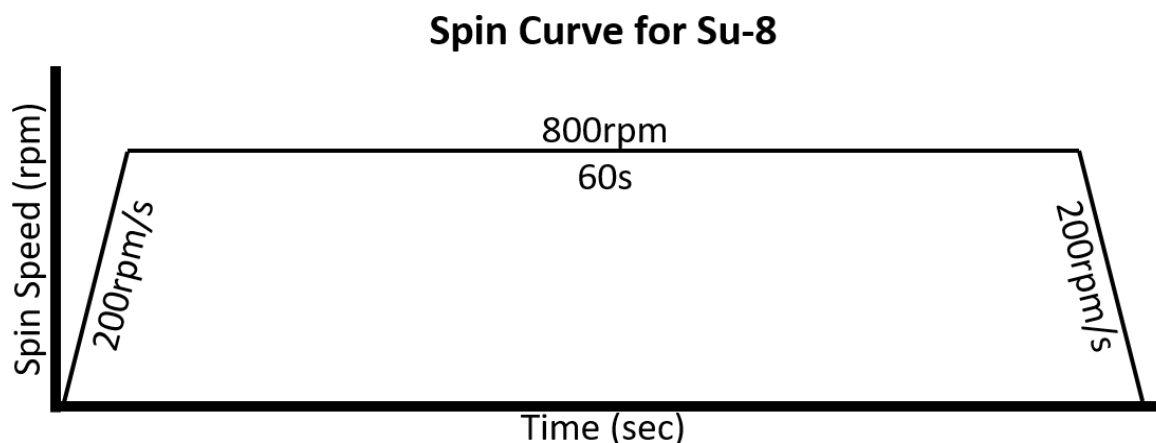


Figure 6.4: Su-8 Spin curve. Pour Su-8 over two-thirds of the area of the wafer. This spin curve results in 150 μ m for Su-8 100 and approximately 50 μ m for Su-8 50.

Before spinning SU-8 50 or Su-8 100, which are quite viscous, the photoresist must be poured on the wafer, and allowed to spread to over two-thirds of the wafer's surface area. This is done to prevent streaking. The spin curve for Su-8 100 results in a 150 μ m thick layer, and for Su-8 50, it results in a 50 μ m thick layer (**Figure 6.4**). Su-8 may be spun twice with a partial soft bake in between to achieve up to 300 micron thickness; if much thicker than this leaves the material is susceptible to cracking due to thermal expansion differences with the underlying silicon substrate.

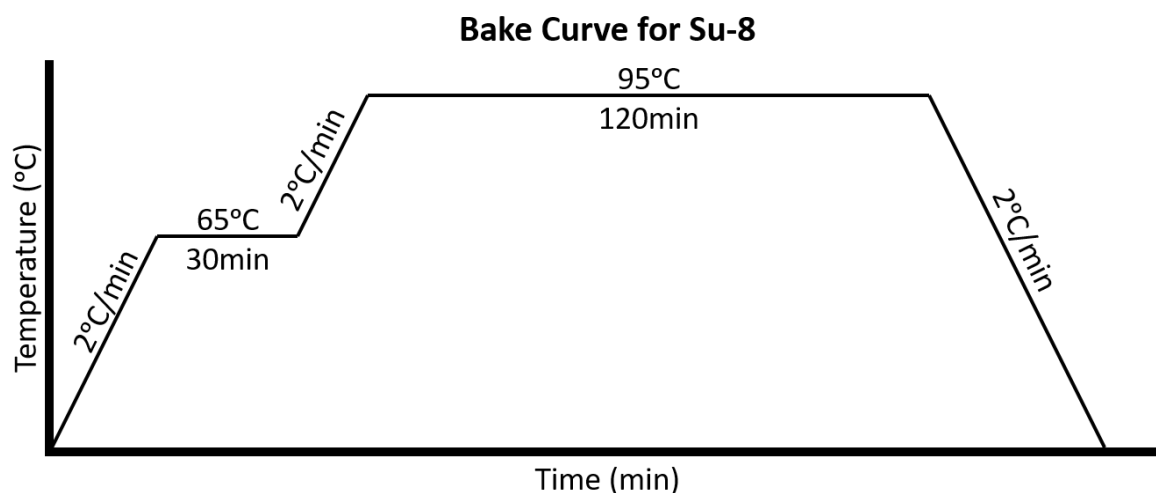


Figure 6.5: Hotplate temperature curve for Su-8 soft baking and post-exposure baking. The soak times at 65°C and 95°C in the curve are soft baking for 2x150 μ m layers. The post-exposure bake for the same thickness is 30 minutes at 65°C and 30 minutes at 95°C.

The ramp-up in heating processes for both soft and hard baking must be sufficiently slow that the entire thickness equilibrates to reduce the stress build up in the material. This is even more important in the hard baking stage, as there is significantly less solvent present than in soft baking. The ramp curve is given in **Figure 6.5**, noting that the dwell times at 65°C and 95°C are dependent on layer thickness. Baking times increase with the square of the increase in thickness.

For a 300µm thick Su-8 layer, the exposure time is 140 seconds (3.4mW/cm² at 400nm, and 1.5mW/cm² at 365nm). However, this exposure imparts significant heat to the photoresist, which can result in cracking. For this reason, the exposure is split into 40 second intervals with 1 minute rests between exposures to allow the Su-8 photoresist to cool.

Wafer development is done with MicroChem's Su-8 developer, and takes 20 minutes with heavy agitation. Within the last minute, the wafer should be placed into fresh solution to rinse out any partially dissolved Su-8 gunk. The wafer should then be soaked in isopropyl alcohol, before a rinsing in deionized water.

Multilayer patterns can be made through repetition of spinning, soft backing, developing and PEB (skipping the development step). In doing so, care must be taken with the patterns such that each subsequent mask does not expose an area that was previously left unexposed. The dimensions of the oxygenator's reservoir exceeded the thickness limit of less than 500µm that can be easily achieved with the Su-8 process.

6.2.2 DRY-FILM PHOTORESIST PATTERNING: DUPONT WBR2120

DuPont's WBR™ 200 series of microlithographic polymer films were the solution to the mold limitations. These films were manufactured to be deformable to allow patterning over device bumps and vias, while minimizing the air trapped beneath them. This means that the material was soft enough to not crack, when laminated over a non-flat surface. This flexibility of the material means it may allow for much thicker laminations with reduced stress build up and cracking.

The material was developed for in-via and mushroom electroplating bumping, photo stenciling, and etching applications. It is available in 50µm, 75µm, 100µm, and 120µm thicknesses, the 120µm is the most amenable for 1mm thick molds with the fewest layers.

Optimization of this polymer film lithography was conducted with Dr. Jun Park. Using a General Binding Corporation Model No. Eagle 35 laminator, the optimal settings were found to be a travel speed of 3.8mm/s (speed of 1), with a roller temperature of 95°C. For a silicon wafer, a roller separation of 1 (as marked by the machine) gave the best adherence. For best adhesion, the wafer should be cleaned with piranha solution to remove any organic contaminants from the surface. However, the polymer film adheres better to itself than to silicon. The substrate for any lithography should be a blank layer of the film, which is exposed and post-exposure baked. To prevent the photoresist from sticking to the masks, all masks were pre-coated with 5µm of Parylene-C before being used. This allows the wafers to separate from the masks with ease and maintain a glassy surface finish on the polymer. Using the protective polyester cover film to prevent adhesion between wafers and masks results in a matte surface finish.

To act as a mold, this polymer film must be coated with a layer that isolates it from the silicone. The platinum catalyzed silicones does not cure properly on the photoresist. A layer of Parylene-C, which is very chemically inert, acted as a separating layer and aided demolding any patterns.

In the following procedure, the lithographic polymer film will be referred to as dry-film photoresist

1. Laminate 1 layer of the dry-film photoresist onto a clean wafer. Using a razor blade parallel to the edge of the wafer, cut away all excess film adhering the wafer to the paper substrate used to feed through the laminator.
2. Expose this first layer using a blank mask to create a substrate for all subsequent patterns. After exposing, the polyester film covering the resist must now be removed before heating. Failure to do so will cause ripples to form on the photoresist and the coefficients of thermal expansion between the polyester and photoresist are different.
3. Laminate subsequent layers of photoresist, comprising the first mask. Multiple layers can be exposed at once. This was successfully tested with up 6 layers (720µm) at the same time.
4. The layers are exposed together, with the optimal exposure time being tabulated in **Table 6.1**.

5. The wafer is post-exposure baked on a hotplate at 95°C for 1 minute. This allows crosslinking to occur in the exposed polymer.
6. If the device requires more masks, lamination is repeated once again. After the polyester film is removed, and before alignment and exposure, Sodium hydroxide developer, such as AZ340, is applied with an eye dropper over the alignment patterns. Doing so increases the contrast of any alignment patterns.
7. The wafer can then be aligned to the mask and exposed.
8. This procedure can be repeated for any set of masks required, though if the process exceeds 1mm in height, the bowing of the silicon wafer becomes significant. As the dry-film photoresist is laminated at an elevated temperature, when cooled to room temperature, the film applies a stress to the underlying silicone which has a different coefficient of thermal expansion. Two solutions are to include stress release lines between devices, or use a thick pane of glass as a substrate in place of a wafer for thick laminations.
9. After all exposures are complete, the wafer can be baked as a hybrid post-exposure baking and soft baking process at 65°C for 20 minutes to 1 hour in a convection oven, depending on the number of layers. This is then allowed to cool slowly to room temperature at a slower than 5°C/min.
10. The wafer can then be developed in a dilute sodium hydroxide solution, 1 part AZ340 to 4 parts deionized water, with constant agitation. This development process can take up to 30 minutes.
11. The molds then receive a 5µm coat of Parylene-C. This coat both allows silicone to properly cure within the mold, by isolating the silicone from the dry film, and allows the silicone to de-adhere easily from the mold. For fine features the coating must be considered in the masks, which should be made larger to account for it.

Table 6.1: Exposure time for DuPont WBR2120 under $6.47\text{mW}/\text{cm}^2$ at 365nm and $13.8\text{mW}/\text{cm}^2$ at 400nm

| NUMBER OF LAYERS EXPOSED | EXPOSURE TIME (S) |
|--------------------------|-------------------|
| 1 LAYER | 60 |
| 2 LAYER | 80 |
| 3 LAYER | 100 |

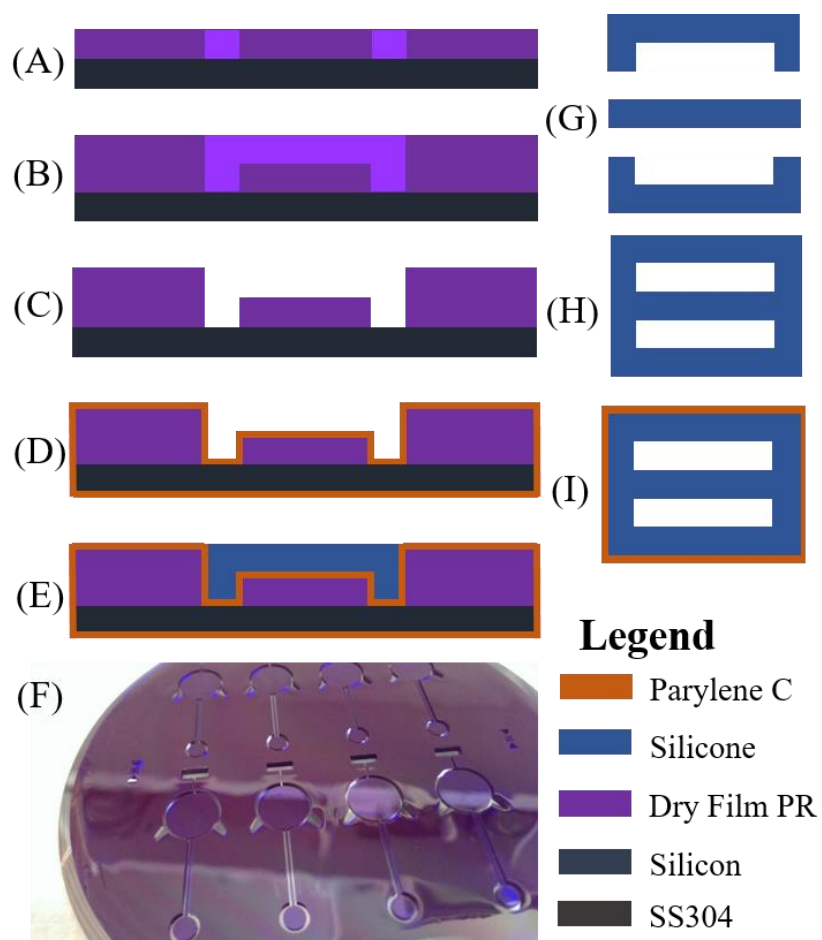


Figure 6.6: DuPont WBR2120 dry film fabrication process. (A) Laminate WBR2120 to the desired thickness and expose. (B) Repeat and expose the second layer. (C) Develop using 1:4 AZ340:DI water. (D) Parylene Coat. (E) Pour and degas silicone. (F) Example of a completed mold for version 0 of the device. (G) Three sections are demolded. (H) They are joined by uncured silicone. (I) The cured shape is coated in Parylene-C.

6.3 SILICONE CASTING

Negative photoresists require exposure to light to cure. If a pattern has two layers, and the top mask exposes a region that is unexposed on the lower layer, that region on the lower layer will be cured as well, and will not dissolve in the developer. However, if the top mask exposes a region in the lower layer, there is no change to that lower region. Therefore, to preserve the patterns exposed into the

lower layer, the upper layer can only expose regions that have already been exposed in the lower layer. Any enclosed shape will have exposed areas in the middle layer that are unexposed in the bottom layer. As this cannot occur with a negative photoresist, any enclosed shape must be built in two parts (**Figure 6.6**).

With completed molds, the next process is silicone casting. The silicone is thoroughly mixed for 5 minutes at a 10 to 1 mixture of part A to part B of NuSil MED4-4210. The silicone is then poured and spread over the entirety of the wafer. It is important to make sure that every device is completely covered with the silicone. As the mixing process traps bubbles, the mold is placed in a vacuum chamber to degas fully. After no bubbles were visible, the mold is removed from the vacuum chamber and a fresh razor blade is dragged across the surface to remove excess silicone. If performed properly, no cleanup of the flashing should be required after during. The mold is placed into the vacuum chamber for another 15 minutes to allow the silicone to settle and remove any air that was trapped during scraping process. Finally, the mold is cured in a convection oven at 110°C for 5 minutes, which only partially cures the silicone to the point at which it can be handled.

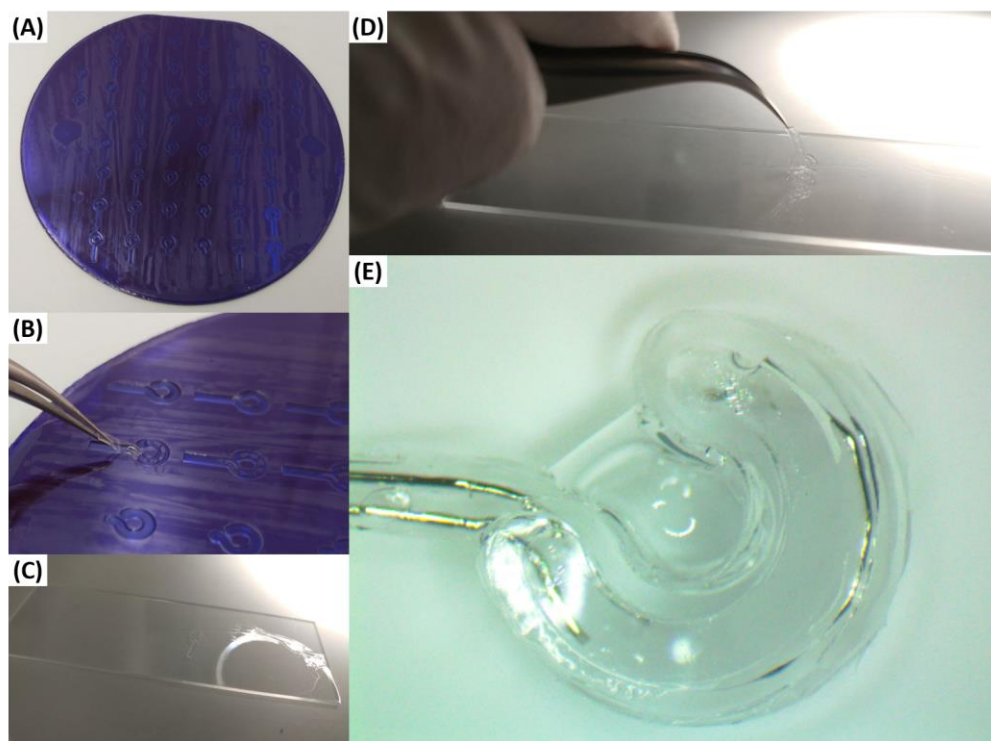


Figure 6.7: Silicone molding process using dry film mold. (A) WBR-2120 mold after silicone is cured into shape. (B) Demolding with a tweezer. (C) Uncured silicone spread over a clean glass slide with silicone part pressed against slide. (D) Peeling silicone part from uncured silicone. (E) Assembled diffuser.

The silicone parts can be demolded by grabbing their cast handles with tweezers and peeling with care, as shown in **Figure 6.7**. These shapes can be glued together using uncured silicone to construct more complex devices and enclosed pieces.

6.3.1 MAKING AN ENCLOSED SHAPE

The demolded silicone parts do not enclose anything due to limitations of the negative photoresist process. Therefore, the silicone parts must be bonded to a substrate or another part to make enclosed structures such as bags, microchannels, or other complex shapes.

A common approach is to treat the silicone surface with oxygen plasma and bond two treated surfaces together. If the two pieces are brought in contact quickly after the treatment, the bond is resilient. This approach was used to create the electrolysis test device of section 4.2. There are two drawbacks with this technique. The first is that it offers a limited alignment time, meaning complex devices are difficult to reliability assemble. The parts bond soon after being brought into contact, so repositioning is not possible without hurting bond strength. The second drawback is that the bond is weaker than the silicone itself and generally separates before the silicone tears. Furthermore, the bond strength is dependent on the time exposed to atmosphere between plasma treatment and bonding. Therefore the bond strength can be very variable.

Uncured silicone was used to bond parts together. Silicone would be mixed as per specification and thoroughly degassed. Once degassed, the silicone would be spread thin over a glass slide using a razor blade. The partially cured silicone parts would then be pressed against this thin layer of uncured silicone. After this the wetted sides can be aligned under a microscope until satisfied and then partially cured for 5 minutes at 110°C in a convection oven. This procedure can be repeated for an arbitrary number of parts allowing complex shapes to be built up.

There is a concern with any enclosed shapes. As a part is cured at a high temperature, any trapped air in between silicone pieces that have yet to cure will attempt to escape through the seam. This can cause unpredictable holes in any part. There are two solutions to this: to lower the temperature and increase the duration of the curing process, or, if the design permits, to add a vent hole to be filled in at a later time. The vent hole gives the design a predictable flaw that can be remedied afterwards by adding silicone onto a preheated part. Heating the part on a hot plate reduces the temperature

difference between it and the oven, meaning the uncured silicone sealing over the part will not get pushed out by the internal pressure.

Concerns about the strength of this bond (partially cured silicone glued with uncured silicone) was tested two ways. The first involved spinning a thin sheet of silicone on a wafer (1krpm on a spinner for 1 minute with a ramp rate of 300rpm/s), and partially curing it for 3 minutes at 110°C in a convection oven. The silicone was then removed from the oven and a 5mm wide section was removed from the sheet. Uncured silicone was poured in its place, degassed, and then the entire sheet was fully cured at 150°C for 90 minutes. Samples were cut from the sheet such that they were centered on the 5mm wide new silicone. The stress-strain curves for the samples were measured on a TA Instruments DMA Q800 (**Figure 6.8**). The slope over different strains was extracted and compared to a control sample which had no silicone replaced from it. The statistic over 10%-20% strain was 1.4, falling short of the two-tailed critical value, 2.7, for $\alpha = 0.05$, and over 40%-60% strain it was 0.88 falling short of 3.18 for the same alpha. This means the control and test populations are not statistically different.

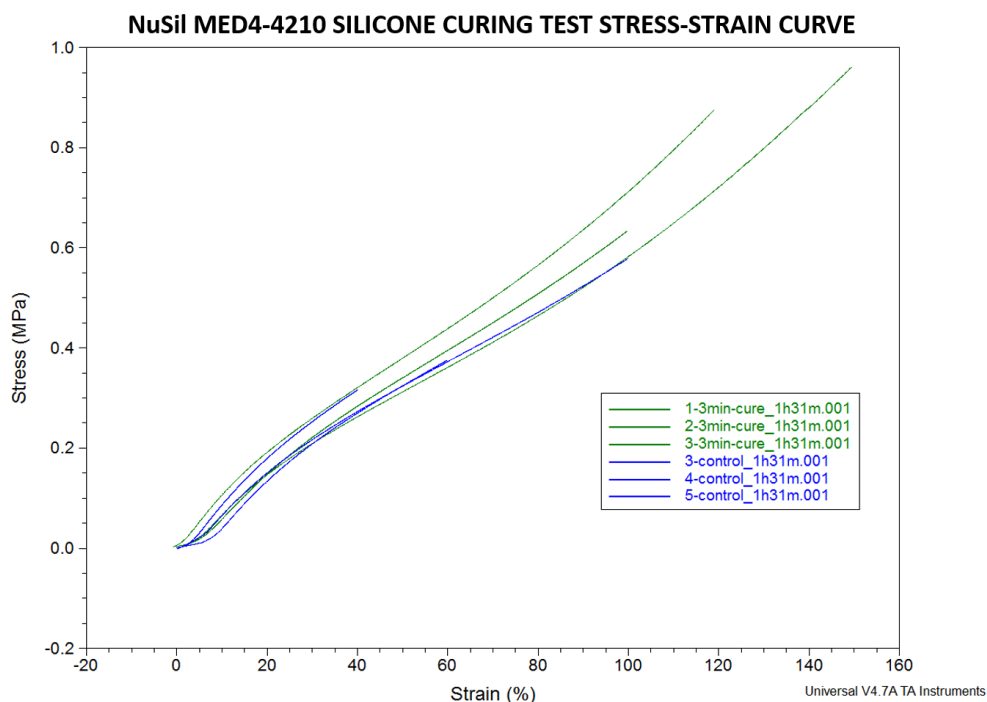


Figure 6.8: NuSil MED4-4210 silicone curing test. Uncured silicone was spun at 1krpm on a Parylene-C coated wafer. The silicone was cured for 3 minutes, after which point a section was removed from the now partially cured silicone sheet and uncured silicone was put in its place. **Table 6.2** contains the slopes of the curves plotted here over two strain regions (10%-20%, and 40%-60%).

Table 6.2: Slopes for silicone curing test. Three samples are stretched for each group. The bold values are the test statistic for each sections in the curve. Both test statistics are smaller than their two-tailed critical value.

| SLOPE (MPA/%) FROM 10%-20% STRAIN | | SLOPE (MPA/%) FROM 40%- 60% STRAIN | |
|--------------------------------------|--------------|---------------------------------------|--------------|
| CONTROL | 3 MIN CURING | CONTROL | 3 MIN CURING |
| 0.9282 | 0.9011 | | 0.559 |
| 0.9528 | 0.8478 | 0.5299 | 0.5876 |
| 0.8505 | 0.804 | 0.4958 | 0.4929 |
| 1.427761424 | | 0.877012037 | |

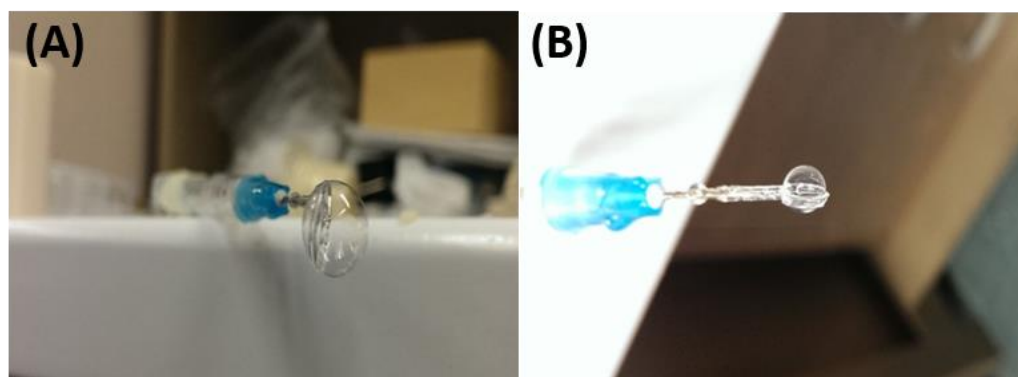
The second test checked how air tight the samples are, by inflating a flat disk of silicone. The silicone was cast in two halves and joined along the edge. A 30Ga needle was then epoxied onto the bag, which was then inflated using Nitrogen gas. As the bag was inflated, both the pressure and size of the bag where measured (**Figure 6.9**). As the seam along the edge makes difficult the calculation of the exact strain on the joint, the test demonstrates that only air tight designs can be built, which can withstand 100kPa. A conservative estimate on the force on the seam can be attained by:

$$F = \pi r^2 P \quad (6.1)$$

where r is the initial radius along the seam. At 100kPa, the force is 0.38N along the seam. No failures were observed along the seam. The stress averaged across the area of the seam is given by:

$$\sigma = \frac{\pi r^2 P}{((r + t)^2 - r^2)\pi} \quad (6.2)$$

which results in a stress of 300kPa. The bond strength is therefore at least a tenth the breaking strength of cast silicone, and such a shape is air-tight and can withstand a pressure of 1atm above atmosphere.



Silicone Bag During Inflation

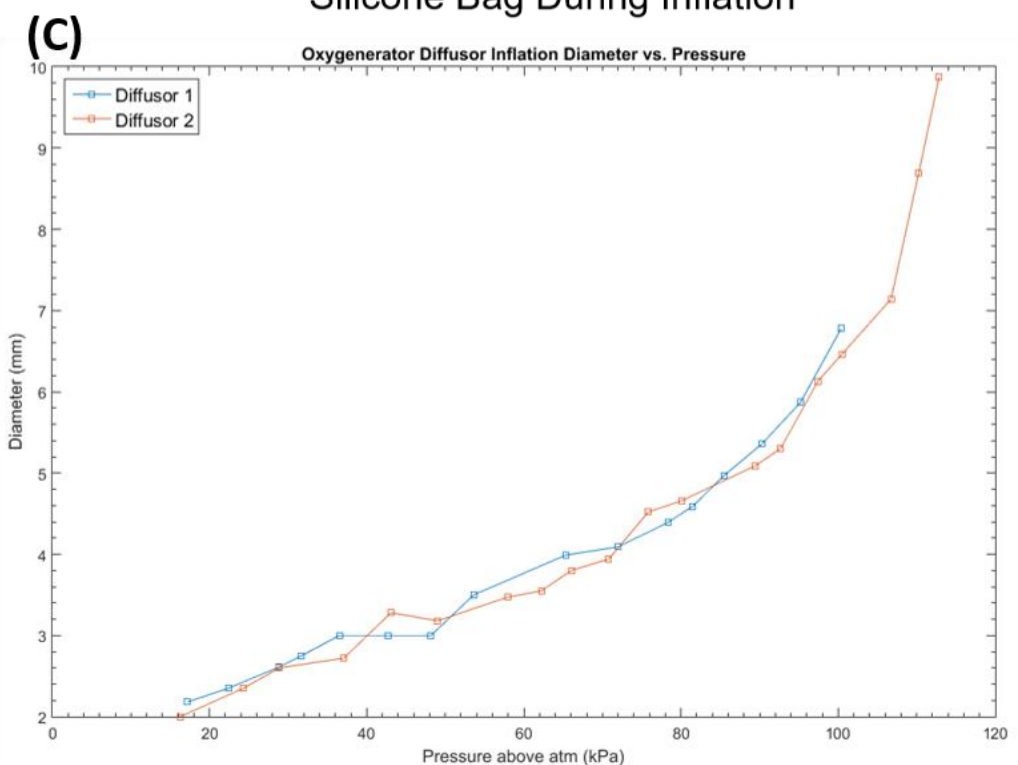


Figure 6.9: Silicone bag resilience. A 3mm in diameter silicone disk shaped diffusor is epoxied to a 23Ga needle. The diffusor has an inner diameter of 2.2mm with a 0.4mm wide sidewall. The seam lies midway along the sidewall. (A-B) Calipers were used to measure the inflated height of the disk. The disk was inflated with nitrogen gas, whose pressure was recorded. (C) Plot of pressure versus height of the diffusor. This test was repeated for two separate diffusers.

6.3.2 PARYLENE ON SILICONE RESERVOIR

While the earlier inflation test demonstrates the strength of the seam, a large change in reservoir volume would subject the eye to increased intraocular pressure. To reduce the expansion of the reservoir under the pressure of electrolysis, Parylene-C may be coated. This has the added benefit of reducing gas permeability of the reservoir, so increasing the efficiency of the diffusor. To test this

idea a device reservoir was coated with parylene and inflated nitrogen gas through an epoxied needle. This was done for both the reservoir and the diffusor, and compared to an uncoated device (**Figure 6.10**).

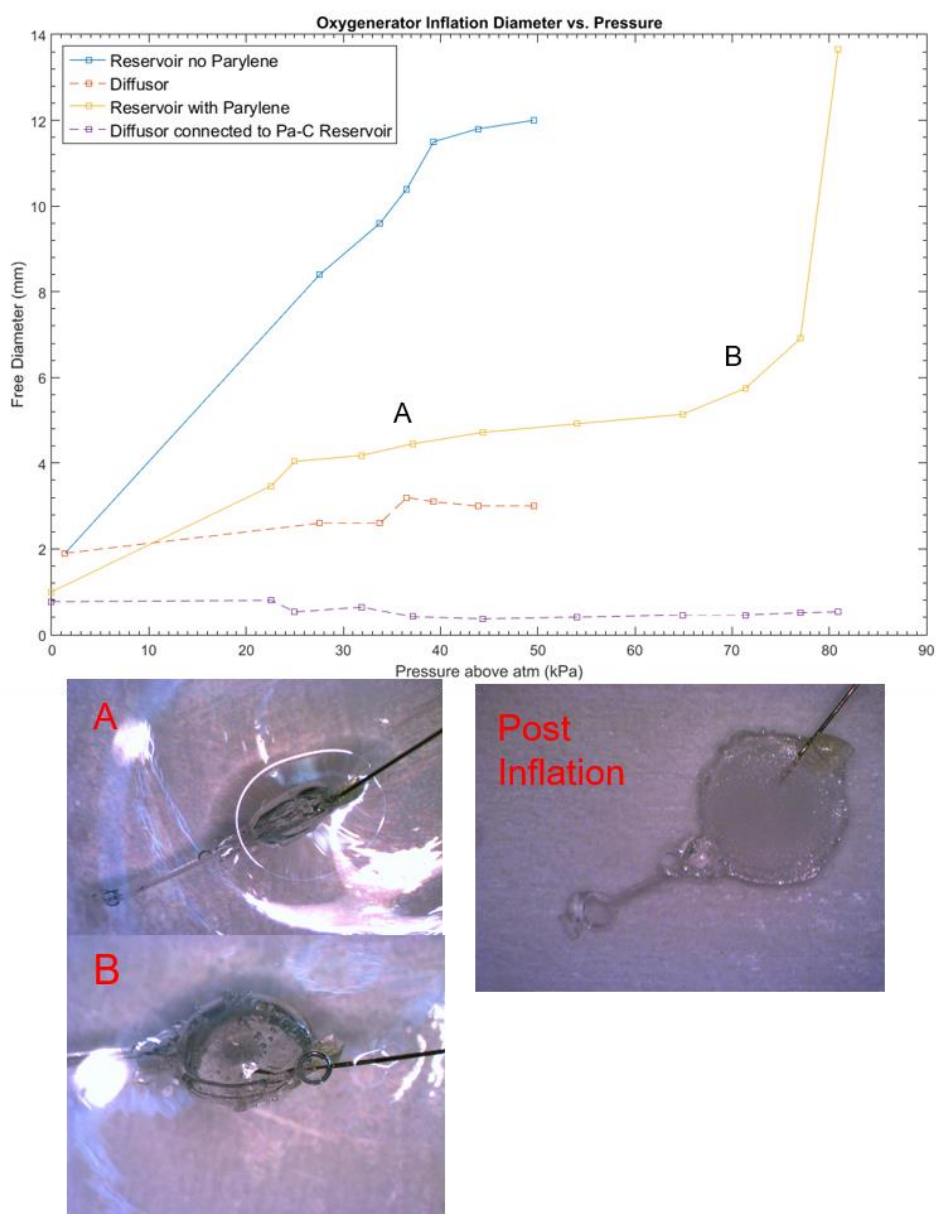


Figure 6.10: Parylene coated silicone bag resilience. Points (A) and (B) show the inflation of the Parylene coated device at 37kPa above atmosphere and 72kPa above atmosphere. After inflating the device, above 65kPa bubbles are observed exiting the silicone, which are the result of the Parylene coating cracking.

From the plot in **Figure 6.10**, it is clear that Parylene does have the desired effect. With a central pillar anchoring both surfaces, the initial volume change is reduced even further. Here the coating is

seen to work until 65kPa, at which point Parylene-C has been strained beyond its breaking point. After this the curve rises steeply as the Parylene coating is no longer restricting the silicone from expanding. Given that 65kPa above atmosphere equates to 421mmHg O₂, far above the desired oxygen tension in the device, this limit on maximum pressure is acceptable. Note, the diffuser did not experience any meaningful expansion whether coated or uncoated, even though it had an open gas channel connecting it to the reservoir. As expansion of the diffuser is unlikely to occur and to cause a significant rise in intraocular pressure.

The test also demonstrates that a Parylene coating on silicone is resilient, as the Parylene cracks before it delaminates from the silicone.

6.3.3 FUSED DEPOSITION PRINTING OF RESERVOIR MOLDS

The reservoir of the device sits on the sclera, which is a curved surface approximating a sphere of 24mm in diameter. Therefore, a curved reservoir would conform better to the sclera and make it easier for the conjunctiva to cover the device. However, while lithography allows tall, high accuracy molds to be fabricated with ease, they are planar. It is difficult to induce a curve into a lithographic mold, and lithography over a 3 dimensional surface is challenging.

It is much easier to use 3D printing technology to design an out enclosure for the reservoir electronics that has smooth curves. A stainless steel ball bearing with the same diameter as the eye provides the appropriate shape for the back surface.

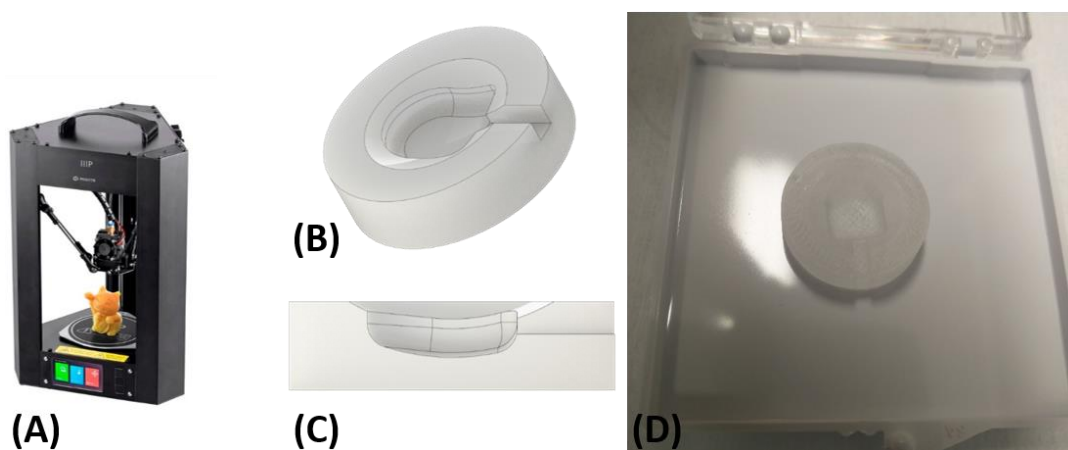


Figure 6.11: FDM 3-D printing molds. (A) Monoprice MP Mini Delta printer. (B) SolidWorks model of the reservoir mold. (C) Cross section of the mold. (D) 3D printed mold out of ABS plastic with a 0.05mm z-layer height.

The molds were designed with SolidWorks CAD software, and printed with Monoprice MP Mini Delta fused deposition modeling (FDM) 3D printer (**Figure 6.11**). The mold was printed at 100% infill, and 0.05mm z-layer height out of clear acrylonitrile butadiene styrene (ABS). To prevent loss of features, no smoothing was done to the mold. To release the silicone from the mold, Mann Release Technologies Ease Release 200 was applied to both the mold and steel ball bearing before casting silicone.

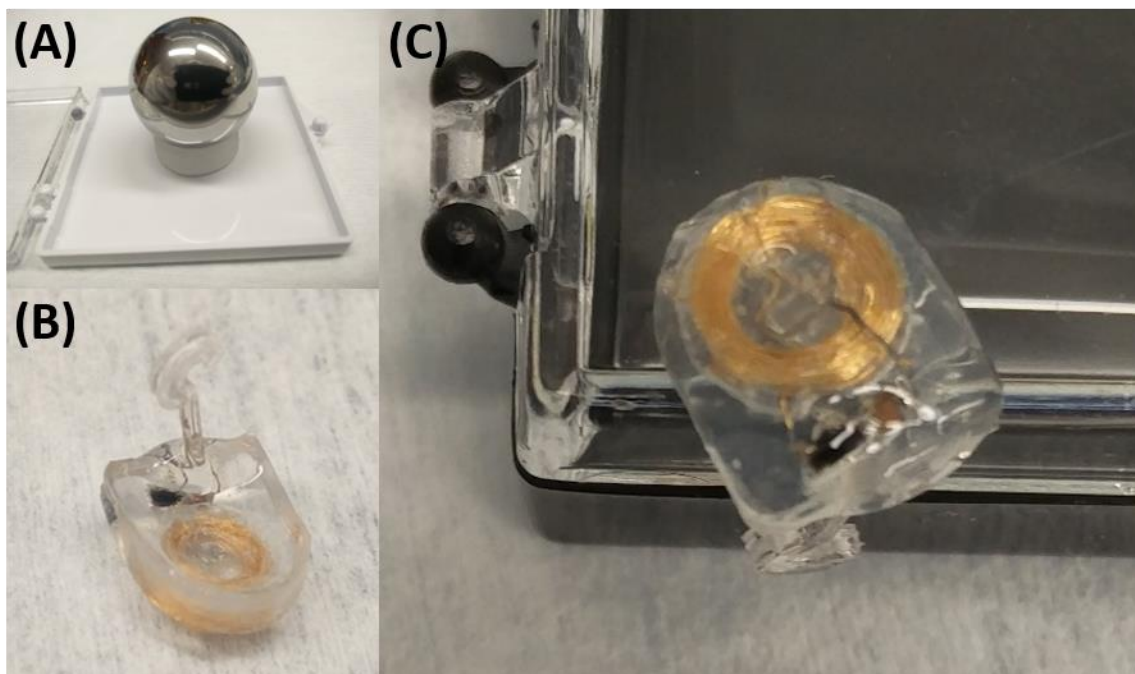


Figure 6.12: 3D molded silicone device. (A) Stainless steel ball pressing against mold to form lower side of the device. (B) The curvature from this ball is visible on the underside of the device (version 8). (C) Top side of the device.

A thin layer of silicone was painted onto the surface of the mold, vacuum degassed, and cured at 85°C for 20 minutes. The electronics can then be placed into the mold with care to make sure the electrodes are fed through the groove in the mold. The mold is filled to the brim with silicone and degassed fully. Once no more air bubbles appear, the ball bearing is pressed into the mold until it seats properly against the mold (**Figure 6.12**). Any squeeze out is wiped off with a Texwipe paper towel, before the mold is fully cured at 85°C for 3 hours.

Once the mold is taken out from the oven, the ball is carefully removed, and a tweezer is used to peel the oxygenator from the mold. Dipping the oxygenator in 2 parts hexane to 1 part silicone, smooths the visible grooves from the 3D printed layers. This is left at atmospheric temperature and

pressure for 2 hours after the dip coat to allow the hexane to fully evaporate. The device can then be fully cured at 150°C for 2 hours. The final result is a complex 3D shape as seen in **Figure 6.12bc**.

6.4 DEVICE ITERATIONS AND CONSIDERATIONS

The device has gone through 9 iterations. Each iteration shrunk the footprint and increased reliability or made the device more amenable to implant. The diffuser and the reservoir are built separately and combined after the reservoir was coated with Parylene. Differences between each iteration are covered in **Figure 6.13**.

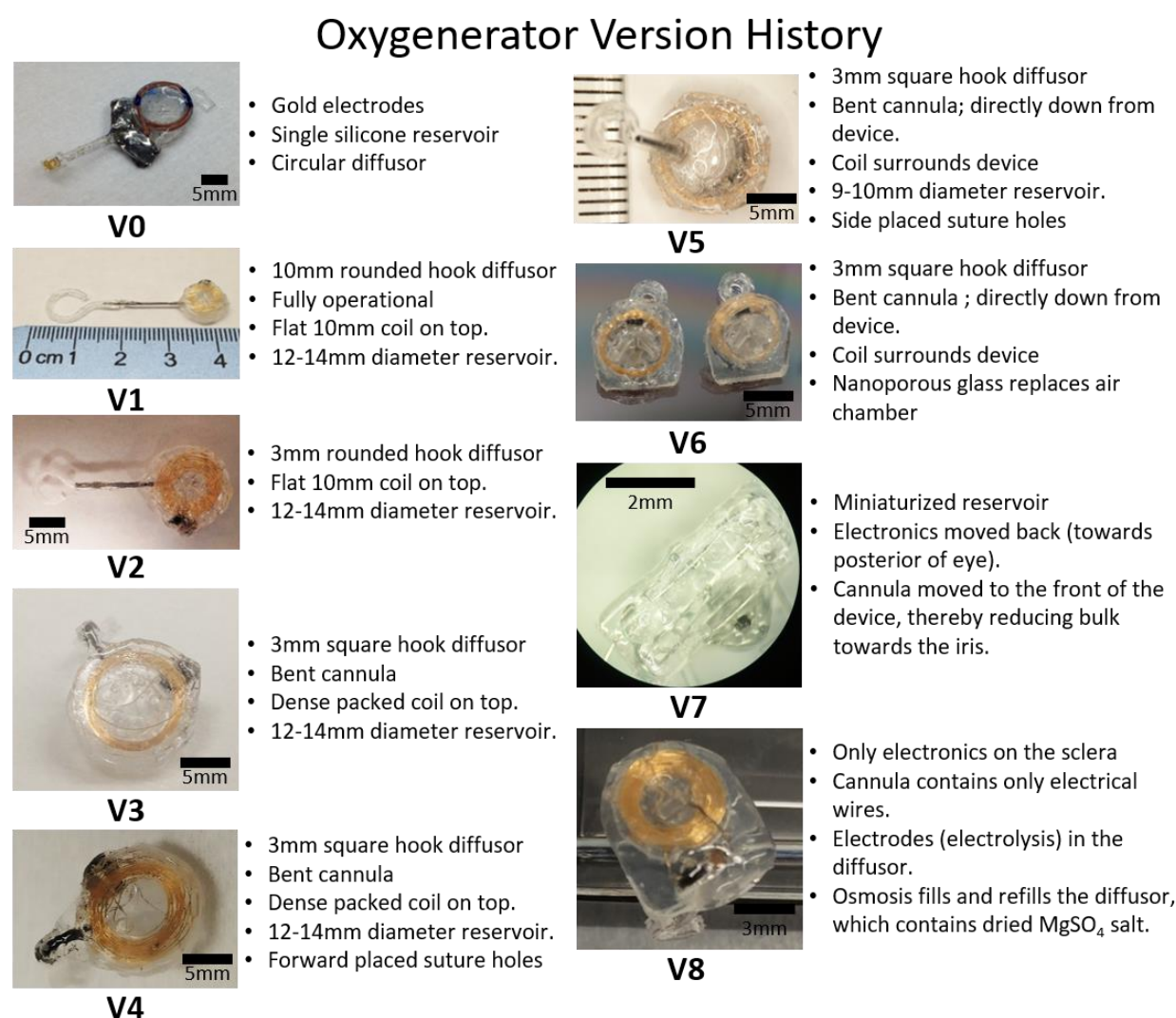


Figure 6.13: Different versions of the oxygen generating device. Changes across different versions of the device. Note from the scale part, the device has shrunk to 25% of its size: from a 14mm diameter by 3mm tall, planar device (V1) to a 7mm wide by 8mm long by 2mm tall, curved device (V8).

Version 0 of the Oxygenerator was a prototype using a copper 44 Litz wire and a Parylene PCB. The reservoir and diffuser were filled with electrolyte. The electrodes activated in the diffuser. This oxygenerator had issues transporting electrolyte from the reservoir to the diffuser, and suffered adhesion issues where the Parylene PCB entered the cannula. Subsequent designs, versions 1-7, had the electrolyte separated from the diffuser. The air conduit referred in section 4.4.1 shuttled oxygen from the liquid reservoir to the diffuser. In versions 1-5 this air conduit contained a set of pillars to maintain the shape of the chamber (**Figure 6.14**) and prevent collapse—under pressure from electrolysis—of the membrane that separates the conduit from the liquid reservoir.

The coil changed along with the oxygenerator design and different fabrication methods. Versions 1 and 2 used a planar coil, whose fabrication is discussed in section 5.3.2.1. Version 3 and 4 used a hand spun coil and a metal spindle. This flat coil remained above the device but opened a window for injecting electrolyte from above. Versions 5-8 used an automatically wound coil as described in section 5.3.2.3. In versions 5 and 6, the coil surrounds the electronics pocket and the reservoir. These versions of the oxygenator are covered in a cast shell of silicone to give the device an appropriate shape.

Version 6 replaced the air conduit with nanoporous, hydrophobized Vycor glass. However, the nanoporous tack pushed the location of the cannula 2 mm back, which was problematic for implant, since the cannula needed to enter through the 3mm to 4mm wide pars plana. Version 7 reverted to an air conduit and moved the cannula to the very front.

Version 8 is a departure from the approach in earlier versions, as the reservoir region contains only the electronics. The diffuser contains the electrodes and performs electrolysis. This change was brought about by changing the method of replenishment from injections to osmosis. In doing so the liquid reservoir could shrink.

The fabrication steps for versions 1 through 7 are fairly similar. The description below is for version 1 of the device, but applicable for every version. Only one fabrication procedure is presented to avoid repetition.

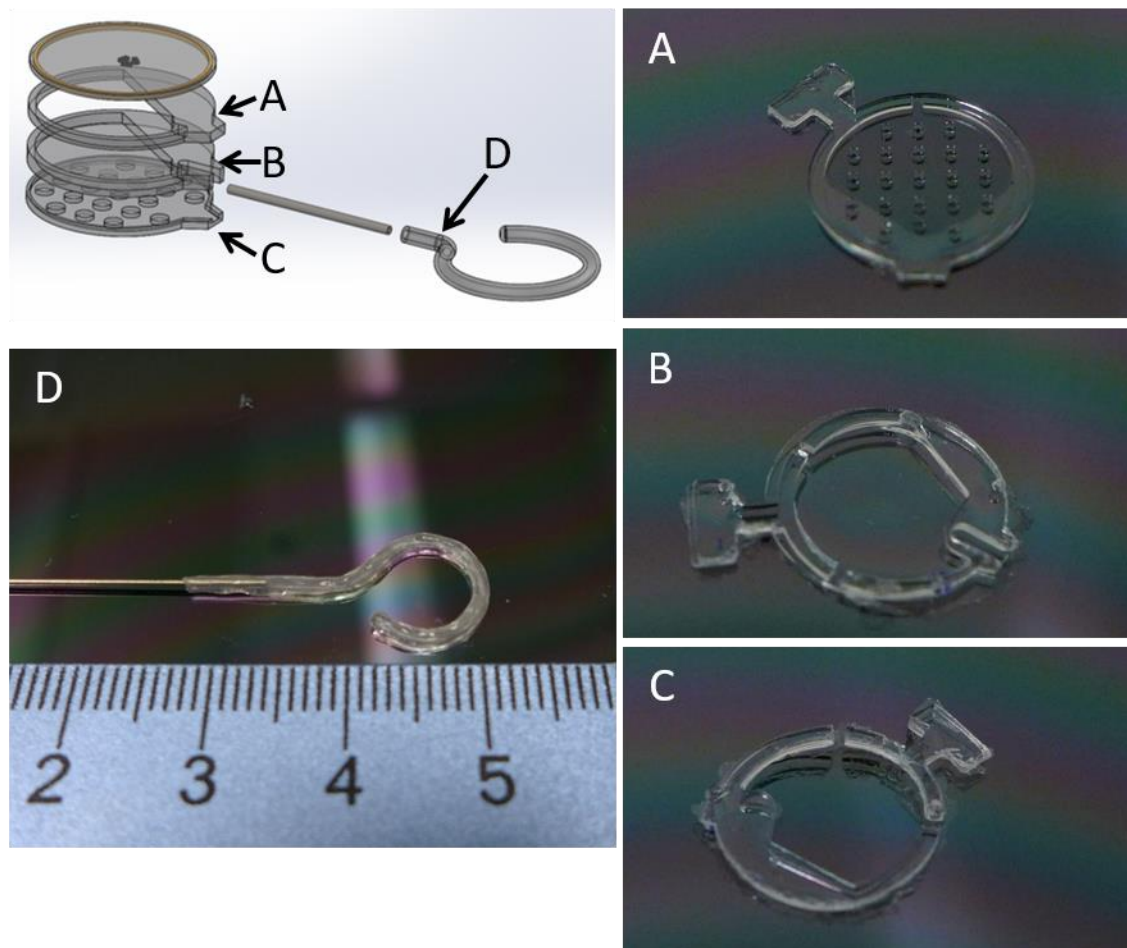


Figure 6.14: Fabrication of version 1 of the oxygen generating device. The silicone for the reservoir was cast in dry-film photoresist molds, while the (D) diffuser was made by dip-coating a Parylene-coated wire in silicone. Subsequent models contained a cast diffuser made using dry-film molds. (B) Note in that there is a small conduit in the lower right side of the diagram where the cannula sits. Such a feature exists in versions 1 through 7 as the cannula is much larger than the $120\mu\text{m}$ height of the (A) air chamber. The final product can be found in **Figure 6.13-V1**.

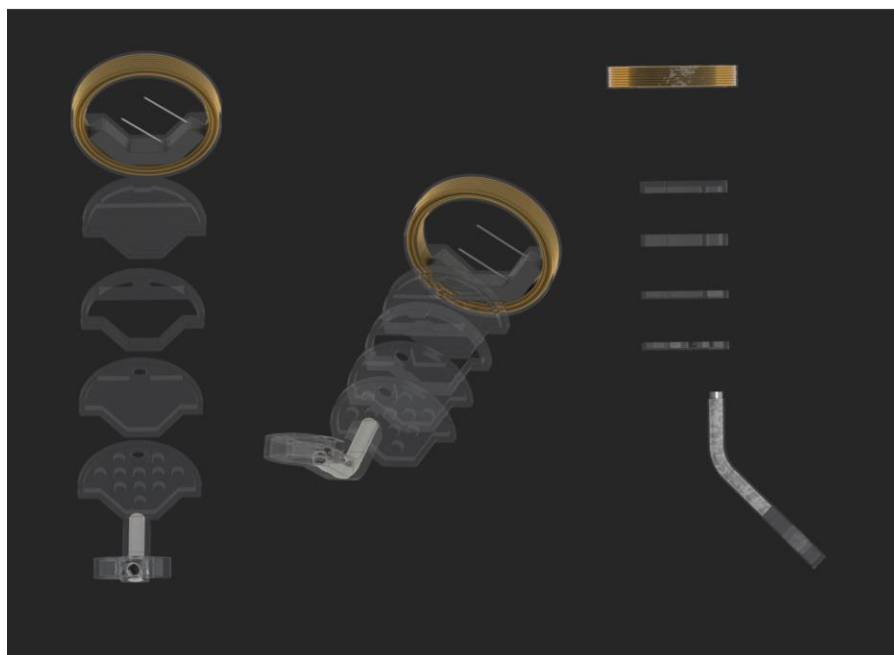


Figure 6.15: Computer rendering of parts of version 5 of the device. Notice the commonality in the design process with version 1. Here placing the coil and electronics around the reservoir helps reduce its footprint to 10mm in diameter.

The reservoir was cast in silicone using MEMS fabricated molds. It was made in 3 sections, as seen in **Figure 6.14a-c**; each with a separate mold made by laminating negative dry film photoresist (DuPont™ WBR2120). To fabricate a mold, first, the dry film is laminated onto a silicon wafer at 95°C. With all necessary layers for a given pattern applied, the dry film is baked for 20 minutes at 65°C, and followed by UV patterning ($\sim 250\text{-}600\text{mJ/cm}^2$, depending on number of layers). The film is then post exposure baked to cure the pattern at 95°C for 1 minute. Further layers can be applied, and the process repeated. When all patterns have been defined, the wafer is developed in an AZ340 develop-water solution (1:4) for approximately 40 minutes. The resultant mold is coated in Parylene-C as a release agent. The electrolyte chamber has a 5-layer lamination (600 μm tall) for the walls of the chamber, and a 2-layer lamination (240 μm tall) for the membrane separation from the air chamber. The air chamber, **Figure 6.14a**, has pillars to prevent its collapse when pressure builds in the adjacent electrolyte chamber. The final mold defines the top of the electrolyte chamber. Each of these molds is filled with a mixed two-part medical-grade silicone (MED4-4210 from NuSil Technologies, LLC) and degassed. After degassing, the excess silicone is wiped from the mold using a fresh razor blade, and placed in the oven at 100°C for 3 minutes to partially cure. The three sections are released from their molds and bonded together using uncured silicone as a glue under a microscope. The assembled sections are cured in an oven at 100°C for 3 minutes. Two platinum

wires (0.004in from California Fine Wire) are then inserted through the sidewall of the silicone into the electrolyte chamber to act as the electrodes. The 304 stainless steel cannula is glued to the opening in the air chamber using uncured silicone. The other side of the cannula is temporarily plugged with silicone, and then the oxygenerator is placed in an oven at 100°C for 4 hours to fully cure. The oxygenerator is CVD (Chemical Vapor Deposition) coated with Parylene-C to reduce oxygen permeation through the reservoir into the conjunctiva.

6.5 REFERENCES

- [6.1] Nusil.com. (2019). *Glossary: Cure Systems / NuSil*. [online] Available at: <https://nusil.com/glossary> [Accessed 11 Apr. 2019].
- [6.2] Stöver T, Lenarz T. Biomaterials in cochlear implants. *GMS Curr Top Otorhinolaryngol Head Neck Surg*. 2011;8:Doc10. doi: 10.3205/cto000062
- [6.3] Specialty Coating Systems™. “PDS 2010 LABCOATER 2 Parylene Deposition System Operators Manual,” Rev. FF, pp. 19 (2003).
- [6.4] Parylene Properties. *Paratech* (2018).
- [6.5] Specialty Coating Systems™. “SCS Military Coatings,” SCS, A Kisco Company, (2018).
- [6.6] Specialty Coating Systems™. “Electronics Coatings” (2019) Retrieved from <https://scscoatings.com/parylene-coatings/parylene-services/electronic-coatings/> [Accessed 11 Apr. 2019].
- [6.7] Meng, E. “Biomedical Microsystems,” CRC Press, 1st Ed., ISBN 9781420051230, pp. 47 (2011).
- [6.8] Kang D., Matsuki S., Tai Y.C. "Study of the hybrid parylene/PDMS material," *2015 28th IEEE International Conference on Micro Electro Mechanical Systems (MEMS)*, Estoril pp. 397-400. (2015_ doi: 10.1109/MEMSYS.2015.7050973

CHAPTER 7 – OXYGEN DISTRIBUTION

The performance of the completed oxygenerator is validated along several criteria:

- Longevity of the soft polymer packaging the electronics
- Device response time, and duration and spatial distribution of stored oxygen
- Ability to modulate oxygen tension
- Distribution of oxygen in an animal
- Metabolic changes in an animal with retinal ischemia

7.1 LONGEVITY OF THE OXYGENERATOR: ACCELERATED LIFETIME TEST

Medical implants have to contend with the natural salinity (0.9% by weight NaCl). The difference in the anodic index between two dissimilar metals in contact with a salt solution generates galvanic corrosion. The corrosion is exacerbated in the presence of an electrical potential. To prevent this, the rate of water ingress into the electronics' compartment must be reduced. The earliest version of the oxygenerator relied on a silicone coat over the Parylene circuit board and a titanium film to insulate the electronics (**Figure 7.1**). However, the film could not entirely encapsulate the electronics, and significant corrosion was observed after 2 days of soaking at 90°C in saline. The titanium adhesion layer in the Parylene circuit board, which lies between the gold traces and the Parylene, was significantly damaged (**Figure 7.2**).

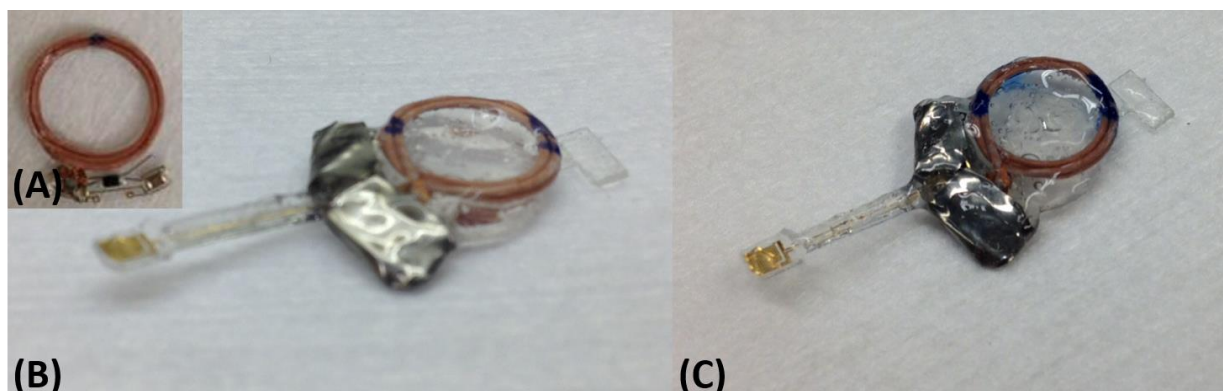


Figure 7.1: Soak testing Parylene PCB. (A) Parylene PCB circuit. (B) Version 0 of the device, with titanium film encapsulation of electronics. (C) After two days of soaking at 90°C in saline. Externally, there are no signs of corrosion.

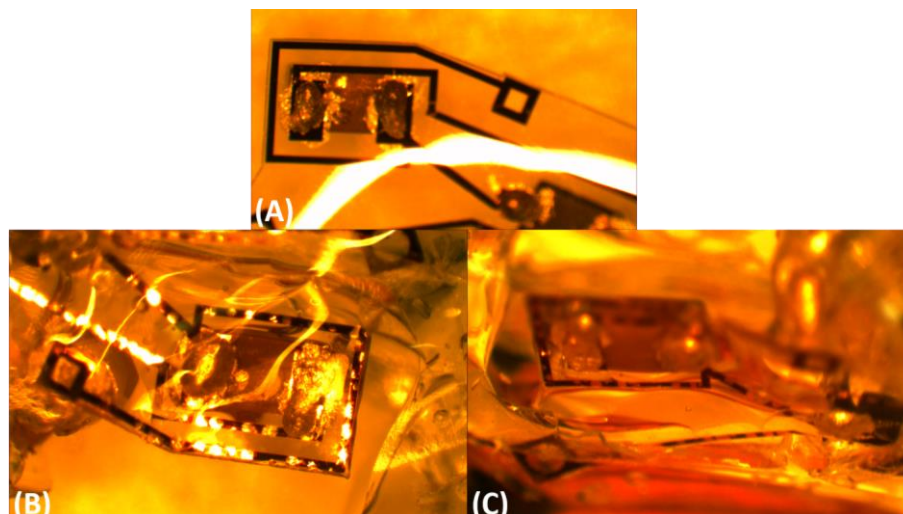


Figure 7.2: Close up of Parylene PCB soak test. (A) Parylene PCB. Since the view is from the underside, the titanium layer of the traces is visible. (B) Capacitor after 2 days soaking at 90°C. Note the non-uniform coloration on the traces suggesting corrosion of the titanium layer. (C) Similar corrosion visible on another capacitor on the same circuit board.

Subsequent versions of the oxygenator relied on Parylene coats of 10 microns. The oxygenator (version 8) has the electronics coated in Parylene, and then potted in silicone. This version was soaked for 163 days in saline at 77°C and remained operational until the experiment's end. The device was energized weekly for 10 minutes to verify functionality. At the experiment's end, corrosion was observed at the solder points, but this corrosion did not affect functionality (**Figure 7.3**).

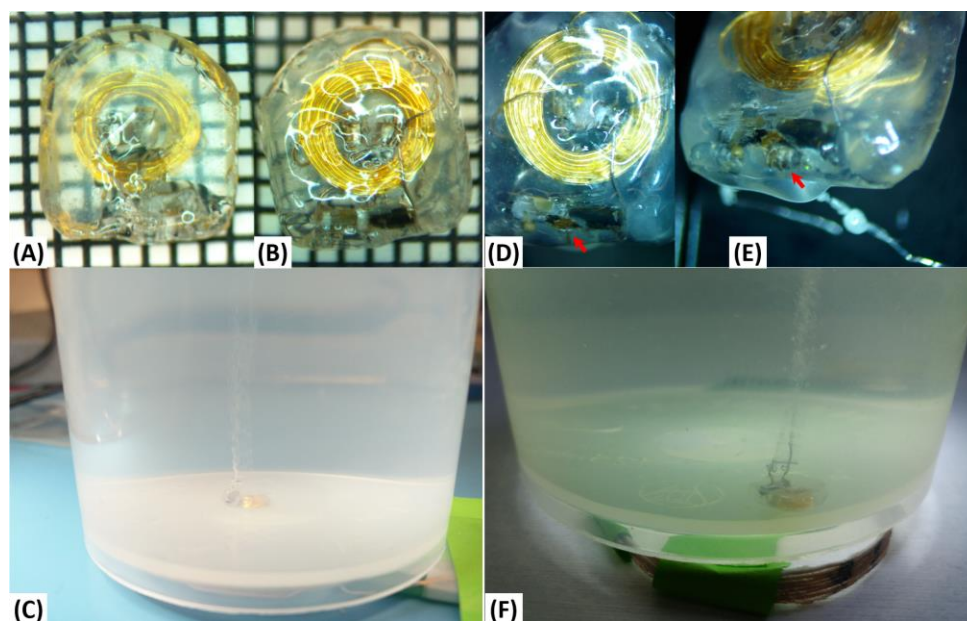


Figure 7.3: Soak testing osmotically refilled device electronics. (A) Bottom view on day 0 before soaking over a 1mm square grid. Note that there is no diffuser attached. Electrolysis is performed directly into the saline solution, leading to a visible trail of bubbles. (B) Top view of the

device. (C) Testing the device on day 0. The primary side coil is placed underneath the container. (D) Top view of the device after 167 days of soaking. Note the corrosion indicated by the red arrow. (E) Better view of the corrosion in the device. The corrosion occurs where the exposed positive platinum wire joins the rectifying diode and capacitor. (F) Function test of the device after 167 days. Note the primary coil underneath the container powering the device.

Using the Arrhenius equation, the equivalent longevity at 37°C for the 77°C test can be calculated:

$$A_f = \exp\left(-\frac{E_a}{k}(T_1^{-1} - T_2^{-1})\right) \quad (7.1)$$

where E_a is the activation energy, and T is temperature. Note that the acceleration factor, A_f , depends strongly on the activation energy, which be taken from literature. Accordingly, the device may last 8.2 years, assuming an activation energy of -0.69eV for a 40 micron Parylene-C with 5mm silicone [7.1], which results in $A_f = 18.37$.

7.2 OXYGEN PRODUCTION IN DEVICE WITH A RESERVOIR

The oxygen tension over time was measured on devices with a reservoir before integrating the electronics, to confirm their functionality before animal experiments (**Figure 7.4**).

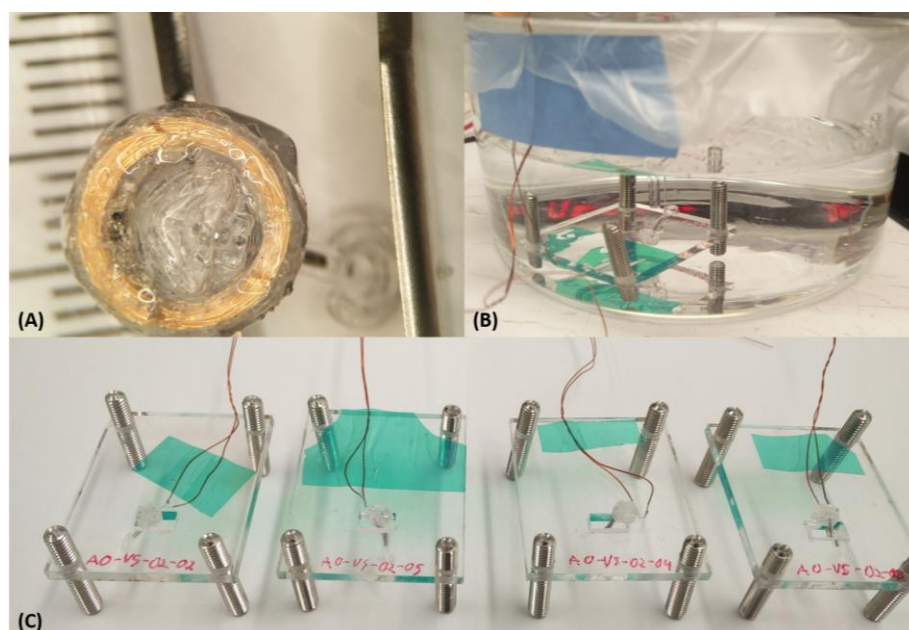


Figure 7.4: Bench testing needle refilled oxygen generating device. (A) Fully assembled version 5 of the device. The injection plate is centered over the gold coil. (B) Device without electronics being tested. The water bath is purged of oxygen and oxygen is blown over top. (C) A Batch of 4 devices to test before integrating with electronics.

Oxygen tensions at different distances from the oxygenator's diffuser were measured on bench with an AL-300 AP-coat Fluorometrics Instruments oxygen probe and a NeoFox reader. The oxygen production rate of 0.24nmol/s was found by fitting a COMSOL simulation of the oxygenator to the oxygen tension data, as seen in **Figure 7.5** (reduced- χ^2 of 1.16). This production rate matches the flux required by the AXSY model.

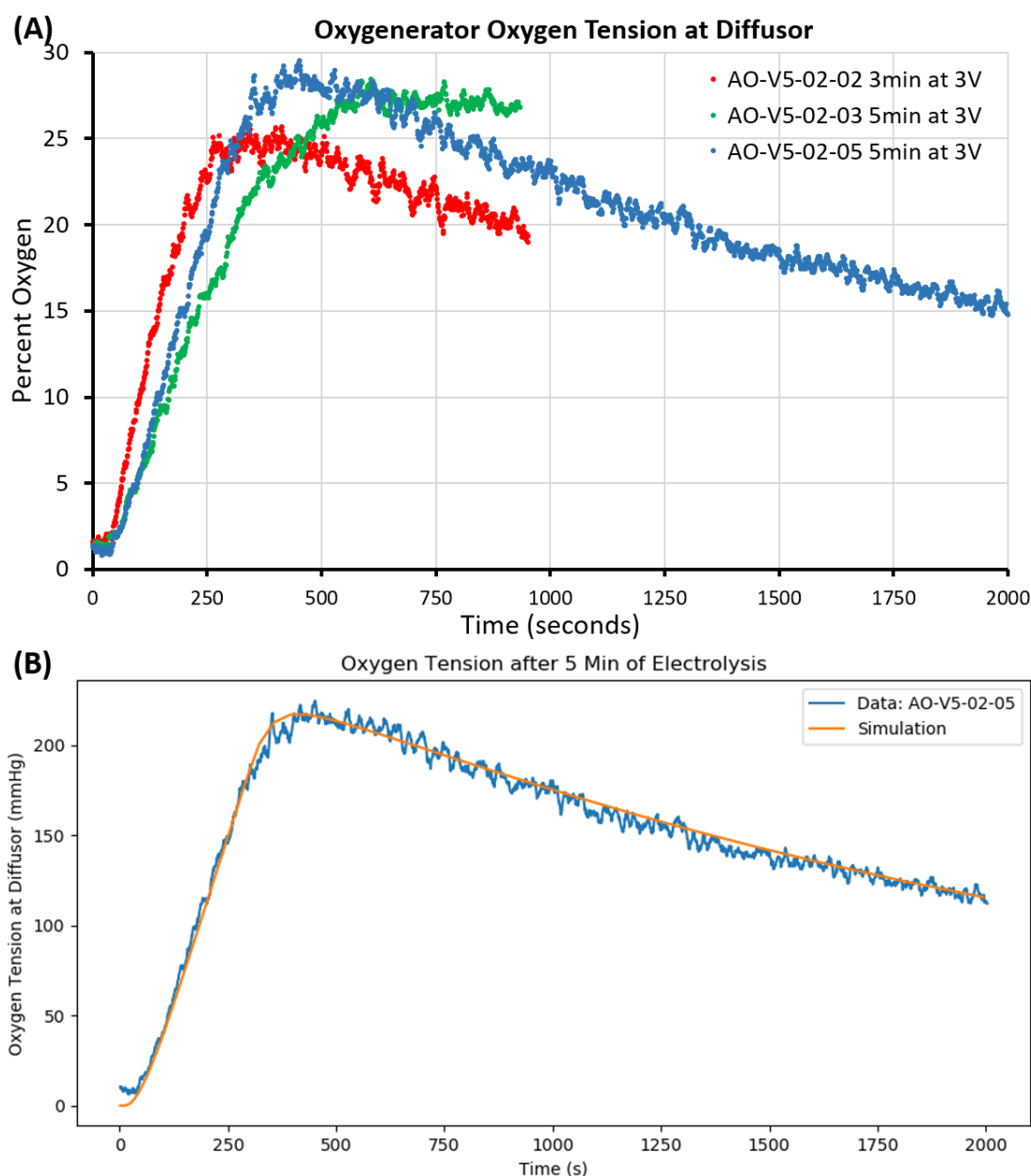


Figure 7.5: Oxygen profile during electrolysis for needle refilled device. (A) Output oxygen curves from devices with liquid reservoirs. The electrodes were energized directly from a power supply. (B) COMSOL model matched to the data of one of the devices in (A). The model was fitted by sweeping the rate of electrolysis, which was assumed to be constant during the active

period (5 minutes). The fit is in good agreement with a reduced- χ^2 of 1.16 for a rate of 0.24nmol/s of oxygen.

Note that oxygen flux can be increased by reducing the thickness of the silicone walls in the diffusor (currently 360 μ m). Using the COMSOL simulation of the oxygenator, oxygen tension away from the diffusor is plotted in **Figure 7.6**. The drop in oxygen tension at 1 mm away from the diffusor shows the importance that must be given to its placement.

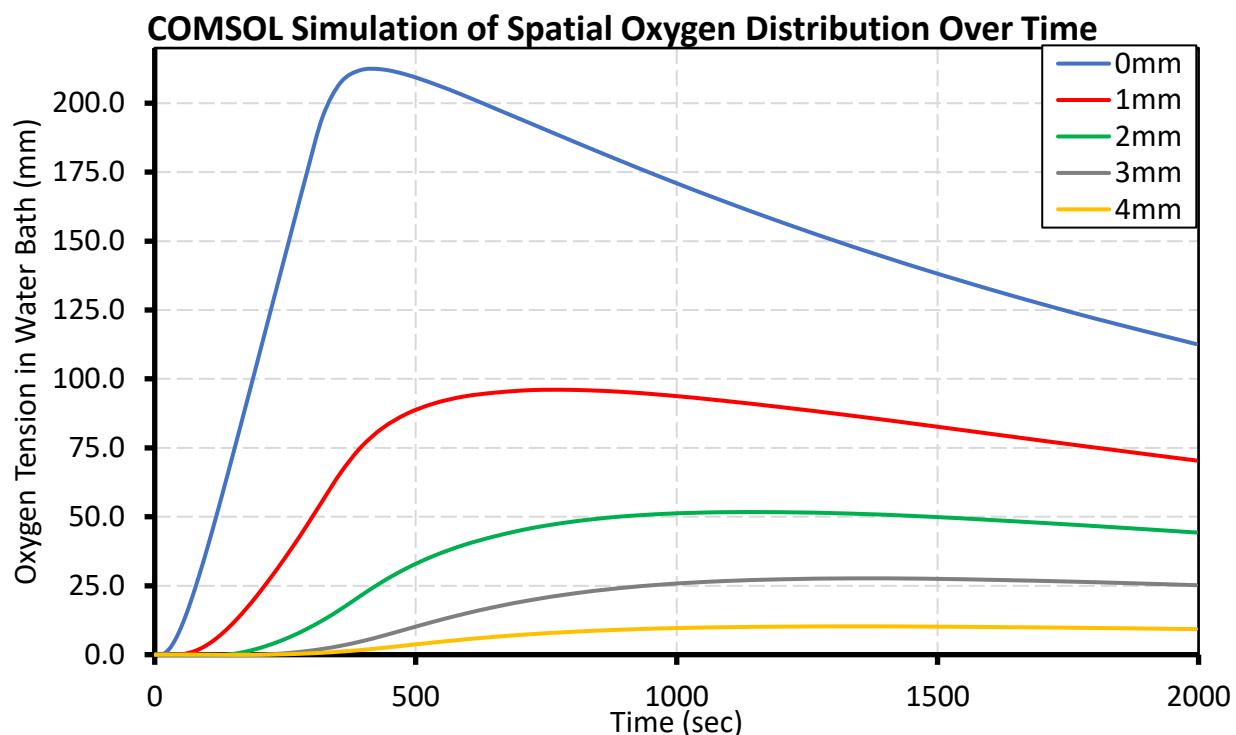


Figure 7.6: Simulation of partial oxygen distribution over time for needle refilled device; using the model in **Figure 7.5B**. Note the peak oxygen tension occurs later as the probe moves farther away from the diffusor. This shows the large impact the time constant of water on the oxygen distribution. Peak oxygen tension 1mm away is less than half that at the device. On the other hand, the oxygen tension is much more stable, taking 20 minutes to decrease by 25mmHg, vs 5 minutes at the device.

This simulated spatial oxygen distribution matches a measurement, made 2000s after electrolysis, from an earlier oxygenator (version 1) (**Figure 7.7**). The delay in measurement reduced the rate of change of oxygen tension at all measurement points.

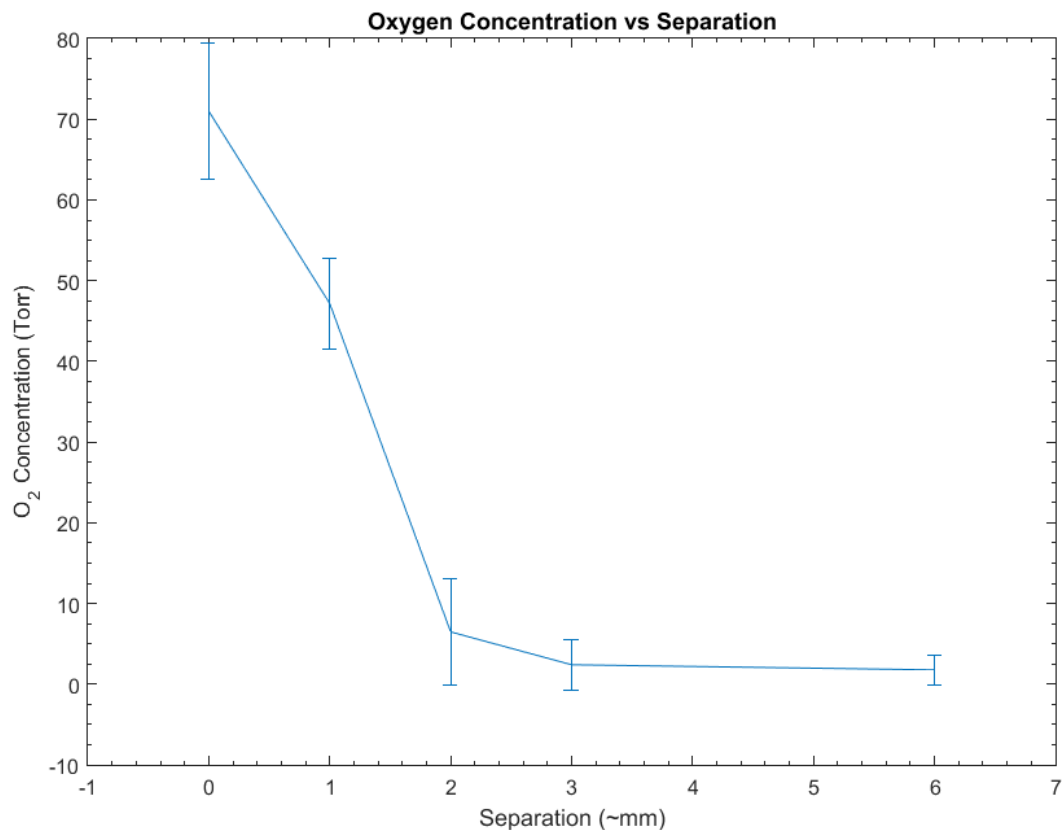


Figure 7.7: Oxygen tension vs. distance from diffuser. Oxygen measurements taken moving away from the device 30 minutes after electrolysis. Note the rapid decline in oxygen tension over 2mm.

7.2.1 IMPLANTATION OF THE OXYGENERATOR IN RABBITS

Oxygenerators (version 5) were implanted on 6 healthy pigmented rabbit eyes by Dr. Juan Carlos-Ramirez at the USC Medical Center.

The devices were sterilized by gas-phase ethylene oxide (ETO). The surgical procedure is illustrated in **Figure 7.8**. Before surgery, the rabbits were anesthetized, and the reservoir was filled with electrolyte. A peritomy was performed to open the conjunctiva in the supra-temporal quadrant. The reservoir was sutured to the sclera at the two front ears of the device. The diffuser was placed in the mid-vitreous humor with the cannula entering through the sclera at the pars plana. There were no surgical complications.

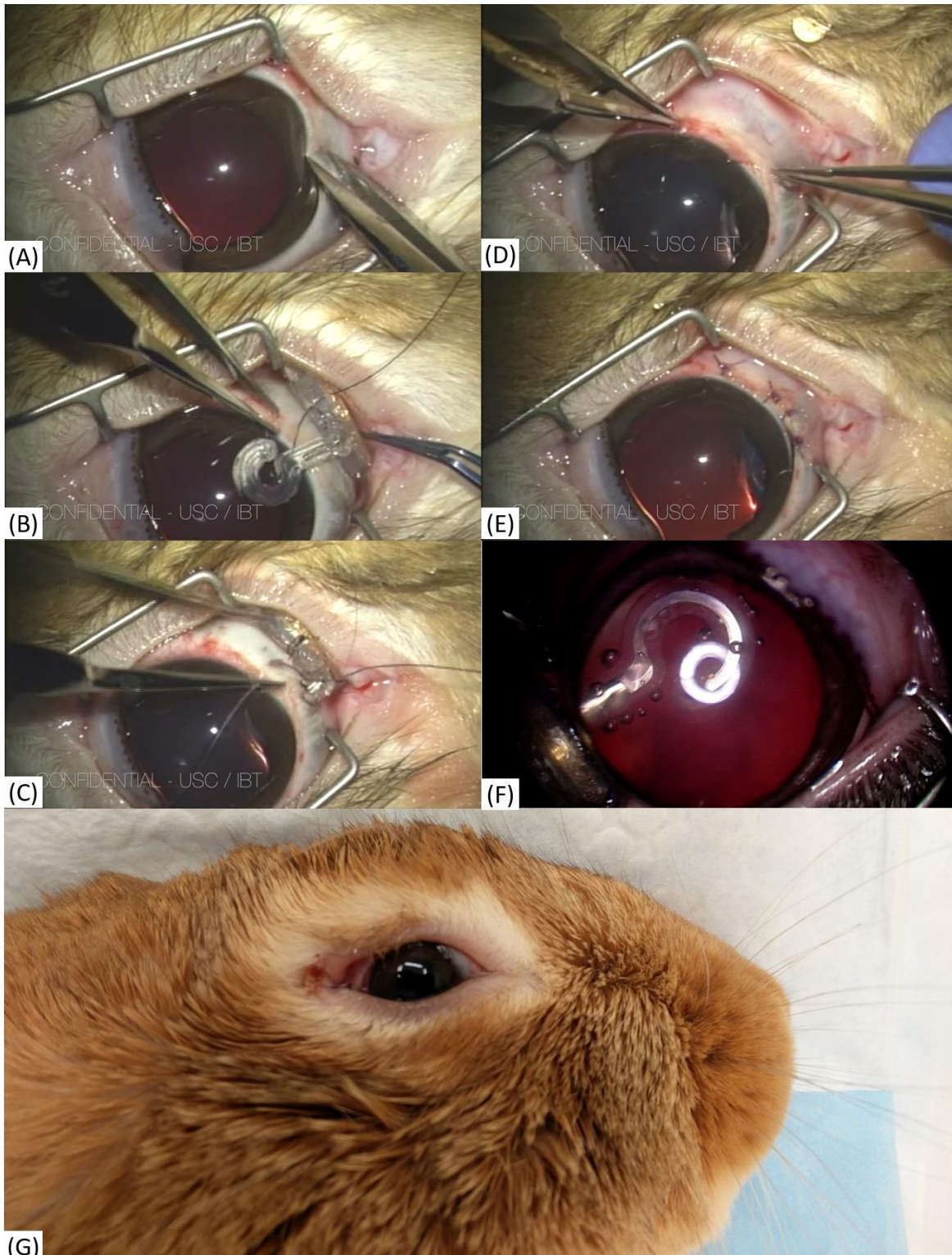


Figure 7.8: Rabbit implant procedure. (A) Marking the entry point through the sclera at the pars plana. (B) The reservoir is positioned on the sclera. (C) Sutures affix the reservoir to the eye. (D) The conjunctiva is pulled over the device, and (E) sutures close the conjunctiva over the device. (F) The diffusor viewed through the lens when activated. (G) The rabbit recovering from surgery after the device was implanted.

Table 7.1: One week rabbit trials with devices with liquid reservoir.

| Rabbit # | Device # | Comments |
|-----------------|-----------------|---|
| Rb003 | AO-V5-2-03 | <ul style="list-style-type: none"> • No inflammation • Leak on injection port after 1 week. • Implanted in fellow eye (L) after 1 week for acute experiment. |
| Rb004 | AO-V5-2-05 | <ul style="list-style-type: none"> • Cornea opaque with inflammation around device. • Implanted in fellow eye (L) after 1 week for acute experiment. |
| Rb005 | AO-V5-2-01 | <ul style="list-style-type: none"> • Implanted farther back (no inflammation) • Well covered by conjunctiva • No leaks. |
| Rb006 | AO-V5-2-02 | <ul style="list-style-type: none"> • Leak out of injection block • Device still functional after 1 week (confirmed in same eye). |

Oxygen measurements surrounding the diffusor were taken before and after activation for a minimum of 3 minutes (**Figure 7.9**). There were no issues with power coupling through tissue. According to the measurements, the oxygenerator had a statistically significant effect on the oxygen levels in the vitreous. After 7 days, the rabbits were re-anesthetized to measure the oxygen tension surrounding the diffusor. One device out of 4 caused inflammation after the week-long trial, the 3 other devices showed no intraocular damage. The devices survived the implant and maintained performance one week after (**Figure 7.10**).

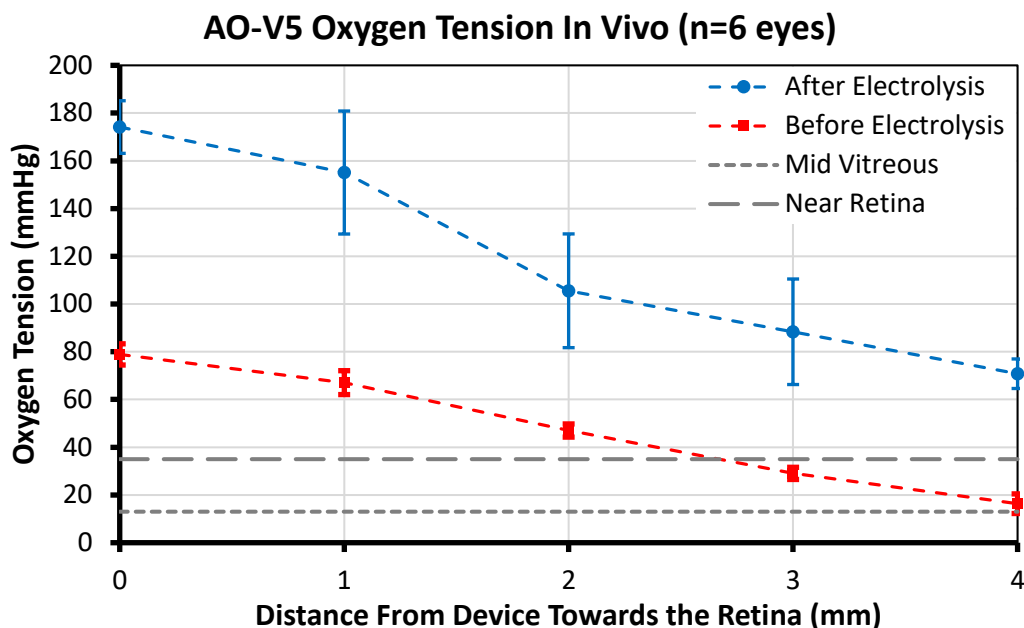


Figure 7.9: *In vivo* spatial oxygen distribution from the device. Four pigmented rabbits weighing 2-3kg were used for this study. An oxygen probe measures the oxygen concentration away from the device and towards the retina before and after activating the device for 3 to 5 minutes. The pre-activation values are elevated over the vitreous baseline, since the device acts like a passive transporter while its residual atmospheric oxygen diffuses out.

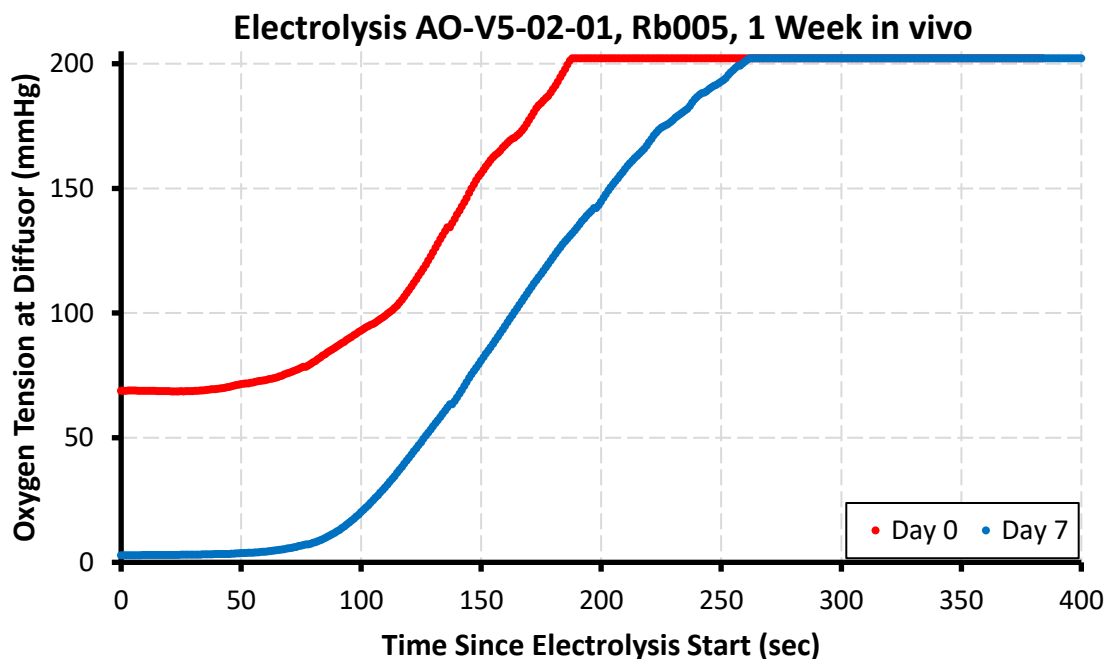


Figure 7.10: *In vivo* oxygen tension during electrolysis. The graph compares performance between day 0 (when the device is implanted), and day 7 (the end of the study). After 7 days the device performs as expected having the exact same oxygen curve. The initial oxygen tension at the diffusor is near 0 when the device is energized on day 7, since this eye was treated with laser photocoagulation to create a retinal vein occlusion to mimic ischemia.

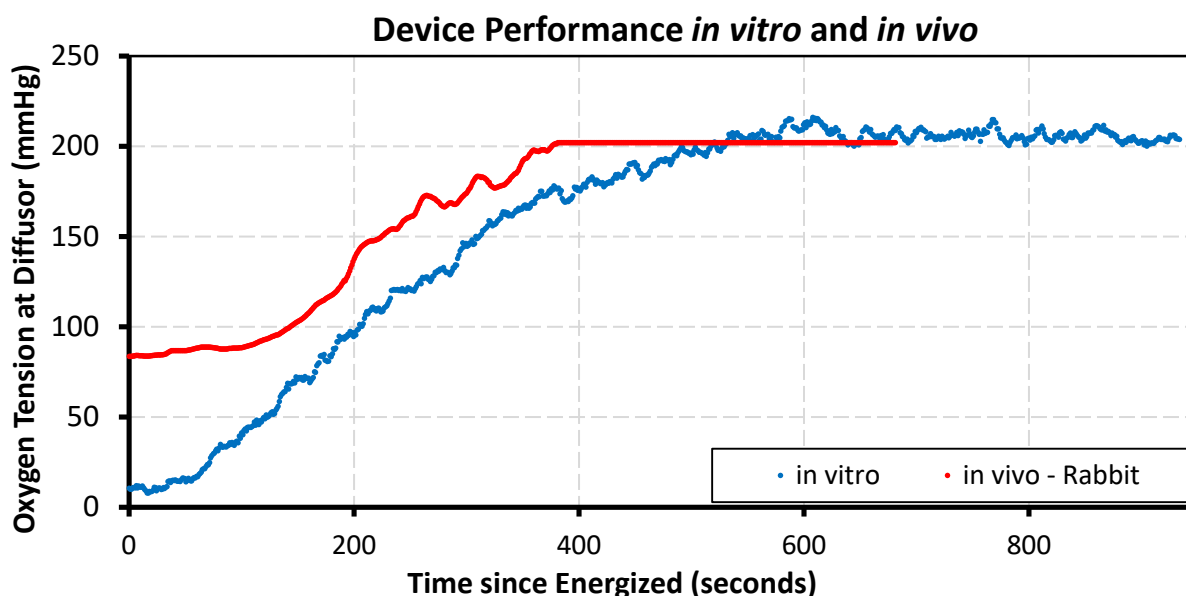


Figure 7.11: *in vivo* vs. *in vitro* oxygen tension during electrolysis. Oxygen tension at the diffusor with 5 minutes of electrolysis for the same device, AO-V5-02-05, in the bench test, and after animal implant. The probe used in animal is different from the bench probe, and saturates at 200mmHg resulting in a flat line for any oxygen values above that point.

It is important to confirm whether the bench model characterizes the behavior of the device. **Figure 7.11** shows that the device behaved identically *in vivo* and *in vitro*. Sterilization and implantation did not affect performance. Anesthesia is time constrained, thus one cannot wait, as in benchtop, for the device internal oxygen tension to reach zero. This fact is reflected in the difference between the two curves of **Figure 7.11**.

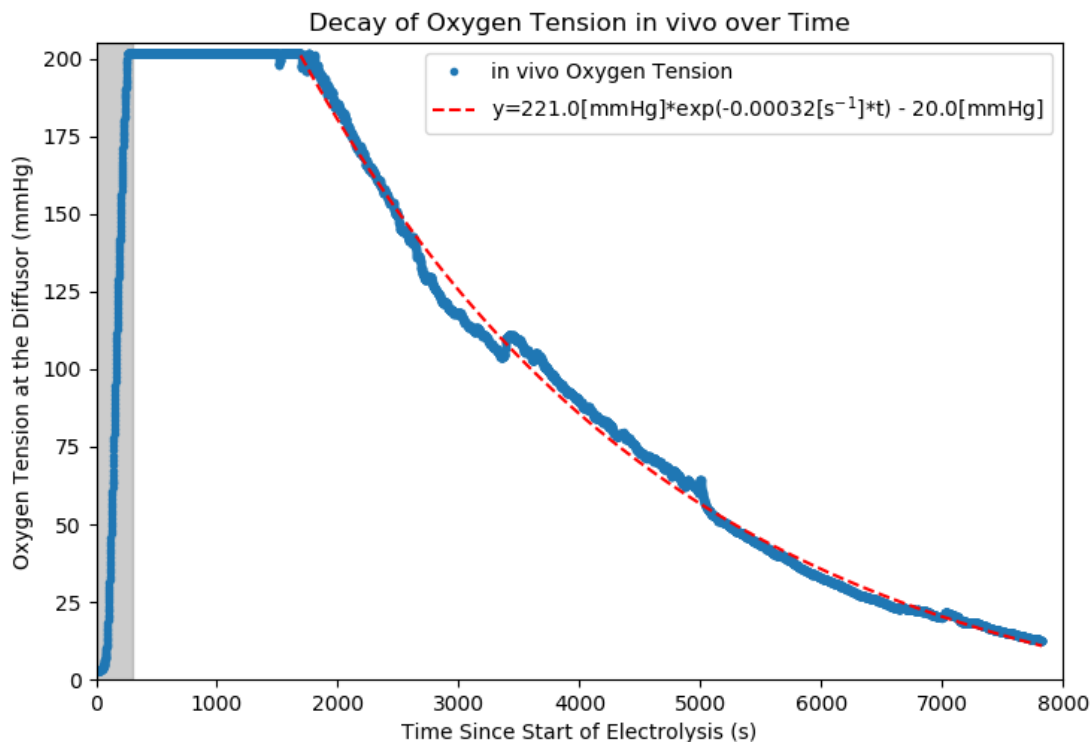


Figure 7.12: The decay time of 5 minute in vivo activation of the device with a liquid on day 7 after implantation in a pigmented rabbit. The blue represents the actual oxygen tension at the diffusor which is 4mm away from the retina. The oxygen probe saturates at values over 200mmHg, so the plot is flat above that value. The grey area represents the region of time during which the device was activated. This was fit with an exponential, the red dashed line, with an R^2 value of 99.5.

In the rabbit, the oxygen tension decays to near zero in 2.5 hours (**Figure 7.12**). Estimates from the AXSY model (**Figure 2.19**, **Figure 2.20**, and **Figure 2.21**) inform that 5 minutes of electrolysis will supply sufficient oxygen tension to treat a moderate retinopathy (22.7% ischemia) for 1 hour.

The decay rate of oxygen tension *in vivo* depends on the permeability of the vitreous, on the diffusor's distance from the retina, and on the retinal consumption. Based on the oxygen tension decay, one can calculate the flux out of the diffusor:

$$\dot{n} = AJ \quad (7.2)$$

where A is the area of the diffusor, J is the flux, and \dot{n} is the molar change with respect to time. Given Fick's law of diffusion, the flux, J , can be estimated as:

$$J = -P_{vit} \frac{\partial p_{O_2}}{\partial r} \approx -P_{vit} \frac{p_{O_2}}{L} \quad (7.3)$$

where p_{O_2} is the partial pressure of oxygen, P_{vit} is the vitreous's permeability to oxygen, and L is the diffusor's distance from the retina. Assuming the diffusor's membranes are much higher than of the vitreous, the moles of oxygen in the device can be estimated as follows:

$$n = \frac{V_{res}}{H_{H_2O}} p_{O_2} + \frac{V_{air}}{RT} p_{O_2} \quad (7.4)$$

Therefore, the oxygen flux can be modeled as:

$$\frac{dp_{O_2}}{p_{O_2}} = -P_{vit} \frac{A}{L} \left(\frac{V_{res}}{H_{H_2O}} + \frac{V_{air}}{RT} \right)^{-1} dt \quad (7.5)$$

which has a solution of the form:

$$p_{O_2} = p_{O_2,i} e^{-Bt} \quad (7.6)$$

such that the time constant, B , is:

$$B = P_{vit} \frac{A}{L} \left(\frac{V_{res}}{H_{H_2O}} + \frac{V_{air}}{RT} \right)^{-1} \quad (7.7)$$

The regression (segmented red curve) of rabbit data from **Figure 7.12** with $R^2=99.5$ and $B = (3.2 \pm 0.013) \times 10^{-4} s^{-1}$ fits equation (7.6). Note that the molar flux is given by:

$$\dot{n} = AJ = -B \left(\frac{V_{res}}{H_{H_2O}} + \frac{V_{air}}{RT} \right) p_{O_2,i} e^{-Bt} \quad (7.8)$$

Because the values for solubility of oxygen in water, area of the diffusor ($A=5.8mm^2$), and volumes of the different chambers of the device are known ($V_{res}=6mm^3$, and $V_{air}=7.3mm^3$), the flux is estimated as:

$$\dot{n} = -(2.7 \cdot 10^{-11} [mol/s]) \cdot e^{-(3.2 \cdot 10^{-4} [s^{-1}]) \cdot t} \quad (7.9)$$

One should be extremely mindful of the size of the diffuser in relation to the eye size and the distance from the retina at which the diffuser is implanted.

Naturally, the smaller the volume of the eye the smaller the radius of the diffuser should be: for the rabbit eye the diffuser's radius should be 1.5mm, and for the human eye, 5mm (**Figure 7.13**). The oxygen flux scales with the square of the radius; at peak, with the diffuser 4mm from the retina, the flux is 0.042nmol/s for the rabbit and 0.19nmol/s for humans. If the diffuser is brought closer to the retina, the flux increases proportionally to the inverse of the distance; since $B \propto L^{-1}$; implanting the diffuser at 2mm from the retina would increase the oxygen tension to 0.084nmol/s for the rabbit and to 0.38nmol/s for humans. A vitreous permeability of 1900Ba was regressed from this data.

It is worth noting that measurements were taken with eyeballs anesthetized, so convection resulting from eye movement does not increase oxygen flux.

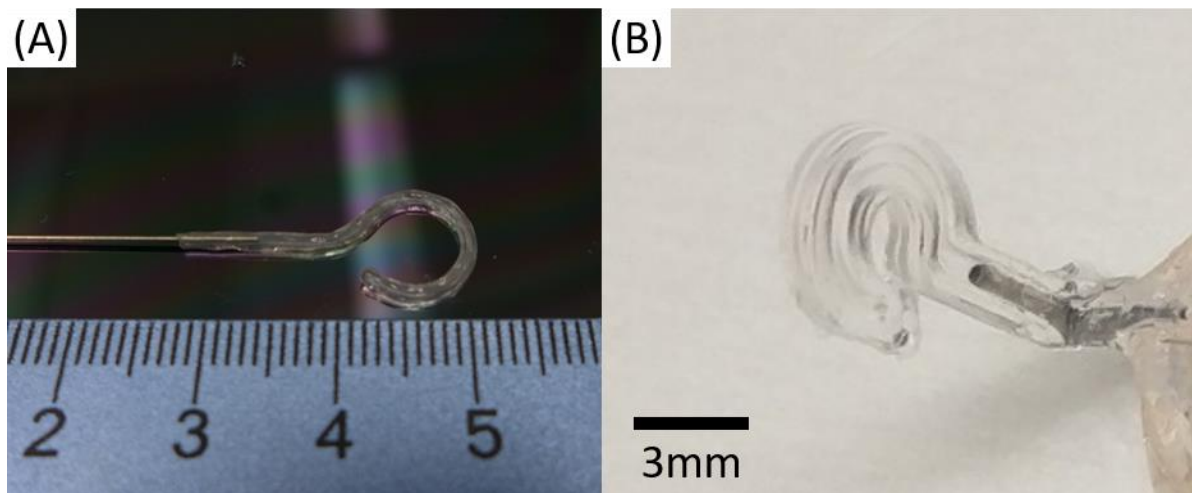


Figure 7.13: Human diffuser versus rabbit diffuser. (A) Diffuser sized for the human macula, diameter of 10mm, as integrated in version 1 of the device. (B) Diffuser sized for the rabbit eye with a 3mm active area, and a total diameter of 5mm.

7.3 MODULATING OXYGEN PRODUCTION IN AN OSMOSIS REFILLABLE DEVICE

Steady state oxygen tension is achieved by pulse width modulation of the primary side.

7.3.1 OXYGEN PRODUCTION IN AN OSMOSIS REFILLABLE DEVICE

As noted in section 4.4.2, this oxygenator design eliminates the complications associated with refilling an implanted device. With no reservoir, the small volume of the diffuser requires frequent activation.

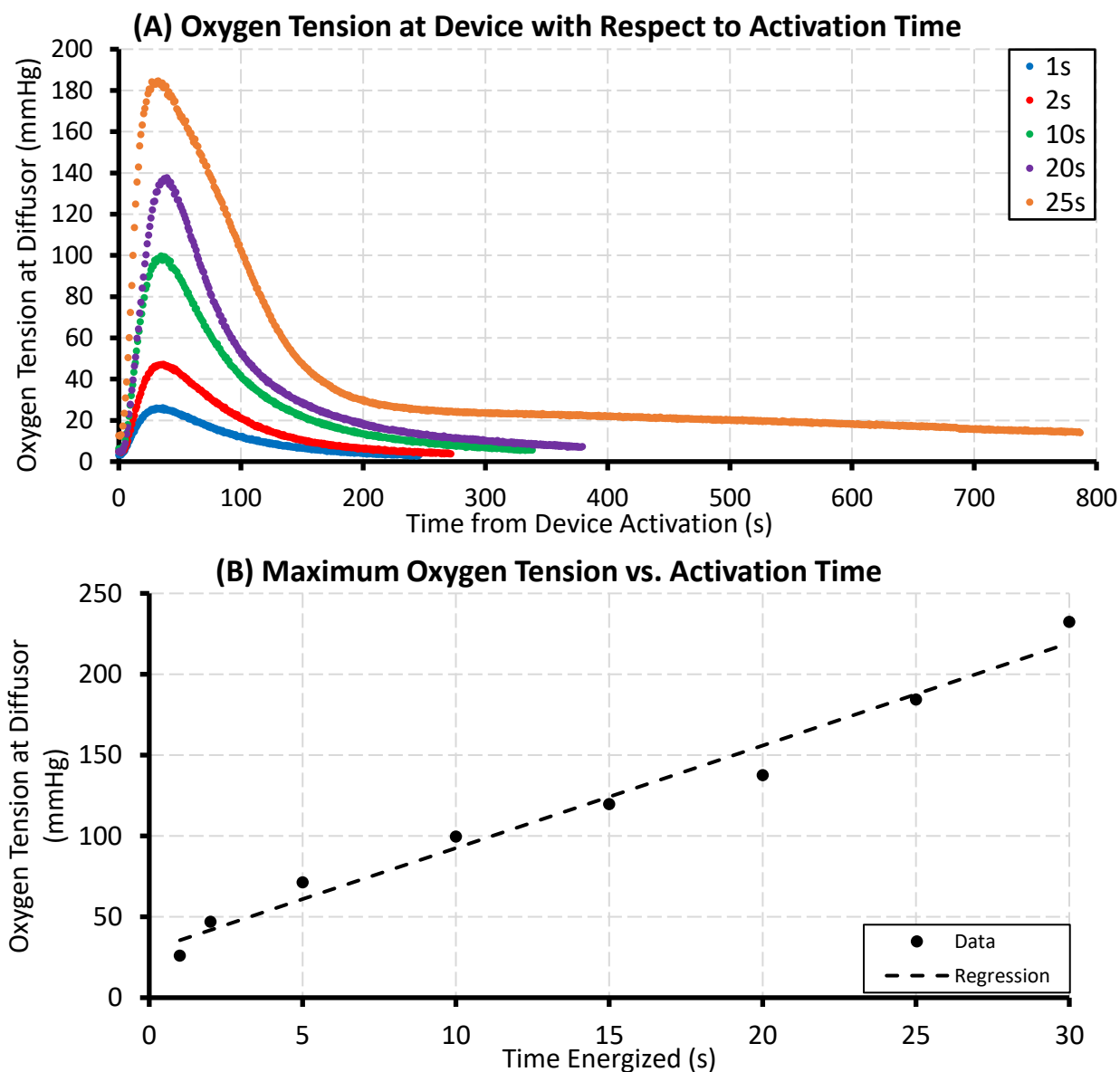


Figure 7.14: Bench oxygen tension during electrolysis vs. activation time. (A) An oxygen probe was placed next to a $120\mu\text{m}$ thick diffuser, and the device is energized for different lengths of time.

This test was done in an anoxic liquid with nitrogen gas blowing over top. The diffuser was placed 6mm from the surface of the liquid. **Figure 7.19a** is an image of the test setup. (B) The maximum oxygen tension with respect to amount of time electrolysis occurs for. The regression has an R^2 value of 0.97, with the fit $y = (6.33 \pm 0.41)[\text{mmHg/s}] t + (29.2 \pm 6.9)[\text{mmHg}]$. The y-intercept relates to the nonlinear gas generation of oxygen that occurs when the electrodes are devoid of occluding bubbles. This seems to stabilize over the first 2 seconds.

The oxygen flux out of the diffuser is estimated from the 5 oxygen decay curves in **Figure 7.14A**. The time constant, B , of those curves, as defined in equation (7.6), is $(2.0 \pm 0.2) \times 10^{-2} \text{s}^{-1}$; for short durations in which the device is energized, the time constant is invariant (only 0.004s^{-1} difference from a mean of 0.02s^{-1}). By knowing the diffuser's volume, V_{diff} , the oxygen flux out of the diffuser can be found by modifying equation (7.8):

$$\dot{n} = AJ = -B \left(\frac{V_{diff}}{RT} \right) p_{O_2} \quad (7.10)$$

which results in a flux per oxygen partial pressure of $B \left(\frac{V_{diff}}{RT} \right) = (1.66 \pm 0.16) \times 10^{-12} \text{mol} \cdot \text{s}^{-1} \cdot \text{mmHg}$. For a flux of 0.25nmol/s , as required by the AXSY model in a human-sized diffuser, the oxygen tension must be at least 150mmHg .

The maximum oxygen tension is approximated as a linear relationship with activation time (**Figure 7.14B**). This implies that total area occluded by gas reaches its equilibrium rapidly, which is in agreement with video recordings of electrolysis in the diffuser (**Figure 4.15**). Note that the response time of 45 seconds in this benchtop experiment agrees with an acute animal test of the device, where a $50 \mu\text{m}$ osmosis diffuser with electrodes reached 200mmHg in 100 seconds (**Figure 7.15**).

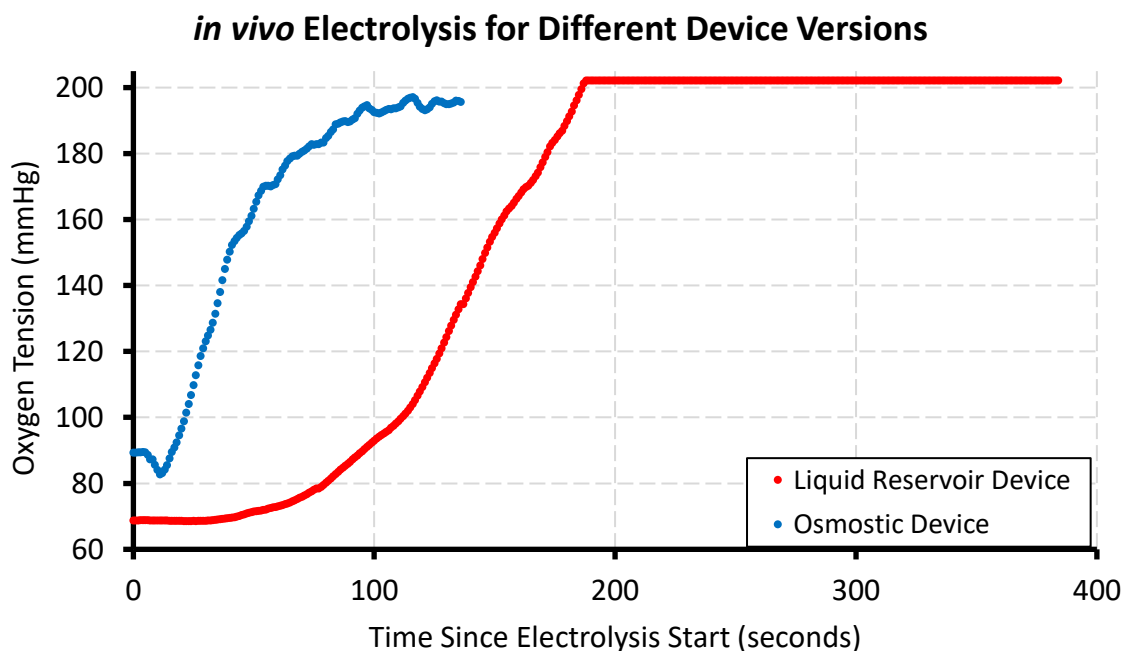


Figure 7.15: *In vivo* comparison of different device versions implanted in pigmented rabbits. Both devices are within 4mm of the rabbit's retina. The probe saturates around 200mmHg.

Also, note that the diffusor is sized for rabbit experiments with an outer diameter of 3.5mm and that the flux scales with the square of the diameter of the diffusor, because oxygen flux is dominated by the thinner top and bottom walls of the device.

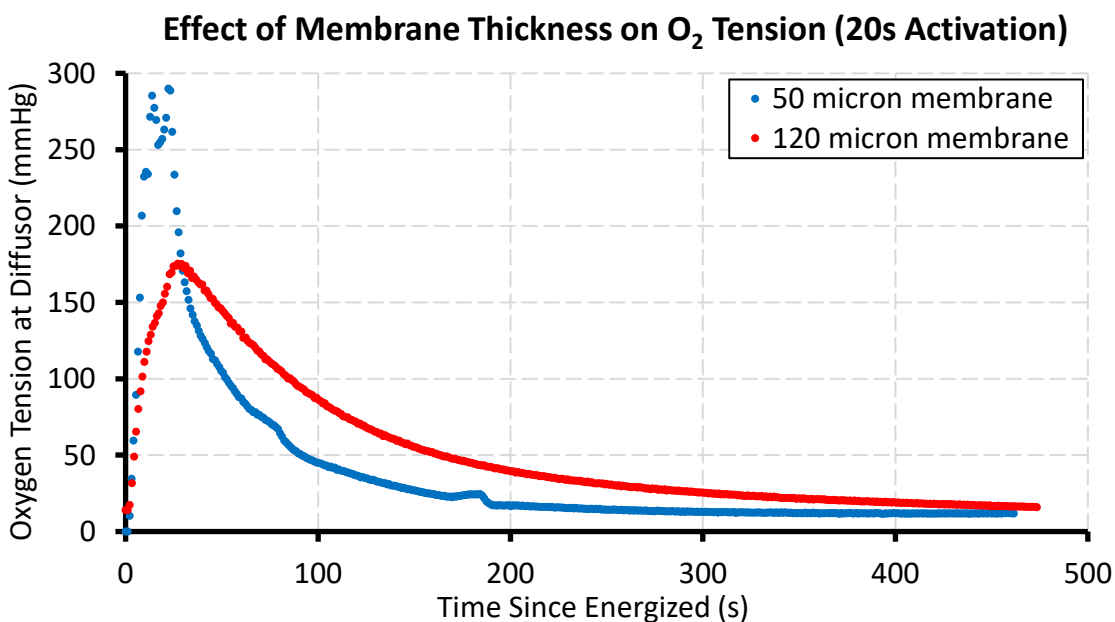


Figure 7.16: Effect of diffusor membrane thickness on oxygen response. Two diffusors of the same size are tested with an oxygen probe against the diffusor in an anoxic water bath. Diffusors were powered by activating the primary side for 20 seconds.

The effect of membrane thickness is plotted in **Figure 7.16**. As expected, the peak oxygen value is lower in the 120 μm thick diffusor membrane with a longer time constant, $(1/B)$, of 79 seconds versus 51 seconds for the 50 μm thick diffusor membrane. Oxygen oversupply can be controlled by increasing the membrane thickness.

7.3.2 PULSE-WIDTH MODULATION CONTROL OF OXYGEN TENSION

Using the dynamics of the device from the section 7.3.1, the device may be controlled with pulse-width modulation. The time averaged value for oxygen can be taken as the treatment value, because the time constants for cell death and activity are measured in tens of minutes [7.2]. The period of pulse width modulation is on the order of a minute, since electrolysis increases the oxygen tension in the vicinity of the diffusor within tens to hundreds of seconds. The percentage of on time is dependent on the desired average oxygen tension.

This primary side modulation is achieved by controlling power sent to the amplifier. A high side PMOS switch circuit (**Figure 7.17**) connected to a microcontroller can achieve the effect. For this experiment, the microcontroller communicates with a computer to allow the period, on time and initial on time to be changed with ease. In an implant for humans, the primary circuit can be integrated into glasses or a sleep mask.

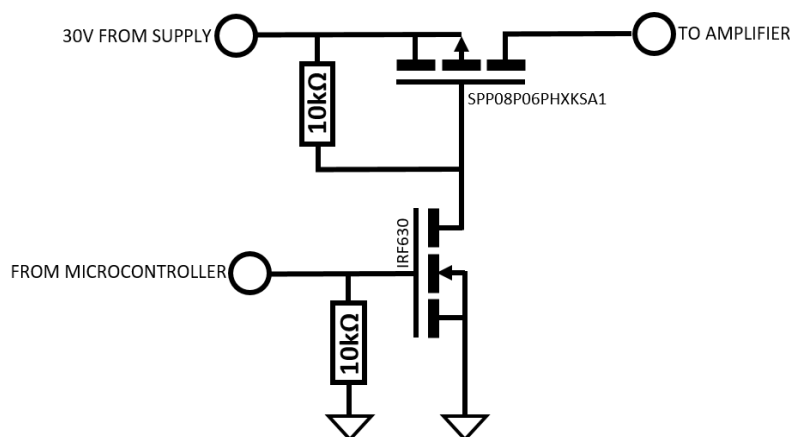


Figure 7.17: Power amplifier P.W.M. control circuitry. Arduino UNO (Atmel ATmega 328P) controls the power supply voltage into the amplifier for the primary side coil through this high side switch.

The only additional circuitry required in the secondary is to limit the maximum voltage sent to the electrodes. Limiting the voltage removes the variability of delivered power based on the separation

between the primary and secondary sides (**Figure 5.20**). All orientations, where the two coils are sufficiently close and aligned to deliver sufficient power, will deliver the same voltage. An LED acts as a visual indicator of sufficient voltage.

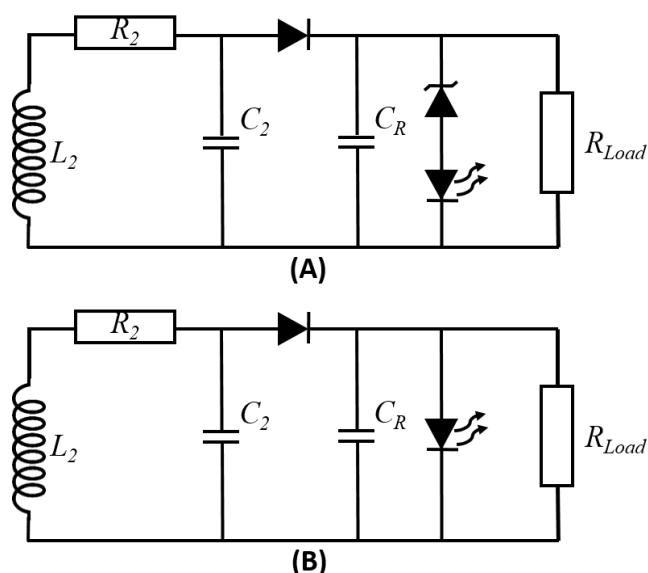


Figure 7.18: Secondary side diode feedback circuit. (A) Secondary side circuit using an infrared LED. (B) Similar results can be achieved using a 3.5V blue LED. This is acceptable for benchtop tests, but for an actual implant the blue LED may be uncomfortable. On the other hand, an infrared from an IR LED will penetrate tissue (**Figure 5.1**).

LEDs flatten the voltage-distance curve by shunting current to ground, such that the resistance of the system reduces the voltage at the electrodes (**Figure 7.18**).

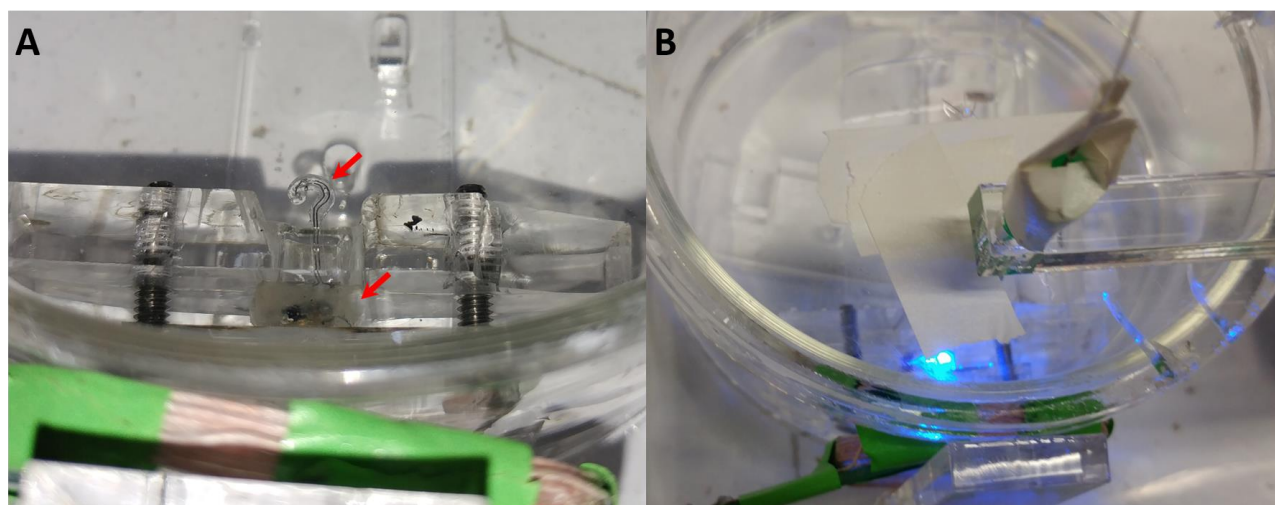


Figure 7.19: Implant bench test setup. (A) Close up on the diffuser mounting. Red arrows point to the electronics package (lower), and to the diffuser with platinum electrodes (upper). (B) Device is energized with oxygen probe in contact with diffuser.

Oxygen tension is measured using an AL-300 AP-coat Fluorometrics Instruments oxygen probe and a NeoFox reader. To simulate the eye, the device is submerged with the diffuser placed 4mm below the surface of the water. Nitrogen gas circulates in the chamber above the water; acting as a consumption source for the generated oxygen (**Figure 7.19**).

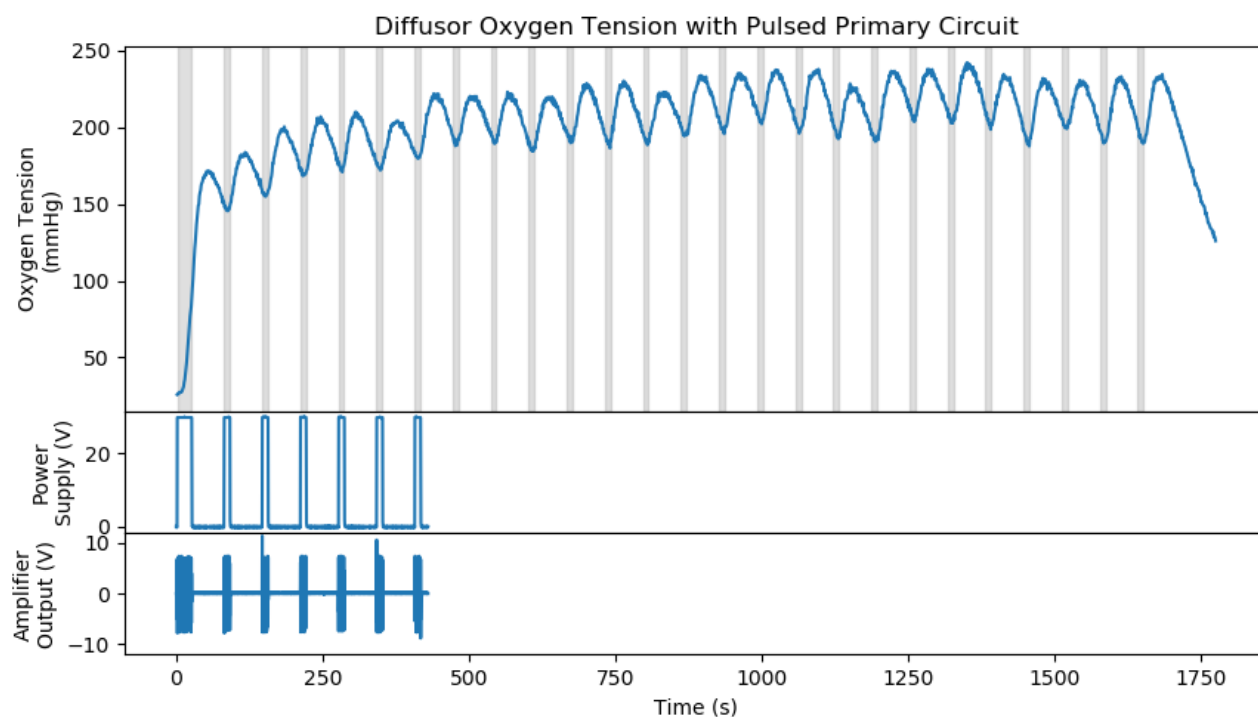


Figure 7.20: Pulse width modulated oxygen output from primary side control with a 50 μm thick diffuser. A longer pulse of 25 seconds is used to bring the oxygen tension closed to the steady state value. Afterwards the power supply is pulsed at a repeatable 10 seconds on with a period of 65 seconds. The grey shaded area overlays activation onto the oxygen plot. The Amplifier voltage output, and the power supply output were acquired from an oscilloscope. The maximum acquisition time on the oscilloscope is limited by what can be displayed on the window, which is significantly less than the duration of this run.

A pulse-width modulated (PWM) signal controls the primary with an on time of 10 seconds and an off time of 55 seconds. Doing so maintains the oxygen tension in the device to $214 \pm 29 \text{ mmHg}$ for the 25 cycles (27.5 minutes) of the experiment; this process can be maintained indefinitely. Using the final decay portion of the oxygen data, the time constant, B , is determined to be $(2.29 \pm 0.4) \times 10^{-3} \text{ s}^{-1}$ ($R^2 = 99.85$). The instantaneous oxygen flux out of the device is given by equation (7.10), which can be integrated over time to provide the number of moles of oxygen provided by the diffuser:

$$n = \int \dot{n} dt = - \int B \left(\frac{V_{diff}}{RT} \right) p_{O_2} dt \quad (7.11)$$

Applying this integration to the data set results in 44nmol of oxygen, and an average flux of 0.037nmol/s. A larger 10mm diffuser is estimated to provide 0.17nmol/s, since it has 4.5 times the area and the volume of the diffuser scales with its area as $V_{diff} = A_{diff}H$. These parameters match the requirements estimated by the AXSY model with 22.7% ischemia to treat moderate DR.

Pulse width modulation allows the ophthalmologist to adjust treatment in a human implant by adjusting the primary side without modifying the implant.

7.4 METABOLIC CHANGES IN THE RABBIT

To test the changes in the retinal metabolism caused by the devices on the presence of retinal vein occlusions (RVO), a study was requested to medical researchers at the University of Southern California. Tests on the oxytransporter and the oxygenator were planned, but constraints limited the study to the oxytransporter. The study was performed by Professor Juan Carlos Martinez-Camarillo, Dr. Alejandra Gonzalez-Calle, Dr. Ronald W. Irwin and Professor Enrique Cadenas.

The rabbits weighed between 2 and 3 kilograms. The rabbits were split in groups of 6: 6 as control or healthy (without occlusion and without implant), 6 as non-treated (with occlusion and with non-functional implant), 6 as treated (with occlusion and with functional implant) for 3 hours, and 6 as treated (with occlusion and with functional implant) for 96 hours.

The retinal veins were occluded by laser photocoagulation. Fluorescein angiography confirmed the occlusion 3 days after, and the protein, Hypoxia Inducible Factor-1 α (HIF-1 α), the hypoxia. **Figure 7.21** shows a rabbit's RVO. During the day of the implant and for 6 hours afterwards, oxygen was blown intermittently over the oxytransporters.

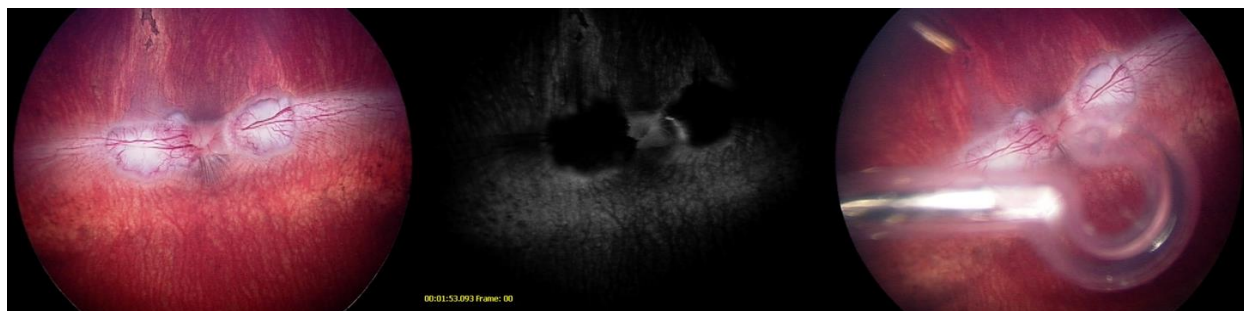


Figure 7.21: Laser-induced RVO on a rabbit. This image is taken 3 days later when an oxygenator was implanted. The top image shows the image using visible light. While the middle image looks fluorescence from for fluorescein angiography. The lack of fluorescence in the laser treated regions implies no reperfusion has occurred. The lower image was taken after an oxygenator device was implanted

Protein expression changes post- retinal vein occlusion

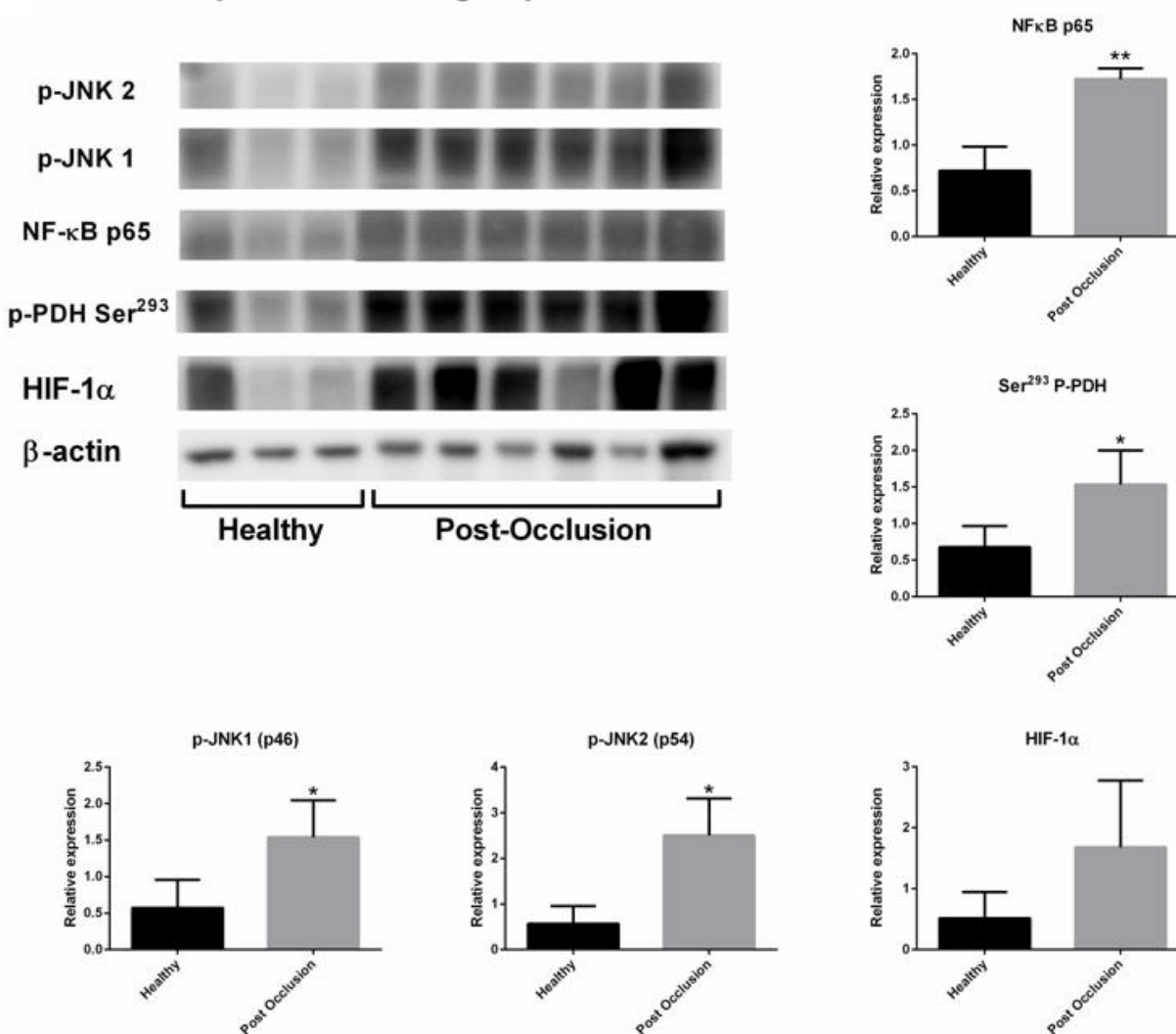


Figure 7.22: Changes in protein expression after laser-induced retinal vein occlusion. P-PDH, and HIF-1 α upregulation imply hypoxia. NF- κ B upregulation combined with IKK α (Figure 7.23) implies inflammation secondary to hypoxia.

The study, using Actin as the non-hypoxic and non-inflammatory protein reference, looked for up regulation or down regulation of the following proteins in the hypoxic and inflammatory pathways: Hypoxia Inducible Factor-1 α (HIF-1 α), Pyruvate Dehydrogenase (PDH), Nuclear Factor Kappa-Light-Chain-Enhancer of Activated B Cells (NF- κ B), I κ B Kinase α (IKK α), and c-Jun N-Terminal Kinases 1 and 2 (JNK1 and KNJ2).

HIF-1 α is upregulated in hypoxia exclusively; PDH is upregulated in hypoxia and also in other conditions, but retains value as a weak marker of hypoxia because PDH relates to cellular oxygen. The ratio NF- κ B / IKK α is elevated in inflammation.

HIF-1 α , the strongest hypoxia marker, was calculated only for the control or healthy group and for the non-treated group, unfortunately reducing the usefulness of this marker to confirmation of hypoxia (**Figure 7.22**). JNK1 and KNJ2 are multi-causal. One is, thus, left from the study, with PDH as weak marker of hypoxia and the ratio NF- κ B / IKK α as strong marker of inflammation.

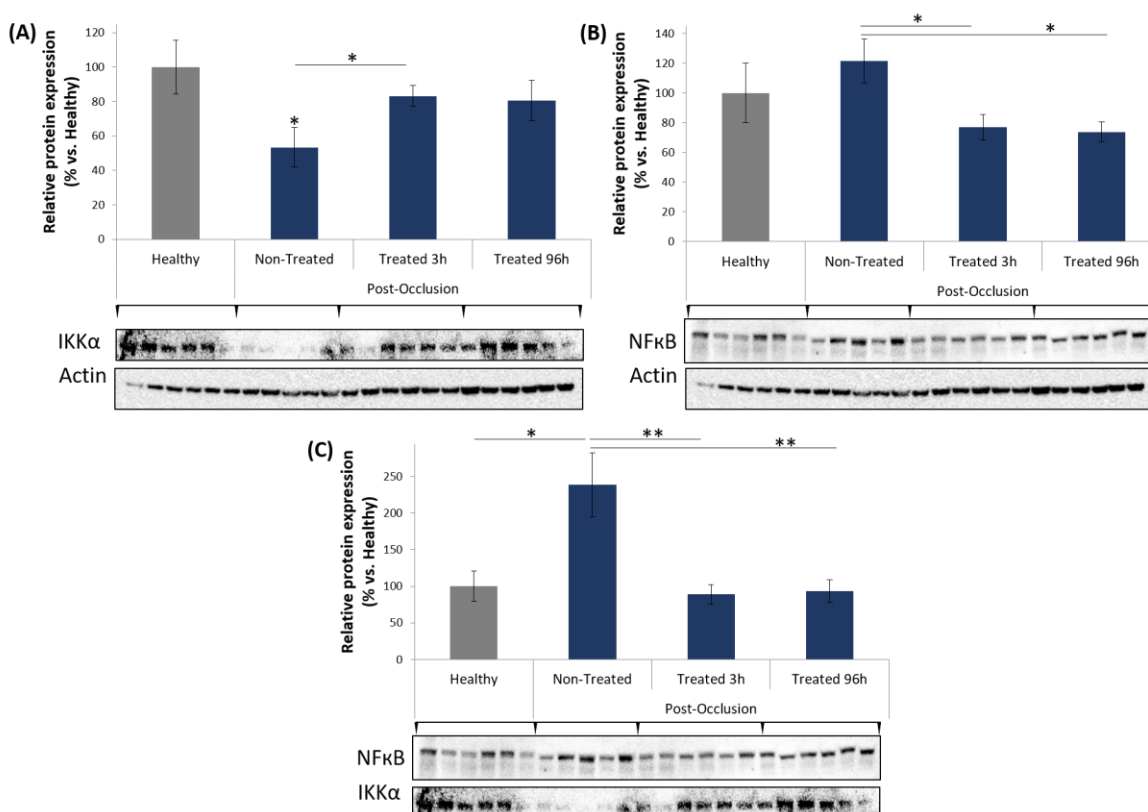


Figure 7.23: Effect of oxytransporter on NF- κ B and IKK α expression in rabbit. (A) NF- κ B is downregulated in the presence of the oxygenator compared to the RVO model, and elevated in

the RVO model (non-treated) compared to the healthy case. Actin is used as a baseline for this analysis. (B) $IKK\alpha$ shows the opposite trend. (C) The relative expression of $NF-\kappa B$ compared to $IKK\alpha$ is not statistically different from the healthy case in the presence of the oxygenator, but significantly elevated in sham treatment (non-treated). The (*) over the graphs represents a statistically significant difference between those groups.

Unfortunately as well, the oxytransporter was implanted at a minimum of 4mm from the retina instead of at 1mm to 1.5mm from the retina, as plotted in **Figure 2.19**, **Figure 2.20**, and **Figure 2.21**. As consequence, the oxygen tension provided to the retina was insufficient.

The ratio $NF-\kappa B / IKK\alpha$ of the treated groups (3 hours and 96 hours) were similar to the control or healthy group, and lower than in the non-treated group. Since both comparisons are statistically significant, one can say the oxytransporter reduced inflammation (**Figure 7.23**). The association between the ratio of $NF-\kappa B$ and $IKK\alpha$ with hypoxia suggests that oxygen delivery may ameliorate the inflammatory response, which is consistent with the expected behavior of the device.

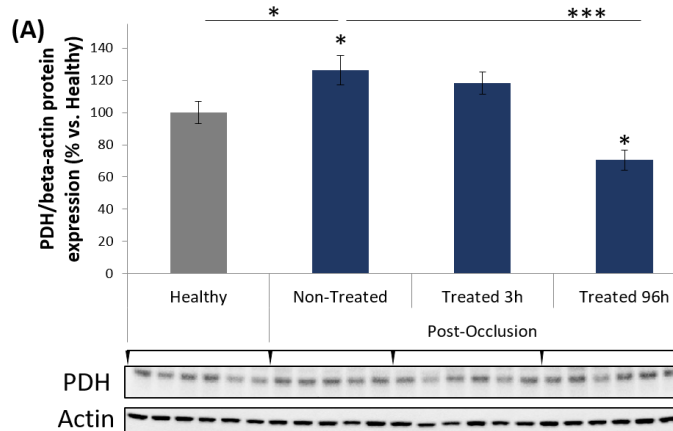


Figure 7.24: Effect of oxytransporter on PDH and JNK expression in rabbit. PDH is downregulated in treated tissue compared to untreated. The (*) over the graphs represents a statistically significant difference between those groups.

PDH expression was higher in the non-treated group than in the control or healthy group. The 96hr treatment group had a lower PHD expression than to the non-treated group. Since the comparison is statistically significant, but PDH upregulation is multi-causal, one can say the oxytransporter may reduce hypoxia (**Figure 7.24**).

Notwithstanding limitations, these conclusions are encouraging and warrant a repetition of the experiment in accordance with the parameters calculated in this thesis.

7.5 CONCLUSION

The motivation of this thesis lies in the relationship revealed between oxygen supply and consumption by the treatment of diabetic retinopathies through laser photocoagulation. This treatment ablates retinal cells to reduce oxygen consumption, so it is natural to wonder why not supply the hypoxic retina with more oxygen instead? The analysis of the eye and modeling of the retina and its oxygen distribution, the design and optimization of MEMS devices to implant in the eye and efficiently supply oxygen to the retina, the selection of the proper materials and methods to fabricate those devices, the resolution of condensation in the devices, the optimum power source, and the implants in animals, followed and are explained on the pages of this thesis.

Here only the main conclusions are posited:

- The computational model of oxygen distribution developed for a retina with 9 calculates the oxygen tension required to treat humans for mild (100mmHg) to severe (250mmHg) diabetic retinopathy, the location of the diffusor in the vitreous (0.2mm to 1mm from the retina), and the oxygen flux (0.25nmol/s) the diffusor must supply.
- Two MEMS devices that were designed—the oxytransporter (transports oxygen from the atmosphere) and the oxygenator (generates oxygen by electrolysis of water taken from the vitreous through osmosis)—performed similar in rabbits and in benchtop: oxygen tension of 100mmHg at the oxytransporter's diffusor, and oxygen tension greater than 200mmHg at the oxygenator's diffusor. The oxygenator provided 0.042nmol/s of oxygen in the rabbit, equivalent to 0.19nmol/s for a human-sized diffusor.
- The metabolic study of ischemia in rabbit eyes implanted with the oxytransporter showed improvement on inflammatory markers that are associated with hypoxia, suggesting the device may affect hypoxia. More robust trials are needed.

7.6 REFERENCES

[7.1] J. H. Chang, Y. Liu and Y. Tai, "Long term glass-encapsulated packaging for implant electronics," *2014 IEEE 27th International Conference on Micro Electro Mechanical Systems (MEMS)*, San Francisco, CA, pp.1127-1130. (2014) doi: 10.1109/MEMSYS.2014.6765844

[7.2] Schnichels S, Blak M, Hurst J, et al. "Establishment of a retinal hypoxia organ culture model". *Biol Open*.6(7):1056-1064. (2017). doi:10.1242/bio.025429

[7.3] D'Angelo G., Duplan E., Boyer N., Vigne P., Frelin C. "Hypoxia up-regulates prolyl hydroxylase activity: a feedback mechanism that limits HIF-1 responses during reoxygenation." *J Biol Chem*. **3**;278(40):38183-7. (2003) doi: 10.1074/jbc.M302244200 Epub 2003 Jul 21.

[7.4] Ridder D.A., Schwaninger M. "NF-kappaB signaling in cerebral ischemia." *Neuroscience*. **6**;158:3. pp.995-1006. (2009) doi: 10.1016/j.neuroscience.2008.07.007. Epub 2008 Jul 10.

[7.5] Shen H.M., Liu ZG. "JNK signaling pathway is a key modulator in cell death mediated by reactive oxygen and nitrogen species." *Free Radic Biol Med*. **15**;40:6 pp.928-39. (2006) doi: 10.1016/j.freeradbiomed.2005.10.056 Epub 2005 Nov 21.

[7.6] Bessero A.C., Chiodini F., Rungger-Brandle E., Bonny C., Clarke P.G.H. "Role of the c-Jun N-terminal kinase pathway in retinal excitotoxicity, and neuroprotection by its inhibition." *J. Neurochem*. **113**, pp..1307–1318. (2010) doi: 10.1111/j.1471-4159.2010.06705.x